# A critical assessment of possible pitfalls in absolute configuration assignment using Vibrational Circular Dichroism.

**Elke Debie**

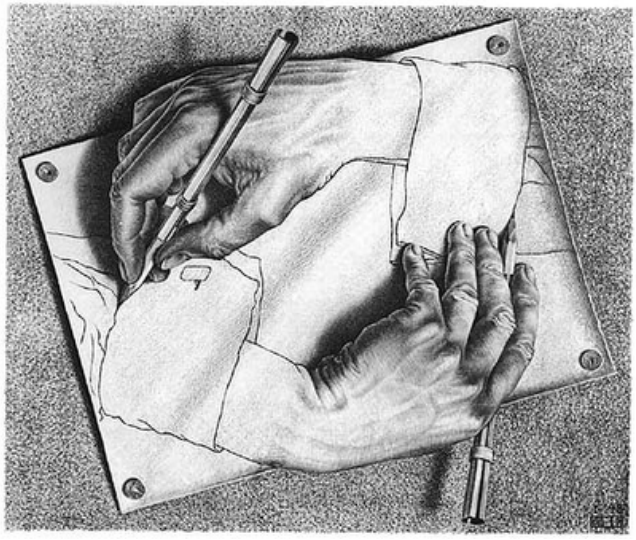

# A critical assessment of possible pitfalls in absolute configuration assignment using Vibrational Circular Dichroism.

**Elke Debie**

Promotor : Prof. Dr. P. Bultinck, Ghent University
co-promotor: Prof. Dr. W.A. Herrebout, University of Antwerp

Thesis submitted in fulfillment of the requirements for the degree of Doctor (Ph.D.) in Sciences : Chemistry

Department of Inorganic and Physical Chemistry
Faculty of Sciences
2008

UNIVERSITEIT GENT

Faculteit Wetenschappen

Dit werk kwam tot stand in het kader van een beurs van het FWO-Vlaanderen (Fonds voor Wetenschappelijke Onderzoek)

# Contents

# Abbreviations

| | |
|---|---|
| AAT | atomic axial tensor |
| AC | absolute configuration |
| APT | atomic polar tensor |
| BO | Born-Oppenheimer |
| CPL | circularly polarized light |
| DFT | density functional theory |
| DO | distributed origin |
| DPM | dual polarization modulation |
| ECD | electronic circular dichroism |
| EMEA | European agency for the evaluation of medicinal products |
| ESI | enantiomeric similarity index |
| FDA | food and drug administration (US) |
| FTIR | Fourier transformed infrared |
| FPC | fixed partial charge |
| GIAO | generalized including/invariant atomic orbitals |
| HF | Hartree-Fock |
| IR | infrared |
| KS | Kohn-Sham |
| LB | linear birefringence |
| LDA | local density approximation |
| LIA | lock-in amplifier |
| LOA | London atomic orbitals |
| LPL | linearly polarized light |
| MCT | mercury cadmium telluride (detector) |
| MFPT | magnetic field perturbation theory |

| | |
|---|---|
| MO | molecular orbital |
| MP2 | second-order Møller-Plesset perturbation theory |
| NMR | nuclear magnetic resonance |
| OR | optical rotation |
| PCM | polarizable continuum model |
| PEM | photoelastic modulater |
| PES | potential energy surface |
| RCP/LCP | right/left circularly polarized light |
| RHWP | rotating half-wave plate |
| S/N | signal to noise ratio |
| SCF | self consistent field |
| VCD | vibrational circular dichroism |
| VCD | vibronic coupling theory |
| XRD | X-ray diffraction |
| ZPD | zero path difference |

# 1

# Introduction

## 1.1 Chirality

The term chiral is used to describe an object that is non-superimposable on its mirror image and is derived from the Greek word for hand, $\chi\epsilon\iota\rho$. It is clear that *chiral* refers to a spatial property of objects, including molecules. Two mirror images of a molecule that cannot be superimposed onto each other are referred to as enantiomers or optical isomers. For chemists, the R / S system is the most important nomenclature system for denoting enantiomers. It labels each chiral center R or S according to a system by which its substituents are each assigned a priority, according to the Cahn Ingold Prelog priority rules, based on atomic number [8]. An enantiomer can also be named by the direction in which it rotates the plane of polarized light. If it rotates the light clockwise (as seen by a viewer toward whom the light is traveling), that

enantiomer is labeled (+). Its mirror-image is labeled (-). Enantiomers are identical with respect to ordinary chemical reactions and properties (i.e. will have the same mass, will have identical NMR spectra, identical IR spectra, etc. ), but differences arise when they are in the presence of other chiral molecules or objects. Different enantiomers of chiral compounds often taste and smell differently and have different effects as drugs. Both isomers of limonene e.g., have different odors: (-)-limonene smells piny and turpentine like and (+)-limonene has a pleasing orange scent. Molecules that contain more than one chiral center can form isomers that have opposite configurations at one or more of the chiral centers but are not mirror images of each other. Diastereomers have different physical properties.

Chiral molecules are constituents of a large proportion of therapeutic agents. By the end of the 20th century ca. half of the chiral drugs were single-enantiomers and the other half racemic. The situation is different today. The market share of single-enantiomers is rising annually [9, 10, 11, 12]. One enantiomer may be less active, inactive, toxic or may give rise to a totally different pharmacological response. The best known example that illustrates the possible differences in activity between enantiomers is $Thalidomide^{®}$, also known as $Softenon^{®}$. Thalidomide was first marketed in Europe in the late 1950's. It was used as a sleeping pill and to treat morning sickness during pregnancy. At that time no one knew the teratogenic S enantiomer caused birth defects [13]. Some of the new single-enantiomeric drugs are obtained via a *chiral switch*, in which a single enantiomer from an existing racemic drug is developed as a new drug [12]. An illustration of such a drug is $Ibuprofen^{®}$. Its main analgesic activity resides predominately in the S enantiomer [14].

There are various reasons to prefer single-enantiomers over racemic mixtures as new drugs. The single-enantiomeric drug consists of one agent instead of a mixture of two distinct drugs, which simplifies the interpretation of the basic pharmacology, therapeutic and toxic effects, pharmacokinetic properties and the relationship of plasma concentrations to effects. Other advantages may include reduced dosage, reduced drug interactions and reduced toxicity. These factors have led to an increasing preference for single enantiomers in both industry and regulatory authorities. In 1992 the FDA (Food and Drug Administration

USA) issued its guidelines governing the development of new chiral drugs [15]. Other regulatory bodies around the world such as the European Agency for the Evaluation of Medicinal Products in Europe (EMEA) followed. Until 1987, the FDA did not explicitly require the inclusion of information on the enantiomer composition of the chiral substances in new-drug applications. In fact a broad and serious examination of the role of chirality in new-drug development only began during the 1980s. This has resulted from the considerable advances in the synthesis, analysis and separation of chiral molecules [11].

The demand for enantiopure chiral components is not only rising in pharmaceutical industry but also in other sectors, as flavor and aroma chemicals, agricultural chemicals and specialty materials [10, 11]. Given the combination of the rapidly growing market for chiral drugs and the general need to determine absolute configurations of the chiral molecules, there is evidently a need for tools that allow accessible absolute configuration determining.

Single-crystal X-ray diffraction (XRD) using anomalous scattering is the most frequently used tool to reveal absolute configurations [16, 17]. This technique, however, requires the availability of well-defined crystals and the presence of heavy atoms in order to subject the crystal to anomalous scattering. These conditions are not always met. In case of NMR, chiral solvents or chiral shift-reagents are needed to form diastereomers and therefore to eliminate the degeneracy of the enantiomers [18, 19]. A third technique is electronic circular dichroism (ECD) in which the differential absorption between left and right circularly polarized light is measured in the UV/VIS region [20, 21, 22, 23, 24]. When a chiral molecule does not contain a UV-chromophore, ECD has the disadvantage that it requires extra synthetic steps to introduce chromophores. Optical rotation [25, 26, 27] obviously is also a well-known technique. Another method, determining the absolute configuration through retrosynthesis, is very labor-intensive.

Another relatively new method in this context is vibrational circular dichroism (VCD). It combines the structural specificity of IR spectroscopy with the stereochemical sensitivity of circular dichroism (CD). Its main advantage is that measurements can be made for solutions. In Table 1.1 the different methods are compared, by considering their advantages and disadvantages.

**Table 1.1:** Overview of the different techniques that can be applied for absolute configuration assignment.

| Technique | Advantage | Disadvantage |
|---|---|---|
| X-ray diffraction (XRD) | -reliable<br>-regulatory standard | -need for good quality single crystals<br>-need for dispersive scatters |
| Nuclear Magnetic Resonance (NMR) | -well known technique | -need for chiral shift reagents, chiral additives or derivatization |
| Electronic Circular Dichroism (ECD) | -applicable for molecules in solution | -only a few bands are available<br>-introduction/presence of chromophores |
| Optical Rotation (OR) | -relatively easy to measure | -high level calculations necessary<br>-only one property/value is measured/calculated<br>-sign depends on the solvent used |
| Vibrational Circular Dichroism (VCD) | -applicable in solution<br>-applicable for a wide range of molecules | -assignments are not straightforward |

## 1.2 Vibrational Circular Dichroism

Circular Dichroism (CD) is the difference in absorption of left (LCPL) and right (RCPL) circularly polarized light (CPL). Because of their handedness, only chiral molecules, show a CD signal different from zero. Moreover, enantiomers have CD of equal magnitude, but opposite signs. In contrast to visible-UV CD, which arises from electronic transitions, VCD originates from vibrational transitions [28, 29, 30, 31]. As a consequence even molecules lacking an UV chromphore can be studied. Moreover, the VCD spectra contain more spectral features than electronic CD spectra. Another technique using CPL in the IR region is Raman Optical Activity (ROA). This method relies on the difference in Raman intensity for right and left circularly polarized light [29]. This method, however, will not further be discussed.

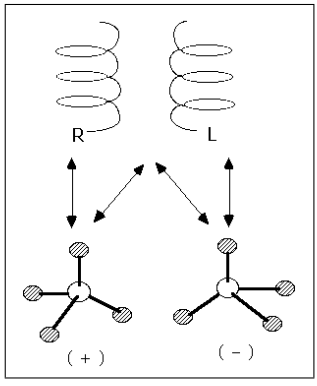


**Figure 1.1:** The interaction of right circularly polarized light (RCPL) and left circularly polarized light (LCPL) with a chiral molecule.

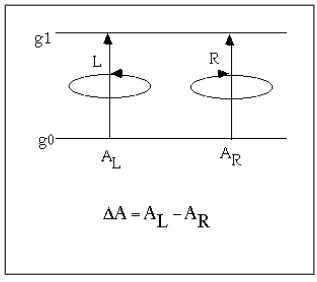


**Figure 1.2:** Differential absorption of LCPL and RCPL.

In classical IR absorption spectra no stereochemical information is embedded. Mirror image molecules have identical unpolarized IR absorption intensities, but show opposite VCD spectra. The latter is a reflection of the chiral nature of the compound that was measured. However, it does not provide direct information about the actual absolute configuration. For a reliable evaluation, VCD intensities are to be calculated for the specified isomer. Comparing the signs of the experimental VCD bands with those in the calculated VCD spectrum allows us to assign the stereochemistry of the molecule [32, 33, 34, 35].

The principal area of application of VCD is structure elucidation of biologically significant molecules including peptides, proteins, nucleic acids, carbohydrates, natural products and pharmaceutical molecules [36, 37, 38, 39]; also, as mentioned above, it has growing potential as a chiral diagnostic probe.

### 1.2.1 Absolute configuration determination by VCD: procedure

To determine the absolute configuration of a molecule, the following steps have to be taken:

- Measurement of the experimental VCD spectrum.
- Construction of a theoretical VCD spectrum.
    1. Conformational analysis
    2. DFT calculation of the VCD spectra for each conformer found.
    3. Construction of a population-weighted VCD spectrum.
- Assignment of the absolute configuration by comparing theory and experiment.

### 1.2.2 Brief historical overview

In the early 1970s, before VCD was experimentally observed, theoretical studies and predictions of VCD were performed [40, 41, 42], using empirical models. These indicated that VCD intensities should be strong enough to be observed. The first experimental VCD measurements were reported in 1973 by Holzwarth et al. [43]. In 1978 Nafie implemented the FTIR VCD spectrometer [44, 45]. In 1997 the first commercial VCD

spectrometer, called the Chiral*IR* [46] was made by BioTools. Nowadays FTIR VCD instruments are available from various manufacturers.

In the mid 1980s a theory that permitted the prediction of VCD spectra was developed [47, 48]. This theory was implemented using ab initio computational methods. The first calculations were based on Hartree-Fock methods. Introduction of post-HF methods, such as MP2 generally improved the simulated spectra. However, due to the large computational cost, this approach was practically not feasible [49]. The development of density functional theory (DFT) and the introduction of hybrid functionals in the early 1990s, led to a breakthrough in the calculation of VCD intensities [50]. DFT methods are able to provide better accuracy at a moderate computational cost. The VCD algorithms are implemented in several software packages.

## 1.3 Scope

Vibrational circular dichroism (VCD) is no longer a curious novelty in the field of molecular spectroscopy. As described above, VCD spectrometers are commercially available and the algorithms to calculate the spectra are implemented in various software packages. This implies the routine applicability of VCD for determining absolute configurations. Nowadays, around 30-40 research groups all over the world, both in universities and industrial companies (especially pharmaceutical industry), use VCD. The technique also has been accepted by regulatory agencies (e.g. FDA) as a proof of absolute configuration (AC). The aim of this thesis is to study the limits of the routine applicability of VCD. It is of vital importance that all assignments are done correctly. One misassignment can have serious consequences.

In Chapter 2 the algorithms are discribed, necessary for the calculation of VCD intensity. In Chapter 3 the experimental setup is discussed in further detail to describe the procedure for the comparison of the experimental spectra with theory (Chapter 4). The rest of the thesis is devoted to my experimental results.

In Chapter 5 the question was considered whether it would be useful to distinguish diastereomers through VCD. To this end the VCD spectra of four bicyclo[3.3.0]octane derivates, each containing four chiral centers, have been recorded and calculated. All diastereomers have

been taken into account. This chapter also gives a nice overview about the procedure, followed during an assignment.

Various issues, however, may hinder the interpretation of the experimental VCD spectra: First of all, the conformational analysis of molecules with high flexibility is not straightforward at all. Since vibrational spectroscopy is extremely sensitive to the structure of the molecule, it is very important to find all stable conformers. One conformer can have very large peaks and not taking into account that conformer can hinder the simulation of the experimental spectra. Unfortunately, it is not unthinkable that during conformational analysis one of the conformers was overlooked. Furthermore, flexible molecules give a large number of conformers, for which the VCD spectra need to be calculated. Therefore a huge amount of CPU resources is needed. A VCD assignment of a large and flexible pharmaceutically interesting molecule will be discussed in Chapter 6, as well as a proposal to skirt the problem.

Another issue is that VCD measurements are performed in solution, while the calculations are performed for a single molecule in vacuum. Intermolecular interactions can cause discrepancies between experimental and theoretical spectra. In some cases, chiral molecules in solution are likely to interact mutually. The dimerization will, logically, have an effect on the experimental VCD spectrum. This is mentioned during the VCD study of borneol (Chapter 7). On the other hand, solute molecules can interact with the solvent. The influence of the solvent on the experimental VCD spectrum has been discussed in Chapter 7 for camphor and pulegone.

Additionally, the influence of temperature on the VCD spectra was studied. It was assumed that the interpretation of the experimental spectra would be simplified at lower temperatures. Decreasing temperature implies also a decreasing number of conformers that are to be taken into account for the construction of the Boltzmann weighted spectrum. This was tested in Chapter 8 for 3-methylcyclohexanone, borneol and limonene.

# 2

# Calculation of VCD Intensities

## 2.1 Introduction

In this chapter, an overview of the theory for the calculation of VCD intensities is given. At the outset, it should be mentioned that, within the Born-Oppenheimer (BO) approximation, the electronic contribution to the vibrational magnetic dipole transition moment vanishes. Since both electric and magnetic dipole transition moments are required, the calculation of VCD intensities is not trivial. In order to skirt this problem several ad hoc models were developed [51]. In the simplest model, generally referred to as the fixed partial charge (FPC) model, electric and magnetic dipole transition moments are calculated by attaching charges to each atom. Many extensions of this model were developed, allowing more flexibility in the description of the molecular charge distribution during nuclear displacement. The most direct approach is to adopt

molecular wave functions more accurately than those specified by the BO approximation. This requires in essence the enlargement of the number of adiabatic electronic states contributing to the vibrational eigenfunctions, i.e., BO functions associated with excited electronic states must be mixed into the ground-state eigenfunctions.

In this chapter the vibronic coupling theory of Nafie and Freedman [52] and subsequently, the magnetic field perturbation theory of Stephens are introduced [47]. The implementation and evaluation of the VCD expressions will be discussed [53].

## 2.2 Theory of VCD

Under Beer's law, for a transition, o→ n, the integrated absorbance, $\epsilon$, and differential absorbance (CD), $\Delta\epsilon$, of a substance are proportional to the dipole and rotational strengths $D_{on}$ and $R_{on}$ respectively:

$$D_{on} = \langle \Psi_o \left| \mu_{elec} \right| \Psi_n \rangle \bullet \langle \Psi_n \left| \mu_{elec} \right| \Psi_o \rangle \tag{2.1}$$

$$R_{on} = -Im \left[ \langle \Psi_o \left| \mu_{elec} \right| \Psi_n \rangle \bullet \langle \Psi_n \left| \mu_{mag} \right| \Psi_o \rangle \right] \tag{2.2}$$

The dipole strength is related to the intensity of an IR absorption band through the extinction coefficient, $\epsilon$ [25]:

$$D_{on} = 9.184 \cdot 10^{-39} \int_{band} \epsilon \frac{d\bar{\nu}}{\bar{\nu}} \tag{2.3}$$

$\bar{\nu}$ (in wavenumbers) refers to the frequency of the fundamental transition. The units of $D_{on}$ are $esu^2\ cm^2$. The extinction coefficient (in $Lmol^{-1}cm^{-1}$) is related to the absorbance through Beer's Law:

$$A = \epsilon l C \tag{2.4}$$

$l$ is the path length (in $cm$) and $C$ the molar concentration (in $mol\ L^{-1}$).

During VCD experiments the difference in absorption, $\Delta A$, between left circularly and right circularly polarized IR light is measured:

$$\Delta A = A_L - A_R \tag{2.5}$$

The rotational strength (in $esu^2\ cm^2$) is proportional to the integrated intensity of the VCD absorption band through the differential molar absorptivity ($\Delta\epsilon$) [25]:

$$R_{on} = 2.296 \cdot 10^{-39} \int_{band} \Delta\epsilon \frac{d\bar{\nu}}{\bar{\nu}} \tag{2.6}$$

The electric and magnetic dipole operators, $\mu_{elec}$ and $\mu_{mag}$ in equations 2.1 and 2.2 respectively, are the sums of electron and nuclear operators:

$$\mu_{elec} = \mu^e_{elec} + \mu^n_{elec} = -\sum_i e\vec{r_i} + \sum_I Z_I e\vec{R_I} \tag{2.7}$$

$$\mu_{mag} = \mu^e_{mag} + \mu^n_{mag} = -\sum_i \frac{e}{2mc}\vec{r_i} \times \vec{p_i} + \sum_I \frac{Z_I e}{2M_I c}\vec{R_I} \times \vec{P_I} \tag{2.8}$$

The quantities $e$, $m$, $\vec{r_i}$ and $\vec{p_i}$, are the charge, mass, position and momentum of the $i$'th electron, whereas, $Z_I e$, $M_I$, $\vec{R_I}$ and $\vec{P_I}$ refer to the charge, mass, position and momentum of the $I$'th nucleus. $c$ is the speed of light. As can be deduced from equation 2.2, the rotational strength is positive or negative depending on the angles between the two transition vectors. The rotational strength is zero for an angle equal to $\frac{\pi}{2}$. Assuming that the transition involved is a vibronic transition between the lowest and the first vibrational levels on the ground electronic state of the adiabatic BO potential energy surface, the states $o$ and $n$, may be labeled as (0,0) and (0,1), respectively. The first label refers to the electronic state, whereas the second label corresponds with the vibrational state. If the wave functions in equations 2.1 and 2.2 can be written in BO form:

$$\Psi_o = \Psi(r,Q)_{0,0} = \psi(r,Q)_0 \Phi(Q)_{0,0} \tag{2.9}$$

$$\Psi_n = \Psi(r,Q)_{0,1} = \psi(r,Q)_0 \Phi(Q)_{0,1} \tag{2.10}$$

The total vibronic wave functions are approximated as the product of the vibrational($\Phi(Q)$) and electronic ($\psi(r,Q)$) wave functions, where the implicit dependence of the wave functions on the electronic and nuclear coordinates is given, the latter in terms of displacements along normal coordinates, Q=$Q_1$,...,$Q_{3N-6}$. The electric and magnetic dipole

transition moments with the implicitly normalized wave functions 2.9 and 2.10 are:

$$\langle \psi_0 \Phi_{0,0} | \mu_{elec} | \psi_0 \Phi_{0,1} \rangle = \langle \Phi_{0,0} | \langle \psi_0 | \mu^e_{elec} | \psi_0 \rangle^e + \mu^n_{elec} | \Phi_{0,1} \rangle^n \tag{2.11}$$

$$\begin{aligned} \langle \psi_0 \Phi_{0,0} | \mu_{mag} | \psi_0 \Phi_{0,1} \rangle &= \left\langle \Phi_{0,0} \left| \left\langle \psi_0 \left| \mu^e_{mag} \right| \psi_0 \right\rangle^e + \mu^n_{mag} \right| \Phi_{0,1} \right\rangle^n \\ &= \left\langle \Phi_{0,0} \left| \mu^n_{mag} \right| \Phi_{0,1} \right\rangle^n \end{aligned} \tag{2.12}$$

The $e$ and $n$ superscripts, related to the brackets, refer to the integration over the electronic or nuclear coordinates respectively.

Because of the Hermitian and imaginary nature of $\mu^e_{mag}$, together with the fact that the singlet non-degenerate electronic ground state $\psi_0$ can be chosen to be real, the electronic contribution to the magnetic dipole transition moment is canceled. In order to introduce the electronic contribution to the magnetic dipole transition moment, many empirical models were developed which explicitly incorporate nuclear displacements and the electronic - nuclear interaction in some fashion [47]. Alternatively one is forced to a treatment, beyond BO, to arrive at the description at the VCD intensities [52]. The wave function is expanded in terms of adiabatic BO wave functions. For an arbitrary electronic - vibrational state ($e$',$v$') one may write:

$$\Psi(r,Q)_{e',v'} \approx \psi(r,Q)_{e'} \Phi(Q)_{e',v'} - \sum_{e(\neq e'),v} a(Q)_{e'v',ev} \psi(r,Q)_e \Phi(Q)_{e,v} \tag{2.13}$$

where the coefficients, $a(Q)_{e'v',ev}$, are defined, on the basis of Rayleigh-Schrödinger perturbation theory [54] using the part of the nuclear kinetic energy which was neglected in the BO approximation, as:

$$a(Q)_{e'v',ev} = \frac{\left\langle \psi(r,Q)_e \Phi(Q)_{e,v} \left| \hat{T} \right| \psi(r,Q)_{e'} \Phi(Q)_{e',v'} \right\rangle_0}{(E(Q)_{e,v} - E(Q)_{e',v'})_0} \tag{2.14}$$

with

$$\hat{T} = -\frac{\hbar^2}{2} \left[ \left( \frac{\partial^2}{\partial Q^2} \right)_e + 2 \left( \frac{\partial}{\partial Q} \right)_e \left( \frac{\partial}{\partial Q} \right)_n \right] \tag{2.15}$$

In equation 2.15, the subscripts indicate whether the operator acts on the electronic or the nuclear part of the wave function. Since electrons do not make a transition from one electronic state to the other during a vibration, these terms were neglected in the adiabatic approximation.

The nuclear dependence of the electronic wave function may be expressed as a Taylor expansion around the equilibrium geometry of the ground electronic state, truncating after the linear term:

$$\psi(Q)_{e'} \approx (\psi_{e'})_0 + (\frac{\partial \psi_{e'}}{\partial Q})_0 Q \tag{2.16}$$

This equation is also known as the Herzberg-Teller coupling [52] or adiabatic coupling, since electron and nuclear wave functions can still be separated:

$$\Psi(r,Q)_{e',v'} \approx \left[(\psi_{e'})_0 + (\frac{\partial \psi_{e'}}{\partial Q})_0 Q\right] \Phi_{e',v'} \tag{2.17}$$

The first term of equation 2.15 will be omitted from further consideration since it is a second order term. Substitution of equations 2.14 and 2.17 in equation 2.13, yields, for the wave function of interest for VCD:

$$\begin{aligned}\Psi(r,Q)_{0,v'} \approx\ & (\psi_0)_0 \Phi_{0,v'} + (\frac{\partial \psi_0}{\partial Q})_0 Q \Phi_{0,v'} \\ & + \hbar^2 \sum_{e(\neq 0),v} \frac{\left\langle \psi_e \left| \frac{\partial \psi_0}{\partial Q} \right\rangle_0 \left\langle \Phi_{e,v} \left| \frac{\partial \Phi_{0,v'}}{\partial Q} \right\rangle_0 \right.\right.}{(E_{e,v} - E_{0,v'})_0} (\psi_e)_0 \Phi_{e,v}\end{aligned} \tag{2.18}$$

A BO corrected wave function was derived using adiabatic and non-adiabatic coupling. Introducing a general operator $\theta = \theta^e + \theta^n$, the transition moment between the vibronic states $0,0 \rightarrow 0,1$ can be written as:

$$\begin{aligned}\langle \Psi_{0,0} |\theta| \Psi_{0,1} \rangle \approx\ & \langle \psi_0 \Phi_{0,0} |\theta| \psi_0 \Phi_{0,1} \rangle_0 \\ & + \left\langle \psi_0 \Phi_{0,0} |\theta| \frac{\partial \psi_0}{\partial Q} Q \Phi_{0,1} \right\rangle_0 + \left\langle \frac{\partial \psi_0}{\partial Q} Q \Phi_{0,0} |\theta| \psi_0 \Phi_{0,1} \right\rangle_0 \\ & + \hbar^2 \sum_{e(\neq 0),v} \langle \psi_0 \Phi_{0,0} |\theta| \psi_e \Phi_{e,v} \rangle \frac{\left\langle \psi_e \left| \frac{\partial \psi_0}{\partial Q} \right\rangle_0 \left\langle \Phi_{e,v} \left| \frac{\partial \Phi_{0,1}}{\partial Q} \right\rangle_0 \right.\right.}{(E_{e,v} - E_{0,1})_0} \\ & + \hbar^2 \sum_{e(\neq 0),v} \frac{\left\langle \psi_e \left| \frac{\partial \psi_0}{\partial Q} \right\rangle_0 \left\langle \Phi_{e,v} \left| \frac{\partial \Phi_{0,0}}{\partial Q} \right\rangle_0 \right.\right.}{(E_{e,v} - E_{0,0})_0} \langle \psi_e \Phi_{e,v} |\theta| \psi_0 \Phi_{0,0} \rangle\end{aligned} \tag{2.19}$$

Splitting the operator in its electrical and nuclear parts gives:

$$\langle \Psi_{0,0} | \theta^n | \Psi_{0,1} \rangle = \langle \Phi_{0,0} | \theta^n | \Phi_{0,1} \rangle \tag{2.20}$$

Only the first term is retained. Other terms can be reduced to zero due to the orthonormality of the electronic wave functions ($\psi$).

$$\begin{aligned}
\langle \Psi_{0,0} | \theta^e | \Psi_{0,1} \rangle \approx & \langle \psi_0 \Phi_{0,0} | \theta^e | \psi_0 \Phi_{0,1} \rangle \\
& + \left\langle \psi_0 \Phi_{0,0} | \theta^e | \frac{\partial \psi_0}{\partial Q} Q \Phi_{0,1} \right\rangle_0 + \left\langle \frac{\partial \psi_0}{\partial Q} Q \Phi_{0,0} | \theta^e | \psi_0 \Phi_{0,1} \right\rangle_0 \\
& + \hbar^2 \sum_{e(\neq 0),v} \langle \psi_0 \Phi_{0,0} | \theta^e | \psi_e \Phi_{e,v} \rangle \frac{\left\langle \psi_e \left| \frac{\partial \psi_0}{\partial Q} \right. \right\rangle_0 \left\langle \Phi_{e,v} \left| \frac{\partial \Phi_{0,1}}{\partial Q} \right. \right\rangle_0}{(E_{e,v} - E_{0,1})_0} \\
& + \hbar^2 \sum_{e(\neq 0),v} \frac{\left\langle \psi_e \left| \frac{\partial \psi_0}{\partial Q} \right. \right\rangle_0 \left\langle \Phi_{e,v} \left| \frac{\partial \Phi_{0,0}}{\partial Q} \right. \right\rangle_0}{(E_{e,v} - E_{0,0})_0} \langle \psi_e \Phi_{e,v} | \theta^e | \psi_0 \Phi_{0,0} \rangle
\end{aligned} \tag{2.21}$$

The first term of equation 2.21 does not contribute to the vibrational transition moment as no overlap is possible between the vibrational levels of the same electronic state. For the remaining term nuclear dependence of the vibrational integrals is obtained through Q and $\frac{\partial}{\partial Q}$. If the assumption is made that the energy differences between specific vibronic levels on different electronic energy surfaces is approximately equivalent to the separation of the BO surfaces at the equilibrium geometry, regardless of the vibrational excitations, it can be written that:

$$\frac{1}{(E_{e,v} - E_{0,v'})_0} \approx \frac{1}{(E_e - E_0)_0} \tag{2.22}$$

This is based on the fact that energy differences between vibrational states are much smaller than between electronic states. After some further manipulation and recognizing the antisymmetry of the operator,

$\frac{\partial}{\partial Q}$, one arrives at:

$$\begin{aligned}\langle \Psi_{0,0} | \theta | \Psi_{0,1} \rangle \approx & \langle \Phi_{0,0} | \theta^n | \Phi_{0,1} \rangle \\ & + \left[ \left\langle \psi_0 | \theta^e | \frac{\partial \psi_0}{\partial Q} \right\rangle + \left\langle \frac{\partial \psi_0}{\partial Q} | \theta^e | \psi_0 \right\rangle \right]_0 \langle \Phi_{0,0} | Q | \Phi_{0,1} \rangle \\ & + \hbar^2 \sum_{e(\neq 0)} \frac{\langle \psi_0 | \theta^e | \psi_e \rangle_0 \left\langle \psi_e \left| \frac{\partial \psi_0}{\partial Q} \right. \right\rangle_0}{(E_e - E_0)_0} \left\langle \Phi_{0,0} \left| \frac{\partial \Phi_{0,1}}{\partial Q} \right. \right\rangle \\ & + \hbar^2 \sum_{e(\neq 0)} \frac{\left\langle \psi_0 \left| \frac{\partial \psi_e}{\partial Q} \right. \right\rangle_0 \langle \psi_e | \theta^e | \psi_0 \rangle_0}{(E_e - E_0)_0} \left\langle \Phi_{0,1} \left| \frac{\partial \Phi_{0,0}}{\partial Q} \right. \right\rangle \end{aligned} \tag{2.23}$$

In equation 2.23 the second term traditionally is considered as adiabatic whereas the last two terms are non-adiabatic and beyond the BO approximation. Specifying the operator as being the electric dipole operator (equation 2.7), the non-adiabatic terms will cancel. This is due to the anti-symmetric property of the $\frac{\partial}{\partial Q}$ operator with respect to interchange of the wave functions.

$$\left\langle \Phi_{0,0} \left| \frac{\partial}{\partial Q} \right| \Phi_{0,1} \right\rangle = - \left\langle \Phi_{0,1} \left| \frac{\partial}{\partial Q} \right| \Phi_{0,0} \right\rangle \tag{2.24}$$

Because $\mu^e_{elec}$ is Hermitian it can be written that:

$$\langle \psi_0 | \mu^e_{elec} | \psi_e \rangle = \langle \psi_e | \mu^e_{elec} | \psi_0 \rangle \tag{2.25}$$

Taking into account these two properties, the expression for the electric dipole transition moment becomes:

$$\begin{aligned}\langle \Psi_{0,0} | \mu_{elec} | \Psi_{0,1} \rangle = & \langle \Phi_{0,0} | \mu^n_{elec} | \Phi_{0,1} \rangle \\ & + 2 \left\langle \psi_0 | \mu^e_{elec} | \frac{\partial \psi_0}{\partial Q} \right\rangle_0 \langle \Phi_{0,0} | Q | \Phi_{0,1} \rangle \end{aligned} \tag{2.26}$$

The non-adiabatic terms cancel and equation 2.26 is entirely attributable to the Herzberg-Teller coupling. This means that the electronic contribution to the induced dipole moment, which is the result of charge distribution changes induced by vibrational transitions, can be properly described by introducing explicit nuclear position dependence to the ground electronic wave function.

Due to the Hermitian and imaginary nature of $\mu^e_{mag}$, the integrals by wave function interchange are anti-symmetric. So, for $\theta$ being the magnetic dipole operator, the first two terms will cancel.

$$\langle \psi_0 \left| \mu^e_{mag} \right| \psi_e \rangle = - \langle \psi_e \left| \mu^e_{mag} \right| \psi_0 \rangle \tag{2.27}$$

The expression for the magnetic dipole transition moment becomes:

$$\langle \Psi_{0,0} \left| \mu_{mag} \right| \Psi_{0,1} \rangle = \langle \Phi_{0,0} \left| \mu^n_{mag} \right| \Phi_{0,1} \rangle + 2\hbar^2 \sum_{e(\neq 0)} \frac{\langle \psi_0 \left| \mu^e_{mag} \right| \psi_e \rangle_0 \left\langle \psi_e \left| \frac{\partial \psi_0}{\partial Q} \right\rangle_0 \right.}{(E_e - E_0)_0} \left\langle \Phi_{0,0} \left| \frac{\partial \Phi_{0,1}}{\partial Q} \right\rangle \right. \tag{2.28}$$

In this expression a non-vanishing electronic contribution to the magnetic dipole moment is obtained by expanding the wave function in terms of adiabatic BO wave functions. Therefore excited electronic states are involved ("sum over states"). The electronic part of the induced magnetic moment is caused by the changes of the motion state of the electrons which are a direct response to the changes in the nuclear momentum. The response to the ground electronic state is described by mixing excited electronic states into the unperturbed ground electronic state wave functions. Equations 2.26 and 2.28 constitute the Vibronic Coupling Theory (VCT) of Nafie en Freedman [52]. These formulations, however, fail to arrive at usable equations, since the result obtained, when corrections to the BO approximation are included, all contain sums over complete sets of excited electronic states. Even if exact adiabatic electronic wave functions were to be calculable, these formulations would still require an infinite number of such functions. Drastic truncation of such sums or invocation of the average-energy approximation permits their evaluation; however, the accuracy of the results obtained is indeterminate. This problem was by-passed by Stephens' magnetic field perturbation theory (MFPT) [47]. The perturbation of the electronic wave function, which manifests itself in equation 2.28 as a sum over excited electronic states, may be treated in an explicit manner by invoking the magnetic field dependence of the wave function. This magnetic field dependence of the electronic ground state can be expressed as a Taylor expansion, again truncated after the linear term:

$$\psi(\vec{B})_0 \approx (\psi_0)_{\vec{B}=0} + \left( \frac{\partial \psi_0}{\partial \vec{B}} \right)_{\vec{B}=0} \cdot \vec{B} \tag{2.29}$$

The derivatives in the second term of equation 2.29 are evaluated in absence of the magnetic field ($\vec{B} = 0$). The perturbed electronic Hamiltonian in the presence of a magnetic field perturbation can be written to the first order:

$$H(\vec{B}) = H^0 + \mu^e_{mag} \cdot \vec{B} \tag{2.30}$$

with $H^0$ being the unperturbed Hamiltonian in the absence of a magnetic field and the first order perturbation Hamiltonian ($H'(\vec{B})$) is given by:

$$H'(\vec{B}) = \mu^e_{mag} \cdot \vec{B} \tag{2.31}$$

Using these perturbation series, the electronic ground state wave function can be written as:

$$\psi(\vec{B})_0 \approx (\psi_0)_{\vec{B}=0} - \sum_{e(\neq 0)} \frac{\langle \psi_e | \mu^e_{mag} | \psi_0 \rangle}{E_e - E_0} \cdot \vec{B}\psi_e \tag{2.32}$$

Combining equations 2.32 and 2.29, one may identify the following relationship:

$$(\frac{\partial \psi_0}{\partial \vec{B}})_{\vec{B}=0} = - \sum_{e(\neq 0)} \frac{\langle \psi_e | \mu^e_{mag} | \psi_0 \rangle}{E_e - E_0} \psi_e \tag{2.33}$$

Insertion of the complex conjugate of equation 2.33 into the electronic part of equation 2.28 yields an expression in which the sum over states does not appear. The electronic contribution to the magnetic dipole transition moment is proportional to the overlap of two derivatives of the ground state electronic wave function:

$$\begin{aligned} \langle \Psi_{0,0} | \mu_{mag} | \Psi_{0,1} \rangle = & \langle \Phi_{0,0} | \mu^n_{mag} | \Phi_{0,1} \rangle \\ & + 2\hbar^2 \left\langle \frac{\partial \psi_0}{\partial \vec{B}} \middle| \frac{\partial \psi_0}{\partial Q} \right\rangle_0 \left\langle \Phi_{0,0} \middle| \frac{\partial \Phi_{0,1}}{\partial Q} \right\rangle \end{aligned} \tag{2.34}$$

where the subscript 0 indicates that the derivatives are to be evaluated at zero magnetic field and at the equilibrium geometry, respectively.

Invoking the harmonic oscillator nuclear wave functions, a number of simplifications are possible. The potential energy of the ground state can be written as:

$$E_0(Q) = E_0(Q_0) + \frac{1}{2} \sum_{k=1}^{3N-6} \kappa_k Q_k^2 \tag{2.35}$$

Each normal coordinate $Q_i$ is associated with a frequency $\omega_i = \sqrt{\kappa_i}$. For the $0 \rightarrow 1$ excitation of the $i^{th}$ vibrational normal mode, it is known that:

$$\langle \Phi_{0,0} | Q_i | \Phi_{0,1} \rangle = \sqrt{\frac{E_{0,1} - E_{0,0}}{2\omega_i^2}} = \sqrt{\frac{\hbar}{2\omega_i}} \tag{2.36}$$

with

$$E_{0,1} - E_{0,0} = \hbar\omega_i \tag{2.37}$$

Using the commutator relationship

$$[Q_i, T_N] = \hbar^2 \frac{\partial}{\partial Q_i} \tag{2.38}$$

it can be written that:

$$\left\langle \Phi_{0,0} | \frac{\partial \Phi_{0,1}}{\partial Q_i} \right\rangle = \sqrt{\frac{\omega_i}{2\hbar}} \tag{2.39}$$

The displacements of atomic coordinates from the equilibrium values, $R^0_{I\alpha}$ are related to normal coordinates, $Q_i$, by the relations:

$$\begin{aligned} R_{I\alpha} - R^0_{I\alpha} &= \sum_i S_{I\alpha,i} Q_i \\ \frac{\partial R_{I\alpha}}{\partial Q_i} &= S_{I\alpha,i} \\ \frac{\partial}{\partial Q_i} &= \sum_{I\alpha} \frac{\partial}{\partial R_{I\alpha}} S_{I\alpha,i} \end{aligned} \tag{2.40}$$

$S_{I\alpha}$ is the displacement vector of the $I^{th}$ atom in direction $\alpha$, incorporating the factor $\frac{1}{\sqrt{M_I}}$.

Using equations 2.36 and 2.40, $\langle \Psi_{0,0} | \mu_{elec} | \Psi_{0,1} \rangle$ can be rewritten in the atomic polar tensor notation (APT):

$$\begin{aligned} \langle \psi_0 \Phi_{0,0} | (\mu_{elec})_\beta | \psi_0 \Phi_{0,1} \rangle &= \sqrt{\frac{\hbar}{2\omega_i}} \sum_{I\alpha} \left( \frac{\partial (\mu^0_{elec})_\beta}{\partial R_{I\alpha}} \right)_0 S_{I\alpha,i} \\ &= \sqrt{\frac{\hbar}{2\omega_i}} \sum_{I\alpha} P^I_{\alpha\beta} S_{I\alpha,i} \end{aligned} \tag{2.41}$$

The atomic polar tensor $P^I_{\alpha\beta}$, is a measure of the change in the $\beta$'th component of the adiabatic dipole moment of the ground electronic state

with respect to the displacement from equilibrium $R_{I\alpha} - R^0_{I\alpha}$ of the $I$'th nucleus in direction $\alpha$, and is readily available by numerical or analytical methods from quantum chemistry codes such as GAUSSIAN [55] and others.

The magnetic dipole transition moment may be written in a similar fashion in terms of atomic axial tensors $M^I_{\alpha\beta}$. Taking into account equation 2.39 and the transformations in equation 2.40, the electronic part of the magnetic dipole transition moment can be rewritten as:

$$\begin{aligned}\left\langle \Psi_{0,0} \left| \left(\mu^e_{mag}\right)_\beta \right| \Psi_{0,1} \right\rangle &= -2\hbar^2 \sum_\alpha \left\langle \frac{\partial \psi_0}{\partial \vec{B}_\beta} \left| \frac{\partial \psi_0}{\partial R_{I\alpha}} \right\rangle_0 \left\langle \Phi_{0,0} \left| \frac{\partial \Phi_{0,1}}{\partial Q_i} \right\rangle S_{I\alpha,i} \right. \right. \\ &= -2\sqrt{\frac{\hbar^3 \omega_i}{2}} \sum_\alpha \left\langle \frac{\partial \psi_0}{\partial \vec{B}_\beta} \left| \frac{\partial \psi_0}{\partial R_{I\alpha}} \right\rangle_0 S_{I\alpha,i} \right.\end{aligned} \tag{2.42}$$

$\beta$ refers to the Cartesian component of the uniform magnetic field. Expressing the nuclear part in terms of the displacement from equilibrium $\vec{R}_I = \vec{R}^0_I + \left(\vec{R}_I - \vec{R}^0_I\right)$ for a particular normal mode, one has for the nuclear contribution:

$$\begin{aligned}\left\langle \Phi_{0,0} \left| \left(\mu^n_{mag}\right)_\beta \right| \Phi_{0,1} \right\rangle &= \left\langle \Phi_{0,0} \left| \sum_I \frac{Z_I e}{2M_I c} \left(\vec{R}^0_I \times \vec{P}_I\right)_\beta \right| \Phi_{0,1} \right\rangle \\ &= \left\langle \Phi_{0,0} \left| \sum_I \frac{-i\hbar Z_I e}{2M_I c} \left(\vec{R}^0_I \times \frac{\partial}{\partial \vec{R}_I}\right)_\beta \right| \Phi_{0,1} \right\rangle \\ &= \sum_{\alpha\gamma} \sum_I \frac{Z_I e}{2ic} \sqrt{\frac{\omega_i}{2\hbar}} \epsilon_{\alpha\beta\gamma} \vec{R}^0_{I\gamma} S_{I\alpha,i}\end{aligned} \tag{2.43}$$

The first part of equation 2.43 results from the fact that, for a normal mode: $\left\langle \Phi_{0,0} \left| \left(\vec{R}_I - \vec{R}^0_I\right) \times \vec{P}_I \right| \Phi_{0,1} \right\rangle = 0$. In deriving the second part we have used $\vec{P}_I = -i\hbar \left(\frac{\partial}{\partial \vec{R}_I}\right)$. The final result arises from the relations 2.36 and 2.40 and

$$\left\langle \Phi_{0,0} \left| \frac{\partial}{\partial \vec{R}_I} \right| \Phi_{0,1} \right\rangle = \frac{M_I}{\hbar^2} \omega_i \left\langle \Phi_{0,0} \left| \left(\vec{R}_I - \vec{R}^0_I\right) \right| \Phi_{0,1} \right\rangle \tag{2.44}$$

By introducing the Levi-Civita tensor $\epsilon_{\alpha\beta\gamma}$ [56], which is an isotropic unit tensor of rank 3 the cross product in equation 2.43 could be rewritten in terms of vector components. The total magnetic dipole transition moment is then written as:

$$\begin{aligned}\left\langle \Psi_{0,0} \left| (\mu_{mag})_\beta \right| \Psi_{0,1} \right\rangle_i &= -\sqrt{2\hbar^3\omega_i} \sum_{I\alpha} \left[ \sum_\gamma \epsilon_{\alpha\beta\gamma} R^0_{I\alpha} \frac{Z_I e i}{4\hbar c} \right. \\ &\left. + \left\langle \frac{\partial \psi_0}{\partial B_\alpha} \middle| \frac{\partial \psi_0}{\partial R_{I\alpha}} \right\rangle_0 \right] S_{I\alpha,i} \\ &= -\sqrt{2\hbar^3\omega_i} \sum_{I\alpha} M^I_{\alpha\beta} S_{I\alpha,i}\end{aligned} \tag{2.45}$$

where the atomic axial tensor (AAT) $M^I_{\alpha\beta}$ is defined as the quantity in the square brackets in equation 2.45.

The atomic polar and axial tensors, $P^I_{\alpha\beta}$ and $M^I_{\alpha\beta}$ can be separated into electronic $E$ and nuclear $N$ parts:

$$P^I_{\alpha\beta} = E^I_{\alpha\beta} + N^I_{\alpha\beta} \tag{2.46}$$

where

$$N^I_{\alpha\beta} = Z_I e \delta_{\alpha\beta} \tag{2.47}$$

and

$$E^I_{\alpha\beta} = 2 \left\langle \psi_0 \left| (\mu^e_{elec})_\beta \right| \frac{\partial \psi_0}{\partial R_{I\alpha}} \right\rangle_0 \tag{2.48}$$

Similarly one can write:

$$M^I_{\alpha\beta} = I^I_{\alpha\beta} + J^I_{\alpha\beta} \tag{2.49}$$

with:

$$J^I_{\alpha\beta} = \sum_\gamma \epsilon_{\alpha\beta\gamma} R^0_{I\alpha} \frac{Z_I e i}{4\hbar c} \tag{2.50}$$

and

$$I^I_{\alpha\beta} = \left\langle \frac{\partial \psi_0}{\partial B_\alpha} | \frac{\partial \psi_0}{\partial R_{I\beta}} \right\rangle \tag{2.51}$$

Expressions for the dipole and rotational strengths for the $i$'th normal mode, can be written by substituting equations 2.41 and 2.45 into equations 2.1 and 2.2.

$$D_{i,01} = \frac{\hbar}{2\omega_i} \left( \sum_{\beta} \sum_{I\alpha} P^I_{\alpha\beta} S_{I\alpha,i} \right)^2 \tag{2.52}$$

$$R_{i,01} = i\hbar^2 \sum_{\beta} \left( \sum_{I\alpha} P^I_{\alpha\beta} S_{I\alpha,i} \sum_{I'\alpha'} M^{I'}_{\alpha'\beta} S_{I'\alpha',i} \right) \tag{2.53}$$

These equations allow us to calculate the vibrational dipole and rotational strengths. In GAUSSIAN equation 2.53 was implemented using Hartree-Fock (HF) or Density Functional Theory (DFT). In the next sections a brief explanation will be given for these two levels of calculations.

## 2.3 Implementation

### 2.3.1 Hartree-Fock (HF) [1, 2, 3]

An exact solution for the Schrödinger equation is impossible, except for the most trivial systems. Simplifying a number of procedures leads to an approximate solution for a large number of molecules. In a first approximation, the electronic wave function $\psi$ is written as a determinant, composed of molecular orbitals (MO), $\chi_i$. These MO are considered as the product of spin functions and spatial orbitals: $\chi_i(\mathbf{x}) = \phi_i(\vec{r})\alpha(\vec{\omega})$ or $\chi_i(\mathbf{x}) = \phi_i(\vec{r})\beta(\vec{\omega})$. The preferred MO set is orthonormal. The determinant, that satisfies these requirements is called the Single-Slater determinant (SSD):

$$\Psi_0 \approx \Phi_{SD} = \frac{1}{\sqrt{N!}} \begin{vmatrix} \chi_1(\vec{x}_1) & \chi_2(\vec{x}_1) & \cdots & \chi_n(\vec{x}_1) \\ \chi_1(\vec{x}_2) & \chi_2(\vec{x}_2) & \cdots & \chi_n(\vec{x}_2) \\ \vdots & \vdots & \vdots & \vdots \\ \chi_1(\vec{x}_N) & \chi_2(\vec{x}_N) & \cdots & \chi_N(\vec{x}_N) \end{vmatrix} \tag{2.54}$$

This equation meets the antisymmetry principle:

$$\Psi(\vec{x}_1, \vec{x}_2, \ldots, \vec{x}_N) = -\Psi(\vec{x}_2, \vec{x}_1, \ldots, \vec{x}_N) \tag{2.55}$$

In another approximation the spatial MOs are expressed as a linear combination of a set of one-electron functions (= basis functions):

$$\phi_i = \sum_{\mu=1}^{N} c_{\mu i} f_\mu \tag{2.56}$$

where $c_{\mu i}$ refers to the molecular expansion coefficients. The basis functions $f_\mu$ are chosen to be normalized. The program Gaussian uses Gaussian atomic functions, with general form:

$$g(\alpha, \vec{r}) = cx^n y^m z^l e^{-\alpha r^2} \tag{2.57}$$

Linear combinations of primitive gaussians are called the contracted gaussians:

$$f_\mu = \sum_p d_{\mu p} g_p \tag{2.58}$$

The $d_{\mu p}$-values are constants and stay invariable within a certain basis set. This way one can write down the following expansion for the molecular orbitals:

$$\phi_i = \sum_\mu c_{\mu i} f_\mu = \sum_\mu c_{\mu i} \left( \sum_p d_{\mu p} g_p \right) \tag{2.59}$$

The problem is now reduced to the determination of the coefficients $c_{\mu i}$ in order to find an optimal approximation for the real wave function $\Psi$. This can be done by using the variational principle. Those values for $c_{\mu i}$ need to be found, that minimize the corresponding energy or:

$$\sum_\mu^N \left( F_{\nu\mu} - \epsilon_i S_{\nu\mu} \right) c_{\mu i} = 0 \tag{2.60}$$

$N$ refers to the number of electrons. Equation 2.60 can be written more compactly:

$$FC = SC\epsilon \tag{2.61}$$

$\epsilon$ is a diagonal matrix of orbital energies $\epsilon_i$; $F$ is the Fock-matrix and represents the average effect of the field, originating from all electrons in each orbital. For closed shell systems, its elements can be written as:

$$F_{\nu\mu} = H_{\nu\mu}^{core} + \sum_{\lambda=1}^{N} \sum_{\sigma=1}^{N} P_{\lambda\sigma} \left[ (\nu\mu|\lambda\sigma) - \frac{1}{2} (\nu\lambda|\mu\sigma) \right] \tag{2.62}$$

$H_{\nu\mu}^{core}$ represents the energy of 1 electron in a field of nuclei in which other electrons are absent. $P$ refers to the charge and bond matrix with:

$$P_{\lambda\sigma} = 2 \sum_{i=1}^{occupied/2} c_{\lambda i}^* c_{\sigma i} \tag{2.63}$$

$S$ represents the overlap matrix and contains the elements:

$$S_{\nu\mu} = \int f_\nu^* (\vec{r})\, f_\mu (\vec{r})\, d\vec{r} \tag{2.64}$$

The terms $(\nu\mu\,|\lambda\sigma)$ and $(\nu\lambda\,|\mu\sigma)$ represent the two-electron repulsion integrals. In HF theory each electron considers the other electrons as an average distribution.

Both the Fock-matrix and density overlap matrix depend on the molecular orbital expansion coefficients. Equation 2.61 therefore needs to be resolved iteratively by the Self Consistent Field (SCF) method.

### 2.3.2 Density Functional Theory (DFT) [1, 4]

Density functional theory states that all aspects of the electronic structure of a system of interacting electrons, in the non-degenerate ground state, in an 'external' potential $V_{ext}$ are completely determined, within a constant, as a functional of the electron density, $\rho(\vec{r}_1)$. The electron density determines the probability of finding any of the n electrons within the volume element $d\vec{r}_1$ with arbitrary spin:

$$\rho(\vec{r}_1) = n \int \cdots \int |\Psi(\vec{x}_1, \vec{x}_2, \ldots, \vec{x}_n)|^2\, d\omega_1 d\vec{x}_2 \ldots d\vec{x}_n \tag{2.65}$$

The electron density is the central quantity that allows us to describe all ground state properties. This is an advantage with respect to HF calculations in which the many electron wave function is used for the description of the molecular properties.

Hogenberg and Kohn also proved that the ground state energy of the interacting electrons is a unique functional of $\rho(\mathbf{r})$. The energy value of this functional is at a minimum when the charge density is correct for a given external potential $V_{ext}$.

$$E_0 \leq E[\tilde{\rho}] = T[\tilde{\rho}] + E_{NE}[\tilde{\rho}] + E_{EE}[\tilde{\rho}] \tag{2.66}$$

$\tilde{\rho}$ is any trial density, fulfilling:

$$\tilde{\rho}(\mathbf{r}) \geq 0 \tag{2.67}$$

$$\int \tilde{\rho}(\mathbf{r}) d\mathbf{r} = n \tag{2.68}$$

$n$ refers to the number of electrons in the system. This theorem guarantees the existence of an energy functional $E[\rho]$ that reaches its minimum for the correct density. Yet it gives no explicit prescription for its construction.

The Kohn-Sham scheme expresses the ground state density of the interacting particles of a molecular system in terms of the orbitals of auxiliary non-interacting particles moving in an effective external potential $V_{ext}$. The expression for $E[\rho]$ can be divided in several parts:

$$E\left[\rho\right] = T_S\left[\rho\right] + E_{ext}\left[\rho\right] + E_C\left[\rho\right] + E_{XC}\left[\rho\right] \tag{2.69}$$

$T_S$ refers to the kinetic energy of the system of non-interacting electrons. $E_{ext}$ is the classical Coulomb energy of the electrons moving in the external potential $V_{ext}$, $E_C$ the classical energy due to the mutual Coulomb interaction of the electrons and $E_{XC}$ contains everything else which was not accounted for yet, that is exchange energy, correlation energy and the difference between the true kinetic energy and the kinetic energy of the system of non-interacting electrons.

Due to the fact that the total energy is minimized by the true ground-state density, the following set of equations can be derived:

$$(-\frac{1}{2}\nabla^2 + V_{eff}(\mathbf{r}_1))\varphi_i = \epsilon\varphi_i \tag{2.70}$$

$$\rho(\mathbf{r}) = \sum_{i}^{occ} \left|\varphi_i(\mathbf{r})\right|^2 \tag{2.71}$$

The effective potential in 2.70 is written as a functional of the electron density,

$$V_{eff}(\mathbf{r}_1) = V_{eff}[\rho(\mathbf{r})] = \int \frac{\rho(\mathbf{r}_2)}{\mathbf{r}_{12}} d\mathbf{r}_2 - \sum_{\alpha}^{N} \frac{Z_\alpha}{|\mathbf{R}_\alpha - \mathbf{r}_1|} + V_{XC}(\mathbf{r}_1) \tag{2.72}$$

The last term is the exchange-correlation term, which also is a functional of the density:

$$V_{XC}[\rho] \equiv \frac{\delta E_{XC}[\rho]}{\delta\rho} \tag{2.73}$$

Equations 2.70, 2.71 and 2.72 are known as the KS equations. They need to be solved in an iterative manner, until self-consistency is reached.

This exchange-correlation potential is a universal functional of the density i.e. the functional form is independent of the system that is studied. Its exact expression however remains unknown and is most likely to be approximated by an integral that only contains spin densities and, if desired, their gradients:

$$E^{XC}(\rho) = \int f\left(\rho_\alpha(\vec{r}), \rho_\beta(\vec{r}), \nabla\rho_\alpha(\vec{r}), \nabla\rho_\beta(\vec{r})\right) d^3\vec{r} \tag{2.74}$$

Usually $E^{XC}$ is separated into two parts, the exchange and correlation parts, corresponding to equal spin and mixed spin interactions respectively:

$$E^{XC} = E^X + E^C \tag{2.75}$$

Different types of functionals can be used: local functionals depend only on the electron density $\rho$, gradient corrected functionals depend on $\rho$ as well as on its gradient $\Delta\rho$. The most popular ones, however, are the hybrid functionals. These functionals form a mixture of HF and DFT exchange terms and a DFT correlation term:

$$E^{XC}_{hybrid} = c_{HF}E^X_{HF} + c_{DFT}E^{XC}_{DFT} \tag{2.76}$$

Examples for such hybrid models are Becke's three parameter functional (B3), and the popular B3PW94 [57, 58] and B3LYP [59, 60, 58, 61] functionals. The B3LYP is employed most often throughout this thesis.

The evaluation of the APTs, $P^I_{\alpha\beta}$, and AATs, $M^I_{\alpha\beta}$ requires derivatives of the ground electronic wave function with respect to the nuclear position or the magnetic field, i.e., $\frac{\partial\psi_0}{\partial R_{I\alpha}}$ and $\frac{\partial\psi_0}{\partial B_\alpha}$, as can be seen in equations 2.48 and 2.51. In order to do so with DFT, the Coupled perturbed KS method [62, 63, 64] was used.

### 2.3.3 Origin Gauges [5]

An additional problem associated with the calculations of the AATs is the choice of the coordination system. The AATs are, in contrast with the APTs, dependent on the origin. A change of the origin of the coordination system adds an extra term to the expression of the rotational strength. This term becomes zero for the exact wave functions and then the dependence is dropped. An alternative expression exists

for the electric transition dipole moment operator, in which the velocities instead of the positions of the particles are used. The rotational strengths, calculated in this manner, become independent on the origin. It is, however, much more complex to evaluate the matrix elements, associated with these velocity operators (gradient operators) [65]. In the search for a method that permits calculations, independent on the coordination system, the common origin (CO) gauge is the first method that was implemented. Hereby, one single origin was chosen throughout the evaluation of the dipole transition moments. Unfortunately, different choices for the common origin led to different rotational strengths. A portion of this randomness could be removed by connecting the origin with a structure related point, such as e.g. its center of mass. Subsequently the Distributed Origin (DO) gauge was presented, with the origins distributed at the nuclei. This method was proved to be favorable for the calculation of the AATs compared to the calculations using a CO [48]. Another method adjusts the basis sets. Recently London Atomic Orbitals (LOA), are used. They are also known as gauge-independent or invariant atomic orbitals (GIAO) [66]. In the GIAO method, each atomic orbital is assigned its own gauge origin, defined as the position of the nucleus carrying that orbital. The current state-of-the-art in ab initio VCD rotational strength calculations was published by Cheeseman and Stephens in 1996 [67] with the development of the first GIAO-based DFT codes. The calculations of the rotational strengths, using the Gaussian program, also are performed based on that method.

# 3

# Experimental VCD

## 3.1 Introduction

The first true solution-phase VCD was reported by Holzwarth et al. [43],in 1974. At that time, the experimental technique appeared to be extremely difficult and yielded weak, noisy spectra [68]. Subsequent developments in instrumentation have made routine VCD spectroscopy possible over large spectral regions. Over the years, the signal-to-noise ratio (S/N) problems have been addressed through the development of higher quality instrumentation. Dispersive VCD spectrometers [69] were replaced by FT-IR VCD spectrometers, as first proposed and demonstrated by Nafie and coworkers [70]. BioTools, established by L. Nafie and R. Dukor, provided the first commercially available VCD spectrometer, called the Chiral*IR*, in 1997. Nowadays, standalone and add-on-module FTIR VCD spectrometers are available from various manufac-

tures in addition to BioTools: Nicolet/Thermo (TOM), Jasco [36] (FVC-4000), Bio-Rad [71, 72] (FTS-60A) and Bruker optics (PMA37). In the next sections, the VCD spectrometer, used in this study, is described in more detail.

## 3.2 VCD spectrometer

The VCD spectrometer is based on the Bruker PMA37 module and is coupled to a Bruker IFS 66v interferometer. The performance of the setup was tested by Urbanova et al [73]. The setup is schematically given in Figure 3.1. The parallel Fourier modulated beam, originating from a globar (MIR) source, exits the interferometer and passes through a wire grid linear polarizer. The ZnSe photoelastic modulator (PEM) then modulates the polarization of the beam at a specific frequency. The circularly polarized radiation (CPL) passes through the chiral sample and the transmitted light is focused onto a liquid nitrogen cooled HgCdTe(MCT) detector with $BaF_2$ windows. To prevent detector saturation, an optical filter is placed between the spectrometer and first polarizer. The signal that reaches the detector is a multiplexed signal. This is due to the double modulation. The high frequency modulated *ac* signal is measured using a lock-in amplifier (LIA), the *dc* signal is processed as in a standard FTIR system. More details about the detection process will be discussed below.

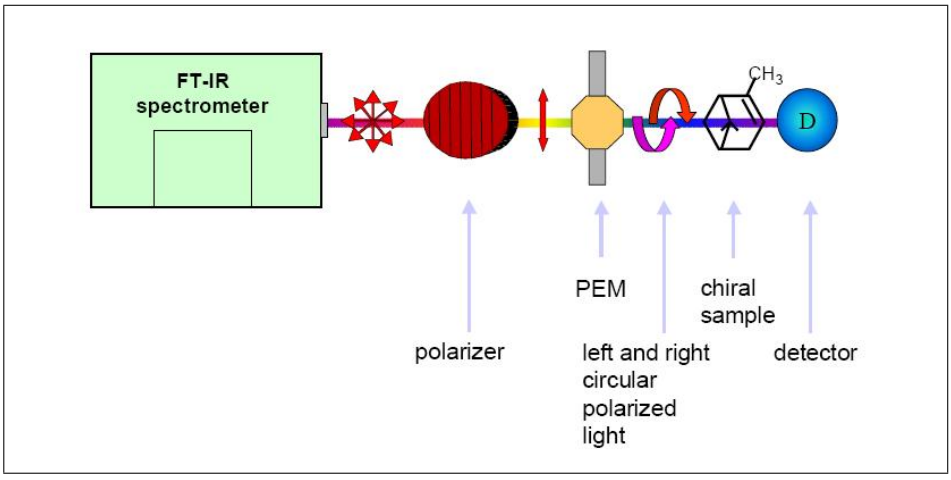


**Figure 3.1:** Experimental setup of a VCD FTIR spectrometer

### 3.2.1 The photoelastic modulator (PEM)

The PEM [74] is a device which enables us to modulate the polarization of light. In case of VCD measurements, linearly polarised light needs to be transformed into left (LCP) and right circularly polarised (RCP) light. Its principle of operation is based on the photoelastic effect. A mechanically stressed sample (the optical element) exhibits birefringence proportional to the resulting strain. If a sample of transparent solid material is stressed by compression or stretching, the material becomes birefringent. Different linear polarizations of light have slightly different speeds of light when passing through the material. The PEM consists of a rectangular bar of a suitable transparent material (fused silica e.g.), attached to a piezoelectric transducer as is shown in Figure 3.2. The bar vibrates along its long dimension, at a frequency determined by the length of the bar and the speed of a longitudinal sound wave in the optical element material. The transducer is tuned to the same frequency (50 kHz) and is driven by an electronic circuit (PEM-90 controller) which controls the amplitude of the vibration. The type, size and shape of the optical material can be varied, leading to a variety of applications.

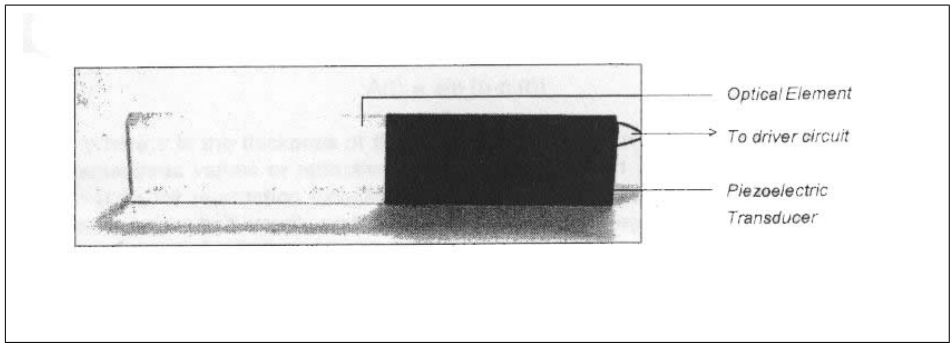


**Figure 3.2:** Representation of a PEM [74]

If the optical element is relaxed, the light passes through without any polarization change. Compressing the optical element causes the polarization component, parallel to the modulation axis to travel slightly slower than the vertical component. The horizontal component then "lags" behind the vertical component after light passes through the modulator. If the optical element is stretched, the horizontal component "leads" the vertical component. The phase difference between the

components at any instant of time is called the retardation or retardance. The peak retardation is the amplitude of the sinusoidal retardation as a function of time and is given by:

$$A(t) = z\left[n_x(t) - n_y(t)\right] \tag{3.1}$$

where z refers to the thickness of the optical element and $n_x(t)$ and $n_y(t)$ are the instantaneous values of the refractive index along the x and y directions. Common units for retardation include distance (nanometers, microns), waves (quarter-wave, half-wave), and phase angle (radians, degrees). A retardation of $\lambda/4$ causes a 90-degree phase shift between the two orthogonal polarization components. The polarization vector then traces a right-handed spiral about the optical axis, RCP is created. Since the electric field applied to the piezoelectric transducer, causes a sinusoidal stress modulation with frequency $\omega_m = 50$ kHz, the phase difference will vary from $-\pi/2$ to $\pi/2$ or, in other words, from LCP to RCP with intermediate elliptical polarization and linear polarized light at a zero phase difference. In Figure 3.3 the phase difference is shown as a function of time. The phase variation in time obeys the following equation:

$$\delta_t = \delta^0_{\bar{\nu}_i} sin\left(2\pi\omega_m t\right) \tag{3.2}$$

where $\delta^0_{\bar{\nu}_i}$ refers tot the maximal phase shift for wavelength $\lambda_i$.

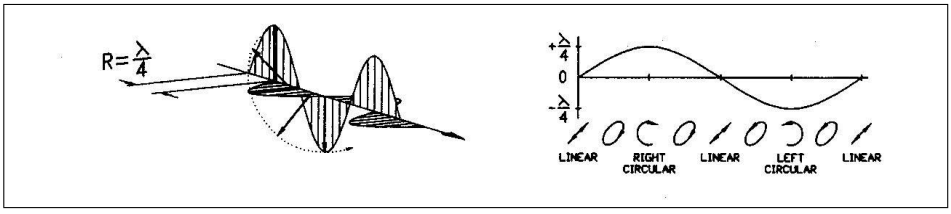


**Figure 3.3:** Quarter-wave retardation. [74]

The PEM may be used in either of two basic modes: as a modulator, to produce polarization modulation of a light beam, or as an analyzer to determine the polarization state of a light beam.

### 3.2.2 Signal detection

The beam that reaches the detector is doubly modulated. First, the light from the source is Fourier modulated. This was subsequently transformed into right and left circularly polarization states at a frequency

of 50 kHz, which is significantly higher than the Fourier frequencies (1-3 kHz). The detector will notice a time-independent signal known as the *dc* signal and time-varying signals or *ac* signals at frequency $\omega_m$, $3\omega_m$. The low-frequency component, due to the Fourier modulations and the high-frequency signal due to the CD are amplified and separated. Passing the signal through a low-pass filter, yields a standard interferogram of the single beam transmission or a *dc* interferogram. This part of the detector signal is constant with respect to the polarization modulation. A 25 kHz high-pass filter attenuates the Fourier modulated signals in the detector signal. The signal at the fundamental frequency $\omega_m$, generally known as the *ac* signal can be isolated by passing the detector signal through a lock-in amplifier tuned to $\omega_m$. The signals from both channels, i.e. the *ac* and *dc* interferograms are subsequently multiplexed into a single channel and are fed to an analog-to-digital converter.

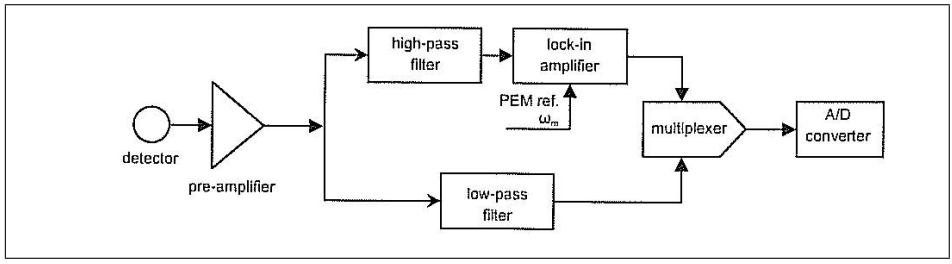


**Figure 3.4:** The electronic block diagram for the PMA37 featuring the high-pass and low-pass channel.

This multiplexed interferogram can then be processed using the macro, provided by Bruker. When separated, the *ac* and *dc* interferograms are Fourier transformed in order to give the *ac* and *dc* intensities $I_{ac}(\nu)$ and $I_{dc}(\nu)$ at the detector. For the Fourier transformation the correct phase correction needs to be determined, which is done during the calibration measurement. Using the intensities,$I_{ac}(\nu)$ and $I_{dc}(\nu)$, the absorbance spectrum and differential absorbance spectrum can finally be determined:

$$A(\nu) = -log\frac{I_{dc}(\nu)}{I_0(\nu)} \tag{3.3}$$

$$\Delta A = \frac{0.8686}{2J_1(\delta^0_{\nu_i})}\frac{I_{ac}(\nu)}{I_{dc}(\nu)}\frac{G_f}{G_l} \tag{3.4}$$

The latter equation was derived by Polavarapu [75]. $J_1(\delta^0_{\nu_i})$ is the first order Bessel function and $\delta^0_{\nu_i}$ is the maximum retardation induced by the PEM at frequency $\nu_i$. $G_l$ and $G_f$ are the gains introduced by the electronics of the lock-in amplifier and filters respectively. The quantity $2J_1(\delta^0_{\nu_i})\frac{G_l}{G_f}$ cannot be determined from a standard VCD measurement, therefore a calibration setup is necessary. This will be discussed in the next section.

### 3.2.3 Calibration

In Fourier transform spectroscopy, interferograms, that plot the intensities as a function of path differences $X$, are transformed into frequency spectra using FT algorithms. In order to perform a phase correction, the zero path difference (ZPD) needs to be determined. This is the point where no optical path difference was observed between the parallel beams coming from the fixed and movable mirrors. Unlike for normal transition interferograms, the $\omega_m$ interferogram will not have a maximum intensity at the ZPD point. In order to determine the ZPD, a calibration setup, using a birefringent plate (CdS multiple wave plate) and an extra polarizer needs to be introduced. The phase correction for this setup can then be transferred to the VCD measurement of a chiral sample using the same electronic and optical path as in the calibration. In our calibration setup, the CdS wave plate is placed in the sample compartment with its fast axis, parallel to the modulation axis of the PEM. The direction of polarization of the analyzer, placed after the birefringent plate, is also parallel to that of the first polarizer. The high-pass signal for this experiment is a typical two-signed interferogram with two intensity maxima; the low-channel filtered transmission interferogram is a classic interferogram. Both are shown in Figure 3.5. After Fourier transforming the interferograms $I_{dc}(X)$ and $I_{ac}(X)$, the calibration spectrum can be obtained by taking the ratio of the resulting spectra. The phase corrections required for the Fourier transformation of $I_{dc}(X)$ can be obtained by the usual procedures employed for one-sided interferograms, because the ZPD is associated with a well-defined intensity maximum. The Fourier transformation of $I_{ac}(X)$, however, requires special care because the intensity maxima occur near $X_c$ and not at ZPD. It can be seen that the ZPD is the midway between the two

highest values in the interferogram with the same sign. Resetting the ZPD to this mean value and carrying out the phase correction by the OPUS macro, which uses the Mertz signed phase correction [73], allows us to successfully transform the calibration interferogram. The *ac*, *dc* spectra and the calibration spectrum, obtained by taking the ratio of the *ac* and *dc* signal, are shown in Figure 3.6.

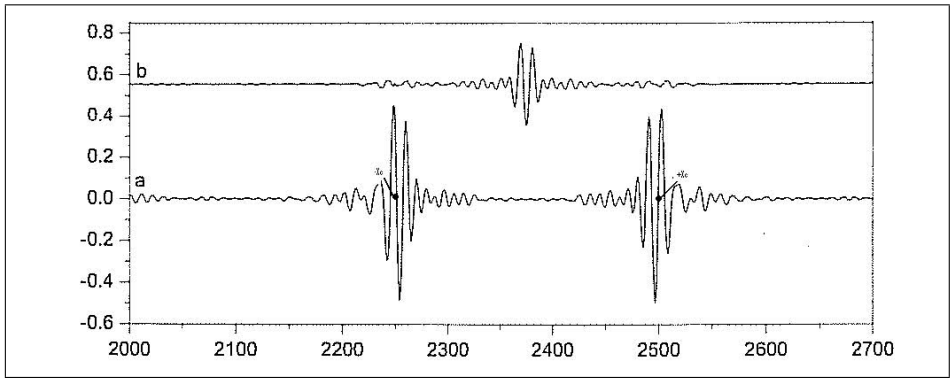


**Figure 3.5:** Interferograms obtained from a calibration experiment. The multiplexed signal is separated in a bi-signate *ac* interferogram (a) and a transmission *dc* interferogram (b).

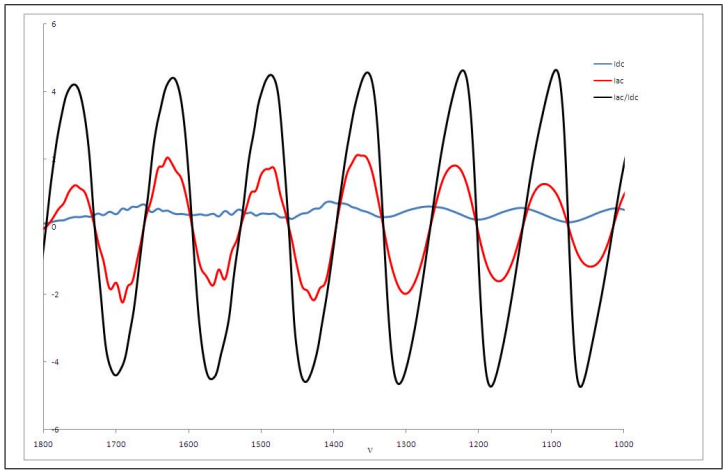


**Figure 3.6:** The calibration spectrum obtained by taking the ratio of the *ac* and the *dc* signal.

The frequency dependent calibration factor $2J_1(\delta^0_{\nu_i})\frac{G_l}{G_f}$ from equa-

tion 3.4 can be determined from the absolute values of the calibration curve at the midpoint of zero-crossings. For the calibration setup, with the fast axis of the birefringent plate in parallel position to that of the PEM and the direction of polarization of the analyzer also parallel to that of the first polarizer, the following equation can be written:

$$\frac{I_{ac}(\bar{\nu}_i)}{I_{dc}(\bar{\nu}_i)} = \frac{-2J_1(\delta^0_{\bar{\nu}_i}) sin\delta^B_{\bar{\nu}_i}}{1 - J_0(\delta^0_{\bar{\nu}_i}) cos\delta^B_{\bar{\nu}_i}} \frac{G_l}{G_f} \tag{3.5}$$

$\delta^B_{\bar{\nu}\,i}$ refers to the phase lag introduced by the birefringent plate, which is static in nature. Equation 3.5 has a non zero value of $-2J_1(\delta^0_{\bar{\nu}_i} G_l/G_f)$ at $cos\delta^B_{\bar{\nu}_i} = 0$ and $sin\delta^B_{\bar{\nu}_i} = \pm 1$. This is applicable when

$$\delta^B_{\bar{\nu}_i} = (2n+1)\frac{\pi}{2} \tag{3.6}$$

A zero magnitude is obtained for equation 3.5 when

$$\delta^B_{\bar{\nu}_i} = n\pi \tag{3.7}$$

According to Nafie et al. [69] and Polavarapu [75] the calibration curve can be determined more accurately by performing a second calibration experiment in which the polarization direction is perpendicular to that of the first polarizer, and the fast axis of the birefringent CdS plate is perpendicular to the modular axis of the PEM crystal. The values of $-2J_1(\delta^0_{\bar{\nu}_i} G_l/G_f)$ can then be considered as the non zero crossings between the curves obtained from the two calibration setups. These values can be interpolated to the desired wavenumber and can be used in equation 3.4 to determine the VCD of a given sample.

## 3.3 Experimental procedure

Nowadays high quality VCD spectra can be obtained fairly easily. Unfortunately measurements can still be complicated due to various problems like e.g. weak VCD signals, baseline artifacts and low S/N ratios.

Baseline artifacts typically arise from the birefringence and dichroism in the optical materials of the instrument. This bias superimposes all the VCD features on a background. The additional birefringence and circular dichroism originate from strain in the lenses and windows and slightly alters the polarization state of the radiation. For our setup

specifically, it was found that large baseline artifacts were induced at the detector. A full alignment of the detector focus-lens, giving a maximum signal at the detector, led to a non-flat baseline. Reducing the normal IR signal at the detector by 10 - 15 %, by moving the lens away from the detector, a much better baseline could be obtained. The baseline deviations, due to strain effects of the cell windows were minimized by choosing the optimal orientation of the cell into the sample holder [76].

Additionally, if the absorbance due to the chiral sample or the applied solvent is too high, a poor $S/N$ ratio is achieved. In VCD measurements it is preferable to keep the absorption at any position of interest below 1.0. An absorbance of the solution between 0.7 - 1.0 absorbance units (A.U.) is found to give an optimal $S/N$ ratio. The presence of intense solvent absorption in the region of interest is very unfavorable. For the region between 1000 $cm^{-1}$ and 2000 $cm^{-1}$ solvents like $CDCl_3$, $CCl_4$ and $CD_2Cl_2$ were found to be very useful. Measurements in $CS_2$ allow us to obtain spectra from 800 $cm^{-1}$. Due to the large solvent absorbance between 1400 $cm^1$ and 1600 $cm^{-1}$, VCD spectra in $CS_2$ are useless for assignment in that region. Path lengths were most often chosen in the range of 100 and 200 $\mu m$, using demountable cells with KBr and $CaF_2$ windows. Varying the concentration of the sample (generally between 0.1M and 1.0M) is another possibility to obtain a favorable IR absorbance.

Various optical filters were placed before the first polarizer, depending on the frequency region of interest. The optical filter with an operational frequency window between 800 $cm^{-1}$ and 1830 $cm^{-1}$ induces large artifacts near 1800 $cm^{-1}$, which is unfavorable for the investigations of e.g. the carbonyl stretch regions. In this frequency region a Spectrogon 1960 $cm^{-1}$ limiting filter was applied. For the VCD study above 2000 $cm^{-1}$, a 3000 $cm^{-1}$ long wave pass filter was used.

In order to correct for the possible artifacts, described above, a baseline correction is performed. This can be done by applying various methods. The general idea is to obtain a background VCD that could be used as a baseline. The racemate of a sample will exhibit no VCD and hence the raw VCD spectrum of a racemate should contain just the background. When the raw VCD of racemate is subtracted from that of an enantiomer, then the background will be subtracted out and the real VCD features of the enantiomer will result. If the racemic mixture is

not available, the VCD spectra of both enantiomers can be measured. The sum of the raw VCD spectra of the enantiomers should be equal to twice the raw VCD spectrum of the racemate. In the same manner, a baseline corrected VCD spectrum can be obtained for a specific enantiomer, by subtracting the VCD of the other enantiomer and divide the resulting spectrum by two. These spectra are often called half-sum and half-difference spectra [77]. Unfortunately, for many chiral molecules, their enantiomers are not readily available. The baseline is then estimated via the measurement of the solvent VCD in the same conditions as the chiral sample. Because the absorbance artifacts for the solvent and and the chiral compound are different, this method only gives an approximate baseline. However, in many cases, the baselines obtained via this method seem to be sufficiently accurate.

In order to determine the background, introduced by the detector, the *background VCD setup* was proposed by Polavarapu [75]. For this setup the sequence of the components is sample, polarizer and PEM. By placing the optically active sample ahead of the PEM and the first polarizer, the VCD signal will only originate from the additional linear dichroism induced by the detector, while the overall absorbance will be maintained as well as the birefringence in sample cell.

Recently, Nafie [78] developed a method called dual polarization modulation (DPM), in order to separate the circular dichroism (CD) spectra from linear birefringence (LB) spectra. Hereby, a second PEM is introduced after the CD sample. Intensity signals at the detector, in phase with each of the two polarization modulation frequencies are demodulated simultaneously in parallel and combined electronically in opposition to eliminate the LB by real-time cancellation. The DPM method permits baseline-corrected CD spectra to be measured without the need for a subsequent CD background measurement. This was claimed in a patent filed by BioTools in 2001, describing a prototype of this spectrometer [79]. Very recently, Nafie et al. [80] also published an article in which they stated that by adding a rotating half-wave plate (RHWP) after the second PEM of the DPM setup even eliminates a final componet of remaining LB, associated with the sample cell. In the DPM setup without the RHWP, all sources of LB are first reduced and then further canceled by real time electronic subtraction, except for this remaining source of LB between the two PEMs.

During our experiments neither *the background VCD setup* nor the DPM method were used for the estimation of the baseline. Depending on the availability of the enantiomers, backgrounds were determined by recording the VCD spectra of both enantiomers or by measuring the VCD signal of the solvent.

# 4

# Comparison of the experimental and calculated VCD spectra

## 4.1 Introduction

An important step of the VCD assignment process, is the comparison of the experimental and calculated spectra. Based on their agreement, the absolute configuration (AC) can be assigned. Hereto the location, sign and intensity of the bands are considered. Unfortunately, experiments are inherently different compared to the spectra obtained from DFT calculations. Due to the finite basis set and harmonic approximation, computed vibrational frequencies are overestimated compared with the experimentally obtained ones. Other differences can appear from the fact that, on the one hand, experimental spectra are recorded for dilute solutions, while the calculations, on the other hand are performed for the free molecule in vacuo. In order to avoid bias caused by

personal interpretation and subjectivity, numerical methods are developed to compare experiment and theory. In this Chapter two different techniques are discussed. The first is the classical, but labor intensive, approach in which all bands in the experimental spectrum are assigned to the calculated modes. A second technique applies a similarity measure for the comparison between experiment and theory.

## 4.2 Construction of the calculated spectra

For each unique geometry found during conformational analysis, the dipole and rotational strengths are calculated. With these data, IR and VCD spectra can be obtained for each conformer. In a next step, the spectrum of each conformer is combined in a Boltzmann weighted manner. Calculated standard free energies ($\Delta G^0$) or standard enthalpies ($\Delta H^0$) were used to determine the Boltzmann populations:

$$w_A = \frac{e^{-\Delta H_A^0/RT}}{\sum_i e^{-\Delta H_i^0/RT}} \tag{4.1}$$

or

$$w_A = \frac{e^{-\Delta G_A^0/RT}}{\sum_i e^{-\Delta G_i^0/RT}} \tag{4.2}$$

The reason why enthalpies are very often used is due to the fact that the calculation of entropies is not straightforward. Moreover the entropy differences are almost equal for most conformers [81].

Computed spectra are line spectra, whereas experimental spectra are composed of bands. In order make computed spectra more comparable to the experimental ones line broadening is introduced. Due to the large similarity with the shapes of the experimental bands, Lorentzian broadening was assumed:

$$f_i(\nu) = \frac{1}{\pi} \frac{\alpha}{(\nu - \nu_i)^2 + \alpha^2} \tag{4.3}$$

Band, $i$, is centered at the frequency $\nu_i$. $2\alpha$ refers to the Lorentzian full width at half maximum (FWHM). The area under the band is normalized due to the factor $\pi^{-1}$. Figure 4.1 shows a Lorentzian band, centered at $\nu_i = 0\ cm^{-1}$ and $\alpha = 5\ cm^{-1}$.

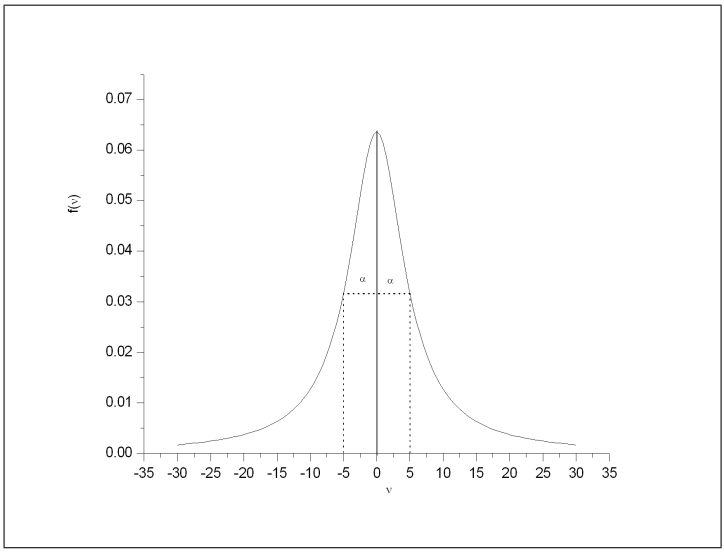


**Figure 4.1:** Lorentzian function $f(\nu)$ with a FWHM ($2\alpha$) of 10 $cm^{-1}$

The broadened Boltzmann weighted spectra can subsequently be converted into molar absorptivity units based on Equations 4.4 and 4.5 [25].

$$\epsilon(\nu) = \frac{1}{9.184 \cdot 10^{-39}} \nu \sum_i D_i f_i(\nu) \tag{4.4}$$

$$\Delta\epsilon(\nu) = \frac{1}{2.296 \cdot 10^{-39}} \nu \sum_i R_i f_i(\nu) \tag{4.5}$$

These simulated spectra are produced to visualize the calculated data and to mimic the experimental spectra. Agreement between experimental and theoretical IR and VCD spectra allows the determination of the AC of the experimental sample. Unfortunately, superimposing both spectra is not sufficient to draw a conclusion about the AC. A more thorough analysis of the available data has to be performed. This is described in the next two sections.

## 4.3 Correlation of the experimental and calculated bands

A reliable approach, to unambiguously assess the agreement between theory and experiment, is the correlation of experimental and simulated

bands. The assignment of the bands is based on the calculated fundamentals. This way, each band in the experimental IR and VCD spectrum is linked with a band in the calculated spectra. IR and VCD absorption frequencies are the same but, because of the differential intensities, VCD spectra have extra discriminating power. As a result, assignment of unresolved IR bands can be performed using the experimental VCD counterpart, and vice versa. Based on the sign of the bands in the VCD spectra, the absolute configuration of the product can be determined. In the ideal case, all bands of the calculated spectrum have either equal signs with respect to the bands in the experiment, or they all are opposite in sign. Since the stereochemistry linked with the calculated spectrum is known, one is able to determine the absolute configuration of the analyzed product.

The correlation between the bands can be studied even more thoroughly by comparing the experimental and calculated rotational and dipole strengths in a quantitative manner as is shown in Figure 4.2. The experimental dipole and rotational strengths are determined by deconvolution of the experimental spectra. In this procedure, Lorentzian functions are fitted against the spectrum, enabling one to estimate the area under the bands. Equations 4.6 and 4.7 show the relation between the area under the bands and the dipole or rotational strengths respectively [25]:

$$D_i = 9.184 \cdot 10^{-39} \frac{1}{\nu_{i,max}} \int \epsilon_i d\nu \tag{4.6}$$

$$R_i = 2.296 \cdot 10^{-39} \frac{1}{\nu_{i,max}} \int \Delta\epsilon_i d\nu \tag{4.7}$$

The obtained experimental dipole and rotational strengths can then be correlated to the calculated values, based on the band assignments. This assignment procedure has already been used in many VCD studies [39, 82, 83, 84]. In this work, correlation between experimental and theoretical dipole and rotational strengths is performed for the bicyclo[3.3.0]octane derivatives (Chapter 5) and pulegone (Chapter 7). Deconvolution was done using Peakfit [85]. The procedure, however, is not unambiguous and strongly depends on the quality of the experimental spectra. During fitting procedure, the baseline is approximated by a polynomial. A capricious baseline will therefore hinder the procedure. The resolution of the bands is another important factor. When bands

overlap it is much more difficult to distinguish them and to find an univocal fit. As a consequence, correlation coefficients around 0.6 are not rare. Another disadvantage is that this method is very labor intensive.

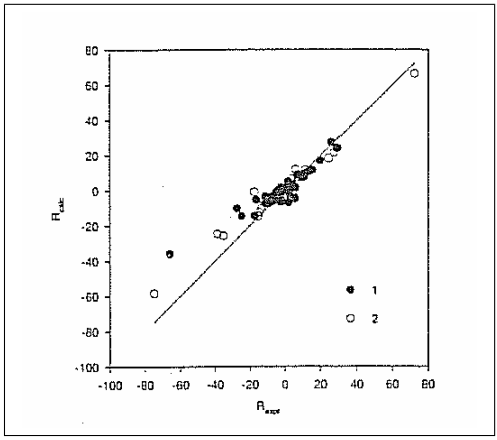


**Figure 4.2:** Comparison of calculated and experimental rotational strengths of camphor (•) and fenchone (○). Experimental rotational strengths were obtained by Lorentzian fitting of the VCD spectra. Rotational strengths are in $10^{-44}$ $esu^2$ $cm^2$ [82].

## 4.4 Similarity measure

Another technique, to quantify the agreement between theory and experiment in a quantitative manner, is the determination of the overlap or similarity between the spectra. The similarity [86] is defined by:

$$S = \frac{\int f(\sigma\nu)g(\nu)d\nu}{\sqrt{\int f^2(\sigma\nu)d\nu \int g^2(\nu)d\nu}} \tag{4.8}$$

$f$ and $g$ represent, respectively, the theoretical and experimental intensities at frequency $\nu$. The denominator is a normalization constant. A scaling factor $\sigma$ was introduced to correct for the overestimated calculated frequencies. Unfortunately, this linear scaling is far from perfect, as simulated bands can still be shifted with respect to their corresponding experimental bands. Hereto it is suggested to take into account the neighborhood in direct proximity of the bands. This can be done by

using a triangular function as a weighting function. The equations are described in more detail in the work of Kuppens et al. [76, 33, 87].

The calculation of the neighborhood similarities for VCD spectra is somewhat more complex than for IR spectra, because the positive and negative part of the spectrum need to be evaluated separately. For both regions the similarities are determined separately and were eventually combined to:

$$S = \frac{S^+ + S^-}{2}$$

The similarity measure, however, was not used nor studied in this thesis.

# 5

# Vibrational circular dichroism DFT study on bicyclo[3.3.0]octane derivatives

## 5.1 Introduction

The development of an efficient asymmetric synthesis of the $C_2$-symmetric *endo*-bicyclo[3.3.0]octane-2,6-diol **1** and bisacetate **2** (Figure 5.1) [88], allowed the application of this interesting rigid framework in the asymmetric synthesis of enantiomerically pure natural products such as the sesquiterpenoids (-)-sulcatine [89] and (+)-kelsoene[90] , prostaglandins [91], the tetramic acid lactam cylindramide [92], as well as its use in the synthesis of chiral ligands for asymmetric catalysis [93, 94, 95]. The racemic ester (±)-**2** can be obtained in one step from commercially available cyclo-octa-1,5-diene via $Pd^{2+}$-catalyzed transannular diacetoxylation, which, after hydrolysis, results in the racemic diol (±)-**1** [96, 88]. Initial interest in the biocatalytic resolution of this class of compounds

was stimulated by their possible use as intermediates for the synthesis of a prostaglandin synthon. Although this method yielded a high enantiomeric excess for at least one enantiomer, it did not provide an easy and practical method to produce both enantiomers with high enantiomeric excess and yield [91, 97]. Nevertheless, *Pseudomonas cepacia* (PS) catalysed kinetic resolution of diol (±)-**1** by transesterification with vinyl acetate in tert-butyl methyl ether was later found to provide an easy procedure for the synthesis of larger quantities of both enantiomers of **1** with high enantiomeric excess and yield, making it particularly attractive for application in the synthesis of chiral auxiliaries or ligands [88].

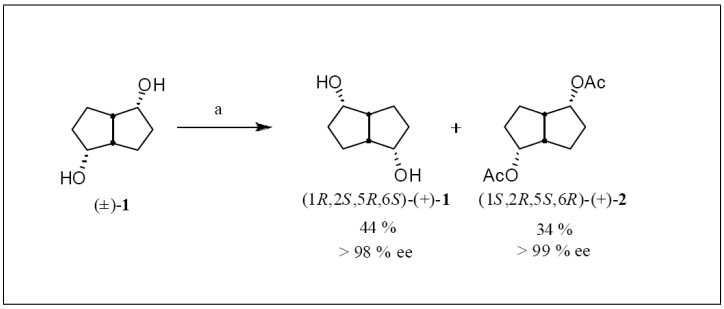


**Figure 5.1:** Reagents and conditions: (a) Vinylacetate, Lipase PS, tBuOMe, $\sim$ 22 °C, 240 h.

Lipase catalysed acylation of (±)-**1** could also be performed with a fluorinated ester, resulting in enantioselective fluorous phase labeling [98]. In most synthetic applications, diol **1** is actually transformed to the $C_2$-symmetric dione **3** (Figure 5.2). This molecule was examined earlier by electronical circular dichroism (ECD) [99]. In its racemic form, the dione also can be synthesized by alternative methods [100, 101, 102]. The absolute configurations of the obtained products were deduced by chemical correlation [91] and used in the determination of the absolute configuration of (-)-sulcatine [89] and (+)-kelsoene [90] as well as in the determination of the stereoselectivity in an enantioselective $\alpha$-deprotonation-rearrangement of *meso*-epoxides [103] and a transannular cyclization of a chiral cyclo-octene derivative [104].

In this work the absolute configurations of the enantiomeric series of $C_2$-symmetric bicyclo[3.3.0]octane compounds **1**, **2**, **3** and **4** (Figure 5.1 and Figure 5.2) are determined by VCD. These molecules contain more

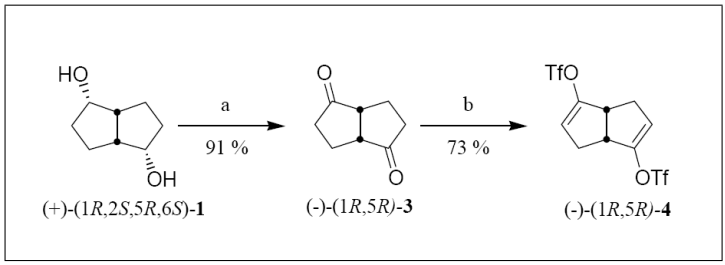


**Figure 5.2:** *Reagents and conditions*: (a) Jones reagent, 1 h, 0 °C, 1h, rt; (b) (i) KHMDS, -78 °C, 65 min. (ii) $PhNTf_2$, -78 °C, 1h 55 min.; 0 °C, 30 min.

than one chiral center. Although other techniques to obtain information about the relative configurations of the substituents and the positions of the rings were available, they have not been taken into account during our VCD analysis. In the end they will only be used to confirm the VCD results. This is analogous to what has been done by Muoz et al. [105]. In other previous VCD studies of molecules, containing more than one chiral center, the relative configurations of the subsituents were always known in advance [106]. To be able to determine the absolute configuration, only by using VCD, all optically active diastereomers have to be taken into account. The VCD spectrum of each diastereomer then has to be compared with experiment. This way the absolute configurations of (+)-**1**, (+)-**2**, (-)-**3** and (-)-**4** were determined.

## 5.2 Experimental

A demountable cell with KBr windows and a 105 $\mu m$ spacer has been used for all samples except for (-)-**4**, for which a $CaF_2$-cell with a 100 $\mu m$ spacer was used. All samples were dissolved in $CDCl_3$. The unpolarized IR absorbance spectra were recorded initially at a resolution of 4 $cm^{-1}$ and the VCD spectra were subsequently recorded at a resolution of 6 $cm^{-1}$. A 1830 $cm^{-1}$ long wave pass filter was used to improve the VCD S/N ratio. The collection time for the VCD spectrum was 90 min, using six blocks of 15 min. Samples of (+)-**1** and (-)-**4** have been prepared in $CDCl_3$ and $CS_2$ at an approximate concentration of respectively 0.3M and 0.1M. The use of both solvents yields a wide spectral range, i.e. 800 $cm^{-1}$-1800 $cm^{-1}$. The IR and VCD spectra of (+)-**2** and (-)-**3** have been recorded in $CDCl_3$ at approximate concentrations of 0.07M and

0.2M respectively. To obtain an estimate of the baseline artifacts, the VCD spectra of the solvents have been recorded, in the same conditions as the sample.

## 5.3 Computational Methods

VCD spectra are composed of the contributions of the different conformations. Therefore it is important to find the geometries of the relevant conformations of the molecule. The conformational landscape was explored by molecular mechanics (MM) and density functional theory. Stochastic searches in the MM3 [107] and MM4 [108] force fields have been executed as well as systematic searches using the MMFF [109, 110] force field. The geometries, that were located by molecular mechanics were subsequently optimized at the B3LYP/6-31G(d) level. A systematic search at the B3LYP/6-31G(d) level was also performed. The key dihedral angles were varied in a 60° grid. After a bump check and taking into account the ring constraints [111], only chemically feasible starting structures were minimized on the B3LYP/6-31G(d) level. The frequencies, dipole and rotational strengths for each B3LYP/6-31G(d) minimum on the potential energy surface are calculated. The obtained line spectra of each conformer are then broadened, using a Lorentzian band shape with a FWHM of 10 $cm^{-1}$. This bandwidth gives the largest resemblance withe the experimental bands. In order to make a comparison with the experimental spectra possible, the spectrum of each minimum is combined in a Boltzmann weighted manner. The conformational populations are based on the free energies of each conformation. Enthalpies and free energies are obtained using statistical thermodynamics [81]. Appropriate scaling factors have been used to correct for the harmonic approximation [4, 112, 113]. For the calculations with the 6-31G(d) basis set a uniform scaling factor of 0.967 has been used, while in case of the cc-pVTZ calculations a factor of 0.977 was used. These values agree with the values found in literature. The DFT calculations were performed with Gaussian 03 revision B05 [55]. The B3LYP functional has been used together with the basis sets 6-31G(d) and cc-pVTZ. The experimental dipole and rotational strengths have been determined by Lorentzian deconvolution of respectively the experimental IR and VCD spectrum.

## 5.4 Results and Discussion

**Synthesis**: The diol (±)-**1**, obtained by $Pd^{2+}$-catalyzed transannular diacetoxylation of cycloocta-1,5-diene and subsequent hydrolysis as mentioned above [88, 96], was subjected to the lipase catalysed kinetic resolution resulting in the enantiomerically pure diol (+)-**1** and diacetate (+)-**2** on multigram scale (∼8-9 g of both (+)-**1** and (+)-**2**) (Figure 5.1) [88]. The diol was further transformed to the dione (-)-**3** by oxidation with Jones reagent (Figure 5.2). Dienolization with KHMDS, followed by treatment with $PhNTf_2$ resulted in the formation of the crystalline bisvinylic triflate (-)-**4**. Vinyltriflates, as diene **4**, can serve as interesting intermediates for further synthetic application [114, 115].

**Conformational Analysis.Bicyclo[3.3.0]octane-2,6-diol (1)**. Compound **1** has 4 chiral centers, leading to 16 possible stereoisomers, from which only 12 are symmetry unique. The combinations, containing an inversion center ((1*R*,2*R*,5*S*,6*S*)-**1**, (1*R*,2*S*,5*S*,6*R*)-**1**, (1*S*,2*S*,5*R*,6*R*)-**1** and (1*S*,2*R*,5*R*,6*S*)-**1**) can be omitted, since they are not optically active. The number of diastereomers, under investigation, is therefore limited to 4: (1*R*,2*R*,5*S*,6*R*)-**1** = RRSR, (1*R*,2*S*,5*R*,6*R*)-**1** = RSRR, (1*R*,2*S*,5*R*,6*S*)-**1** = RSRS and (1*R*,2*R*,5*R*,6*R*)-**1** = RRRR. The first configuration is a trans-coupled bicyclic system, whereas the other configurations are cis-coupled. The conformational space of each of the four configurations can be described by means of the orientation of the exocyclic substituents, denoted by $\tau_1$ and $\tau_2$ and the CO torsions, denoted by $\tau_3$ and $\tau_4$. These are shown in Figure 5.3. The positions of the substituents can be considered as equatorial or axial with respect to the five-membered rings. Three typical minima in the CO torsion potential energy are observed. That is, dihedral angles around 60°, 180° and -60°. These are denoted as G (gauche clockwise), T (trans) and G' (gauche counterclockwise) respectively. In the conformational notation; the group-ring orientation (e or a) and the CO torsions (G, T or G') are given successively for both exocyclic substituents.

A conformational study, as is described in more detail in the previous section, of the first diastereomer, RRSR, leads to 9 relevant conformations. It is observed that the substituent attached to C6 is always positioned axial, whereas the other is positioned equatorial. For the three most stable conformations, the CO bond torsion of the axial substituent

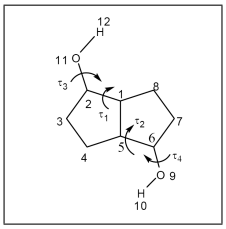


**Figure 5.3:** Conformational analysis of 1 through the variation of four torsions: $\tau_1$ = O11-C2-C1-C5, $\tau_2$ = O9-C6-C5-C1, $\tau_3$ = H12-O11-C2-C1 and $\tau_4$ = H10-O9-C6-C5.

is 180 while the analogous bond torsion of the equatorial substituent varies over the three conformations. The second diastereomer, RSRR, has 36 significant conformations. This number can be rationalised because both substituents can either be equatorial or axial. This leads to 4 times the number of conformations of the previous diastereomer (RRSR). In Table 5.2 it can be seen that their energy difference is very small. Because of the lack of symmetry, for both diastereomers, the substituents are distinguishable. In the analysis of the third diastereomer, RSRS, only 2 relevant conformations were found. Both are stabilized by the H-OH bond interaction, formed between the hydroxy substituents. Due to the $C_2$-symmetry of this configuration, both substituents are indistinguishable. The global minimum can thus be written as aTaG or aGaT. For the fourth diastereomer, RRRR, 11 significant conformations have been found. The two least stable conformations (eGeG and aG'aG') have a $C_2$-symmetry. Table 5.2 shows the labels of the different conformations of each diastereomer together with their corresponding dihedral angles. For each conformation, the Boltzmann populations have been calculated based on their Gibbs free energy differences.

**Table 5.2:** B3LYP/6-31G(d) relative free energies ($\Delta G^0$, in kcal/mol), Boltzmann populations (%F, T = 298.15K), dihedral angles ($\tau_1$, $\tau_2$,$\tau_3$ and $\tau_4$ )and point groups for the localized conformations of each diastereomer of **1**. The labels (a, b, c, etc), found in the first column, are used later on to assign the experimental spectra. The / indicates that the labels of each substituent are distinguishable.

| | notation | $\tau_1$ | $\tau_3$ | $\tau_2$ | $\tau_4$ | $\Delta G^0$ | %F |
|---|---|---|---|---|---|---|---|
| | | | RRSR | | | | |
| 1a | eG/aT | -141 | 65 | -103 | 178 | 0.00 | 22.43 |
| 2b | eG'/aT | -146 | -55 | -103 | -179 | 0.06 | 20.40 |
| 3c | eT/aT | -138 | 179 | -103 | 179 | 0.21 | 15.79 |
| 4d | eG'/aG' | -147 | -58 | -97 | -62 | 0.46 | 10.39 |
| 5e | eG/aG' | -143 | 66 | -97 | -62 | 0.59 | 8.35 |
| 6f | eT/aG' | -140 | -179 | -97 | -61 | 0.63 | 7.80 |
| 7g | eT/aG | -140 | -179 | -106 | 55 | 0.80 | 5.85 |
| 8h | eG/aG | -144 | 69 | -106 | 57 | 0.83 | 5.50 |
| 9i | eG'/aG | -148 | -62 | -106 | 54 | 1.10 | 3.50 |
| | | | RSRR | | | | |
| 1a | aT/aG' | -76 | -174 | 79 | -65 | 0.00 | 9.98 |
| 2b | aT/aT | -77 | -172 | 76 | 176 | 0.05 | 9.16 |
| 3c | aG/aG' | -80 | 59 | 79 | -64 | 0.06 | 9.06 |
| 4d | aG/aT | -81 | 60 | 76 | 177 | 0.33 | 5.67 |
| 5e | eT/aT | -161 | 178 | 73 | 172 | 0.52 | 4.12 |
| 6f | eG'/aT | -168 | -62 | 73 | 171 | 0.59 | 3.70 |
| 7g | eT/eG' | -160 | 176 | 163 | -65 | 0.63 | 3.45 |
| 8h | eG'/eG' | -168 | -62 | 163 | -66 | 0.67 | 3.21 |
| 9i | eG/aT | -164 | 67 | 73 | 173 | 0.67 | 3.20 |
| 10j | aT/eG' | -74 | -172 | 165 | -65 | 0.72 | 2.95 |
| 11k | eG/eG' | -163 | 66 | 163 | -64 | 0.72 | 2.95 |
| 12l | eG/aG' | -164 | 67 | 77 | -71 | 0.75 | 2.84 |
| 13m | aG'/aT | -84 | -62 | 76 | 176 | 0.75 | 2.81 |
| 14n | eT/aG' | -161 | 176 | 77 | -73 | 0.76 | 2.78 |
| 15o | aG/eG' | -78 | 60 | 165 | -64 | 0.81 | 2.52 |

*continued on next page*

*continued from previous page*

| | notation | $\tau_1$ | $\tau_3$ | $\tau_2$ | $\tau_4$ | $\Delta G^0$ | %F |
|---|---|---|---|---|---|---|---|
| 16p | eT/eT | -160 | 178 | 161 | -179 | 0.88 | 2.26 |
| 17q | aG'/aG' | -84 | -58 | 79 | -67 | 0.88 | 2.25 |
| 18r | eG'/eG | -167 | -61 | 168 | 65 | 0.90 | 2.20 |
| 19s | eG'/eT | -167 | -63 | 161 | -179 | 0.92 | 2.12 |
| 20t | eG'/aG' | -168 | -59 | 77 | -72 | 0.93 | 2.06 |
| 21u | eT/eG | -160 | 177 | 168 | 64 | 0.96 | 1.98 |
| 22v | aT/aG | -76 | -173 | 84 | 70 | 0.96 | 1.98 |
| 23w | eG/eG | -162 | 65 | 168 | 63 | 1.09 | 1.59 |
| 24x | aG/aG | -80 | 59 | 85 | 66 | 1.11 | 1.52 |
| 25y | eG/eT | -163 | 66 | 162 | -179 | 1.13 | 1.47 |
| 26z | eG'/aG | -168 | -62 | 81 | 68 | 1.14 | 1.46 |
| 27aa | eT/aG | -162 | -179 | 80 | 66 | 1.14 | 1.45 |
| 28ab | aT/eG | -74 | -173 | 168 | 70 | 1.15 | 1.43 |
| 29ac | aG/eG | -78 | 59 | 169 | 68 | 1.20 | 1.31 |
| 30ad | aT/eT | -75 | -171 | 162 | -178 | 1.21 | 1.29 |
| 31ae | aG'/eG' | -82 | -60 | 165 | -67 | 1.23 | 1.26 |
| 32af | aG/eT | -78 | 59 | 162 | -179 | 1.33 | 1.07 |
| 33ag | eG/aG | -165 | 63 | 81 | 62 | 1.40 | 0.95 |
| 34ah | aG'/aG | -84 | -59 | 84 | 71 | 1.54 | 0.74 |
| 35ai | aG'/eT | -82 | -61 | 162 | -179 | 1.57 | 0.71 |
| 36aj | aG'/eG | -82 | -56 | 168 | 73 | 1.72 | 0.55 |
| | | | RSRS | | | | |
| 1a | aTaG | 75 | 166 | 81 | 47 | 0.00 | 69.61 |
| 2b | aG'aG | 78 | -76 | 81 | 40 | 0.50 | 29.98 |
| | | | RRRR | | | | |
| 1a | eGaT | -163 | 63 | -76 | -174 | 0.00 | 19.01 |
| 2b | eGaG | -163 | 64 | -80 | 59 | 0.00 | 18.97 |
| 3c | aGeT | -80 | 58 | -160 | 176 | 0.09 | 16.37 |
| 4d | aGaT | -78 | 57 | -74 | -174 | 0.34 | 10.79 |
| 5e | eG'aG' | -168 | -61 | -84 | -59 | 0.56 | 7.36 |
| 6f | eG'eT | -168 | -61 | -161 | 179 | 0.60 | 6.94 |
| 7g | eGaG' | -163 | 66 | -83 | -56 | 0.72 | 5.65 |

*continued on next page*

*continued from previous page*

| | notation | $\tau_1$ | $\tau_3$ | $\tau_2$ | $\tau_4$ | $\Delta G^0$ | %F |
|---|---|---|---|---|---|---|---|
| 8h | eGeT | -164 | 65 | -161 | 178 | 0.80 | 4.94 |
| 9i | aG'aT | -82 | -54 | -74 | -173 | 1.00 | 3.50 |
| 10j | aGaG' | -78 | 60 | -82 | -56 | 1.04 | 3.30 |
| 11k ($C_2$) | eGeG | -164 | 65 | -164 | 65 | 1.19 | 2.55 |
| 12l ($C_2$) | aG'aG' | -82 | -58 | -82 | -58 | 2.03 | 0.62 |

**2,6-diacetoxybicyclo[3.3.0]octane (2).** Although **2** contains four chiral centers, again only four diastereomers need to be investigated: (1*R*,2*R*,5*S*,6*R*)-**2** = RRSR, (1*S*,2*R*,5*S*,6*S*)-**2** = SRSS, (1*S*,2*R*,5*S*,6*R*)-**2** = SRSR and (1*S*,2*S*,5*S*,6*S*)-**2** = SSSS. The first configuration is a trans-coupled bicyclic system, whereas the other configurations are cis-coupled. For each of these diastereomers a conformational analysis has been performed. The conformational space can be described by means of the orientation of the acetate groups; besides the group-ring orientation ($\tau_3$ and $\tau_4$), for each substituent, two dihedral angles need to be taken into account: $\tau_2$ (and $\tau_5$) and $\tau_3$ (and $\tau_6$), as shown in Figure 5.4.

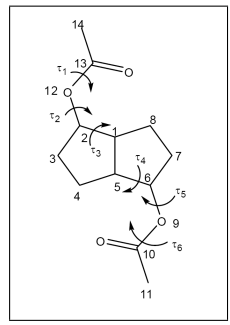


**Figure 5.4:** Conformational analysis of 2 through the variation of six torsions: $\tau_1$ = O12-C2-C1-C5, $\tau_2$ = C13-O12-C2-C1, $\tau_3$ = C14-C13-O12-C2, $\tau_4$ = O9-C6-C5-C1, $\tau_5$ = C10-O9-C6-C5 and $\tau_6$ = C11-C10-O9-C6.

During conformational analysis of the first configuration, RRSR, 46 minima have been found. Based on the energies, only four of them are significant. These conformers have two things in common. One substituent has an equatorial group-ring orientation, while the other substituent is in axial position with respect to the five-membered rings. Secondly, in all cases $\tau_1$ and $\tau_6$ are found to be 180°. These two features give rise to the most stable conformers. Analysis of the second diastere-

omer, SRSS, leads to 135 different minima. Many more combinations are possible because the group-ring orientations of both substituents are not restricted, opposite to the previous configuration. For the most stable conformers, relevant for the construction of the spectra, $\tau_1$ and $\tau_6$ are equal to 180°. Conformational analysis of the third configuration, SRSR, also yields 78 minima. In the third configuration both substituents have the same chirality and are therefore indistinguishable. For some of the conformers the rotational symmetry number is equal to 2. This is to be taken into account during the calculations of the Boltzmann populations, using their Gibbs free energies. Only 10 conformers are significant and will be used for the construction of the spectra. For each of them $\tau_1$ and $\tau_6$ are equal to 180°. Conformational analysis of the last configuration, SSSS, is comparable to that of the third one. The substituents are again indistinguishable, because they have the same absolute configuration. Again for some of the conformers, a twofold rotation axis can be found. In Table 5.4 the conformers of each configuration are given together with their Boltzmann populations and the dihedral angles of each substituent.

**Table 5.4:** B3LYP/6-31G(d) relative free energies ($\Delta G^0$, in kcal/mol) and Boltzmann populations (%F, T=298.15K) for the localized conformations of each diastereomer of **2**. For the substituents the torsions ($\tau_1$, $\tau_2$, $\tau_3$, $\tau_4$, $\tau_5$ and $\tau_6$ in degrees) are given. In case of symmetry, the point group is written between brackets. The labels (a, b, c, etc.), found in the first column are used later on to assign the experimental spectra.

| | $\tau_3$ | $\tau_2$ | $\tau_1$ | $\tau_4$ | $\tau_5$ | $\tau_6$ | $\Delta G^0$ | %F |
|---|---|---|---|---|---|---|---|---|
| | | | | RRSR | | | | |
| 1a | 155 | 84 | 179 | 78 | 95 | 178 | 0.00 | 40.40 |
| 2b | 159 | 165 | -179 | 80 | 165 | 179 | 0.31 | 24.14 |
| 3c | 156 | 84 | 179 | 79 | 163 | -179 | 0.43 | 19.45 |
| 4d | 159 | 165 | -179 | 79 | 93 | 179 | 0.55 | 16.01 |
| | | | | SRSS | | | | |
| 1a | 146 | 78 | 178 | -142 | -93 | -178 | 0.00 | 17.01 |
| 2b | 149 | 158 | -179 | -147 | -159 | 180 | 0.22 | 11.69 |

*continued on next page*

*continued from previous page*

| | $\tau_3$ | $\tau_2$ | $\tau_1$ | $\tau_4$ | $\tau_5$ | $\tau_6$ | $\Delta G^0$ | %F |
|---|---|---|---|---|---|---|---|---|
| 3c | 145 | 78 | 179 | -148 | -159 | 180 | 0.44 | 8.05 |
| 4d | 91 | 104 | 178 | -93 | -82 | -179 | 0.46 | 7.77 |
| 5e | 82 | 161 | -180 | -156 | -160 | 179 | 0.49 | 7.47 |
| 6f | 82 | 162 | 179 | -153 | -95 | -179 | 0.52 | 7.12 |
| 7g | 150 | 159 | -180 | -141 | -93 | -178 | 0.53 | 6.95 |
| 8h | 92 | 105 | 178 | -94 | -161 | 180 | 0.57 | 6.54 |
| 9i | 93 | 159 | -180 | -94 | -161 | 180 | 0.58 | 6.44 |
| 10j | 93 | 158 | -180 | -92 | -82 | -179 | 0.69 | 5.29 |
| 11k | 158 | 159 | -179 | -82 | -84 | -179 | 0.84 | 4.14 |
| 12l | 92 | 99 | 177 | -142 | -85 | -179 | 0.88 | 3.82 |
| 13m | 154 | 82 | 179 | -84 | -162 | 179 | 0.89 | 3.80 |
| 14n | 155 | 82 | 179 | -81 | -84 | -180 | 1.16 | 2.39 |
| 15o | 157 | 159 | -179 | -85 | -161 | 179 | 1.43 | 1.52 |
| | | | | SRSR | | | | |
| 1a | 145 | 77 | 179 | 95 | 160 | -180 | 0.00 | 20.28 |
| 2b | 145 | 78 | 179 | 92 | 103 | 178 | 0.13 | 16.30 |
| 3c | 148 | 159 | -180 | 94 | 158 | -180 | 0.22 | 13.93 |
| 4d ($C_2$) | 155 | 82 | 179 | 155 | 82 | 179 | 0.26 | 13.17 |
| 5e | 155 | 81 | 178 | 158 | 159 | -179 | 0.38 | 10.66 |
| 6f | 92 | 103 | 178 | 148 | 158 | -179 | 0.42 | 9.92 |
| 7g | 91 | 159 | -179 | 89 | 99 | 178 | 0.60 | 7.39 |
| 8h ($C_2$) | 90 | 160 | -179 | 90 | 160 | -179 | 0.76 | 5.65 |
| 9i ($C_2$) | 159 | 158 | -179 | 159 | 158 | -179 | 1.53 | 1.54 |
| 10j($C_2$) | 95 | 95 | 178 | 95 | 95 | 178 | 1.69 | 1.16 |
| | | | | SSSS | | | | |
| 1a | -91 | -82 | -179 | -144 | -95 | -178 | 0.00 | 35.91 |
| 2b | -147 | -159 | 180 | -91 | -82 | -179 | 0.64 | 12.25 |
| 3c | -93 | -161 | -180 | -142 | -95 | -179 | 0.67 | 11.65 |
| 4d | -93 | -161 | 180 | -146 | -160 | 180 | 0.34 | 20.38 |
| 5e ($C_2$) | -82 | -85 | -180 | -82 | -85 | -180 | 1.73 | 1.93 |
| 6f ($C_2$) | -139 | -82 | -179 | -139 | -82 | -179 | 1.00 | 6.60 |
| 7g | -85 | -161 | 179 | -82 | -84 | -179 | 1.29 | 4.07 |

*continued on next page*

*continued from previous page*

| | $\tau_3$ | $\tau_2$ | $\tau_1$ | $\tau_4$ | $\tau_5$ | $\tau_6$ | $\Delta G^0$ | %F |
|---|---|---|---|---|---|---|---|---|
| 8h ($C_2$) | -84 | -162 | 180 | -84 | -162 | 180 | 2.10 | 1.03 |
| 9i | -145 | -159 | 180 | -140 | -84 | -178 | 1.37 | 3.55 |
| 10j ($C_2$) | -148 | -161 | 179 | -148 | -161 | 179 | 1.60 | 2.41 |
| 11k | -154 | 63 | 180 | -90 | -83 | -180 | 3.81 | 0.06 |
| 12l | -90 | -83 | -180 | -154 | 63 | 180 | 3.76 | 0.06 |
| 13m | -93 | -161 | 179 | -155 | 63 | 180 | 3.70 | 0.07 |
| 14n | -140 | -83 | -179 | -153 | 62 | 179 | 4.43 | 0.02 |

**Bicyclo[3.3.0]octane-2,6-dione (3).** This molecule has 2 chiral centers. The trans-coupled bicyclic system contains an inversion center and is optically inactive. Therefore only one diastereomer has to be taken into account to predict the absolute configuration. Calculations of (1*R*,5*R*)-**3** = RR have been performed. During conformational analysis, two different conformers have been found. Their difference in free energy is 1.99 kcal/mol. This leads to populations of 96.6% and 3.3%.

**Bicyclo[3.3.0]octa-2,6-dien-2,6-bistriflate (4).** Because of the same reasons as for 3 only one diastereomer has to be taken into account. Calculations have been performed for (1*R*,5*R*)-**3** = RR. During conformational analysis, four dihedrals have been varied, two of each substituent, shown in Figure 5.5. The substituents are indistinguishable. In Table 5.5 the Boltzmann populations of each conformer together with their dihedral angles are shown. Some of the minima contain a twofold rotation axis.

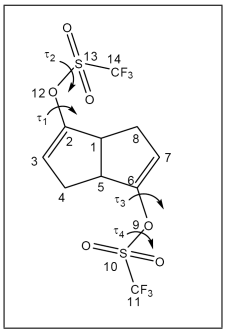


**Figure 5.5:** conformational analysis of 4 through the variation of four torsions: $\tau_1$ = S13-O12-C2-C1, $\tau_2$ = C14-S13-O12-C2, $\tau_3$ = S10-O9-C6-C5 and $\tau_4$ = C11-S10- O9-C6.

**Table 5.5:** B3LYP/6-31G(d) relative free energies ($\Delta G^0$, in kcal/mol) and Boltzmann populations (%F, T= 298.15K) for the localized conformations of **4**. The torsions ($\tau_1$, $\tau_2$, $\tau_3$ and $\tau_4$) of each substituent are written in degrees.The labels (a, b, c, etc.), found in the first column are used later on to assign the experimental spectra.

| RR | $\tau_1$ | $\tau_2$ | $\tau_3$ | $\tau_4$ | $\Delta G^0$ | %F |
|---|---|---|---|---|---|---|
| 1a | -82 | -103 | -122 | 89 | 0.000 | 9.31 |
| 2b | -81 | -102 | -68 | -163 | 0.009 | 9.17 |
| 3c | -101 | 167 | 148 | -85 | 0.103 | 7.82 |
| 4d | -81 | -101 | -98 | 164 | 0.155 | 7.16 |
| 5e | -82 | 109 | -80 | -101 | 0.158 | 7.13 |
| 6f | -97 | 164 | -97 | 164 | 0.160 | 7.10 |
| 7g | 125 | -178 | -100 | 168 | 0.220 | 6.42 |
| 8h ($C_2$) | -82 | -102 | -82 | -102 | 0.278 | 5.82 |
| 9i | -83 | 110 | -103 | 165 | 0.421 | 4.57 |
| 10j | -123 | 89 | -82 | 110 | 0.548 | 3.69 |
| 11k ($C_2$) | -121 | 91 | -122 | 90 | 0.558 | 3.63 |
| 12l | 125 | -179 | -122 | 90 | 0.574 | 3.53 |
| 13m | 125 | 180 | -81 | -103 | 0.579 | 3.51 |
| 14n | 126 | -179 | -82 | 111 | 0.581 | 3.49 |
| 15o | 149 | -85 | -82 | -103 | 0.649 | 3.11 |
| 16p ($C_2$) | 126 | -180 | 126 | -180 | 0.866 | 2.16 |
| 17q | -82 | -102 | 105 | 105 | 0.868 | 2.15 |
| 18r | 110 | 110 | 150 | -83 | 0.990 | 1.75 |
| 19s | 104 | 105 | -121 | 88 | 1.143 | 1.35 |
| 20t | -84 | 108 | 148 | -84 | 1.202 | 1.22 |
| 21u | 148 | -85 | -102 | 163 | 1.349 | 0.96 |
| 22v | -122 | 90 | 149 | -84 | 1.397 | 0.88 |
| 23w ($C_2$) | 147 | -80 | 147 | -80 | 1.441 | 0.82 |
| 24x | 125 | -180 | 150 | -82 | 1.444 | 0.81 |
| 25y | 105 | 105 | -82 | 110 | 1.480 | 0.77 |
| 26z ($C_2$) | 148 | -80 | 148 | -80 | 1.546 | 0.69 |
| 27aa | 125 | 180 | 104 | 106 | 1.637 | 0.59 |
| 28ab ($C_2$) | 104 | 105 | 104 | 105 | 1.872 | 0.40 |

**IR and VCD spectra.** In order to determine the absolute configuration of (+)-**1**, 8 stereo-isomers have to be considered. It is, however, sufficient to perform calculations for the selected diastereomers: RRSR, RSRR, RRRR and RSRS. In Figure 5.6 and Figure 5.7 their Boltzmann weighted IR and VCD spectra respectively are given. One by one they are to be compared to the corresponding experimental spectra. By only considering the unpolarized IR spectra it is very difficult to draw a conclusion about the relative configuration. In the VCD spectrum, however, bands with opposite sign are resolved. This gives extra information during the assignment. The diastereomer with configuration, RSRS, shows the greatest resemblance with the experiment.

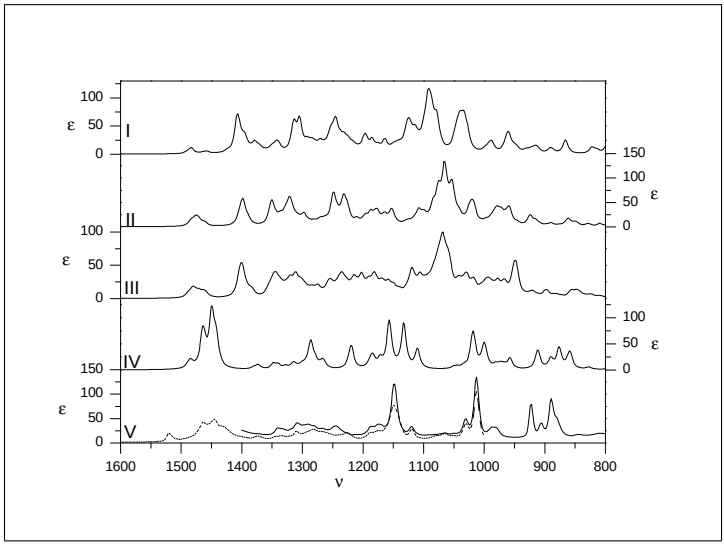


**Figure 5.6:** B3LYP/6-31G(d) IR spectra of each diastereomer of **1**: I - RRSR, II - RRRR, III - RSRR, IV - RSRS. Experimental unpolarized IR absorption spectrum of (+)-**1** (V) in $CS_2$ (solid line, 800 $cm^{-1}$-1400 $cm^{-1}$) and in $CDCl_3$ (dotted line, 1000 $cm^{-1}$-1600 $cm^{-1}$). Experimental and theoretical intensities in $L\ mol^{-1}\ cm^{-1}$; frequencies in $cm^{-1}$.

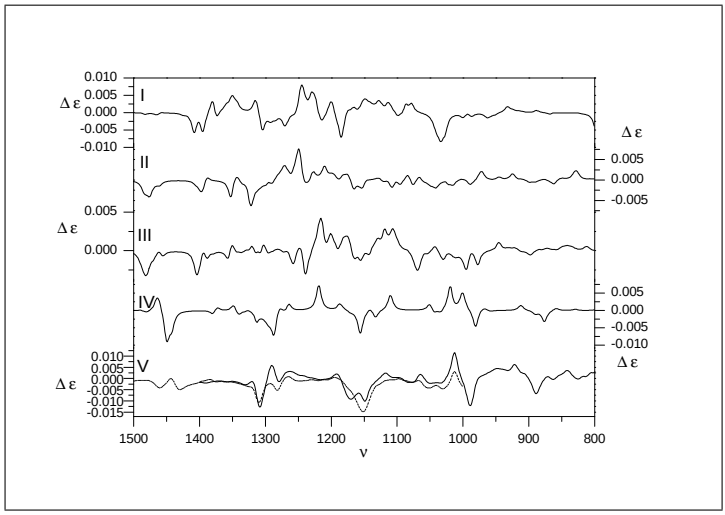


**Figure 5.7:** B3LYP/6-31G(d) VCD spectra of each diastereomer of **1**: I RRSR, II RRRR, III RSRR, IV RSRS. Experimental VCD spectrum of (+)-**1** (V) in $CS_2$ (solid line, 800 $cm^{-1}$-1400 $cm^{-1}$) and in $CDCl_3$ (dotted line, 1000 $cm^{-1}$- 1600 $cm^{-1}$). Experimental and theoretical intensities in $L\ mol^{-1}\ cm^{-1}$; frequencies in $cm^{-1}$.

This, however, is not sufficient to draw a conclusion on the absolute configuration of (+)-**1**. In order to be sure, it is necessary to perform an assignment of the experimental bands, based on the theoretical spectra of the RSRS configuration, calculated at the B3LYP/6-31G(d) level. This is shown in Figure 5.8 and Figure 5.9. Fundamentals designated as "a" originate from conformation aTaG; those designated as "b" represent aG'aG. No label is used when fundamentals of both conformations coincide or have a small difference in frequency. The similarity with the experimental spectrum was found to be much greater than for any of the other possible diastereomers, allowing one to establish the absolute configuration. Yet, there are also several bands that do not agree completely between experiment and theory. First of all, several bands are not completely resolved. In the experimental IR spectrum, fundamental 19 appears to be a shoulder of fundamental 20, while in the calculated spectra there are two separate bands visible. Fundamentals 26/27 and 31/32 are not resolved in the experimental spectrum, while they clearly are in the calculated spectrum. The fundamentals 26/27 are not resolved in the experimental VCD and IR spectra, while they

are separated in the calculated spectrum. The same can be said about fundamentals 31/32. Given the number of bands in the spectra, it is not surprising that sometimes bands overlap in either the experimental or theoretical spectrum.vMore problematic than the band absorption frequencies are the intensities of transitions. These significant differences between theory and experiment are often found . The intensity of fundamental 39/40 seems to be overestimated in the calculated IR spectrum. This is also the case for the intensity of fundamental 36, since the band is not visible in the experimental VCD spectrum. Fundamentals 23/24 are not clearly visible in the experimental VCD spectrum. The band visible at 1520 $cm^{-1}$ in the IR spectrum cannot be explained by the calculations and is probably due to impurities in the solvent during the measurements.

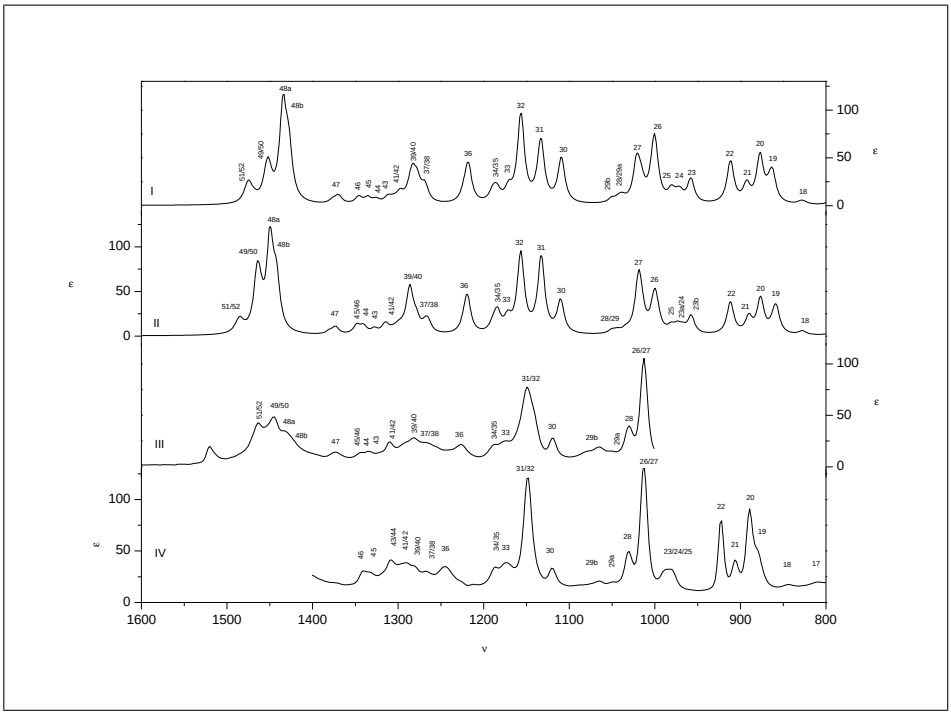


**Figure 5.8:** Assignment of the bands. B3LYP/6-31G(d) (II) and B3LYP/cc-pVTZ (I) simulated IR spectra for (1*R*,2*S*,5*R*,6*S*)-**1**. experimental IR spectrum in $CS_2$ (III) and $CDCl_3$ (IV) of (+)-**1**. Experimental and theoretical intensities in $L\ mol^{-1}\ cm^{-1}$; frequencies in $cm^{-1}$.

More important than the intensities and individual resolution of the

peaks is that the signs of the fundamentals are mostly predicted correctly. The study of the agreement of spectra is, in first instance, based on this agreement. Yet, even then small differences can appear. Fundamentals 41/42 in the VCD spectrum, measured in $CS_2$, have a positive sign while they are predicted to be negative.

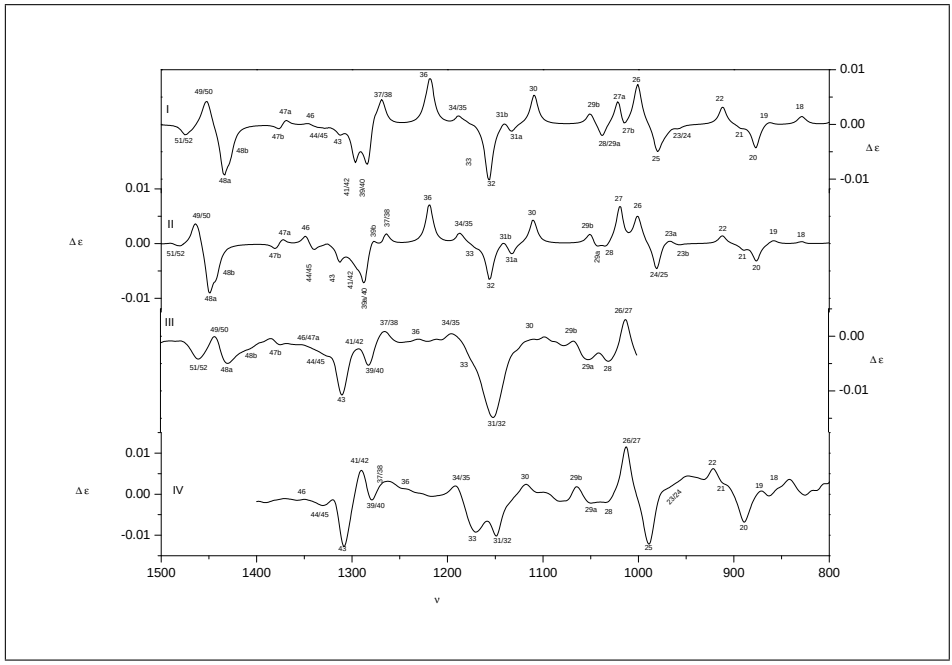


**Figure 5.9:** Assignment of the bands. B3LYP/6-31G(d) (II) and B3LYP/cc-pVTZ (I) simulated VCD spectra for (1*R*,2*S*,5*R*,6*S*)-**1**. experimental VCD spectrum in $CS_2$ (III) and $CDCl_3$ (IV) of (+)-**1**. Experimental and theoretical intensities in $L\ mol^{-1}\ cm^{-1}$; frequencies in $cm^{-1}$.

Next to a rather visual inspection, a quantitative comparison between calculation and experiment can be found in the Figure 5.10 and Figure 5.11 where the calculated dipole/rotational strengths are plotted as a function of the experimental ones. The corresponding tables, including information on the experimental and calculated frequencies, dipole and rotational strengths, are shown in the Supporting Information (S-1). Correlation coefficients of 0.85 and 0.73 are obtained for the dipole and rotational strengths respectively. It is well-known that for VCD these values are quite often relatively low, especially for larger molecules. As such, these quantitative comparisons are not decisive. Moreover, in the ideal case, the slope of the best linear fits is expected to be equal to 1, for the dipole and rotational strengths of **1**, however, a smaller and larger value was found, respectively. Deviations can be explained by a systematical under/overestimation of the calculated dipole or rotational strengths, by the precision of the concentration of the sample ($CDCl_3$ is very likely to evaporate during the measurements) or again by inaccuracies during the fitting procedure. The cc-pVTZ spectra, also shown in Figure 5.8 and Figure 5.9, agree very well with the 6-31G(d) spectra. Given the good agreement between experimental and theoretical (1*R*,2*S*,5*R*,6*S*)-**1** spectra and the lack of any good agreement with the other diastereomers, the absolute configuration of (+)-**1** is concluded to correspond to (1*R*,2*S*,5*R*,6*S*)-**1**.

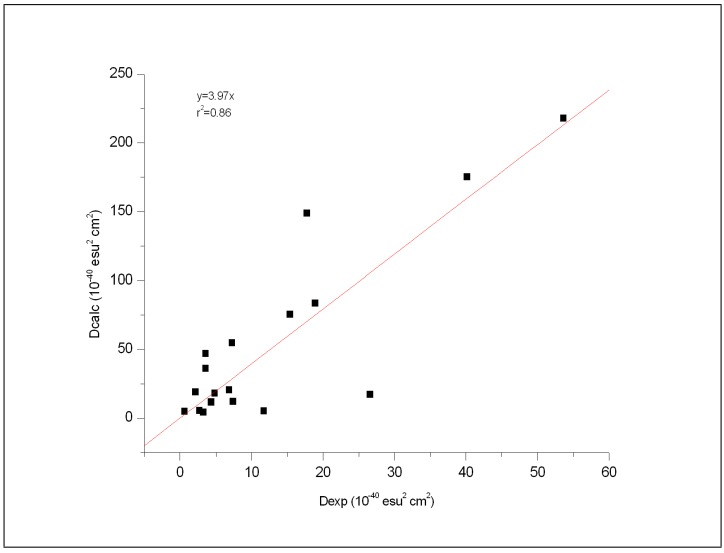


**Figure 5.10:** Comparison of the experimental Dipole strengths and the calculated ones.

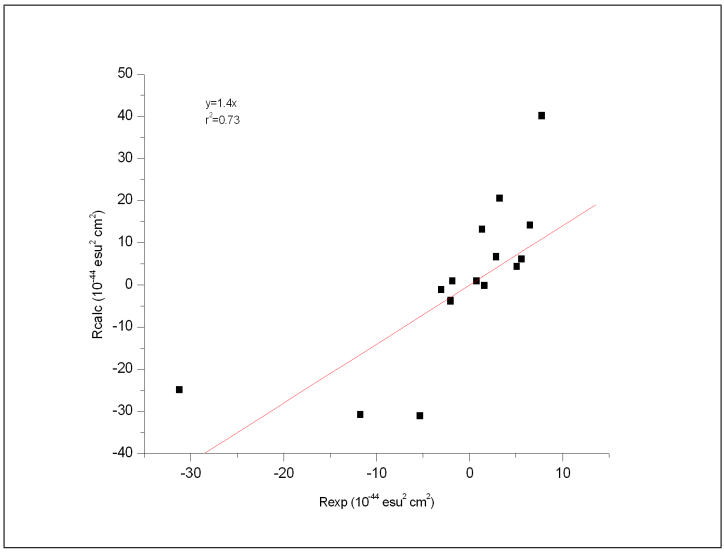


**Figure 5.11:** Comparison of the experimental Rotational strengths and the calculated ones

For each possible configuration of **2**, the Boltzmann weighted IR and VCD spectra have been constructed. In Figure 5.12 and Figure 5.13 the calculated spectra are compared to the experimental IR and VCD spectrum respectively. Taking into account only the IR spectra, no conclusion could be drawn about the discrimination of the diastereomers.

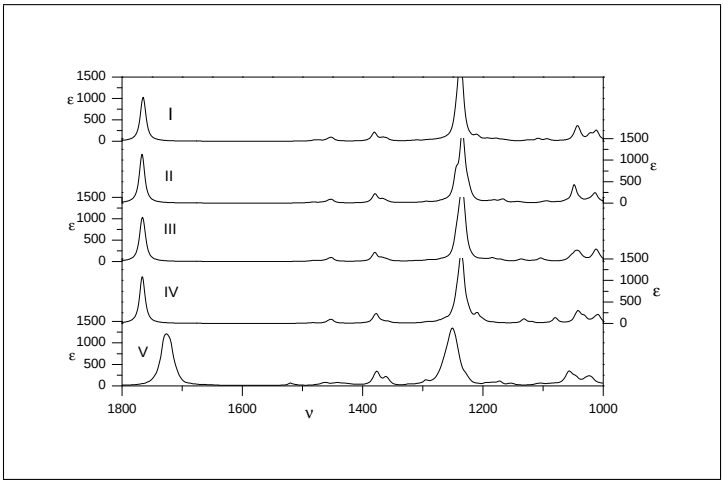


**Figure 5.12:** B3LYP/6-31G(d) IR spectra of each diastereomer of **2**: I - SSSS, II - SRSR, III - SRSS and IV - RRSR. Experimental unpolarized IR absorption spectrum of (+)-**2** (V) in $CDCl_3$ (1000 $cm^{-1}$-1600 $cm^{-1}$). Experimental and theoretical intensities in $L\ mol^{-1}\ cm^{-1}$; frequencies in $cm^{-1}$.

The signs of two patterns in the VCD spectrum give extra information for the assignment. In the calculated spectra of the second (SRSS) and third (SRSR) configuration, an intense positive band is immediately followed by a large negative one in the region between 1200 $cm^{-1}$ and 1300 $cm^{-1}$. This is in agreement with the experimental band signs in that region. The opposite patterns have been found in the calculated spectra of the first (RRSR) and the last (SSSS) configurations, which could suggest their corresponding enantiomers. A second pattern, however, leads to the exclusion of three of the configurations. The VCD pattern of the CO stretching vibration (1700 $cm^{-1}$-1800 $cm^{-1}$) in the experimental spectrum gives rise to an intense positive band, followed by an intense negative band. The corresponding patterns in the calculated VCD spectra of configurations RRSR and SSSS are totally different from the experiment. Only one positive band followed by a negative band is

visible. In configuration SRSS two bands are visible, but opposite in sign compared to the experiment. Only in the SRSR spectrum are the signs of the two patterns described above in good agreement with experiment. This immediately suggests the absolute configuration.

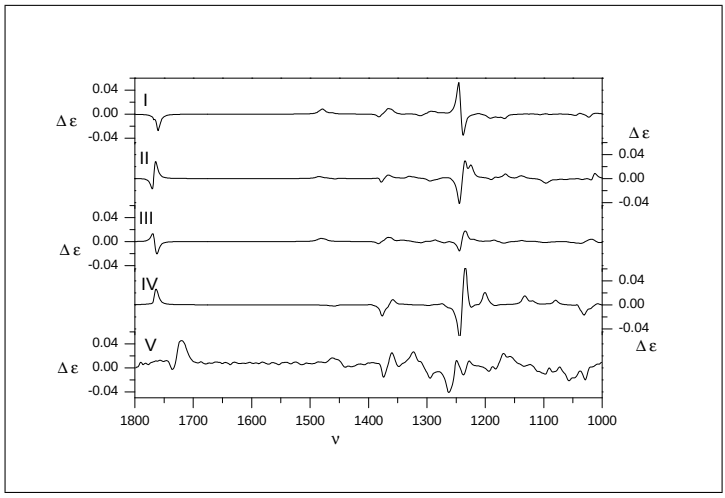


**Figure 5.13:** B3LYP/6-31G(d) VCD spectra of each diastereomer of **2**: I - SSSS, II - SRSR, III - SRSS and IV - RRSR . Experimental VCD absorption spectrum of (+)-**2** (V) in $CDCl_3$ (1000 $cm^{-1}$-1600 $cm^{-1}$). Experimental and theoretical intensities in $L\ mol^{-1}\ cm^{-1}$; frequencies in $cm^{-1}$.

In order to be certain about the determination of the absolute configuration of (+)-**2**, each band in the experimental spectrum has to be linked with a band of the B3LYP/6-31G(d) spectrum of the SRSR configuration. The assignment is shown in Figure 5.14 and Figure 5.15. There is a good overall agreement between the calculated and experimental IR spectra of **2**. Due to the large number of conformations that need to be taken into account, the assignment becomes more complex. Especially in the region 1300 $cm^{-1}$-1500 $cm^{-1}$, the bands are not resolved. This, however, is in agreement with the experiment. Most of the bands in the experimental spectra cannot be attributed to a certain conformation, since their normal modes appear to have nearly identical frequencies. Two bands, however, around 1080 $cm^{-1}$ can only be linked to a conformer with higher energy, and are labeled by "d". The band visible at 1520 $cm^{-1}$ is probably due to impurities in the solvent during the measurements.

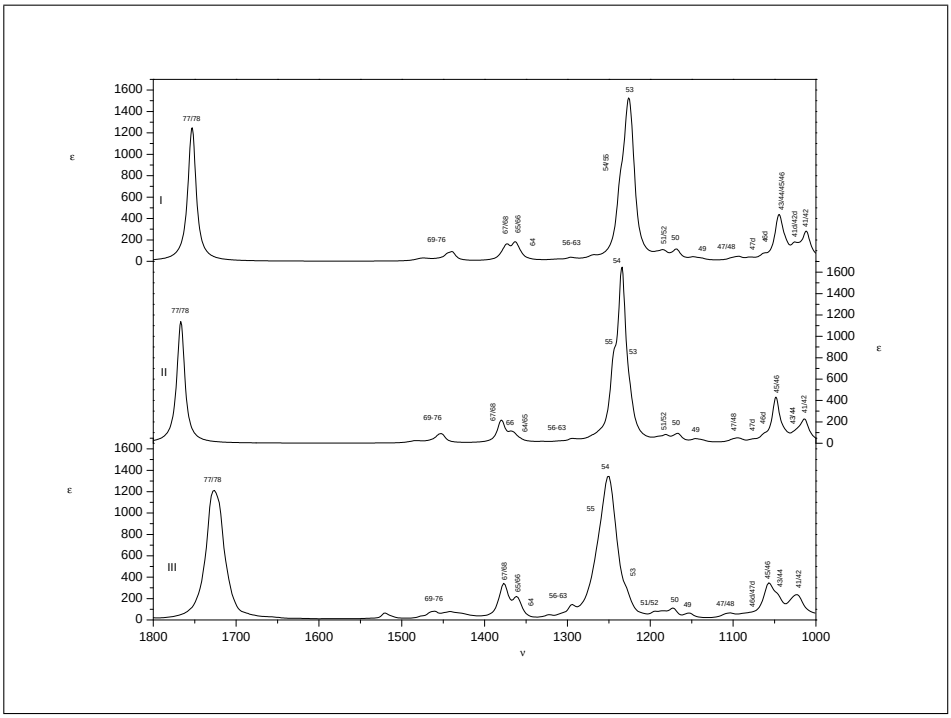


**Figure 5.14:** Assignment of the bands. B3LYP/6-31G(d) (II) and B3LYP/cc-pVTZ (I) simulated IR spectra for (1*S*,2*R*,5*S*,6*R*)-**2**. Experimental IR spectrum in $CDCl_3$ of (+)-**2** (III). Experimental and theoretical intensities $L\ mol^{-1}\ cm^{-1}$; frequencies in $cm^{-1}$.

There is an overall agreement between the calculated and the experimental VCD spectrum of **2**. Again normal modes 46 and 47 originating from the conformer "d", are visible. In the VCD spectrum, the signs resolve some bands. This is especially the case for fundamentals 53/54/55 and 77/78. Still not all modes can be separated by looking at the VCD spectrum. Since the normal mode 51, originating from the minima labeled by "a" and "c", give rise to a positive band and the same mode of the conformers, designated by "b" and "d", leads to a negative band, two separate bands are visible in the VCD spectrum. The conformations, connected with those labels, are described in Table 5.4.

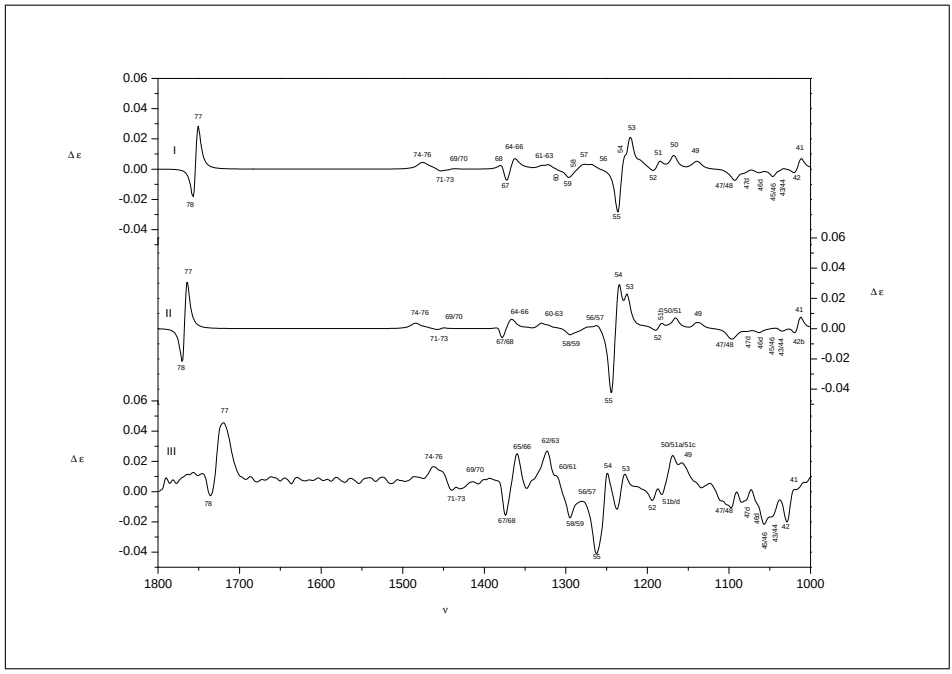


**Figure 5.15:** Assignment of the bands. B3LYP/6-31G(d) (II) and B3LYP/cc-pVTZ (I) simulated IR spectra for (1*S*,2*R*,5*S*,6*R*)-**2**. Experimental IR spectrum in $CDCl_3$ of (+)-**2** (III). Experimental and theoretical intensities $L\ mol^{-1}\ cm^{-1}$; frequencies in $cm^{-1}$.

The assignment of the experimental spectra is confirmed by the scatter plots, given in Figure 5.16 and Figure 5.17. The corresponding tables with more detailed information about the rotational and dipole strengths are shown in the Supporting Information (S-2). The experimental dipole and rotational strengths have been linked to the calculated values. The correlation factors are 0.92 and 0.73 for the IR and VCD spectra respectively.

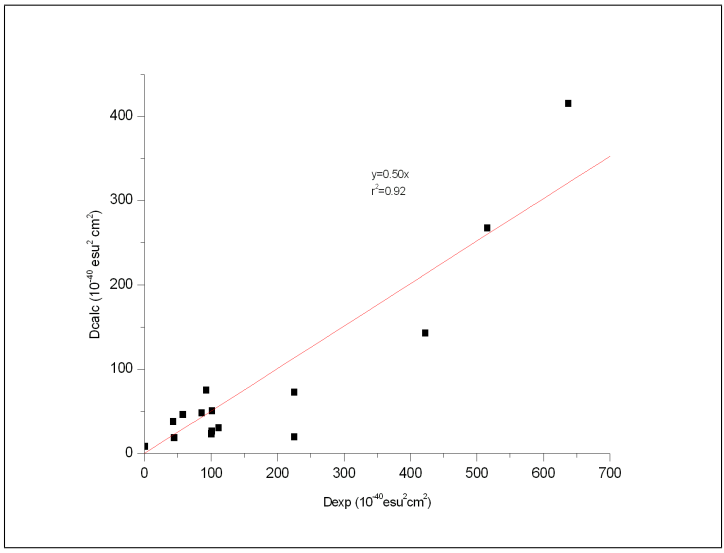


**Figure 5.16:** Comparison of the experimental Dipole strengths with the calculated ones.

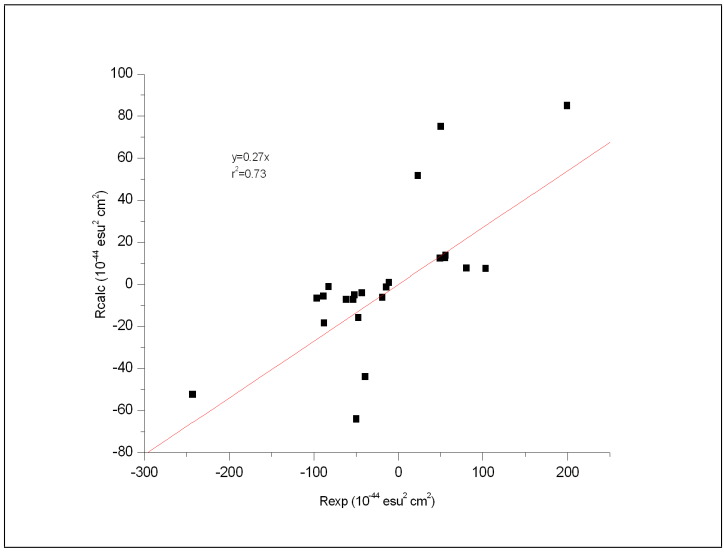


**Figure 5.17:** Comparison of the experimental Rotational strengths with the calculated ones.

For the cc-pVTZ spectra small differences can be observed compared to the 6-31G(d) spectrum. The relative intensities of the normal modes

65/66 and 67/68 are different. In the VCD spectra also a few differences are visible. None of them, however, lead to a different assignment of the bands. The band originating from normal modes 45 and 46 is more important at the cc-pVTZ level. This trend is in better agreement with the experiment. At the cc-pVTZ level, the intensity of fundamental 54 is lower than fundamental 53. This is opposite to the 6-31G(d) calculations and the experiment. The 6-31G(d) basis set seems to be sufficient to determine that the absolute configuration of (+)-**2** corresponds to (1*S*,2*R*,5*S*,6*R*)-**2**. This application of VCD for the determination of the absolute configuration illustrates how not only a good agreement between experiment and theory for one diastereomer is important, but also how the absolute configuration can be established by demonstrating that all other diastereomers give much poorer agreement between theory and experiment.

The spectra of (1*R*,5*R*)-**3** have been calculated at the B3LYP/6-31G* level and were compared with the corresponding experimental spectra of (-)-**3**. There is an overall agreement between both spectra. The assignment of the experimental bands is shown in Figure 5.18 and Figure 5.19. Label "a" corresponds to the conformer with the lowest energy. Bands designated as "b" originate from the minimum with the highest energy. Some differences are observed between the experimental and calculated IR spectra of **3**. In the experimental spectra fundamentals 26a and 26b are resolved, while they form one band in the B3LYP/6-31G(d) spectra. On the other hand fundamental 27 is not visible in experimental IR spectrum, while it clearly is in the calculated spectrum. Fundamental 34 is underestimated in the predicted spectrum. The intensity of band 28 is larger than band 26 in the experimental spectrum; this is opposite to the calculations.

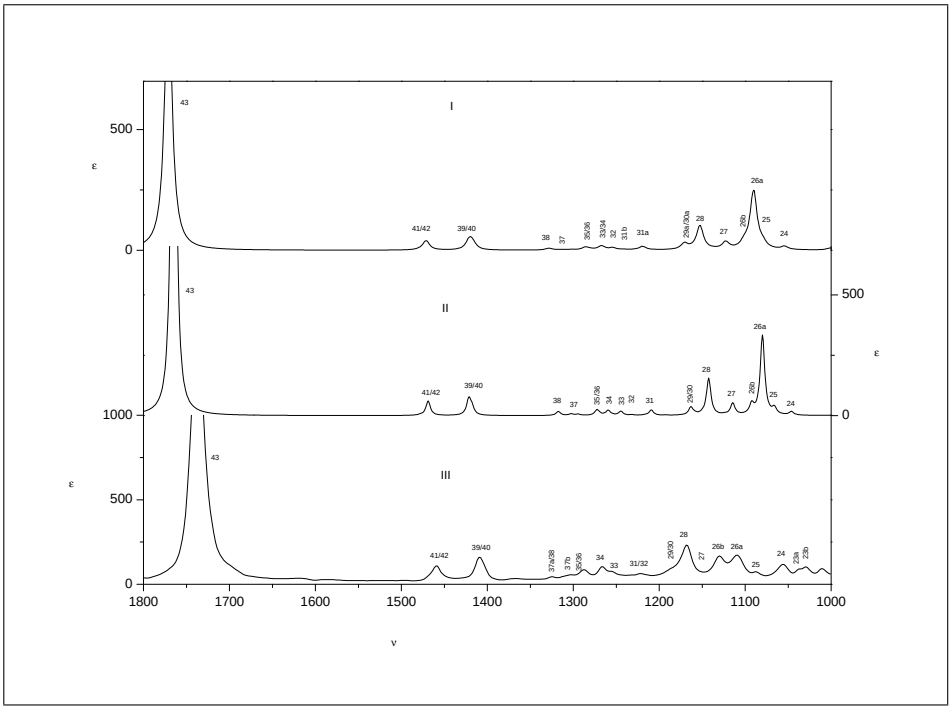


**Figure 5.18:** Assignment of the bands. B3LYP/6-31G(d) (II) and B3LYP/cc-pVTZ (I) simulated IR spectra for (1*R*,5*R*)-**3**. Experimental IR spectrum in $CDCl_3$ of (-)-**3** (III). Experimental and theoretical intensities in $L\ mol^{-1}\ cm^{-1}$; frequencies in $cm^{-1}$.

The agreement between the VCD spectra of **3** is excellent: all signs are predicted correctly.

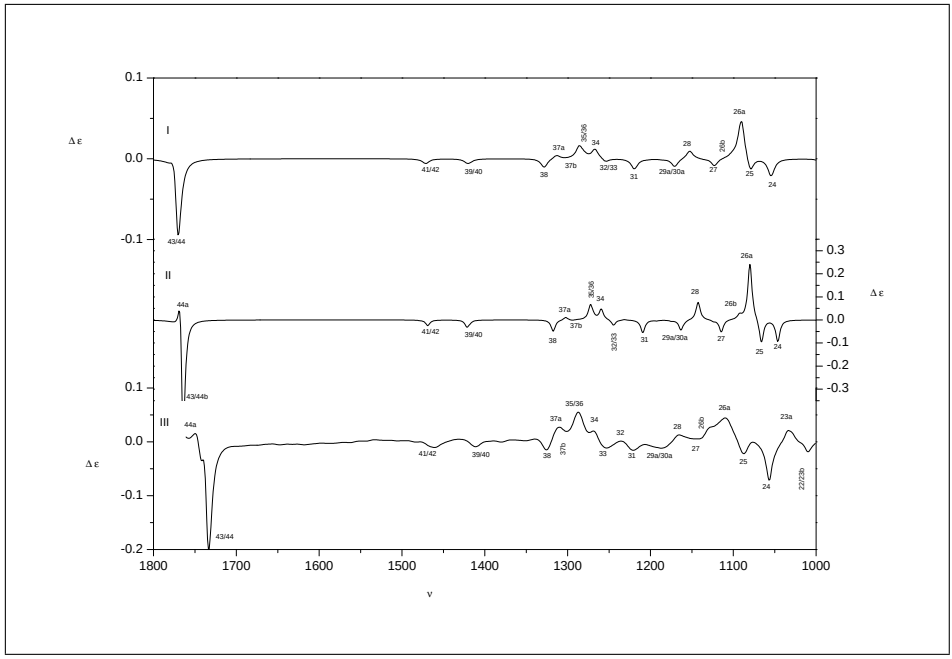


**Figure 5.19:** Assignment of the bands. B3LYP/6-31G(d) (II) and B3LYP/cc-pVTZ (I) simulated VCD spectra for (1*R*,5*R*)-**3**. Experimental VCD spectrum in $CDCl_3$ of (-)-**3** (III). Experimental and theoretical intensities in $L\ mol^{-1}\ cm^{-1}$; frequencies in $cm^{-1}$.

This has been confirmed by comparing the calculated and experimental dipole and rotational strengths of each band. The scatter plots are depicted in Figure 5.20 and Figure 5.21. Extra information on the dipole and rotational strengths can be found in the Supporting Information (S-3). Correlation factors of 0.67 and 0.82 have been obtained for the dipole and rotational strengths respectively.

The cc-pVTZ and 6-31G(d) spectra show no large differences. The B3LYP/6-31G(d) level is sufficient to correctly assign the bands of the experimental spectra. It can be concluded that (1*R*,5*R*)-**3** corresponds to (-)-**3**.

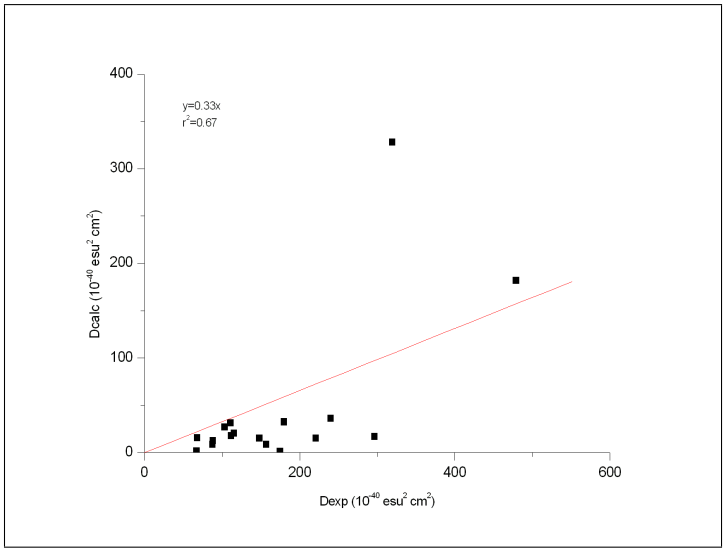


**Figure 5.20:** Comparison of the experimental Dipole strengths and the calculated ones.

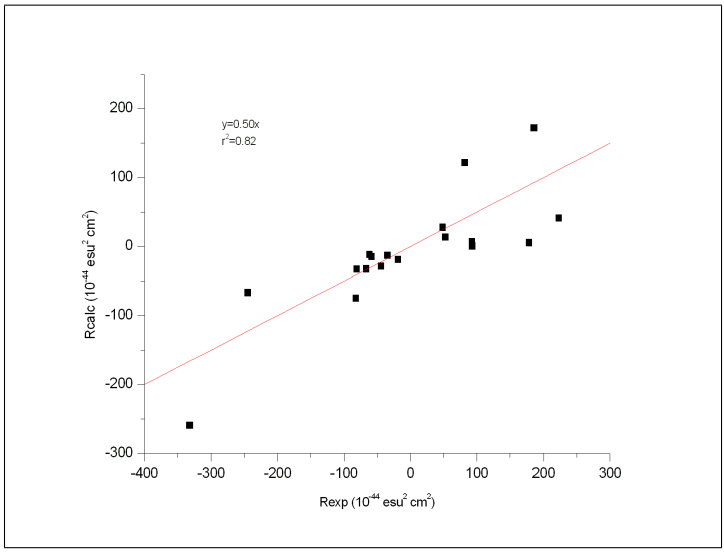


**Figure 5.21:** Comparison of the experimental Rotational strengths and the calculated ones.

Predicted spectra of (1*R*,5*R*)-**4** configuration have been constructed and compared to the experimental spectra of (-)-**4**. Frequencies and intensities have been calculated at the B3LYP/6-31G(d) level. In Figure 5.22 and Figure 5.23 the assignment of each band in the experimental spectra is shown. The corresponding normal modes of all significant conformations are found to coincide. Looking at the most intense peaks, the best agreement occurs for the computed (1*R*,5*R*)-**4** absolute configuration.

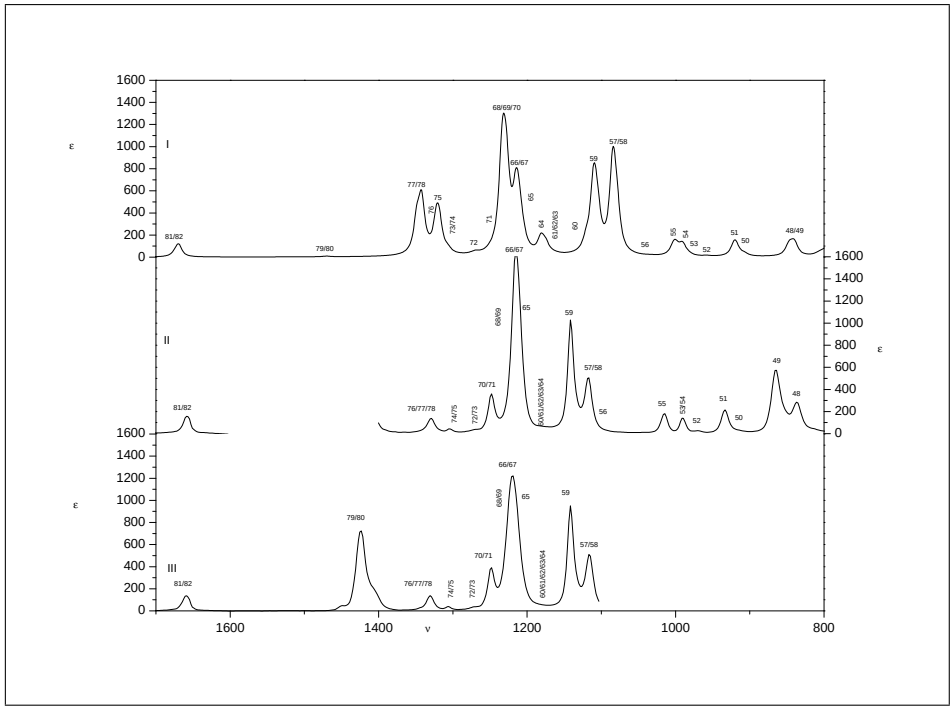


**Figure 5.22:** Assignment of the bands. B3LYP/6-31G(d) (I) simulated IR spectrum for (1*R*,5*R*)-**4**. Experimental IR spectra in $CS_2$ (II) and $CDCl_3$ (III) of ()-**4**. Experimental and theoretical intensities in $L\ mol^{-1}\ cm^{-1}$; frequencies in $cm^{-1}$.

Molecule **4** is a good illustration of the fact that for larger molecules more detailed features of the spectra may disagree between theory and experiment. This shows that then one must focus on the most intense peaks. Again, several bands are not well resolved, although the sign dimension in VCD does allow one to improve on the IR assignment. Coherent with the discussion above, relative intensities are also prob-

lematic for several peaks. All this shows that it is not evident to interpret the experimental VCD spectrum because of the small signal to noise ratio, especially in the frequency regions 1000 $cm^{-1}$-1100 $cm^{-1}$ and 1200 $cm^{-1}$-1300 $cm^{-1}$. The signs of the most intense bands however are predicted correctly. Based on the most intense bands in both the experimental and the calculated VCD spectrum, it can be said that (-)-**4** corresponds to (1*R*,5*R*)-**4**.

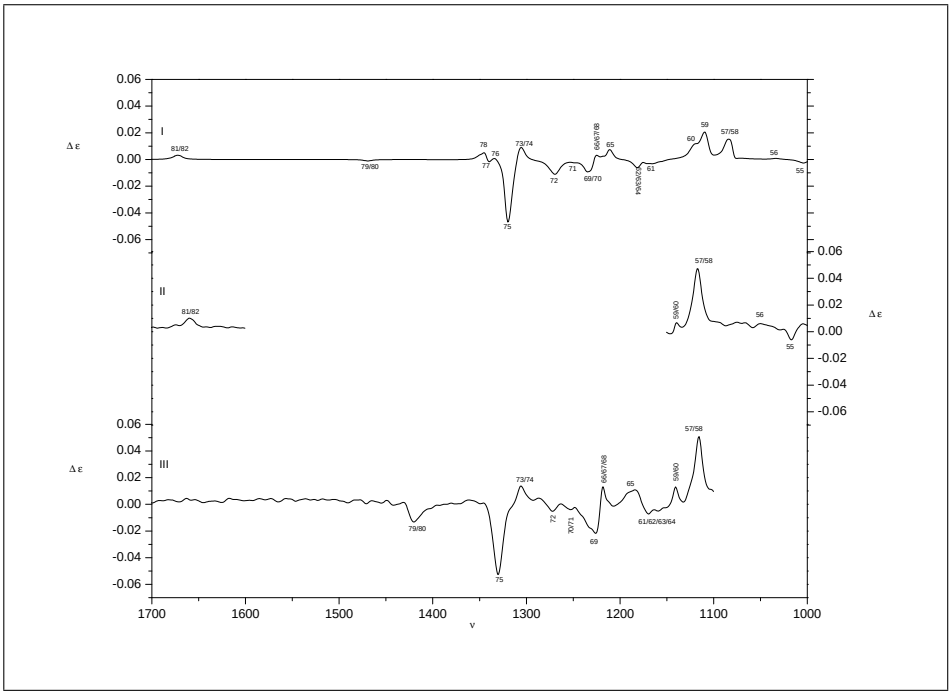


**Figure 5.23:** Assignment of the bands. B3LYP/6-31G(d) (I) simulated VCD spectrum for (1*R*,5*R*)-**4**. Experimental VCD spectra in $CS_2$ (II) and in $CDCl_3$ (III) of (-)-**4**. Experimental and theoretical intensities in $L\ mol^{-1}\ cm^{-1}$; frequencies in $cm^{-1}$.

This is also illustrated by the correlation table, shown in the Supporting Information (S-4), in which the calculated and experimental dipole and rotational strengths have been compared. The calculated Dipole/Rotational strengths are plotted as a function of the experimental values in Figure 5.24 and Figure 5.25. Correlation factors of 0.84 and 0.74 have been obtained for the IR and VCD spectra respectively. Such values are quite typical for VCD based assignments of absolute configu-

ration. The increase in the number of problems one is confronted with for molecules of increasing size is quite typical. This also explains why the application of VCD is most interesting when it is used as early as possible in a synthesis route as then often the molecules are still smaller. We have recently shown how the implementation of VCD as a part of the synthesis strategy can help to establish the absolute configuration of the end product, which was far too large for VCD assignment. Naturally, this may require a re-thinking of the synthetic route as one must be absolutely sure that no change in absolute configuration of racemization could occur in later stages [32].

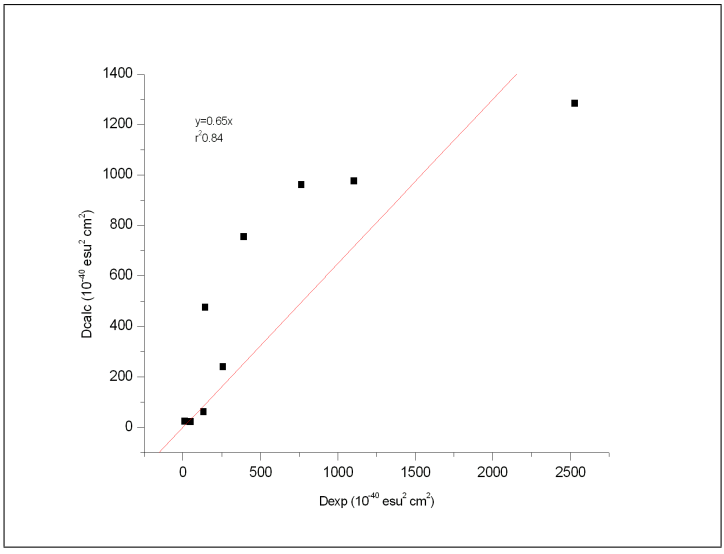


**Figure 5.24:** Comparison of the experimental Dipole strengths with the calculated ones.

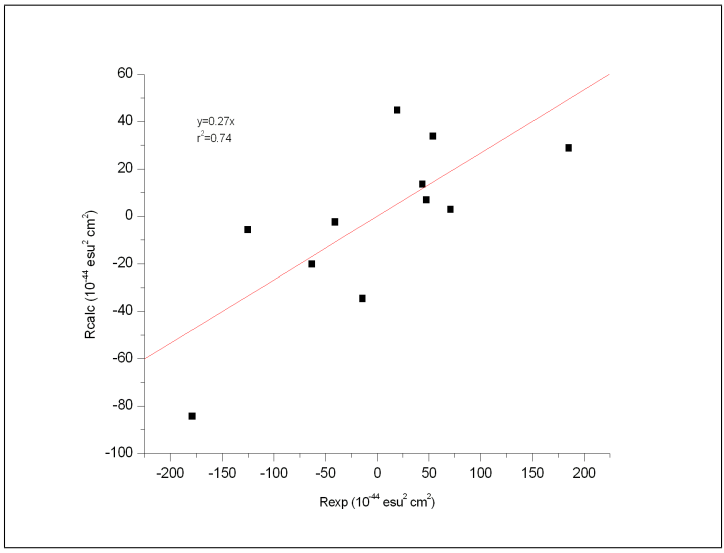


**Figure 5.25:** Comparison of the experimental Rotational strengths with the calculated ones.

## 5.5 Conclusions

Using theoretical predictions based on B3LYP/6-31G(d) and B3LYP/cc-pVTZ calculations, the absolute configurations of (+)-**1**, (+)-2 and (-)-**3** were determined respectively as (1*R*,2*S*,5*R*,6*S*)-**1**, (1*S*,2*R*,5*S*,6*R*)-**2** and (1*R*,5*R*)-**3**. From the VCD study it can be concluded that (1*R*,5*R*)-**4** corresponds to (-)-**4**. For each molecule the 6-31G(d) basis set appeared to be sufficient to allow the assignment. Moreover, no large differences were observed with respect to the cc-pVTZ calculations.

Kuppens et al. [76] tested, whether it was possible to distinguish the different diastereomers by calculating the similarities between experiment and theory. This was done by introducing the enantiomeric similarity index (ESI) as being the difference between both VCD neighborhood similarities of the enantiomers. The diastereomer with the highest ESI would then give us the correct absolute configuration. For **1**, the highest ESI value agrees with the correct configuration. For **2**, however it is not possible to identify the correction configuration, based on the ESI and thorough analysis is needed that identifies each band for 1:1 comparison.

As expected by the chemical interconversions, the absolute configurations of (+)-**1**, (-)-**3** and (-)-**4** are the same i.e. (1*R*,5*R*)-stereochemistry. The absolute configuration of (+)-**2** is opposite[91, 99].

It has been shown that the VCD technique is very useful for the determination of absolute configuration, even when several diastereomers are possible.

# 6

# A Vibrational Circular Dichroism DFT study of Dipeptidyl Peptidase inhibitors

## 6.1 Introduction

### 6.1.1 Inhibitors of dipeptidyl peptidases

Clan SC dipeptidyl peptidases (DPPs) have garnered significant research interest during the last decade. Among the catalytically active DPPs (DPP II, DPP IV, DPP8, DPP9 and FAP-$\alpha$ ), DPP IV is by far the best-studied member and currently a well-validated target in the treatment of type II diabetes with, to date, two small-molecule inhibitors of the enzyme marketed (sitagliptin/*Januvia*® and vildagliptin/*Galvus*®) and several others in different stages of clinical investigation. With a growing number of publications suggesting the drug ability of also the other catalytically active DPPs, research programs aiming at the development

of potent and selective compounds for these enzymes have been initiated both in the pharmaceutical industry and in academia [116]. In structural terms, most published DPP-inhibitors possess a bimodular, substrate-derived overall skeleton, consisting of a P1 cyclic imino building block, and a P2 residue containing an $\alpha$-aminoacyl core (**1**), as is shown in Figure 6.1. A general strategy in selective DPP inhibitor development consists of appending fragments to that basic motif that confer affinity for a specific DPP, inspired by structure-activity relationships (SAR) and/or modeling studies [117]. In a previous study, a synthetic methodology was reported for DPP inhibitors containing (2S,4R) or (2S,4S) 4-alkyl-1,4-diaminobutyryl fragments (Dab) at the P2-position [118]. Dibasic P2-residues of this type serve as recognition points for DPPII, DPP8 and the closely related DPP9 [119, 120]. The potential of maximising inhibitor selectivity and affinity by introducing specific substituents at the 4-position of the Dab moiety, depicted in Figure 6.1, was illustrated with a series of DPPII inhibitors with nanomolar activity and a selectivity index $> 1000$ [118]. An identical approach, choosing a different P1 residue is currently being investigated for the development of selective DPP8 and DPP9 inhibitors. With regards to the results obtained earlier and the further exploration of 4-substituted Dab derivatives as P2 fragments in DPP inhibitors, the assumed absolute configurations of these compounds, deduced by synthetic considerations (vide infra), needed to be established unambiguously. Therefore, a VCD analysis of selected DPP II inhibitors of type **2** was initiated.

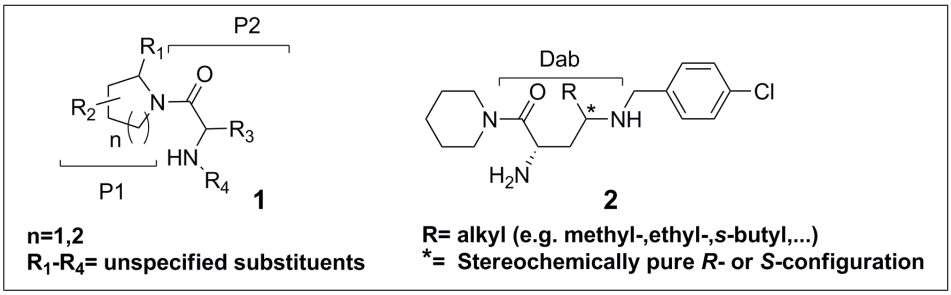


**Figure 6.1:** Generalized structures of substrate-derived DPP-inhibitors (1) and highly selective, nanomolar DPPII-inhibitors containing a 4-alkyl-1,4-diaminobutanoyl P2-residue (2).

### 6.1.2 VCD analysis

A two-stage approach involving vibrational circular dichroism (VCD) for determining the absolute configuration of the DPP II inhibitors belonging to generalized structure type **2** will be described. The reconstruction of the experimental VCD spectra of molecules of similar size is not obvious, however. The conformational analysis, which is a crucial step, needs to be performed very carefully in order to find every stable conformer. Subsequently, for all of these conformers the VCD spectrum needs to be calculated and a Boltzmann weighted spectrum must be constructed. To simplify the conformational analysis, and consequently facilitate the calculations, the molecule can be modified [121, 32] by replacing flexible groups by smaller and/or less flexible components. It is very important, however, to assure that the absolute configuration of the derivate is equal to that of the original molecule.

In this study, we aimed at investigating the diastereomeric pair of DPP II inhibitors **3a** and **3b**, belonging to generalized structure group **2** (shown in Figure 6.2). These compounds contain three stereocenters, two of which are synthetically derived from the optically pure and stereochemically defined building block L-isoleucine (described further), and therefore having identical absolute stereochemistry in both molecules. The configuration of the remaining stereocenter adjacent to the Dab-carboxyl function ('S' in **3a** and 'R' in **3b**) was deduced from synthetic considerations but required unambiguous confirmation from the VCD analysis. During our efforts to directly submit these compounds to the experimental VCD protocol, two practical problems arose. Firstly, dibasic compounds of this type in their di-cationic salt forms had very poor solubility in VCD solvents, like e.g. $CDCl_3$. Likewise, stability problems of these compounds when transformed to their uncharged counterparts by treatment with strong base, urged us to look earlier up the synthetic pathway for intermediates with more suitable characteristics. Benzyloxycarbonyl (Z)-protected analogues obtained in the penultimate synthetic step leading toward finalised inhibitors were selected, since these compounds were deemed to combine significant solubility in organic media with sufficient stability toward the well-known cyclisation tendency of uncharged 1,4-Dab derivatives yielding pyrrolidones (compounds **4a** and **4b**). However, since these are large and flexible molecules, confor-

mational analysis can reasonably be anticipated to be intricate. Therefore, truncated derivatives **5a** and **5b**, for which theoretical conformational analysis was expected to be less complex, were prepared analogously starting from L-alanine and using a methyloxycarbonyl protecting group.

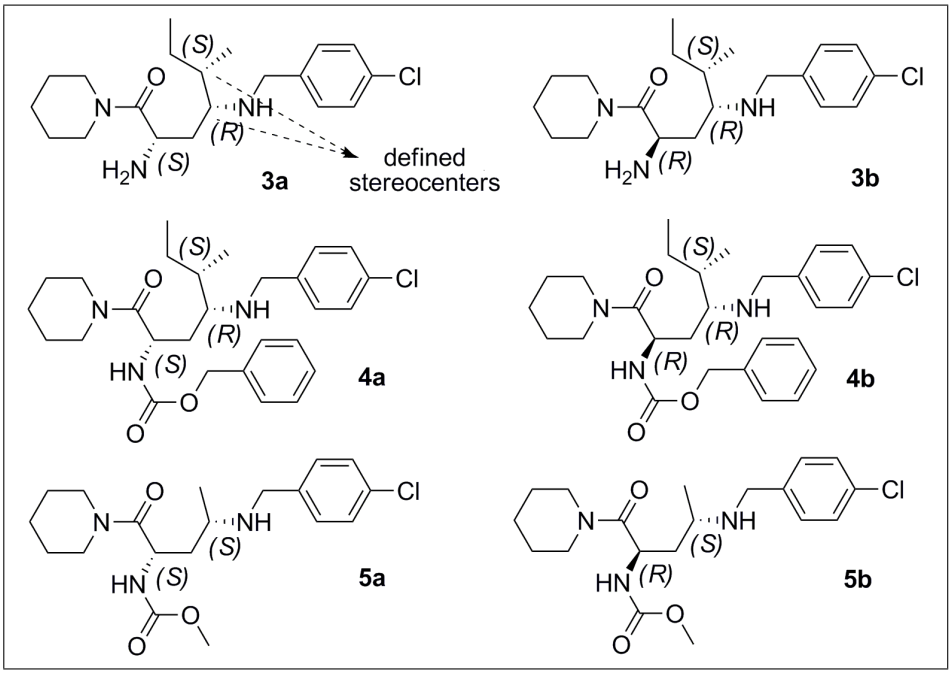


**Figure 6.2:** DPP II inhibitors under study (**3a** and **3b**) and the N-benzyloxycarbonyl (**4a** and **4b**) and truncated analogues (**5a** and **5b**) used in the VCD experiments.

## 6.2 Methods

### 6.2.1 Synthetic preparation of investigated DPP II inhibitors

Figure 6.3 gives an overview of hallmark steps in the synthetic strategy reported earlier for the compounds under study [118]. As starting materials, commercially available, enantiomerically pure amino acids **5** (ee $> 99.5\%$) were used. The latter building blocks contain the structural and stereochemical information present at the 4-position of the diaminobutanoyl moiety of target compounds: the L-isoleucine derived

(R)-*sec*-butyl substituent, containing an additional encoded stereocentre with the (S)-configuration (compounds **4a** and **4b**) and an L-alanine derived (S)-methyl substituent (compounds **5a** and **5b**). In the further course of the synthesis, the (2S) stereocenter is created by stereoselective reduction of intermediate **7** mediated by (R,R) $[Rh(COD)DIPAMP]^+$ $BF_4^-$. This catalyst has been reported to allow stereoselective hydrogenation of $\alpha,\beta$-dehydroamino acids to the corresponding amino acids with a predicted (2S)-configuration [122]. Owing to DPP II's assumed absolute preference for inhibitors with a (2S) configuration, only compounds with this stereochemistry were initially synthesized and their stereochemical homogeneity controlled by HPLC after derivatization of the 2-amino function with (S)-NIFE [123]. The aforementioned high enzyme affinity, observed for these compounds was used as a validation parameter for the presence of the predicted (2S) configuration. Recently, however, (2R)-analogues of compounds **2** were prepared, relying on non-stereoselective $Pd/H_2$-mediated hydrogenation of intermediate **7** followed by reprotection, chromatographic separation from the (2S) diastereomer and control of stereochemical homogeneity. Strikingly, these compounds also exhibited nanomolar DPP II inhibitory potential upon biochemical evaluation, justifying a VCD approach to verify the predicted absolute configuration at the 2-position for this class of Dab derivatives.

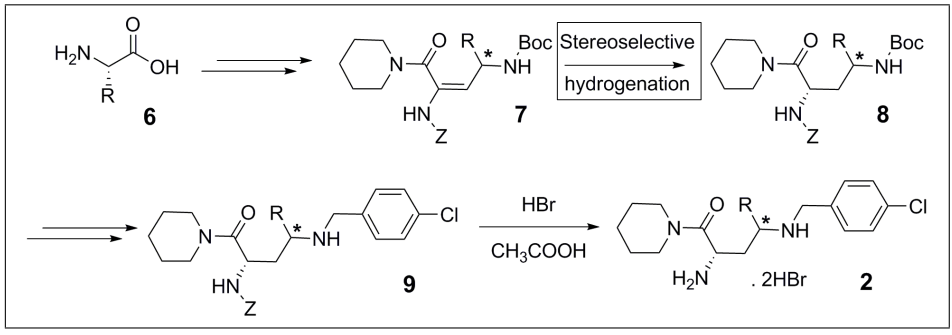


**Figure 6.3:** Overview of hallmark steps in the synthesis of compounds with generalized structure **2** (Z= benzyloxycarbonyl, Boc= t-Butyloxycarbonyl)

### 6.2.2 IR/VCD spectroscopy

The unpolarized IR spectra were measured at a resolution of 4 $cm^{-1}$. The VCD spectra at a resolution of 6 $cm^{-1}$. A 1830 $cm^{-1}$ long wave pass filter was introduced to improve the VCD S/N ratio. The collection time for the VCD measurements was 90 min, using six blocks of 15 min.

All products were dissolved in $CDCl_3$, yielding a spectral range from 1000 $cm^{-1}$ to 1800 $cm^{-1}$. A demountable KBr cell with a path length of 100 $\mu$m was used for all samples. To obtain an estimate of the baseline artifacts, the VCD spectra of the solvent have been recorded, in the same conditions as the sample.

### 6.2.3 Computational Methods

VCD spectra are composed of the contributions of the different conformations. Therefore it is important to determine the relevant conformations of the molecule. In this study, the conformational landscape was explored by molecular mechanics (MM), involving both stochastic searches in the MM3 [107] force fields and Monte Carlo searches using the MMFF [109, 110] force field. The resulting geometries, that were located by molecular mechanics were subsequently optimized at the B3LYP/6-31G(d) level. Subsequently, the frequencies, dipole and rotational strengths for the most stable B3LYP/6-31G(d) minima (selected by using a range of 2 kcal/mole) on the potential energy surface are calculated. Conformers with higher energies are ignored in view of their negligible abundance. The obtained line spectra of each conformer are then broadened using a Lorentzian function with a FWHM of 10 $cm^{-1}$. For the comparison with the experimental spectrum, the simulated spectrum of each minimum is combined in a Boltzmann weighted manner. The conformational populations are based on the enthalpy of each conformation. Enthalpies are obtained using statistical thermodynamics [81]. For the calculations with the 6-31G(d) basis set an uniform scaling factor of 0.967 is used to correct for the harmonic approximation [112, 4, 113]. The DFT calculations are performed with GAUSSIAN 03 revision B05 [55]. The B3LYP functional was used together with the 6-31G(d) basis set.

## 6.3 Results and Discussion

### 6.3.1 Experimental IR/VCD spectra

The samples, **4a** and **4b**, were dissolved in $CDCl_3$. Subsequently, the experimental IR and VCD spectra of the solutions were recorded. These are then to be compared with the calculated spectra of benzyl(2*S*,4*R*,5*S*)-4-(4-chlorobenzylamino)-5-methyl-1-oxo-1-(piperidin-1-yl)heptan-2-ylcarbamate and benzyl(2*R*,4*R*,5*S*)-4-(4-chlorobenzylamino)-5-methyl-1-oxo-1-(piperidin-1-yl)heptan-2-ylcarbamate.

#### VCD analysis of benzyl(2*S*,4*R*,5*S*)-4-(4-chlorobenzylamino)-5-methyl-1-oxo-1-(piperidin-1-yl)heptan-2-ylcarbamate (SRS)

**Conformational Analysis**:In the first step of the conformational analysis, a stochastic search was initiated for the stereo isomer with the SRS configuration. This analysis yielded 1000 initial geometries. This large number of conformations can be explained by the large flexibility of the molecule. The parameters that were varied during conformational analysis are depicted in Figure 6.4. For the next phase, all minima were further optimized at the B3LYP/6-31G(d) level and eventually 18 unique conformers, within a range of 2 kcal/mol from the most stable one, were retained for the frequency calculations. Other minima with higher energies were neglected as their Boltzmann weight becomes smaller than 1%, so that their contribution can safely be ignored. The most stable conformers, based on their relative enthalpies, are compared in Table 6.1.

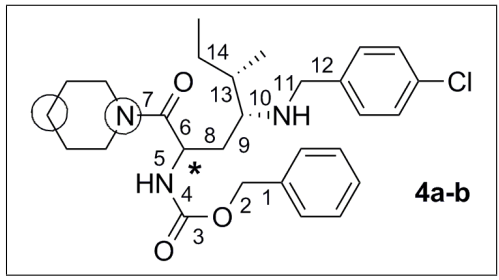


**Figure 6.4:** Numbering of the dihedral angles that were varied during conformational analysis. The circles represent places where ring puckering was introduced.

**Table 6.1:** The relative standard enthalpies ($\Delta H^0$ in kcal/mol) and the corresponding Boltzmann factors (in %) for each stable minimum (a,b,c,d,...) of the SRS configuration.

| | $\Delta H^0$ | w (%) | | $\Delta H^0$ | w (%) |
|---|---|---|---|---|---|
| a | 0.00 | 16.1 | j | 0.74 | 4.6 |
| b | 0.28 | 10.0 | k | 0.76 | 4.4 |
| c | 0.29 | 9.9 | l | 0.86 | 3.8 |
| d | 0.38 | 8.4 | m | 0.98 | 3.1 |
| e | 0.40 | 8.2 | n | 1.14 | 2.4 |
| f | 0.47 | 7.2 | o | 1.50 | 1.3 |
| g | 0.47 | 7.2 | p | 1.64 | 1.0 |
| h | 0.60 | 5.9 | q | 1.67 | 1.0 |
| i | 0.74 | 4.6 | r | 1.71 | 0.9 |

**VCD and IR spectra**: Using the calculated vibrational spectra for each conformer of the stereo isomer with the SRS configuration, the Boltzmann weighted IR and VCD spectra were constructed and the result was compared with the corresponding experimental spectra of **4a**. To assign the absolute configuration of the product, each band of the experimental IR spectrum was linked with a band from the theoretical spectrum. The numbering of the bands corresponds with the numbering of the normal modes, found in the Gaussian output file. The result of this analysis is shown in Figure 6.5. There is a large overall agreement between both spectra, except for the patterns of the bands 150 to 169. The mismatch of the intensity of band 121 can at least partly be attributed to an underestimation of the width of th Lorentzian used in the broadening step.

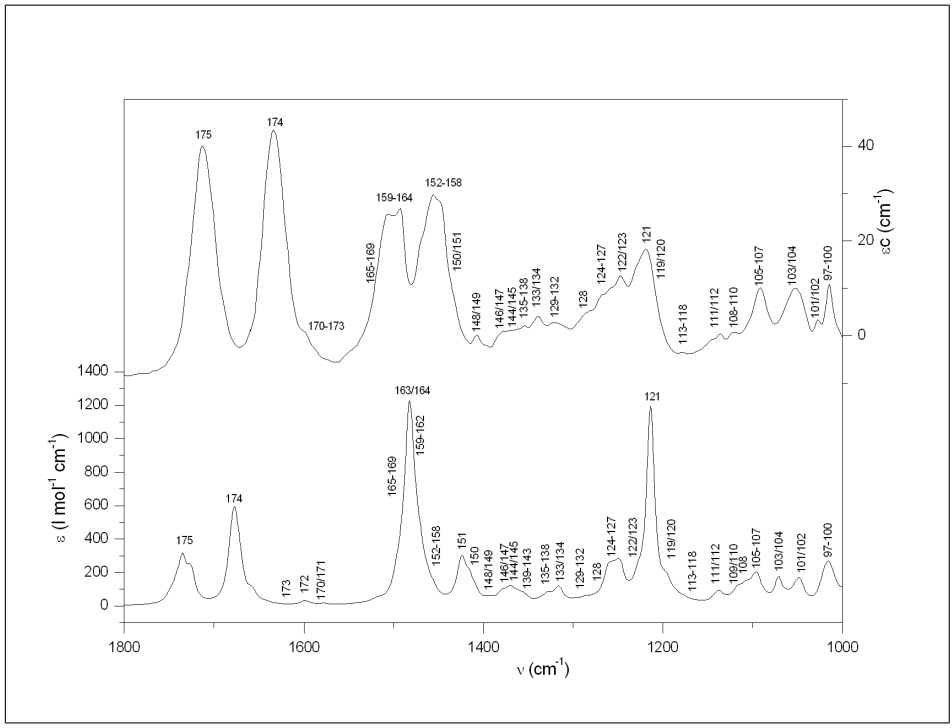


**Figure 6.5:** Assignment of the bands in the experimental IR spectrum (top) of **4a**, by comparing them with the calculated IR spectrum of the SRS diastereomer (bottom).

The correlation of experimental with calculated IR bands enables the assignment of the bands of the experimental VCD spectrum. This is shown in Figure 6.6. Again significant overall agreement is found between both VCD spectra. Because of the possible interactions of carbonyl functions with the solvent(as will be described in Chapter 5), great care must be exercised when drawing conclusions on absolute configurations by merely considering the CO stretching vibrations [7]. Therefore, it is thought difficult to give a conclusive answer on the absolute configuration of the product solely on the basis of the good agreement between calculation and experiment for the bands 174 and 175. Comparing the results in other parts of the spectral region, it is clear that some differences are present. Bands 146/147, 144/145, 139-143 and 138 are predicted to be negative, while in the experimental VCD spectrum they occur with a positive sign. For the bands 129 and 124-126 the sign is calculated to be positive while in the experiment a negative sign is

observed. Band 121, which mainly originates from a NH-COO bending vibration is again very intense in the theoretical spectrum, but is weak in the experimental spectrum, its sign being positive in both spectra. All in all, despite the reasonable overall agreement, the observed discrepancies between theory and experiment prevent that the conclusion that **4a** has the SRS configuration is ascertained beyond doubt.

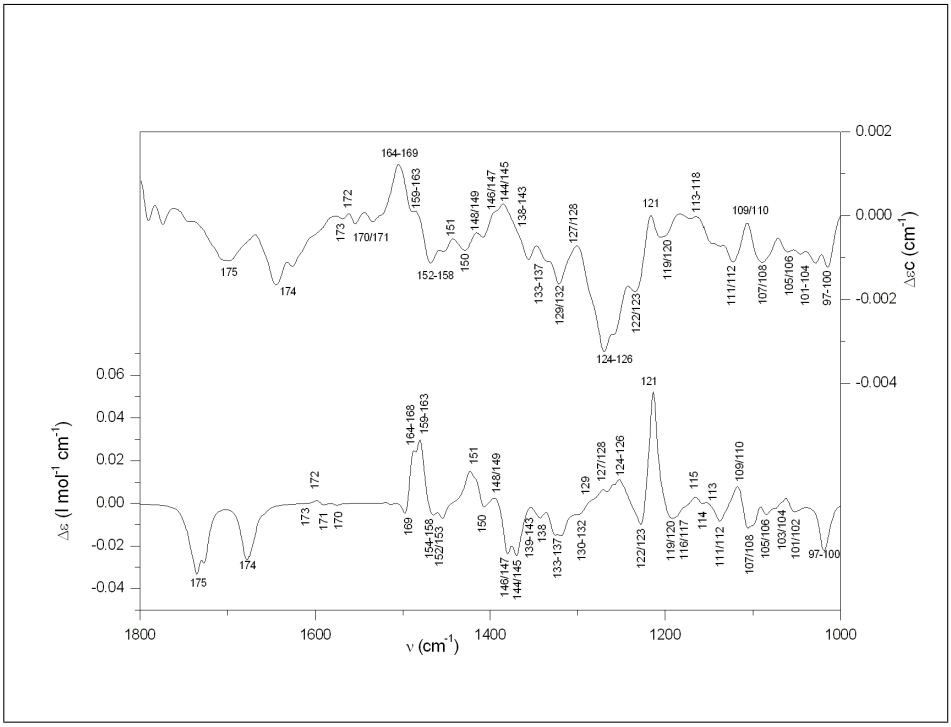


**Figure 6.6:** Assignment of the bands in the experimental VCD spectrum (top) of **4a**, by comparing them with the calculated VCD spectrum of the SRS diastereomer (bottom).

### VCD analysis of benzyl(2*R*,4*R*,5*S*)-4-(4-chlorobenzylamino)-5-methyl-1-oxo-1-(piperidin-1-yl)heptan-2-ylcarbamate (RRS)

**Conformational Analysis**: The first step of the conformational analysis (stochastic search) of the stereo isomer with the RRS configuration, yielded again 1000 minima. After minimization of the initial geometries at the B3LYP/6-31G(d) level, only 20 unique conformers were retained within a range of 2 kcal/mol from the most stable one. The relative enthalpies of each conformer and their corresponding Boltzmann weights are shown in Table 6.2.

**Table 6.2:** The relative standard enthalpies ($\Delta H^0$ in kcal/mol) and the corresponding Boltzmann factors (in %) for each stable minimum (a,b,c,d,...) of the RRS configuration.

| | $\Delta H^0$ | w (%) | | $\Delta H^0$ | w (%) |
|---|---|---|---|---|---|
| a | 0 | 11.1 | k | 0.52 | 4.6 |
| b | 0.17 | 8.3 | l | 0.62 | 3.9 |
| c | 0.23 | 7.5 | m | 0.65 | 3.7 |
| d | 0.30 | 6.6 | n | 0.66 | 3.6 |
| e | 0.30 | 6.6 | o | 0.72 | 3.3 |
| f | 0.30 | 6.6 | p | 0.72 | 3.3 |
| g | 0.34 | 6.2 | q | 0.75 | 3.1 |
| h | 0.36 | 6.1 | r | 0.94 | 2.3 |
| i | 0.43 | 5.4 | s | 1.12 | 1.7 |
| j | 0.52 | 4.6 | t | 1.19 | 1.5 |

**IR and VCD spectra**: Comparison of the Boltzmann weighted spectra with the experimental spectra of **4b** leads to the correlations, shown in Figure 6.7. As before, the overall agreement between both spectra is quite good. The predicted relative intensities of the bands 128-131, 123/124 and 120/121 are somewhat different from the experimental values. The same is true for the relative intensities of the bands 151 and 152-155. In the calculated spectrum bands 103 to 106 are resolved, while in the experimental spectrum only one band is visible. The corresponding VCD spectra and the assignment of the bands are shown in Figure 6.8. Inspection shows the overall agreement between both spectra is weak.

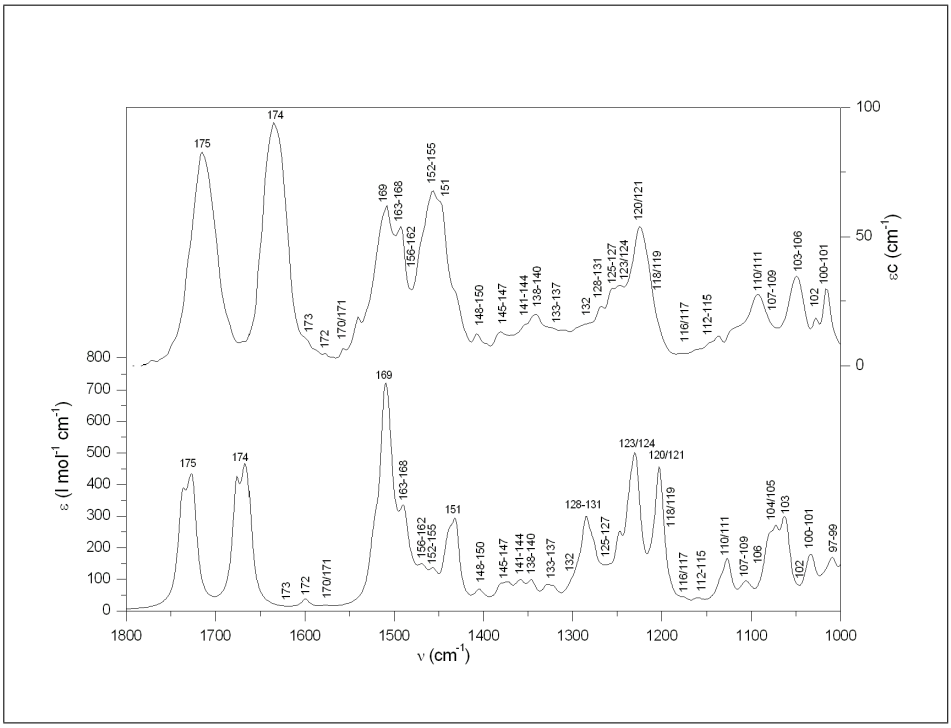


**Figure 6.7:** Assignment of the bands in the experimental IR spectrum (top) of **4b**, by comparing them with the calculated IR spectrum of the RRS diastereomer(bottom).

The predicted bands originating from the CO stretching vibration show opposite signs with respect to the experiment. The predicted pattern of the normal modes from 156 to 168 is rather different from the experimental one. The band 152-155 has opposite signs in both spectra, and this is also the case for band 128-131. The resolution of the experimental VCD spectrum is worse than in the calculated one, which complicates the assignment. It is therefore concluded that the VCD spectra, do not allow a firm conclusion about the absolute configuration of compound **4b**.

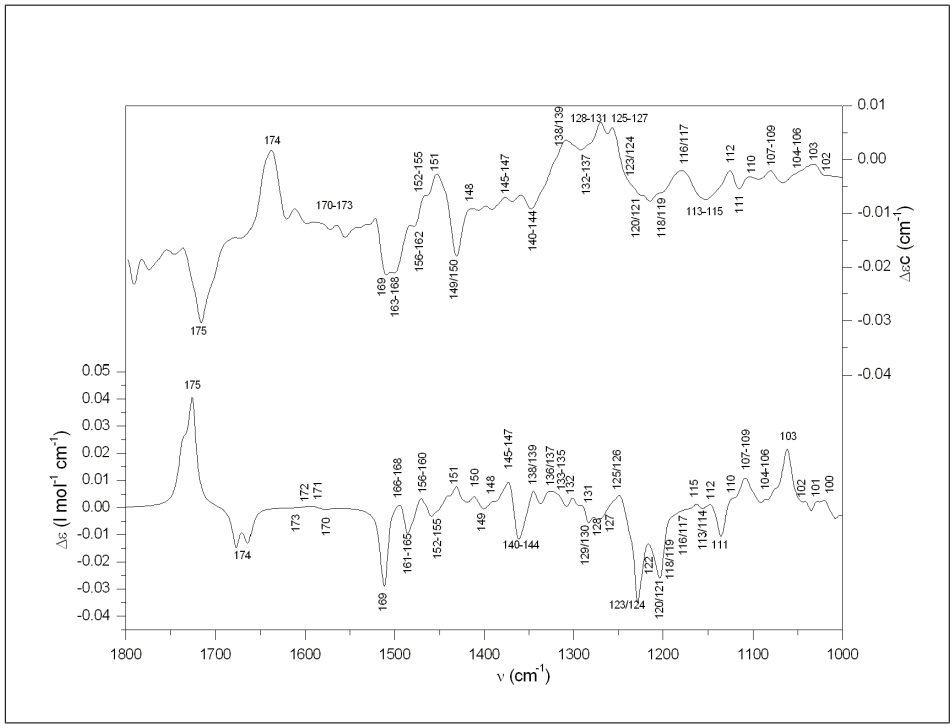


**Figure 6.8:** Assignment of the bands in the experimental VCD spectrum (top) of **4b**, by comparing them with the calculated VCD spectrum of the RRS enantiomer (bottom).

From the above, it is clear that VCD did not allow successful assignment of the absolute configuration of **4a** and **4b**. Their large torsional freedom prevented an accurate simulation of the experimental spectra. One possibility to obtain certainty about the absolute configuration is through a VCD study of a more rigid and/or smaller molecule for which there is sufficient proof that its absolute configuration at the chiral center they have in common, remains the same. This can be accomplished by applying the VCD analysis to a species in an earlier step in the synthesis [32]. In the present case, molecules **5** were used as alternatives to **4**. **5a** is assumed to correspond to (2*S*,4*S*)-4-(4-chlorobenzylamino)-1-oxo-1-(piperidin-1-yl)pentan-2-yl-carbamate (SS) and **5b** to (2*R*,4*S*)-4-(4-chlorobenzylamino)-1-oxo-1-(piperidin-1-yl)-pent-an-2-yl-carbamate (RS). Therefore, the simulated VCD spectra of SS and RS were computed and compared to the experimental data for **5a** and **5b**.

### VCD analysis of (2*S*,4*S*)-4-(4-chlorobenzylamino)-1-oxo-1-(piperidin-1-yl)pentan-2-ylcarbamate (SS)

**Conformational Analysis**: The conformational analysis of the smaller molecule was somewhat simpler. During the initial conformational search, 100 geometries were identified. The structural parameters that were varied during conformational analysis are depicted in Figure 6.9. After optimizing all the obtained minima at the B3LYP/6-31G(d) level and after selecting only the unique conformers that are within a range of 2 kcal/mole from the most stable one, 17 minima were retained for the frequency calculations. Their relative enthalpies and Boltzmann weights are given in Table 6.3.

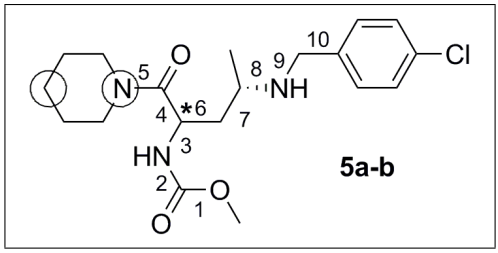


**Figure 6.9:** Numbering of the dihedral angles that were varied during the conformational analysis. The circles represent places where ring puckering was introduced.

**Table 6.3:** The relative standard enthalpies ($\Delta H^0$ in kcal/mol) and the corresponding Boltzmann factors (in %) for each stable minimum (a,b,c,d,...) of the SS configuration.

| | $\Delta H^0$ | w (%) | | $\Delta H^0$ | w (%) |
|---|---|---|---|---|---|
| a | 0 | 26.6 | j | 1.27 | 3.1 |
| b | 0.60 | 9.6 | k | 1.28 | 3.1 |
| c | 0.64 | 9.0 | l | 1.29 | 3.0 |
| d | 0.67 | 8.5 | m | 1.51 | 2.1 |
| e | 0.79 | 7.0 | n | 1.72 | 1.5 |
| f | 0.92 | 5.6 | o | 1.72 | 1.5 |
| g | 0.93 | 5.5 | p | 1.91 | 1.1 |
| h | 1.09 | 4.2 | q | 1.99 | 0.9 |
| i | 1.23 | 3.3 | | | |

**IR and VCD spectra**: In Figure 6.10 the bands of the experimental IR spectrum of **5a** are correlated with the bands of the Boltzmann weighted spectrum of the SS configuration. There is an acceptable overall agreement between both spectra, the main differences occurring in the interval between 1400 $cm^{-1}$ and 1500 $cm^{-1}$. Band 76 is predicted to have a smaller intensity than is observed in the experimental IR spectrum. The CO stretching vibration, originating from different conformers are somewhat resolved in the calculated spectrum, while in the experimental spectrum a single, broader band is observed.

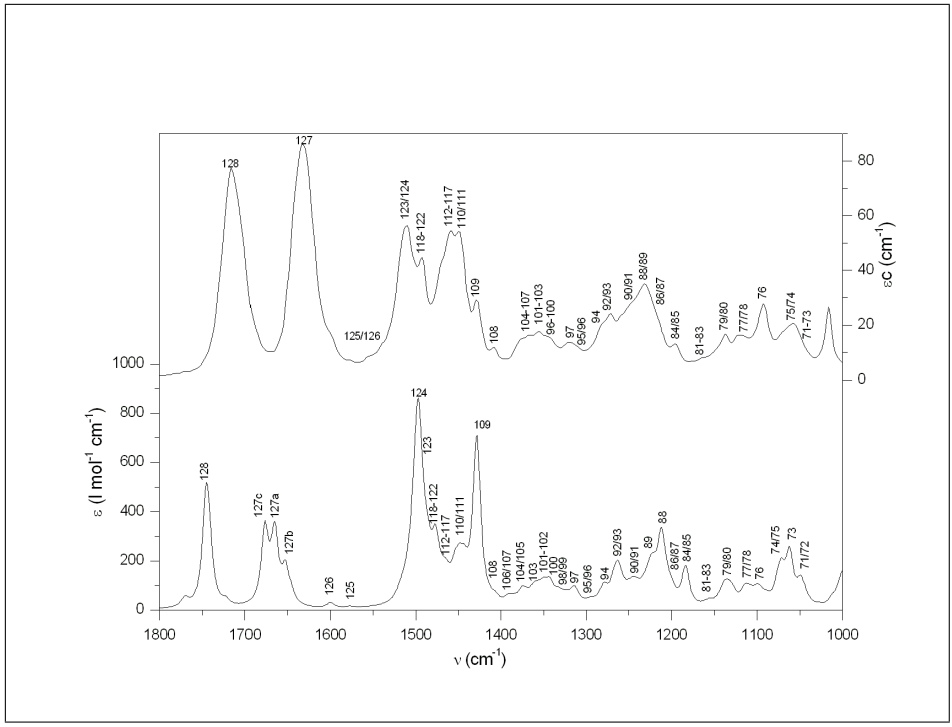


**Figure 6.10:** Assignment of the bands in the experimental IR spectrum (top) of **5a**, by comparing them with the calculated IR spectrum of the SS diastereomer (bottom). Some bands are specified by a lowercase, which refers to the conformer.

In Figure 6.11 the experimental and the calculated VCD spectrum are compared. Inspection shows that, throughout the spectral interval the signs of the bands are correctly predicted. This allows the conclusion that compound **5a** has the SS configuration. In view of the connection

between compounds **4a** and **5a**, this leads to the conclusion that the **4a** has the SRS configuration.

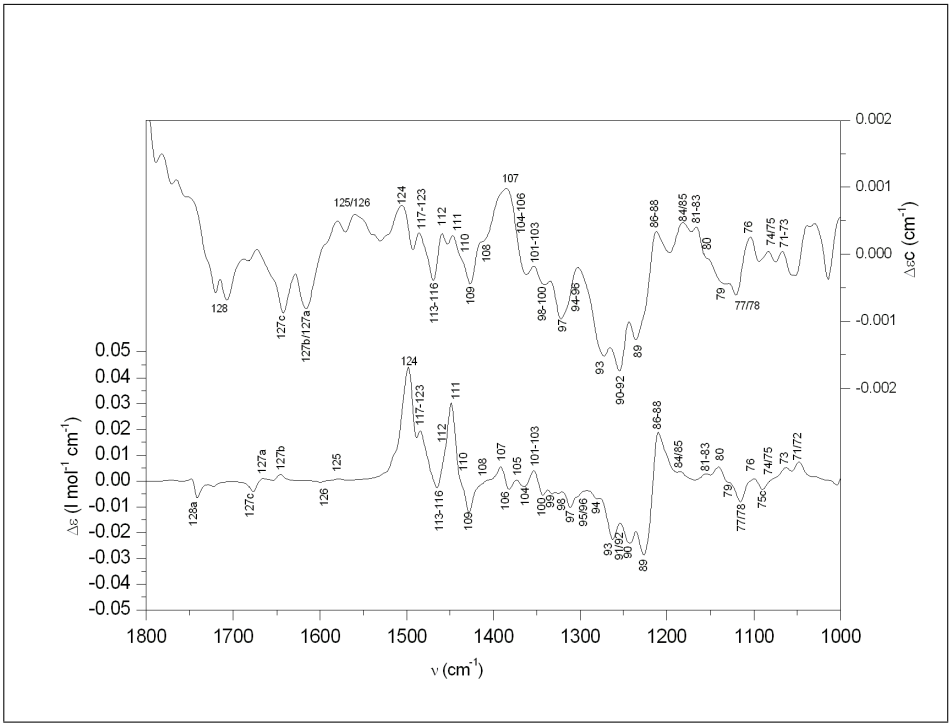


**Figure 6.11:** Assignment of the bands in the experimental IR spectrum (top) of **5a**, by comparing them with the calculated IR spectrum of the SS diastereomer (bottom). Some bands are specified by a lowercase, which refers to the conformer.

### VCD analysis of (2*R*,4*S*)-4-(4-chlorobenzylamino)-1-oxo-1-(piperidin-1-yl)pentan-2-ylcarbamate (RS)

**Conformational Analysis**: During the stochastic search 190 local minima were identified, of which after structural optimization only 8 were found to fall within the 2 kcal/mole range from the global minimum. The relative enthalpies and Boltzmann weights of these are summarized in Table 6.4.

**Table 6.4:** The relative standard enthalpies ($\Delta H^0$ in kcal/mol) and the corresponding Boltzmann factors (in %) for each stable minimum (a,b,c,d,...) of the RS configuration.

| | $\Delta H^0$ | w (%) |
|---|---|---|
| a | 0 | 50.0 |
| b | 0.73 | 14.6 |
| c | 0.93 | 10.4 |
| d | 1.19 | 6.6 |
| e | 1.21 | 6.5 |
| f | 1.37 | 5.0 |
| g | 1.93 | 1.9 |
| h | 1.96 | 1.8 |

**IR and VCD spectra**: The Boltzmann weighted IR spectrum is compared with the experimental spectrum in Figure 6.12. There is again a satisfactory overall agreement between theory and experiment, with only the calculated relative intensities of the bands from 108 to 124, somewhat different from the experimental ones.

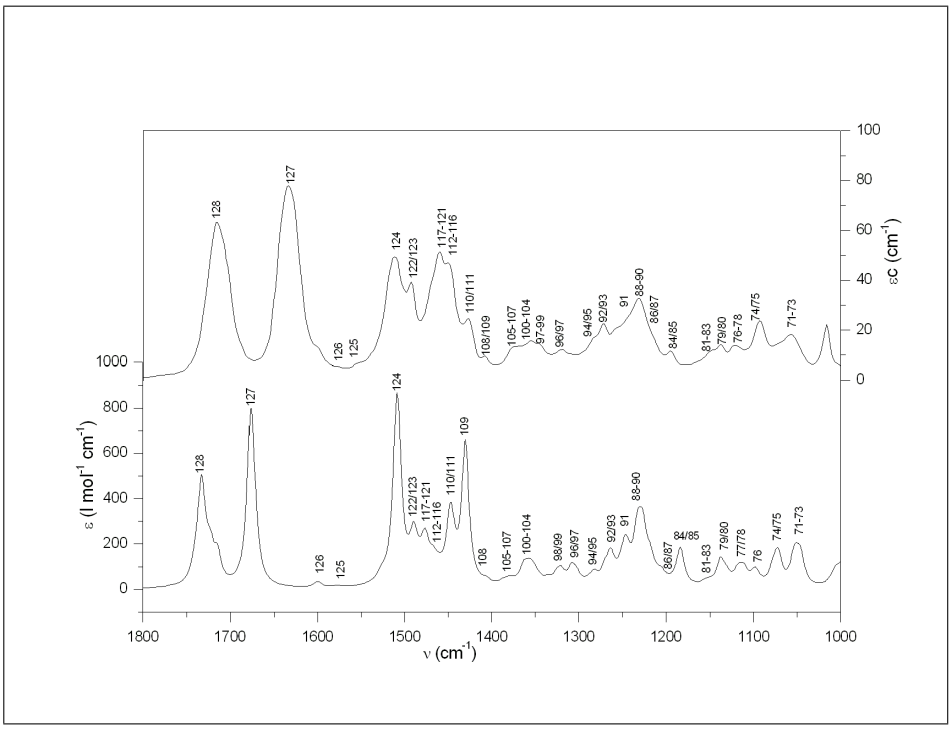


**Figure 6.12:** Assignment of the bands in the experimental IR spectrum (top) of **5b**, by comparing them with the calculated IR spectrum of the RS diastereomer (bottom).

In Figure 6.13 the agreement of the theoretical with the experimental VCD spectrum is compared. In terms of signs of the bands the agreement of theory with experiment is very good, as for most bands the correct sign is predicted. Band 128, originating from the CO stretching vibration, is calculated to be positive while in the experimental spectrum a negative band is present. As mentioned above, the sign for this type of vibration is difficult to predict amongst others because the band can be significantly influenced by the solvent. Attempts to include in the simulations solvent effects the polarizable continuum model (PCM) [124, 125] have failed to produce the correct sign and have, therefore not been continued. In the experimental VCD spectrum, bands 79 to 85 have rather high intensities, while this is not the case in the calculated spectrum.

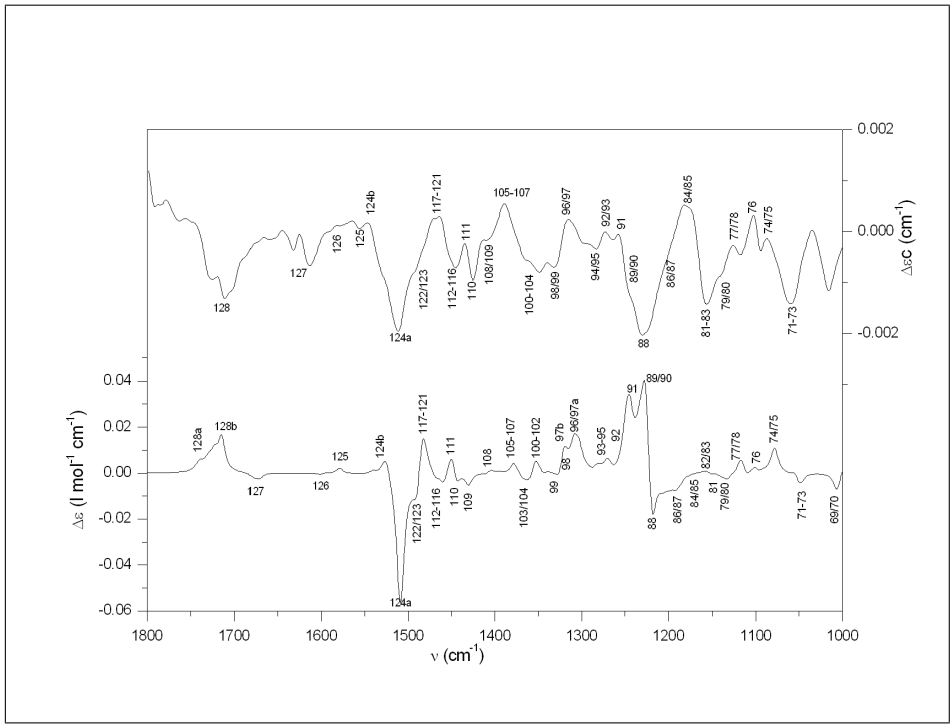


**Figure 6.13:** Assignment of the bands in the experimental VCD spectrum (top) of **4b**, by comparing them with the calculated VCD spectrum of the RS enantiomer (bottom). Some bands are specified by a lowercase, which refers to the conformer.

Despite these small differences and, in view of the problematic situation in the prediction of the sign of the CO stretching band, the agreement of theory with experiment was judged to be sufficient to assure that compound **5b** has the RS configuration. By extrapolation, this then leads to the conclusion that compound **4b** must have the RRS configuration.

## 6.4 Conclusions

In this chapter, the absolute configuration of peptide derived DPP II inhibitors, belonging to generalized structure class **2** (Figure 6.1), was confirmed through VCD. The Benzyloxycarbonyl (Z)-protected analogues (**4a** and **4b**), obtained in the penultimate synthetic step, were studied by VCD. The large flexibility of the molecules prevented accurate reconstruction of the experimental IR and VCD spectra. Therefore, in a next step both products were modified to structurally less complex congeners, thereby reducing the number of chiral centers from 3 to 2, which also facilitated the calculations. Since the absolute configuration of one of both chiral centers is known and is identical to the configuration of the corresponding stereocenter in the original compound, it is deemed justified to determine the chirality of **4a** and **4b** by extrapolating from the truncated molecules, **5a** and **5b**, the chirality of which was determined using VCD spectroscopy. Hence, the technique can, in theory, readily be transposed to other types of protease inhibitors with a similar degree of complexity. Thus, VCD is demonstrated to be a useful technique in the confirmation of the absolute configuration for larger and more flexible molecules.

# 7

# Solute induced solvent chirality: A VCD study of camphor and pulegone in $CDCl_3$

## 7.1 Introduction

During an assignment, VCD measurements are performed in solution, while the corresponding calculations are performed for a free chiral molecule in vacuum. This fact may interfere with the applicability of VCD to molecules exhibiting dimerization or polymerization in general or with the treatment of molecules that exhibit strong interactions with solvent molecules. Recently the effect of dimerization has been investigated in detail mainly for carboxylic acids [126, 127, 128, 129, 130]. In addition, by comparing the spectra recorded using different solvents, experimental information on the influence of solute-solvent interactions was obtained [125, 131, 132]. The solute-solvent interaction can affect the vibrational frequencies, infrared intensities and the rotational

strengths [133, 134, 135]. In this chapter, we examine the effect of the solvent on the VCD spectrum of two fairly simple molecules: camphor and pulegone.

Besides the use of VCD as an analytical technique for the determination of absolute configuration, VCD can be used to prove theoretical issues through experimental means. As a consequence of the so-called holographic electron density theorem [136], the chirality of a molecule is not to be considered limited to a chiral center as it is often (mis)interpreted, but rather is a property of the molecule as a whole. Even in those cases where the chirality comes from, e.g., a single chiral center, the chirality is transferred to distant parts of the molecule as was recently shown through the theory of molecular quantum similarity [136, 137, 138, 139]. In VCD, one also observes chirality transfer to more distant parts of the molecule. For example, a vibrational mode related to a distant functional group can carry a large rotational strength. In the present study we address the issue of induced solvent chirality, by studying the infrared and VCD spectra of solutions of camphor and pulegone in $CDCl_3$ and $CD_2Cl_2$. The choice of these test systems is related to the fact that even at room temperature, significant solute-solvent interactions appear between carbonyl containing molecules and solvents such as chloroform and dichloromethane. These interactions are explained by the appearance of 1:1 associations stabilized by an intermolecular $CD\cdots O$ hydrogen bond, and are characterized by a significant increase of the IR-intensity of the CD stretching vibration [140]. In order to discuss the possible induced solvent chirality, the VCD intensity of the CD stretching mode at 2250 $cm^{-1}$ has been studied for camphor and pulegone dissolved in $CDCl_3$.

## 7.2 A VCD study of camphor in $CDCl_3$ [6]

### 7.2.1 Introduction

In this section, the VCD intensity of the CD stretching mode at 2250 $cm^{-1}$ has been studied for camphor (structure shown in Figure 7.1) dissolved in $CDCl_3$. Subsequently, the experimental spectra are compared with calculated data derived for the 1:1 solute-$CDCl_3$ complexes. To verify the results, associations with $CD_2Cl_2$ also have been examined. Camphor has been chosen because of its lack of conformational flexibility and the fact that its VCD spectrum between 1000 $cm^{-1}$ and 2000 $cm^{-1}$, has already been described elaborately in literature [38, 141, 39, 46]. This allows the present spectra to be carefully checked in this region with respect to other studies to establish the reliability of the present experimental spectra.

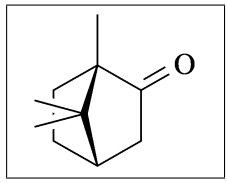


**Figure 7.1:** Structure of Camphor

### 7.2.2 Experimental

R-(+)-camphor (97%) and S-(-)-camphor (99.8%) were purchased from Acros. The solvents, $CDCl_3$ (99.8%) and $CD_2Cl_2$ (99.6%), were obtained from Aldrich and Acros respectively. All products were used without further purification. A demountable cell with $CaF_2$ windows and a 100 $\mu m$ spacer has been used for all samples. The unpolarized IR absorbance spectra were recorded at a resolution of 4 $cm^{-1}$ and the VCD spectra at a resolution of 6 $cm^{-1}$. A 3000 $cm^{-1}$ long wave pass filter was used to improve the VCD S/N ratio. The VCD spectra have been recorded in the region from 1000 $cm^{-1}$ to 3000 $cm^{-1}$, with emphasis on the region between 2000 $cm^{-1}$ and 3000 $cm^{-1}$. The collection time was set to 4h, using sixteen blocks of 15 min and the PEM maximum was positioned at 1500 $cm^{-1}$. Concentrations varied between 1.0 M and 2.0 M. The

VCD spectra of camphor, dissolved in binary mixtures of both solvents, were also studied.

### 7.2.3 Computational Methods

All calculations were carried out using Gaussian03 [55]. VCD spectra were simulated using B3LYP/cc-pVDZ calculations. This level of calculation was previously shown to account sufficiently well for the solvent-solute interactions [142, 143]. The 1:1 associations of camphor with $CDCl_3$ and $CD_2Cl_2$ were modeled explicitly. The resulting DFT harmonic frequencies were uniformly scaled with a factor of 0.9651 [144].

### 7.2.4 Results and Discussion

The VCD spectra of both enantiomers of camphor, dissolved in $CDCl_3$, have been recorded within a spectral range from 1000 $cm^{-1}$ to 3000 $cm^{-1}$. The spectra between 1000 $cm^{-1}$ and 1800 $cm^{-1}$ compare favorably with those found in literature and are therefore not discussed in detail. In Figure 7.2 and 7.3 the overall agreement between theory and experiment for camphor is shown.

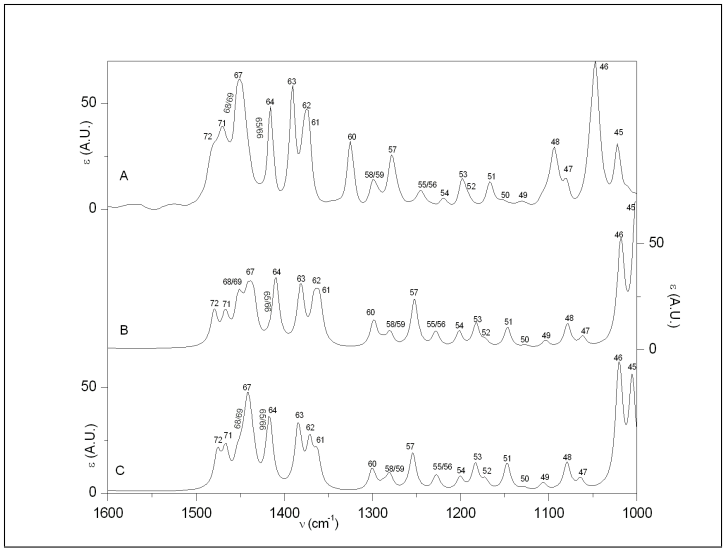


**Figure 7.2:** Comparison of the calculated IR spectra of camphor (B) and the 1:1 camphor.$CDCl_3$ complex (C) with the experimental IR spectrum (A) of camphor in $CDCl_3$ in the frequency region from 1000 $cm^{-1}$ to 1600 $cm^{-1}$.

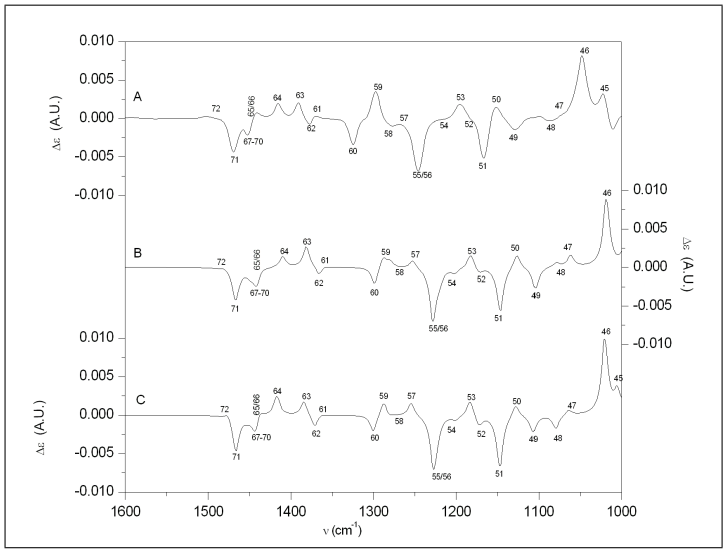


**Figure 7.3:** Comparison of the calculated VCD spectra of S-(-)-camphor (B) and the 1:1 S-(-)-camphor.$CDCl_3$ complex (C) with the experimental VCD spectrum (A) of S-(-)-camphor in $CDCl_3$ in the frequency region from 1000 $cm^{-1}$ to 1600 $cm^{-1}$.

The use of a long wave pass filter at 3000 $cm^{-1}$, allowed us to extend the spectral range up to 3000 $cm^{-1}$. For R-(+)-camphor a negative band could be distinguished from the noise at 2254 $cm^{-1}$, while its enantiomer showed the opposite sign at the same frequency. In order to verify the reproducibility of the bands, measurements of 4 hours for each enantiomer, were necessary. This procedure was repeated for solutions at different concentrations (1.5 M and 2.0 M). As shown in 7.4, the absorption of the band at 2254 $cm^{-1}$ rises with increase of the concentration. Due to its location, this band seems to originate from the CD stretching vibration of $CDCl_3$. The corresponding IR spectra are also depicted in 7.4. After subtracting the IR spectrum of the pure solvent from that of the solution, the band originating from the CD stretching of the $CDCl_3$ molecules still was visible at 2254 $cm^{-1}$. The fact that the CD stretching mode of $CDCl_3$ also provokes a VCD signal, suggests that through the presence of a $C - D \cdots O$ hydrogen bond between $CDCl_3$ and camphor, chirality in the solvent is induced. A similar phenomenon has very recently been observed by Losada and Xu. These authors studied the VCD spectra of methyl lactate in water [145] and observed that the

$H_2O$ bending vibration of the achiral water subunits that are hydrogen bonded to methyl lactate exhibit an experimentally detectable VCD signal. A similar pattern was observed for the antisymmetric carboxylate vibration localized in the non-chiral trifluoroactetic acid which gives rise to a VCD signal upon complexation with chinconidine [146].

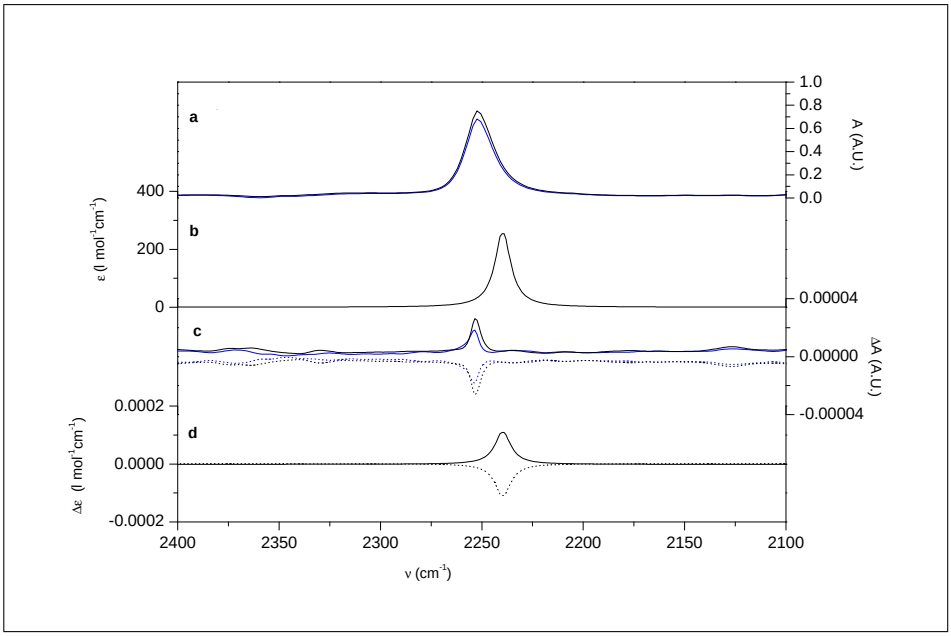


**Figure 7.4:** Experimental IR (a) and VCD (c) spectra of camphor in $CDCl_3$ at different concentrations (blue: 1.5 M, black: 2.0 M). Calculated IR (b) and VCD (d) spectra of the 1:1 camphor.$CDCl_3$ association. The dotted lines represent the complex with R-(+)-camphor, the solid lines originate from the complexes with S-(-)-camphor.

In order to establish the source of this VCD band, ab initio calculations were performed for camphor in both isolated and solvated state. Obviously the calculations of a simple camphor molecule showed no VCD signal in that region. Alternatively, the 1:1 association of camphor with a $CDCl_3$ molecule has been modeled explicitly at the B3LYP/cc-pVDZ level. This has been done using several different starting geometries, in which the orientation of the solvent molecule toward the camphor molecule has been varied. These optimizations all led to the same equilibrium geometry, depicted in Figure 7.5 and characterized by a $D \cdots O$

interatomic distance of 2.21 Å. In Figure 7.4 the simulated IR and VCD spectra in the CD stretching region also are shown. In the IR spectrum, a large band is visible at 2239 $cm^{-1}$, which originates from the CD stretching of the $CDCl_3$ molecule bound to camphor. The R-(+)-camphor complex gives rise to a negative signal in the simulated VCD spectrum, whereas a positive band is visible for the S-(-)-complex. This is in qualitative agreement with the experimental VCD band, which provides the necessary evidence to conclude induced solvent chirality. In order to further support this conclusion, the overall agreement between theory and experiment for the complex is given in Figures 7.2 and 7.3. In the same figures, the calculations of the complex are compared with those of the free camphor molecule. The influence of the complexation on the bands originating from camphor seems negligible.

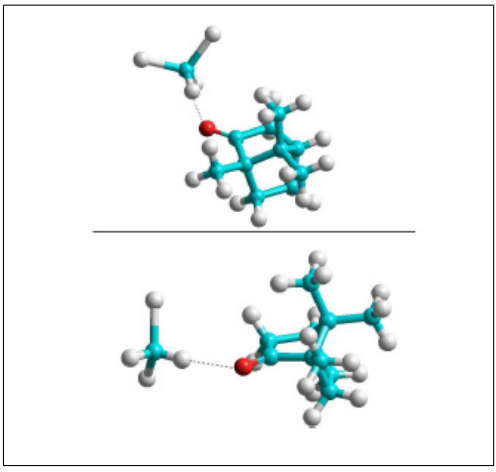

**Figure 7.5:** The B3LYP/cc-pVDZ equilibrium geometries of the camphor.$CDCl_3$ (top) and camphor.$CD_2Cl_2$ (bottom) complexes.

To verify the presence of induced solvent chirality, VCD and IR spectra have also been recorded for camphor, dissolved in $CD_2Cl_2$ and in binary mixtures of both solvents. In Figure 7.6 the recorded IR and VCD spectra of the binary mixtures with different proportions of $CDCl_3$ and $CD_2Cl_2$ are shown: 0/100, 50/50 and 100/0. The concentration of each solution was the same, namely 1.5 M. In the IR spectrum it can be seen that as the $CDCl_3$ fraction increases, an increase of the CD stretching vibration intensity at 2254 $cm^{-1}$ is observed, while the intensities of the

asymmetrical and symmetrical $CD_2$ decrease. In the VCD spectra of the binary mixtures, again a large increase of the CD stretching mode intensity of $CDCl_3$ is visible as the mole fraction $CDCl_3$ rises. For these solutions, the two bands originating from the $CD_2$ stretching mode could not be distinguished from the noise.

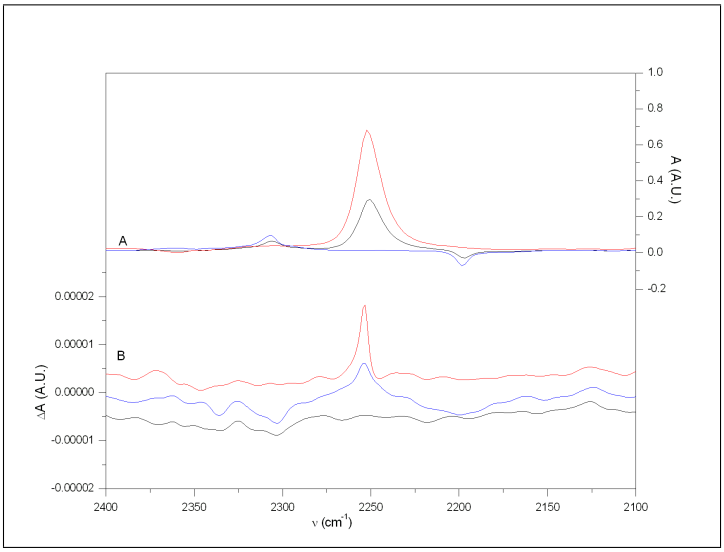


**Figure 7.6:** Experimental IR (top) and VCD (bottom) spectra of S-(-)-camphor in binary mixtures of $CDCl_3$ and $CD_2Cl_2$ ($CDCl_3/CD_2Cl_2$: 100/0 (red), 50/50 (black) and 0/100 (blue))

In order to explain these results, the camphor.$CD_2Cl_2$ complex was also modeled. After optimizing different starting geometries, two equilibrium structures were found. The most stable equilibrium geometry is characterized by a $D\cdots O$ interatomic distance of 2.158 Åand is depicted in Figure 7.5. The second, less stable, structure, is characterized by a $Cl\cdots O$ halogen bond between a Cl atom of the $CD_2Cl_2$ and the oxygen atom of camphor, and can be neglected during further analysis. Figure 7.7 shows the theoretical IR and VCD spectra. In both spectra, two bands due to the symmetric and antisymmetric CD stretching vibrations appear at 2175 $cm^{-1}$ and 2300 $cm^{-1}$, respectively. For S-(-)-camphor both CD stretching modes give rise to a negative band in the VCD spectrum. Naturally for R-(+)-camphor the signs of the bands are reversed. Unfortunately, these bands could not be distinguished from the noise in

the experimental VCD spectra of camphor, dissolved in $CD_2Cl_2$. This might be caused by a smaller abundance of the complex in the solution. The latter obviously is related to the less acidic character of the deuterium atoms of $CD_2Cl_2$. In the experimental IR spectrum of solutions in $CD_2Cl_2$ a negative band is visible at around 2200 $cm^{-1}$. It means that for this band the absorbance of the solvent must be larger than that of the solution. This can be explained by comparing the calculated dipole strength of the symmetric $CD_2$ stretching vibration of a single $CD_2Cl_2$ molecule with that of the complex. The dipole strength of the $CD_2$ stretch of the complex is only 4 times larger than that of the simple solvent molecule (B3LYP/ cc-pVDZ, 48 versus 12). This value is much smaller than that of the antisymmetrical stretching vibration, in which the dipole strength of the complex is about 90 times larger (B3LYP/ cc-pVDZ, 36.7 versus 0.5). This trend, together with the fact that during the measurements of camphor in solution, fewer $CD_2Cl_2$ molecules are present in the optical path, than is the case for measurements of the pure solvent, explains the negative IR band.

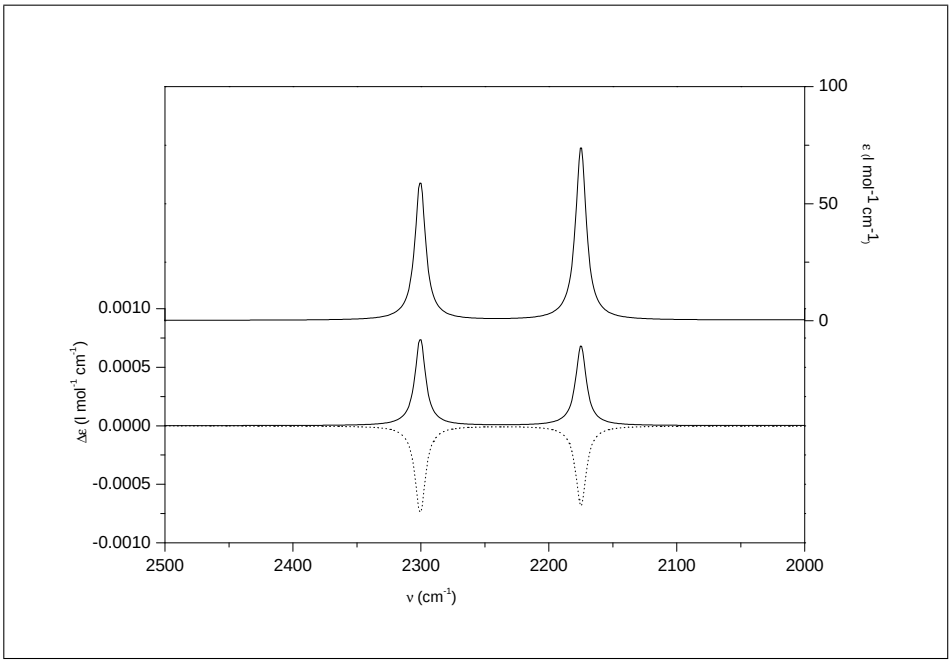


**Figure 7.7:** Calculated IR and VCD spectra of the camphor.$CD_2Cl_2$ association. The dotted line represents the complex, containing the S-(-)-enantiomer of camphor, while the solid line corresponds with the complex of the R-(+)-enantiomer.

The quantitative comparison between the experimental and calculated rotational strengths, shown in Table 7.1, is less satisfactory. The presence of only qualitative agreement can be due to the fact that only 1:1 complexes have been taken into account while other associations are possible as well. Another reason for this disagreement is that the actual number of solvent molecules, taking part in the interaction, is unknown. The disagreement between theory and experiment might also be due to methodological errors as all calculations, including those of the hydrogen bonded species, are performed at the B3LYP level, where dispersion interactions are not accounted for by the exchange and correlation functional. For the experiments in $CD_2Cl_2$, neither the rotational strengths nor the dipole strength of the symmetrical stretching vibration could be obtained. For the antisymmetrical stretching vibration, the experimental frequency agrees well with the computed one. Due to the low S/N ratio, no rotational strength could be obtained from experiment.

It is, however, important to note that for all experimentally observable peaks, the sign of the VCD signal agrees with that obtained from the calculations.

**Table 7.1:** Comparison of the calculated and experimental frequencies (freq in $cm^{-1}$), dipole (D in $10^{-40}$ $esu^2$ $cm^2$) and rotational (R in $10^{-44}$ $esu^2$ $cm^2$) strengths of the CD stretching vibrations in the 1:1 S-(-)-camphor.$CDCl_3$ associations.

| | Experimental | | | Calculated | | |
|---|---|---|---|---|---|---|
| | Frequency | D | R | Frequency | D | R |
| $CDCl_3$ | 2251 | 43.02 | 0.83 | 2240 | 163.43 | 0.18 |
| $CD_2Cl_2$ | | | | 2175 | 48.73 | -1.12 |
| | 2308 | 7.80 | | 2300 | 36.67 | -1.15 |

### 7.2.5 Conclusions

Experimental VCD results of camphor solutions in $CDCl_3$ and $CD_2Cl_2$ have been compared with DFT simulations of the 1:1 associations with $CDCl_3$ and $CD_2Cl_2$ respectively. For solutions in $CDCl_3$ a band was seen at about 2250 $cm^{-1}$ in the experimental VCD spectra. Since the band was found to be reproducible, one can conclude that the CD stretching vibration in $CDCl_3$ gives rise to a VCD signal. Both enantiomers of the chiral solute induced opposite signs, in agreement with the simulations. In order to strengthen these foundings, the VCD spectra of the solutes in binary mixtures of $CDCl_3$ and $CD_2Cl_2$ have also been recorded. It is shown that as the mole fraction of $CDCl_3$ decreases, the CD stretching band gets smaller. This qualitative agreement between experiment and calculations proves that chirality of the solvent can be induced. Intermolecular interactions between the solute and solvent molecules trigger this phenomenon.

## 7.3 Solvent effects on IR and VCD spectra of pulegone [7]

### 7.3.1 Introduction

In the present study, we examine the effect of the solvent on the VCD spectrum of the fairly simple molecule pulegone (shown schematically in Figure 7.8). Pulegone is a naturally occurring organic product, obtained from the essential oils of various plants such as Nepeta cataria, Mentha piperita and pennyroyal. It is used in flavoring agents, perfumes and aroma therapy. Unlike many other monoterpenes [147, 38, 148, 39, 82], pulegone, has not yet been subjected to a VCD study in the mid-IR frequency region, so that only VCD data are available in the CH-stretching fundamental region [149, 150] and in the near-IR region [151]. The reason for this lack of information might be due to the fact that, as we show below, not all observed features can be explained without incorporating the influence of the solvent and specific solute-solvent interactions. Therefore, our first goal is to examine whether by including somehow the solvent in the calculations, we could obtain good agreement between the theoretical and experimental spectra. Since pulegone also contains a carbonyl function, the present study aims at confirming whether the effect of induced solvent chirality, observed is a relatively common fact and exclude that the observation for camphor was unique.

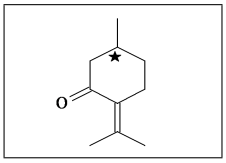


**Figure 7.8:** Structure of pulegone

### 7.3.2 Experimental

R-(+)-pulegone (98%) and S-(-)-pulegone (98%) were obtained from Aldrich. The solvents, $CDCl_3$ (99.8%), $CD_2Cl_2$ (99.6%) and $CS_2$ (99.9%) were obtained from Aldrich, Acros and Riedel-de Haën respectively. All products were used without further purification. The unpolarized IR absorbance spectra were recorded at a resolution of 4 $cm^{-1}$ and the VCD spectra at resolution of 6 $cm^{-1}$. Depending on the spectral range, several parameters were varied. For the measurements from 1000 $cm^{-1}$

till 1800 $cm^{-1}$ a demountable KBr cell with a path length of 100 $\mu m$ was used in combination with a 1850 $cm^{-1}$ long wave pass filter. For the solutions in $CDCl_3$ and $CS_2$, a concentration of 0.25 M was used. The CD stretching region was studied using a demountable $CaF_2$ cell with a path length of 100 $\mu m$ and a 3000 $cm^{-1}$ long wave pass filter. The maximum of the PEM was set to 1500 $cm^1$. Pulegone was dissolved in binary mixtures of $CD_2Cl_2$ and $CDCl_3$, with a concentration of 1.5 M. The collection time for the VCD spectra at higher frequencies was set to 4h , using sixteen blocks of 15 min. For measurements between 1000 $cm^{-1}$ and 2000 $cm^{-1}$ a collection time of 90 min was sufficient. To determine the baseline, the VCD spectrum of the racemic mixture was recorded, using the same conditions as the samples. All VCD spectra were corrected using this baseline.

### 7.3.3 Computational Methods

All calculations were carried out using Gaussian03 [55] at the B3LYP/6-311+G(d,p) level. The reported DFT harmonic frequencies were uniformly scaled with a scaling factor of 0.96741 [152]. The spectra were calculated for the isolated pulegone in vacuo, for pulegone in solution, using the Polarizable Continuum Model (PCM) [153], and for the 1:1 solute-solvent associations, with $CDCl_3$ and $CD_2Cl_2$. Also for the adducts, calculations were performed for the isolated species and for the species embedded in a solvent. In order to find the most stable conformers of free pulegone and for the 1:1 complexes with $CDCl_3$ or $CD_2Cl_2$, a systematic conformational analysis was performed; using the MMFF force field [109, 110]. For the 1:1 associations, the relative orientation of the solvent molecule toward pulegone was described using the dihedral angles $\tau_1$ and $\tau_2$, defined in Figure 7.9. The Boltzmann populations were calculated, based on the relative standard enthalpies.

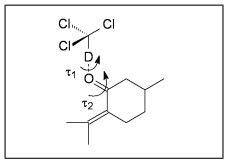


**Figure 7.9:** Definition of the dihedral angles $\tau_1$ and $\tau_2$ used to perform the systematic conformational analysis of the 1:1 complex between pulegone and $CDCl_3$.

### 7.3.4 Results and Discussion

For convenience in the subsequent discussion, it will prove useful to distinguish two regions in the spectra. First, the region between 1000 $cm^{-1}$ and 2000 $cm^{-1}$ is discussed. Afterwards, the spectra between 2000 $cm^{-1}$ and 2500 $cm^{-1}$ will be analyzed.

**Spectral region: 1000 $cm^{-1}$ - 2000 $cm^{-1}$**

**Experimental Spectra**: In this region the spectra were recorded for solutions in $CDCl_3$ and $CS_2$; at a concentration of 0.25 M. The experimental spectra are shown in Figure 7.10 and Figure 7.11. Measurements in $CS_2$ allow us to study the region above 900 $cm^{-1}$. Due to the large absorbance of the solvent around 1400 $cm^{-1}$, the VCD spectrum of pulegone in $CS_2$ could not be studied in that region. The spectra of the solutions in $CS_2$ and $CDCl_3$ are very similar and show that the effect of the solvent in this region is rather small. In $CS_2$, however, the band, originating from the CO stretching vibration (around 1700 $cm^{-1}$) is shifted to higher frequencies.

**Calculations of free pulegone in vacuo**: First, the experimental spectra are compared with the calculated ones of a single pulegone molecule in vacuo. The calculated spectra are also shown in Figure 7.10 and Figure 7.11. The systematic conformational analysis, described above, yielded two different conformers. The conformer with the methyl substituent in axial position is less stable than the conformer containing an equatorial methyl substituent. Its relative standard enthalpy and Boltzmann population with respect to the equatorial conformer is + 1.62 kcal/mole and 6.14% respectively.

The overall agreement between calculation and experiment is very good; each band could be assigned without much difficulty. In the exper-

imental IR spectrum, however, band 58, assigned to the C=C stretching vibration, is spread out, while in the calculated spectrum a narrow intense band is shown.

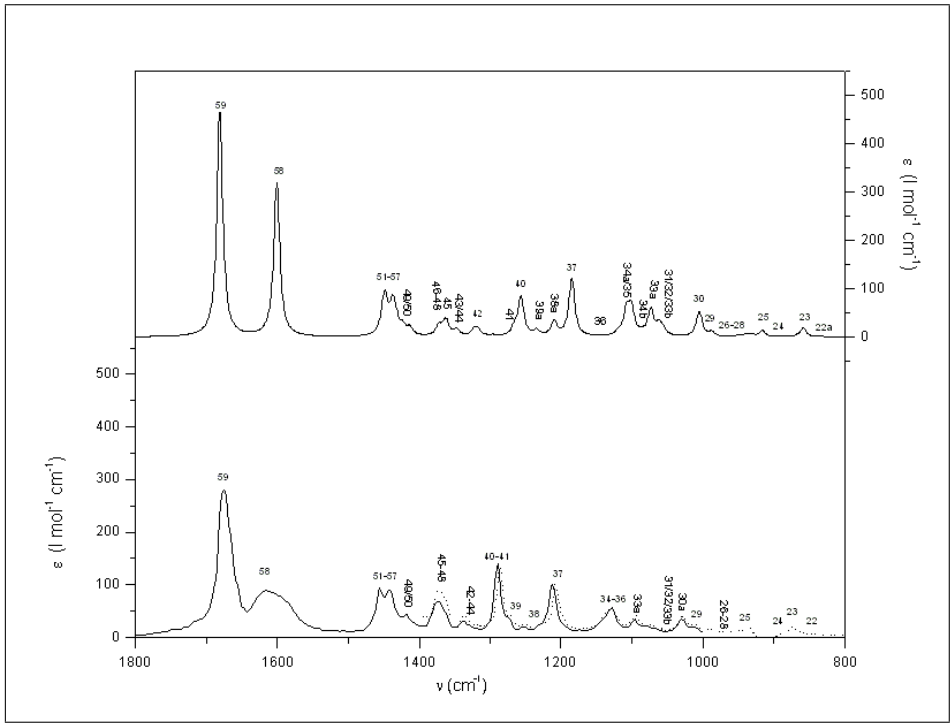


**Figure 7.10:** Comparison of the experimental IR spectra (bottom) of pulegone in $CDCl_3$ and $CS_2$ (dotted line) with the calculations (B3LYP/6-311+G(d,p)) in vacuo (top).

The experimental VCD pattern between 1320 $cm^{-1}$ and 1400 $cm^{-1}$ is only slightly different from the calculated one. The same can be said for the frequency region from 950 $cm^{-1}$ to 1000 $cm^{-1}$. In the calculated VCD spectrum band 59, originating from the C=O stretching vibration, has a positive sign. In the experiment, however, the opposite sign is visible. All other bands are predicted to have the correct sign with respect to the experiment.

As is shown in 7.12, calculations using a larger basis set (cc-pVTZ) were not able to convert the sign of band 59. The contradiction between theory and experiment can be due to the fact that the C=O stretching, more than other kinds of vibrations, is very sensitive to interactions with

the surrounding molecules.

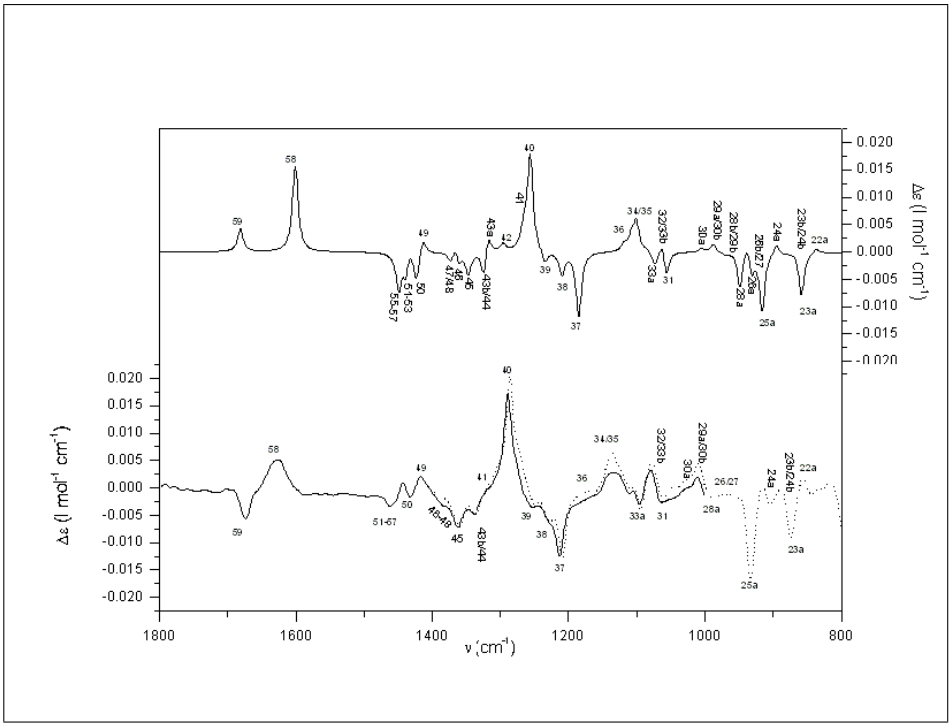


**Figure 7.11:** Comparison of the experimental VCD spectra (bottom) of R-(+)-pulegone in $CDCl_3$ and $CS_2$ (dotted line) with the calculations (B3LYP/6-311+G(d,p)) in vacuo (top).

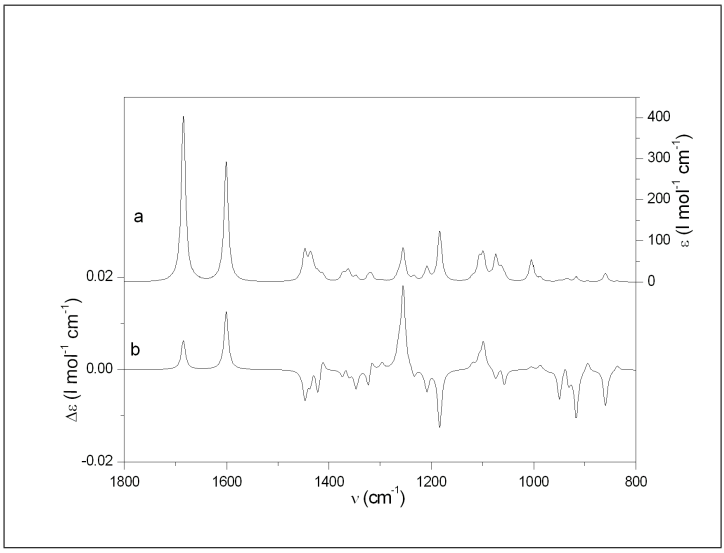


**Figure 7.12:** The calculated IR (a) and VCD (b) spectra of R-pulegone, using a cc-pVTZ basis set. In order to scale the frequencies, a scaling factor of 0.965 [152] was used.

**PCM-calculations**: To shed some light on the influence of the surrounding solvent, in a next step, PCM models were considered. In Figure 7.15 and Figure 7.16 the spectra obtained from the PCM calculations, the calculated spectra for isolated pulegone and the experimental spectra are compared. The largest frequency differences are found for the C=O and C=C stretching vibrations, where the incorporation of solvent effects lowers the frequencies of the modes. For the C=C stretching the intensity is increased in the IR spectrum. The most striking observation is that, by using PCM, the sign of the VCD band of the C=O stretching vibration is inverted. This means that for band 59, PCM calculations are necessary in order to obtain the same sign as in the experimental spectra. For the other normal modes only small differences are observed between both kind of calculations. With PCM, the broad band at 1614 $cm^{-1}$ in the IR spectrum still has not been correctly reproduced. In Figure 7.13 the recorded IR spectra in $CS_2$ are compared with the spectra in $CDCl_3$ and the PCM calculations in $CS_2$. For the C=O stretching vibration, the band is found at a higher frequency in the spectra recorded in $CS_2$ compared to the measurements in $CDCl_3$. This trend was predicted in a correct manner by the PCM calculations

in $CS_2$ and $CDCl_3$. The fact that the frequencies of the bands, originating from the C=O bending vibrations (at 1208 $cm^{-1}$ and 1285 $cm^{-1}$) in $CDCl_3$ are higher than for measurements in $CS_2$, is less visible in the PCM calculations of both solvents. For the VCD spectra recorded in $CS_2$, band 59, similar to the measurements in $CDCl_3$, also gives rise to a negative sign. This is illustrated in Figure 7.14. The experimental VCD spectra for $CDCl_3$ and $CS_2$ are very similar and suggest that the precise nature of the solvent does not play a significant role. However, in order to obtain the correct sign for the CO stretching vibration, in this case, it is necessary to account for solvent effects, using a polarized continuum model. The absence of significant differences between the experimental VCD spectra, most presumably, is related to the fact that the dielectric constants of the solvents used are comparable (4.9 for $CDCl_3$ and 2.6 for $CS_2$). To further elucidate the effect of the dielectric constant, additional PCM calculations for pulegone were performed, using $H_2O$ and ethanol as solvent. The dielectric constants of these solvents are 78.39 and 24.55, and are both significantly larger than those of $CDCl_3$ and $CS_2$. For the PCM calculations using $H_2O$, the sign of the band originating from the CO stretching vibration, was predicted to have a positive sign. For the calculations ethanol, a negative band similar to the one, obtained for $CDCl_3$ and $CS_2$ was predicted. This means that the dielectric constant determines the sign of the band originating from the CO stretching vibration.

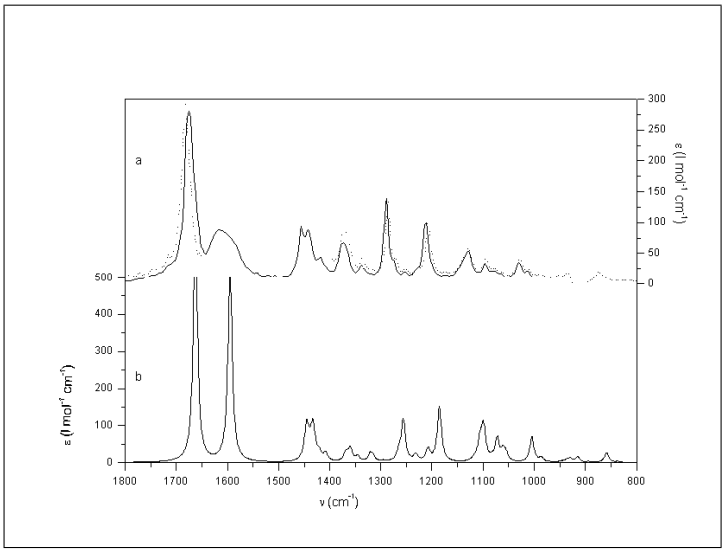


**Figure 7.13:** Comparison of the experimental IR spectra (a) of pulegone in $CDCl_3$ (solid line) and in $CS_2$ (dotted line) with the PCM calculations (b) of pulegone in $CS_2$.

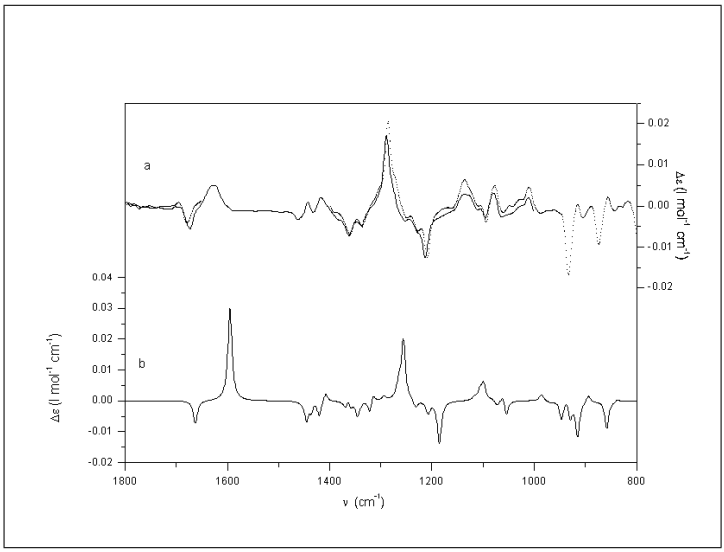


**Figure 7.14:** Comparison of the experimental VCD spectra (a) of (+)-pulegone in $CDCl_3$ (solid line) and in $CS_2$ (dotted line) with the PCM calculations (b) of R-pulegone in $CS_2$.

**Calculations of the 1:1 pulegone.$CDCl_3$ complexes**: As already

described above, significant interactions arise between the carbonyl function of pulegone and the heavily polarized carbon-deuterium bond of $CDCl_3$. This is why the VCD spectra of the 1:1 solute.solvent associations were also considered. Due to the characteristics of $CS_2$ it is less likely that similar complexes will be formed in $CS_2$ and these interactions were not considered. The complexes with $CDCl_3$ were modeled explicitly. The conformational search, yielded 9 unique minima. The resulting values for $\Delta H^0$ , the Boltzmann weighted populations and the dihedral angles $\tau_1$ and $\tau_2$ of the conformers are summarized in Table 7.2. Based on $\tau_2$, three different groups could be distinguished. Considering those groups, with increasing energy, the values of the torsion angle are approximately $-5°$, $-130°$ and $-75°$ respectively. All have their methyl substituent in the equatorial position. The conformers with an axial methyl substituent were not taken into account since they all have significantly higher energies. Depending on the orientation of the solvent molecule, slightly different theoretical spectra were obtained.

**Table 7.2:** The differences in standard enthalpy, $\Delta H^0$ (in kcal/mol), Boltzmann populations (w in%) and torsions $\tau_1$ and $\tau_2$ (in degrees) of the stable conformers of the 1:1 complexes between pulegone and $CDCl_3$ in vacuo and in PCM.

| | Vacuo | | | | PCM | | | |
|---|---|---|---|---|---|---|---|---|
| Conformer | $\Delta H^0$ | w | $\tau_1$ | $\tau_2$ | $\Delta H^0$ | w | $\tau_1$ | $\tau_2$ |
| A | 0.00 | 13.2 | 39 | -5 | | | | |
| B | 0.00 | 13.2 | 18 | -7 | | | | |
| C | 0.01 | 13.0 | -4 | -8 | | | | |
| D | 0.14 | 10.5 | 36 | -125 | 0.02 | 32.9 | 36 | -125 |
| E | 0.17 | 9.9 | 18 | -137 | | | | |
| F | 0.18 | 9.8 | 74 | -138 | 0.01 | 33.4 | 74 | -138 |
| G | 0.18 | 9.7 | 126 | -142 | 0.00 | 33.7 | 126 | -142 |
| H | 0.19 | 9.7 | 69 | -141 | | | | |
| I | 0.23 | 8.9 | -159 | -77 | | | | |

The Boltzmann weighted VCD and IR spectra are shown in Figure 7.15 and Figure 7.16 and are compared with the PCM model, the calculations in vacuo and the experiment. The frequency shifts of the bands 58 and 59 correspond with those of the PCM calculations. In the cal-

culated IR spectra of the 1:1 associations, two bands are distinguished, both originating from the C=C stretching vibrations. Depending on the orientation of $CDCl_3$ toward the pulegone molecule, the geometry of the ring is altered and therefore the frequency of the band is shifted. In the theoretical VCD spectrum of the 1:1 associations, band 59 unfortunately is predicted to have a positive sign, opposite to the experiment. Its intensity, however, is smaller than for the calculations of the free pulegone in vacuo.

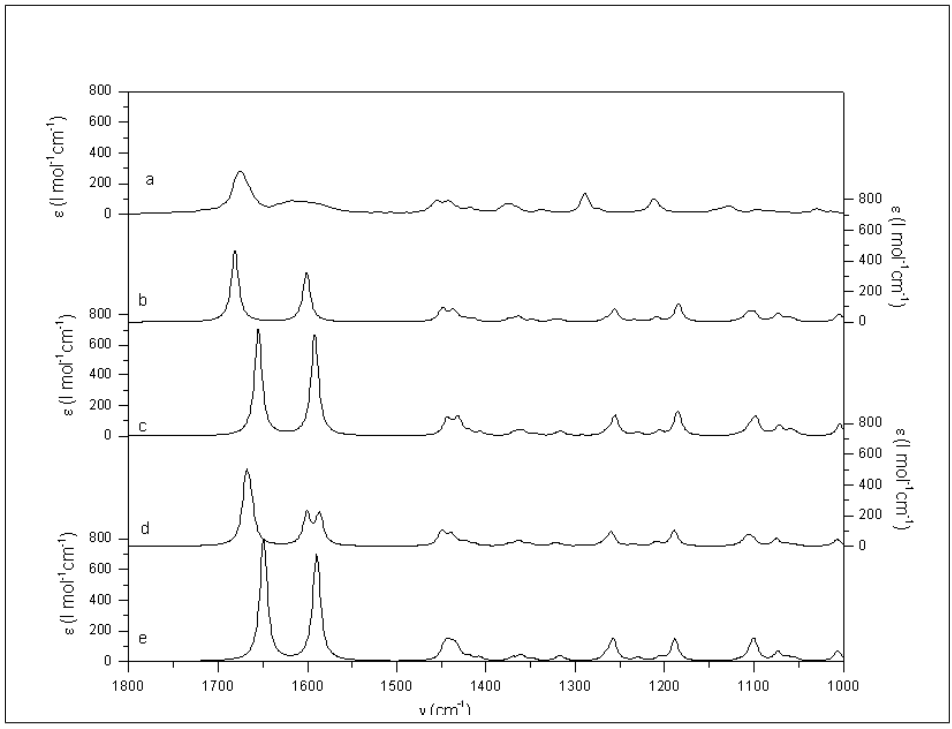


**Figure 7.15:** Comparison of the experimental IR spectrum of pulegone in $CDCl_3$ (a) with the calculations of pulegone in vacuo (b), PCM calculations in $CDCl_3$ (c), calculations of the pulegone.$CDCl_3$ complexes (d) and PCM calculations of the 1:1 associations (e).

**PCM calculations of the 1:1 pulegone.$CDCl_3$ complexes**: In a last step the spectra of the significant 1:1 associations were recalculated, using the PCM model. With PCM, the number of minima was reduced from nine to three. For all other conformers at least one imaginary frequency was found. Their relative standard enthalpies ($\Delta H^0$), Boltz-

mann populations and torsions ($\tau_1$ and $\tau_2$) are shown in Table 7.2. The torsion angles of the conformers were very similar for the calculations in vacuo and those using PCM. The calculated spectra of the 1:1 associations using PCM are also depicted in Figure 7.15 and Figure 7.16. The only improvement compared to the calculations of the 1:1 associations in vacuo is that in the VCD spectrum, band 59 is now also predicted to have the correct sign with respect to the experiment.

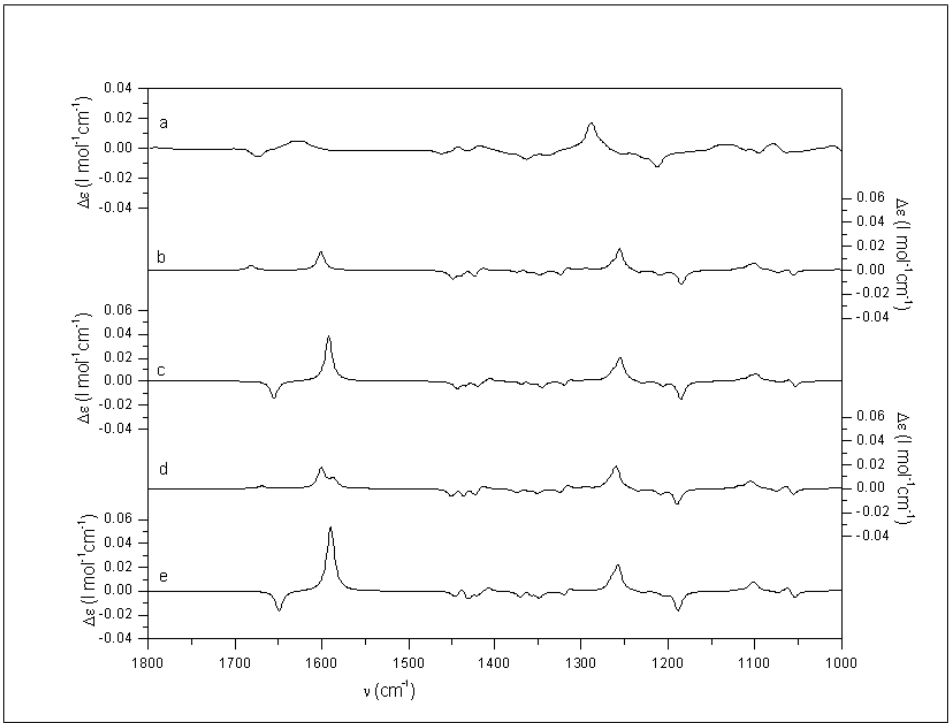


**Figure 7.16:** Comparison of the experimental VCD spectrum of (+)-pulegone in $CDCl_3$ (a) with the calculations of R-pulegone in vacuo (b), PCM calculations in $CDCl_3$ (c), calculations of the R-pulegone.$CDCl_3$ complexes (d) and PCM calculations of the 1:1 associations (e).

It should be noted that with none of these methodologies used we were able to explain the broadness of band 58. A possible reason for this relatively broad band, to our opinion, may be found in the flexibility of the cyclohexane ring and the influence of the resulting conformational dynamics on the C=C stretching fundamental. Some support for this conclusion was obtained by performing additional calculations for the 1:1

complexes in vacuo, characterized by different ring geometries and thus leading to various C=C stretching frequencies. Additional calculations were performed for pulegone in which the ring was held planar. The C=C stretching frequency is red shifted by 10 $cm^{-1}$.

**Quantitative comparison theory-experiment**: For the different theoretical models used, all bands were compared quantitatively with experiment. The scatter plots in which the calculated and experimental dipole and rotational strengths are compared, are depicted in Figures 7.17 and Figure 7.18. The corresponding tables, including information on the experimental and calculated frequencies, dipole strengths and rotational strengths, are also shown in the supplementary information (S-1,S-2 and S-3). The PCM models seem to overestimate the dipole as well as the rotational strengths a little. It should be noted explicitly that, although the PCM calculations have a better qualitative agreement with the experiment, the largest values for $r^2$ were obtained for the calculations of an isolated pulegone molecule in vacuo and for the calculations of the 1:1 complexes in vacuo. This phenomenon, most likely, is due to the fact that during the calculations of $r^2$, the error caused by the CO stretching mode was compensated by those for the other normal modes. It is well-known that for VCD the $r^2$-values are quite often smaller than for IR [154].

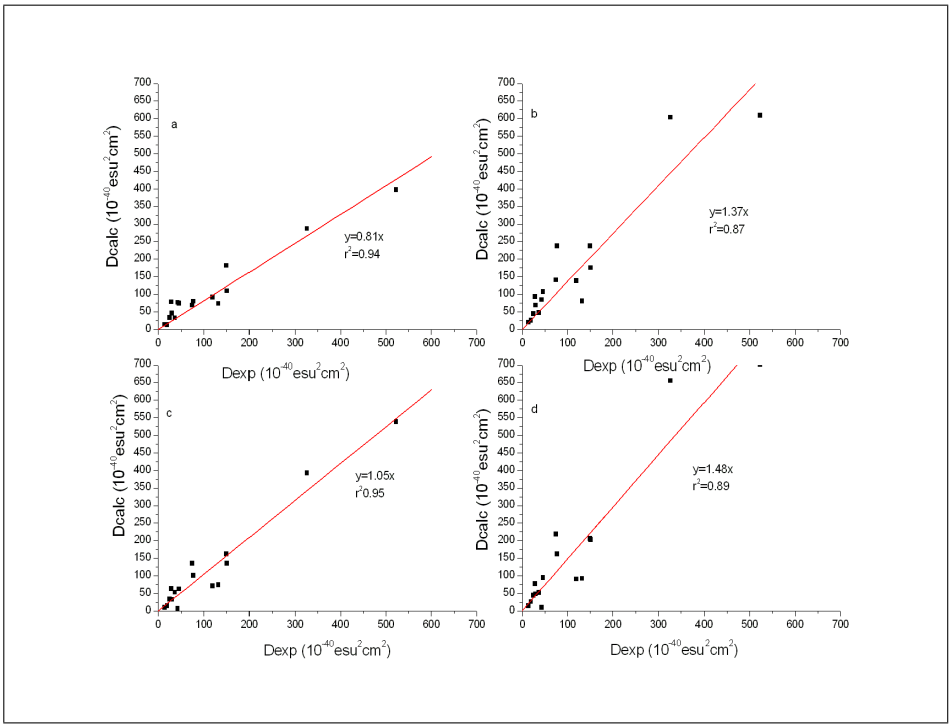


**Figure 7.17:** Comparison of the experimental dipole strengths and the calculated ones: (a) calculations of pulegone in vacuum, (b) PCM calculations of pulegone, (c) calculations of the 1:1 pulegone.$CDCl_3$ associations and (d) PCM calculations of the complexes.

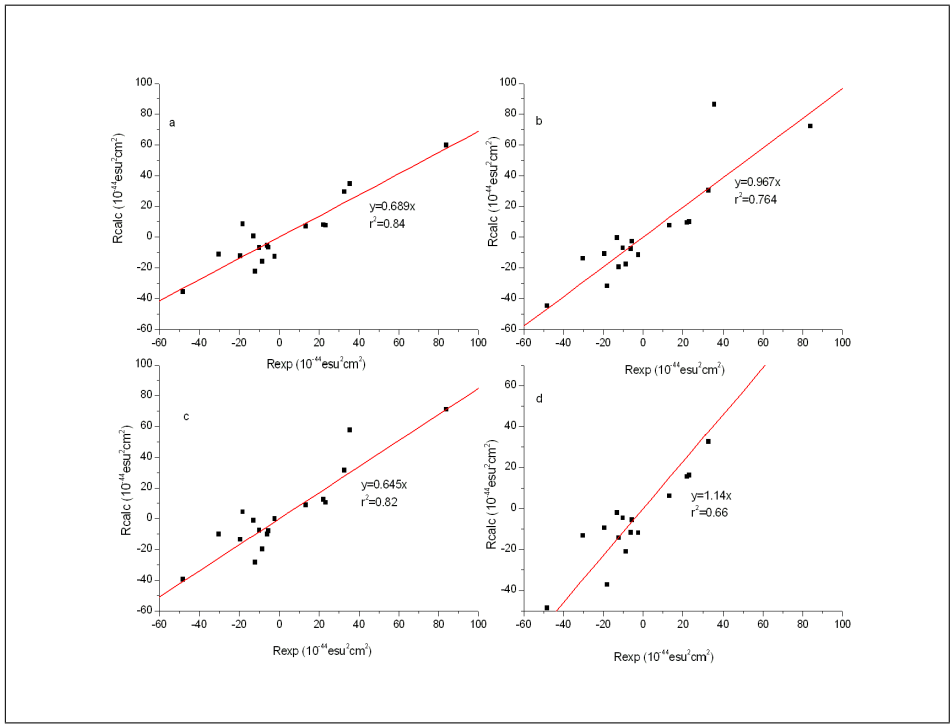


**Figure 7.18:** Comparison of the experimental Rotational strengths and the calculated ones: (a) calculations of R-pulegone in vacuum, (b) PCM calculations of R-pulegone, (c) calculations of the 1:1 R-pulegone.$CDCl_3$ associations and (d) PCM calculations of the complexes.

A quantitative comparison was also made for the measurements in $CS_2$ and their corresponding calculations. The graphs with the experimental dipole and rotational strengths versus the calculated ones are depicted in Figure 7.19. The corresponding table is given in the Supplementary information (S-4). The $r^2$-values are smaller than those observed for the measurements in $CDCl_3$. This is most probably due to the fitting procedure necessary to extract the D and R values from the experimental spectra, as this was less straightforward for the solutions in $CS_2$. The calculations in PCM gave only slightly larger dipole and rotational strengths. Due to the smaller dipole moment of $CS_2$, the difference between the PCM calculations and the calculations in vacuo for solutions in $CS_2$ is smaller than those for solutions in $CDCl_3$.

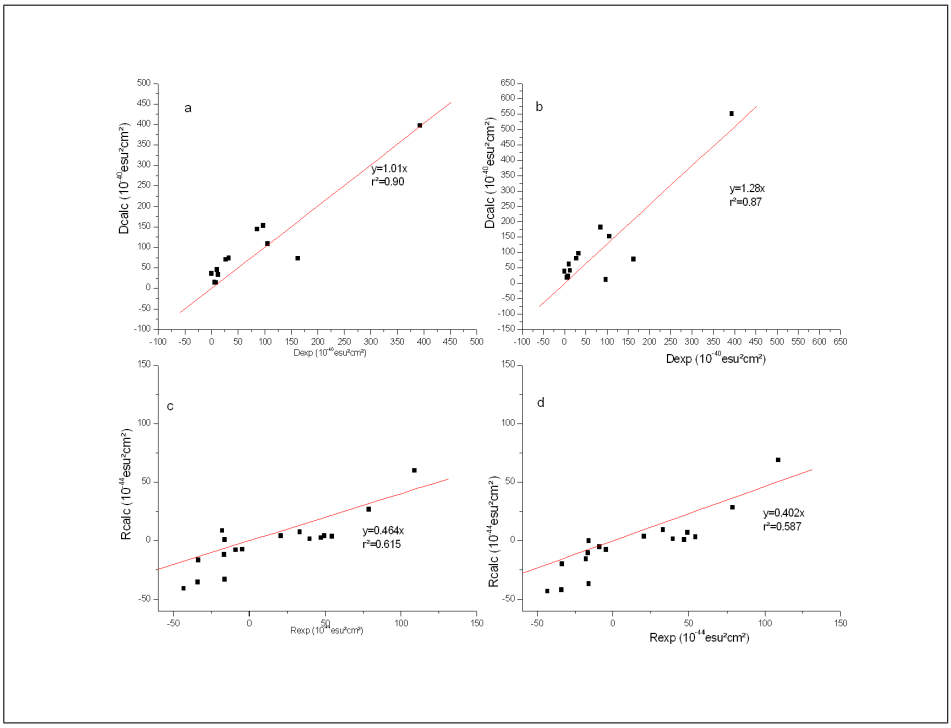


**Figure 7.19:** Comparison of the experimental Dipole strengths and the calculated ones: (a) calculations of pulegone in vacuum, (b) PCM calculations of pulegone in $CS_2$.Comparison of the experimental Rotational strengths and the calculated ones: (c) calculations of R-pulegone in vacuum, (d) PCM calculations of R-pulegone in $CS_2$.

### Spectral region: 2000 $cm^{-1}$ - 2500 $cm^{-1}$

By replacing the 1850 $cm^{-1}$ long wave pass filter with a 3000 $cm^{-1}$ filter, higher frequencies could be studied. This was done for solutions in binary mixtures of $CDCl_3$ and $CD_2Cl_2$, always at a concentration of 1.5 M. The following proportions of $CDCl_3$ and $CD_2Cl_2$ were used: 100/0, 50/50 and 0/100. Care was taken that the IR absorbance was not too high in order to obtain reproducible VCD measurements.

**Measurements in $CDCl_3$**: First the VCD spectra of both enantiomers of pulegone in $CDCl_3$ were recorded. As is shown in Figure 7.22, for R-(+)-pulegone a positive band could be distinguished from the noise at 2250 $cm^{-1}$. For its enantiomer a band with opposite sign was observed at the same frequency. In order to obtain reproducible VCD spectra in

that region, it was necessary to measure both enantiomers during 4h. Due to its location, this band seems to originate from the CD stretching vibration of $CDCl_3$. In the corresponding IR spectrum, after subtraction of the solvent, the band arising from the CD stretching vibration of $CDCl_3$ still was visible at 2250 $cm^{-1}$. This is depicted in Figure 7.21. In Figure 7.20 the IR spectrum of the solution, without solvent subtraction, and that of pure $CDCl_3$ are shown. The figure gives a nice illustration of the increase of the CD stretching band intensity in the presence of the solute, which may be related to the formation of a $C-D\cdots O$ hydrogen bond between solute and solvent. The fact that the CD stretching mode of the solvent also provokes a VCD signal, indicates that through the interaction chirality was induced in the solvent molecule. This confirms our previous VCD results, earlier in this chapter, of camphor solutions in $CDCl_3$ [6].

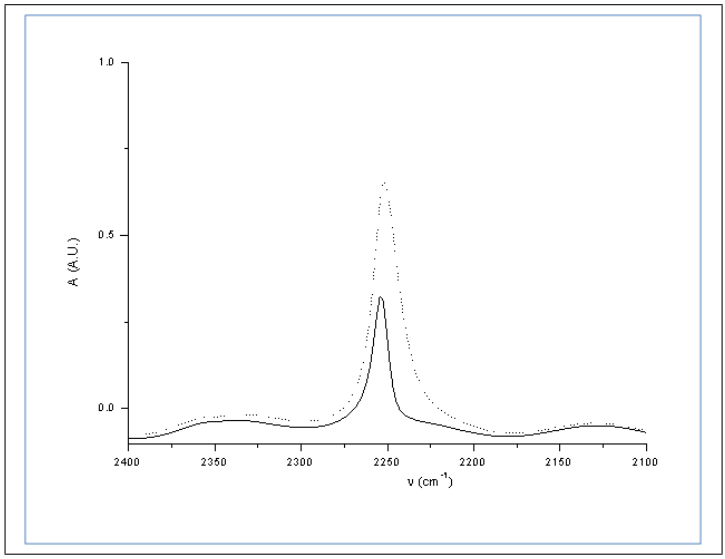


**Figure 7.20:** The IR-spectra of pure $CDCl_3$ (solid line) and of pulegone in $CDCl_3$, without solvent subtraction (dotted line).

In order to establish the source of this VCD band, ab initio calculations and PCM calculations were performed for pulegone in both isolated and solvated state. As is seen in Figure 7.21 and Figure 7.22, the ab initio calculations of the isolated pulegone molecule nor its PCM calculations were able to reproduce the VCD signal in that region. The

Boltzmann weighted VCD spectrum of the 1:1 pulegone.$CDCl_3$ associations on the other hand, gave rise to a band at around 2250 $cm^{-1}$. In the case of R-(+)-pulegone a positive band was seen, which is in agreement with the experiment. Considering the band around 2250 $cm^{-1}$ for each stable pulegone.$CDCl_3$ complex found during the conformational analysis the same three groups, as described above, could be distinguished. The VCD spectra of the conformers, belonging to the first, and most stable group, with a $\tau_2$ of $-5°$, exhibit a negative band at 2240 $cm^{-1}$. The second group with $\tau_2$ equal to $-130°$ shows a large positive band at 2250 $cm^{-1}$ and for the third group, in which $\tau_2$ equals $-75°$, a very small positive band was seen at 2270 $cm^{-1}$. The combination of all conformers led to a band with positive sign. For the S-(-)-pulegone complex obviously the opposite sign is predicted. This observation proves that the CD stretching vibration of the $CDCl_3$ molecule of the association gives rise to a VCD signal. This means that chirality can be induced in the solvent through an intermolecular interaction with a chiral molecule, in this case, pulegone. The same conclusion was drawn from the VCD study of camphor, earlier this chapter.

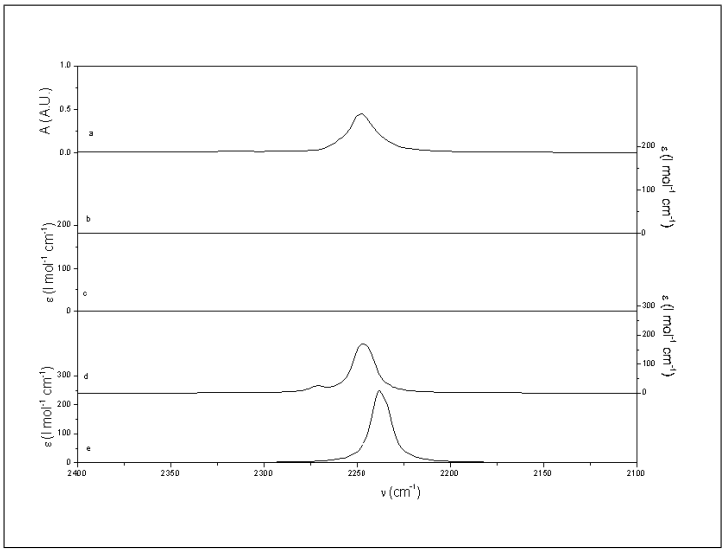


**Figure 7.21:** Experimental (a) and calculated IR spectra of pulegone in $CDCl_3$ in the frequency region from 2100 $cm^{-1}$ to 2400 $cm^{-1}$: (b) calculations of pulegone in vacuo, (c) PCM calculations in $CDCl_3$, (d) calculations of the pulegone.$CDCl_3$ associations in vacuo, (e) PCM calculations of the complexes in $CDCl_3$.

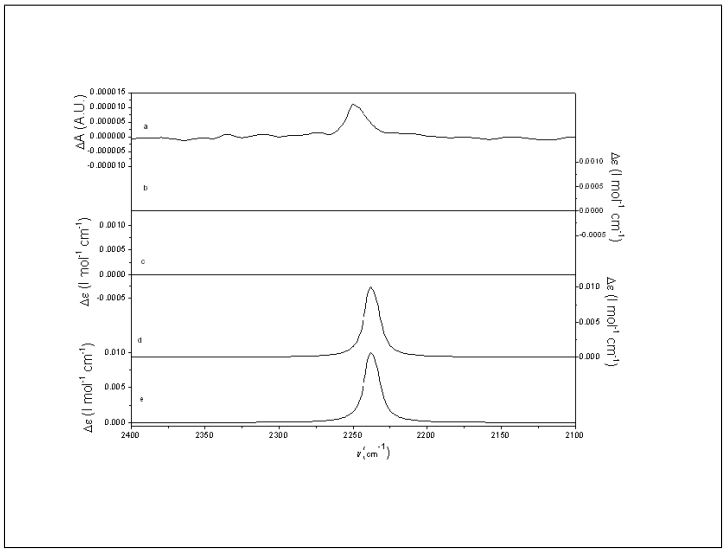


**Figure 7.22:** Experimental (a) and calculated VCD spectra of R-(+)-pulegone in $CDCl_3$ in the frequency region from 2100 $cm^{-1}$ to 2400 $cm^{-1}$: (b) calculations of pulegone in vacuo, (c) PCM calculations in $CDCl_3$, (d) calculations of the pulegone.$CDCl_3$ associations in vacuo, (e) PCM calculations of the complexes in $CDCl_3$.

In Table 7.3 a quantitative comparison was made between the experimental and calculated dipole and rotational strengths. The predicted values seem to be somewhat larger than the experimental ones.

**Table 7.3:** A quantitative comparison of the theoretical and experimental Rotational ($10^{-44}$ $esu^2$ $cm^2$) and Dipole ($10^{-40}$ $esu^2$ $cm^2$) strengths of the CD and $CD_2$ stretching vibrations.

| | Experimental | | | Calculated | | |
|---|---|---|---|---|---|---|
| solvent | Frequency | D | R | Frequency | D | R |
| $CDCl_3$ | 2247 | 55.4 | 2.1 | 2250 | 153.8 | 7.7 |
| $CD_2Cl_2$ | 2199 | | | 2180 | 56.6 | -0.8 |
| | 2302 | 5.3 | | 2307 | 50.1 | -0.9 |

**Measurements in binary mixtures of $CDCl_3$ and $CD_2Cl_2$**: In order to prove the statement of induced chirality into the solvent, pulegone in binary mixtures of $CDCl_3$ and $CD_2Cl_2$ was studied. This again is in analogy with the VCD study about camphor [6]. The IR and VCD

spectra of R-(+)-pulegone in $CDCl_3/CD_2Cl_2$ solutions with ratios of 100/0, 50/50 and 0/100 are shown in Figure 7.23 and Figure 7.24. For each solution, the concentration was equal to 1.5 M. In the IR spectra it can be seen that as the $CDCl_3$ fraction increases, an increase of the CD stretching vibration at 2254 $cm^{-1}$ is observed, while the intensities of the asymmetrical and symmetrical $CD_2$ decrease. In the VCD spectra of the binary mixtures, again a large increase of the CD stretching mode of $CDCl_3$ is visible as the mole fraction $CDCl_3$ rises. For these solutions, the two bands originating from the $CD_2$ stretching mode could not be distinguished from the noise.

In order to verify these observations, the 1:1 pulegone.$CD_2Cl_2$ complexes also were modeled explicitly. A similar conformational search was done as for the associations with $CDCl_3$. This time only one relevant minimum was found. In the case of $CD_2Cl_2$ the possible interactions between the Cl-atom and the carbonyl function of pulegone also were taken into account. The modeled associations, however, all seemed to converge toward the complex with an intermolecular interaction between a deuterium atom and the oxygen of pulegone. In the calculated VCD spectrum of the 1:1 complex, containing R-(+)-pulegone, two negative bands were visible at 2180 $cm^{-1}$ and 2308 $cm^{-1}$, originating from the symmetric and anti-symmetric $CD_2$ stretching vibrations respectively. Naturally for S-(-)-pulegone the signs of the bands are reversed. Unfortunately these bands could not be distinguished from the noise in the experimental VCD spectra of pulegone, dissolved in $CD_2Cl_2$. The same was observed during our VCD study of camphor in $CD_2Cl_2$ and might be due to the fact that the abundance of the complexes with $CD_2Cl_2$ is smaller than those with $CDCl_3$. This obviously is related to the less acidic character of the deuterium atoms in $CD_2Cl_2$. In the experimental IR spectrum a negative band is observed at 2180 $cm^{-1}$. This means that for this band, the absorbance of the solvent must be larger than that of the solution. It can be explained by comparing the calculated dipole strength of the symmetric $CD_2$ stretch of a free $CD_2Cl_2$ molecule with that of the complex. The dipole strength of the $CD_2$ stretch of the complex is only 4 times larger than that of the simple solvent molecule (B3LYP/6-311+G(d,p), 56.6 versus 12.2). This value is much smaller than that of the asymmetrical stretching vibration, in which the dipole strength of the complex is about 113 times

larger (B3LYP/6-311+G(d,p), 50.1 versus 0.5). This observation, together with the fact that during the measurements of camphor in solution, less $CD_2Cl_2$ molecules are present in the optical path, than it is the case for the measurements of the pure solvent, explain the negative IR band.

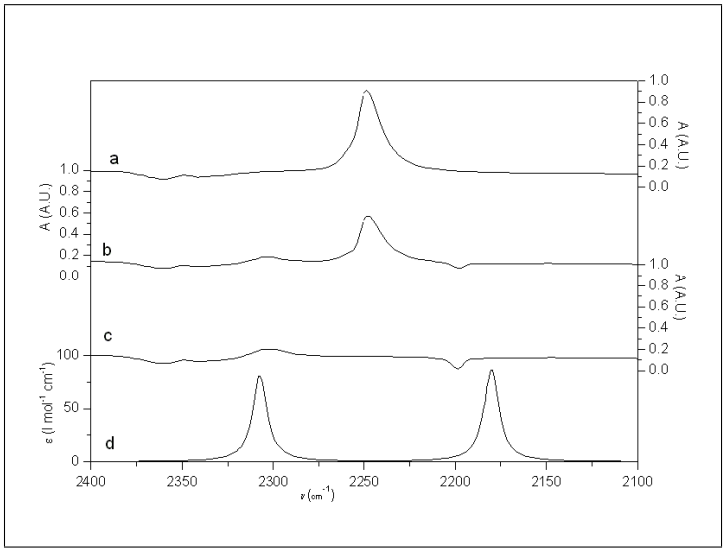


**Figure 7.23:** The experimental IR spectra of pulegone in binary mixtures of $CDCl_3/CD_2Cl_2$: (a) 100/0, (b) 50/50, (c) 0/100 and the calculated spectrum of the pulegone.$CD_2Cl_2$ association(d).

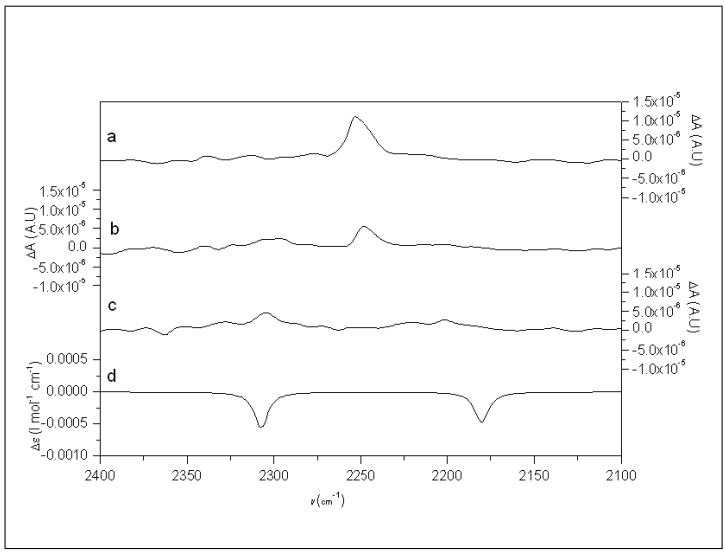


**Figure 7.24:** The experimental VCD spectra of (+)-pulegone in binary mixtures of $CDCl_3/CD_2Cl_2$: (a) 100/0, (b) 50/50, (c) 0/100 and the calculated spectrum of the R-pulegone.$CD_2Cl_2$ association(d).

A quantitative comparison between the experimental and calculated rotational strengths of the $CD_2$ stretching vibrations is also given in Table 7.3. For both solvents the predicted values are larger than the experimental ones. This can be due to the fact that only 1:1 associations have been taken into account, while other associations, with, for example, a higher stoichiometry, are possible as well. At a concentration of 1.5 M, a pulegone molecule is surrounded by approximately 9 $CDCl_3$ molecules, which, in principle, could give rise to several, stronger or weaker, solute-solvent interactions. Since the hydrogen bond between the carbonyl group of pulegone and the deuterium atom of $CDCl_3$ is relatively strong and this interaction protects the carbonyl function from other $CDCl_3$ molecules, it is not likely that these interactions will play a significant role. Experimental evidence supporting the fact that the weaker solute solvent interactions are of minor importance was obtained from the measurements in $CD_2Cl_2$ for which no induced VCD signals were observed. Another reason for this quantitative disagreement is that the average number of solvent molecules taking part in the interaction, remains unknown. Therefore we are not able to convert the absorbance units to extinction coefficients. The disagreement between theory and

experiment might also be due to methodological errors as all calculations, including those of the properties of the hydrogen bonded species, are performed at the B3LYP level. Although this method is often used to study a variety of molecular, properties, it is now generally accepted that some properties of weak hydrogen bonded complexes can be influenced by dispersion interactions and that these interactions, up to now, are not accounted for by the exchange and correlation functionals. It is however important to note that for all experimental data, the sign of the VCD signal is in agreement with that obtained from the calculations.

### 7.3.5 Conclusions

In order to assign all bands of the VCD spectrum of pulegone, dissolved in $CDCl_3$, $CD_2Cl_2$ or $CS_2$, it is necessary to explicitly take into account the solvent effects. During the ab initio calculations of pulegone and the 1:1 pulegone.solvent associations in vacuo, the sign of the band, originating from the C=O stretching vibration, is incorrectly predicted. Using the PCM model, its predicted sign corresponds with the experiment. Even for the measurement in $CS_2$, a solvent with a smaller dipole moment, PCM calculations were necessary in order to obtain the correct sign.

The broadness of the band, originating from the C=C stretching vibration can only be explained by taking into account at least several stable conformations of the 1:1 pulegone.$CDCl_3$ associations. Studying the VCD spectra of pulegone in $CDCl_3$ in the frequency region between 2000 $cm^{-1}$ and 2500 $cm^{-1}$, a signal was observed at about 2250 $cm^{-1}$. For (+)-pulegone, a positive band could be distinguished from the noise while for its enantiomer, a band with opposite sign was found. A signal at that frequency originates from the CD stretching vibration of the solvent, which means that chirality is induced into the solvent. This is possible through an intermolecular interaction, i. e. a hydrogen bond, between the chiral pulegone and a solvent molecule. This was simulated by calculating the spectra of the most stable 1:1 solute.solvent associations. The predicted sign of the band was in agreement with the experiment, which proves our statement about chirality induction. In the theoretical spectra of the free pulegone, or in those obtained from the PCM calculations, no band was observed in the region from 2000

$cm^{-1}$ to 2500 $cm^{-1}$. This is completely in line with our previous VCD study of camphor in that region and therefore indicates that chirality induction into the solvent is a relatively common effect.

Very recently a paper was published by Nicu et al., in which the effects of complex formation on VCD spectra was studied theoretically [155]. The calculated rotational strengths, atomic axial tensors (AATs) and atomic polar tensors (APTs) of the complex were compared with those of the free chiral molecule. For the article, the complexation between benzoyl-benzoic acid (BBA) and an achiral $NH_3$ was studied. Five different types of effects were observed. One of the cases represents the solvent chirality induction, where the modes of the achiral $NH_3$ show nonzero VCD intensities in the molecular complex. The perturbations induced by the complexation with BBA cause the electric and magnetic transition dipole moments of the $NH_3$ fragments to no longer be perpendicular.

This study as well as those referred to in earlier stage of this chapter, show that solvent effects are a hot topic nowadays and that they can no longer be neglected. In this chapter we demonstrated that even for molecules as simple as pulegone and camphor, some bands only can be explained by taking into account the solvent during the calculations.

8

# VCD measurements at lower temperatures

## 8.1 Introduction

During VCD assignments, the conformational analysis is very often the most critical step. As demonstrated in Chapter 4, it is very important to take into account every stable conformer that is present in the solutions. In case of very flexible molecules, this is not very obvious at all. Moreover after finding the important minima on the molecular mechanics potential energy surface, all of them need to be optimized on the ab initio level and subsequently their corresponding VCD spectra need to be calculated. These calculations require a large amount of CPU time. In addition, the assignment of the experimental bands will be complicated by the presence of a large number of conformers. If we were able to diminish the number of conformers necessary for the simulation of the experimental VCD-spectrum, the assignment proce-

dure could be simplified. Using the Boltzmann distribution law as a model for the conformational weights [81], measurements at lower temperatures should reduce populations of higher energy conformations in favor of the global minimum. This would imply the simplification of the interpretation of the experimental VCD spectra. We have studied this assumption by measuring the VCD spectra of 3-methylcyclohexanone, borneol and limonene at various temperatures.

To be able to perform measurements at lower temperatures a Specac variable temperature cell was introduced in the sample space of the PMA 37 module. In this cryostat, the actual liquid cell is suspended in a vacuo shroud. The temperature is controlled by combining a Dewar filled with liquid nitrogen, an electrical heating element, a thermocouple and a Specac temperature controller. The vacuum jacket was equipped with KBr-windows; the heatable sealed liquid cell had $CaF_2$-windows and lead spacers. Different minimal temperatures can be obtained by dissolving the product in various solvents. The solvents used for this temperature study were $CDCl_3$, $CD_2Cl_2$ and $CS_2$ with minimal temperatures of 213K, 183K and 173K and spectral regions of 1000 $cm^{-1}$-1800 $cm^{-1}$, 1050 $cm^{-1}$-1800 $cm^{-1}$ and 1000 $cm^{-1}$-1400 $cm^{-1}$ respectively. To avoid condensation of water, the cell was placed under vacuum at temperatures below 213K.


**Figure 8.1:** Experimental setup for VCD measurements at lower temperatures.

In the literature many papers are found about VCD experiments, performed at various temperatures, ranging from 278 K to 363 K. Usually, the thermal unfolding process or other conformational transitions of secondary structures are discussed [156, 157, 158, 159, 160]. In 1982, Schlosser et al. published an article in which the VCD spectra of matrix-isolated molecules was studied [161]. In this study organic molecules are isolated in inert-gas matrices at cryogenic temperatures. The major advantage is that line widths can be greatly reduced by cooling to cryogenic temperatures. Only very recently some additional papers on that topic were published [**?**, 162, 163].

## 8.2 The influence of temperature on the IR and VCD spectrum of 3-methylcyclohexanone

### 8.2.1 Introduction

The IR and VCD spectra of 3-methylcyclohexanone have already been discussed elaborately in literature. Due to the simplicity of the chiral molecule, it is very often used as a test molecule for several experimental VCD setups, allowing to study various spectral regions [46, 151]. In other studies the CH stretching region was discussed [164, 149]. Earlier, Devlin and Stephens described the complete assignment of the IR and VCD bands of this molecule between 1000 $cm^{-1}$ and 2000 $cm^{-1}$ [165]. Because of its easily interpretable VCD spectrum, 3-methylcyclohexanone was used to study the effects of temperature on the VCD spectrum.

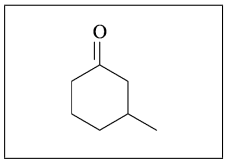


**Figure 8.2:** Structure of 3-methylcyclohexanone

### 8.2.2 Experimental

R-(+)-3-methylcyclohexanone with a purity of 98% and an enantiomeric excess (ee) of 99% was obtained from Aldrich and was used without further purification. Measurements focused on the 1000 $cm^{-1}$ to 1800

$cm^{-1}$ spectral window. IR and VCD spectra were measured in $CDCl_3$, $CD_2Cl_2$ and $CS_2$ solutions. The IR absorption of $CS_2$ constrains the useful region to frequencies below 1400 $cm^{-1}$. A KBr cell with a path length of 100 $\mu$m was used. The temperature studies were performed in a sealed cell with $CaF_2$ windows and a path length of 100 $\mu$m. To get an optimal signal to noise ratio (S/N) each measurement took 90 min (6 x 1210 scans). The minimal temperature in $CDCl_3$ is 223K; in $CD_2Cl_2$ temperatures of 183K can be obtained and in $CS_2$ the lowest temperature possible is 173K. The solutions had a concentration of 1.19M. Due to the large absorption of the CO-stretch, the VCD region under study was limited to 1600 $cm^{-1}$.

To better resolve the different normal modes, IR measurements in liquid Xe were performed, using one of the setups developed in the cryospectroscopy research group. The temperature studies ranged from 203K until 173K. The complete system is attached to a pressure manifold to allow the filling and evacuation of the cell. The cell is cooled by liquid nitrogen. Once the desired temperature has been reached, a small amount of sample is condensed into the cell. The system is then pressurized by xenon gas, which immediately starts to condense, allowing the compound to dissolve. During these experiments a resolution of 0.5 $cm^{-1}$ was used.

### 8.2.3 Computational Methods

Calculations of vibrational frequencies, dipole and rotational strengths were carried out using DFT via the Gaussian program[55]. Two different functionals (BWP91 and B3LYP) and four different basis sets (6-31G(d), TZ2P, cc-pVTZ and 6-311+G(d,p)) were used. During conformational analysis the torsion angle between the methyl substituent and the ring was changed systematically in the MMFF [109] [110] force field. The spectra were broadened using Lorentzian bandshapes; a FWHM of 5 $cm^{-1}$ was used. The spectra of all possible conformations were combined by considering their Boltzmann population, based on the relative enthalpies.

### 8.2.4 Results and Discussion

#### Assignment of the IR and VCD spectrum of R-(+)-3-methylcyclohexanone

During conformational analysis, two stable conformations of R-3-methylcyclohexanone were found. One conformer has its methyl group in equatorial position; the other contains an axial methyl substituent. These two minima were then further optimized using DFT and their calculated enthalpy differences for each level of calculation are shown in Table 8.1.

**Table 8.1:** The relative enthalpies of the two conformers of R-3-methylcyclohexanone, their Boltzmann weights and the scaling factors for each level of calculations.

| level of calculation | $\Delta H^0$ | $w_{eq}$ | $w_{ax}$ | scaling factor |
|---|---|---|---|---|
| B3LYP/6-31G(d) | 1.66 | 94.2 | 5.8 | 0.967 |
| B3LYP/cc-pVTZ | 1.77 | 95.2 | 4.8 | 0.98 |
| B3PW91/6-311+G(d,p) | 1.78 | 95.3 | 4.7 | 0.96 |
| B3PW91/TZ2P | 1.58 | 93.5 | 6.5 | 0.98 |
| B3LYP/TZ2P | 1.61 | 93.8 | 6.2 | 0.98 |

The equatorial conformer is found to be the most stable one for each level of theory. The enthalpy differences were used to calculate the Boltzmann populations. For both conformers the frequencies, dipole and rotational strengths were calculated. In Figure 8.3 and Figure 8.4 the calculated Boltzmann weighted IR and VCD spectra respectively are shown for each level of calculation, together with the experimental spectrum. Due to the harmonic approximation, calculated frequencies are generally overestimated and need to be scaled in order to approach the experimental frequencies. These scaling factors, shown in Table 8.1, depend on the level of theory and were taken from literature [144]. Depending on the level of theory, some differences are observed between the calculated spectra. Varying the functionals gives the largest discrepancies. B3LYP and B3PW91 have the same exchange functional (Becke 3-parameter hybrid functional) but their correlation functional is different. Using B3LYP the bands around 1200 $cm^{-1}$ are clearly resolved in the IR spectra. This is not the case for calculations with B3PW91.

The same can be said for the normal modes between 1000 $cm^{-1}$ and 1050 $cm^{-1}$. In the calculated VCD spectra the band around 1220 $cm^{-1}$ has a positive sign for calculations with the B3LYP functional, while in the case of B3PW91 the band is a part of the negative band formed by the normal modes between 1200 $cm^{-1}$ and 1250 $cm^{-1}$. Considering the calculation with the smallest basis set (B3LYP/6-31G*), there are some additional differences with the other levels of theory in frequency regions from 1250 $cm^{-1}$ to 1300 $cm^{-1}$ and from 1350 $cm^{-1}$ to 1400 $cm^{-1}$. The B3LYP/6-31G(d) calculation is the least similar to the experimental spectrum of R-(+)-3-methylcyclohexanone in $CDCl_3$. In the remainder only the B3PW91/TZ2P calculations will be considered. This level also was used in a previous VCD study by Devlin and Stephens [165].

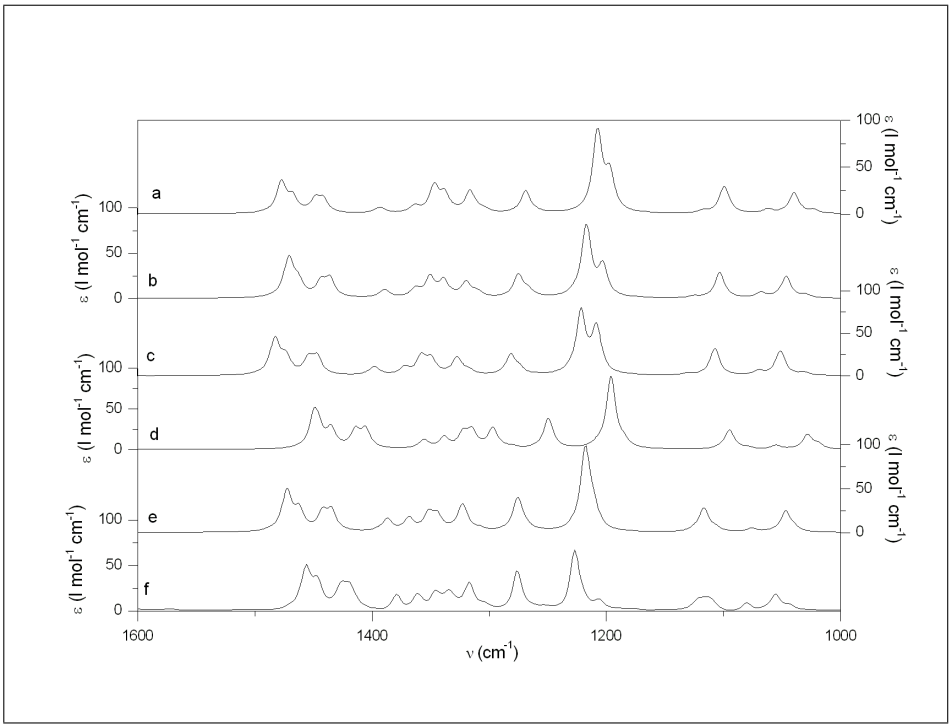


**Figure 8.3:** Comparison of the calculated IR spectra of R-(+)-3-methylcyclohexanone, using different levels of theory: a) B3LYP/6-31G(d), b)B3LYP/cc-pVTZ, c)B3LYP/TZ2P, d)B3PW91/6-311+G(d,p) and e) B3PW91/TZ2P with f) the experimental IR spectrum in $CDCl_3$

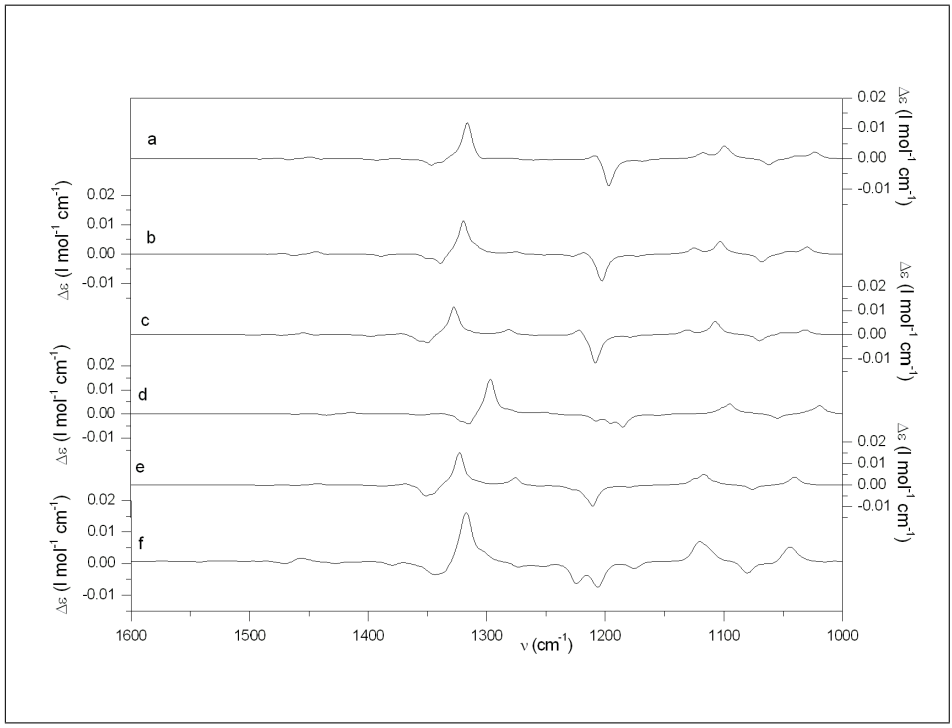


**Figure 8.4:** Comparison of the calculated VCD spectra of R-(+)-3-methylcyclohexanone, using different levels of theory: a) B3LYP/6-31G(d), b)B3LYP/cc-pVTZ, c)B3LYP/TZ2P, d)B3PW91/6-311+G(d,p) and e) B3PW91/TZ2P with f) the experimental VCD spectrum in $CDCl_3$

As is shown in Figure 8.5, the IR spectrum of the equatorial conformation is more similar to the experimental spectrum than that of the axial conformation. This confirms that the first is the dominant conformer of R-3-methylcyclohexanone. By using the calculated Boltzmann populations of Table 8.1, a spectrum composed of a mixture of both conformers can be constructed. The large resemblance of this spectrum with the experimental spectrum leads to an unambiguous assignment of all the fundamentals. The assignment of the bands in the experimental IR spectrum is shown in Figure 8.6. The experimental and calculated VCD spectra of R-(+)-cyclohexanone are compared in the same manner. The frequencies of each fundamental in the experimental spectrum are known from assignment of the IR spectrum. Because of the small differences in the frequencies of the fundamentals from 38 - 41 and the small signals caused by these fundamentals, it is difficult to do the assignment

in the region above 1400 $cm^{-1}$. The assignment of the peaks at lower frequencies led to no further difficulties. Only the fundamentals 22b, 23b, 25b and 28b are separable from the normal modes of the equatorial conformer.

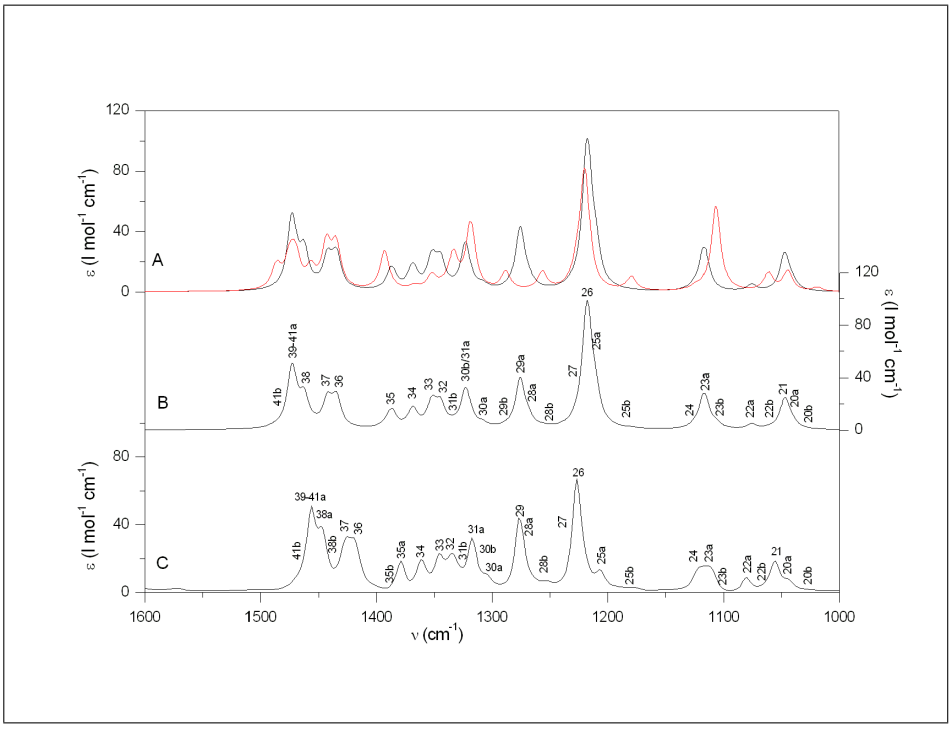


**Figure 8.5:** A)Calculated (B3PW91/TZ2P) IR spectra of both conformers of R-(+)-methylcyclohexanone (black: equatorial conformer, red: axial conformer), B) assignment of the Boltzmann weighted spectrum (labels a and b refer to the equatorial and axial conformer respectively)and C)assignment of the experimental IR spectrum of R-(+)-methylcyclohexanone in $CDCl_3$.

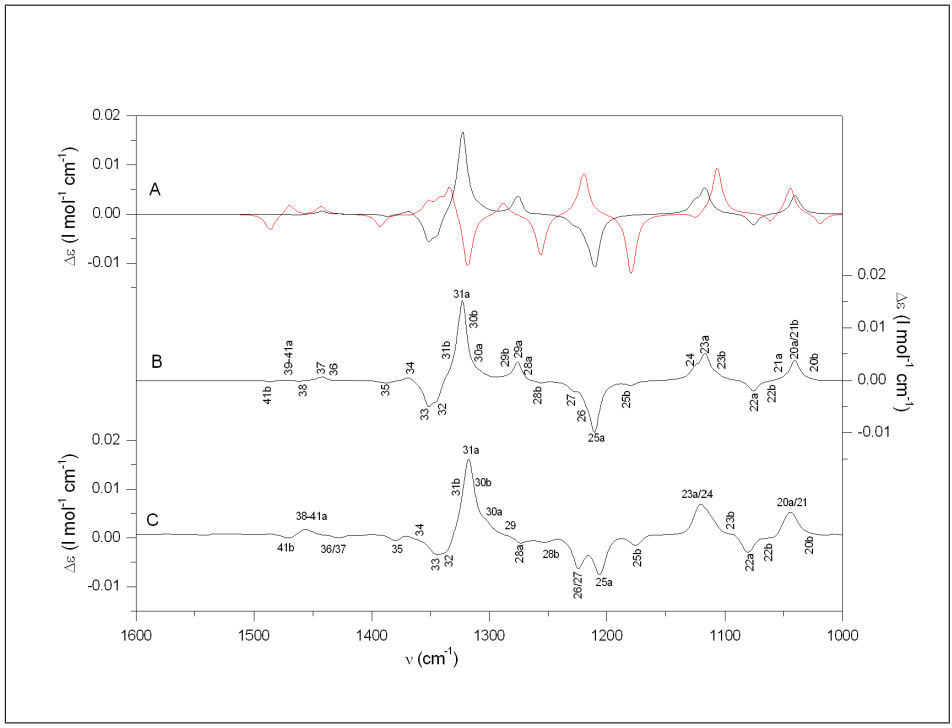


**Figure 8.6:** A) calculated (B3PW91/TZ2P) VCD spectra of both conformers of R-(+)-methylcyclohexanone (black: equatorial conformer, red: axial conformer), B) assignment of the Boltzmann weighted spectrum (labels a and b refer to the axial and equatorial conformer respectively) and C)assignment of the experimental VCD spectrum of R-(+)-methylcyclohexanone in $CDCl_3$.

### Temperature study of the IR and VCD spectra

In order to facilitate the assignment, the conformational freedom needs to be as low as possible. In the ideal case the experimental spectrum is formed only by the most stable conformation. This situation can be approximated by measuring the spectra at low temperatures. The bands attributable to the axial conformation should become smaller while those of the axial conformation are assumed to gain importance. The magnitude of the effects depends on the energy difference between the conformations. For measurements in $CDCl_3$ the IR spectra, shown in Figure 8.7, were recorded at ambient temperature (298K), 243K and at 213K. Almost all bands increase in intensity, because of the higher density at lower temperature. The bands originating from normal modes 20b, 25b and 28b, however, are less explicit at lower temperatures. Unfortunately, the temperature effects are rather small.

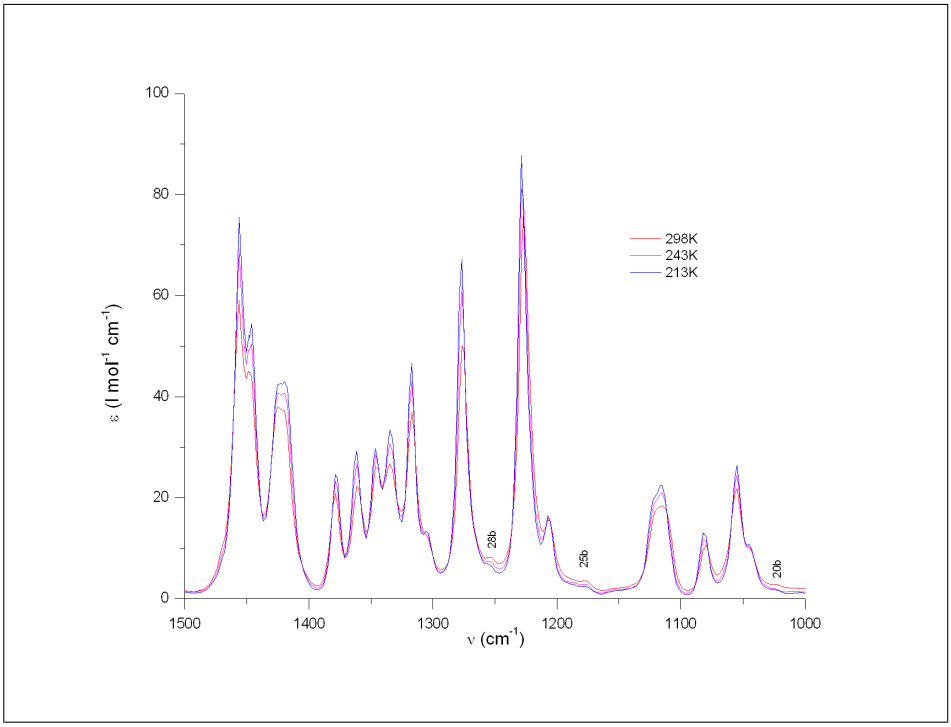


**Figure 8.7:** Comparison of the experimental IR spectra of R-(+)-3-methylcyclohexanone in $CDCl_3$, recorded at various temperatures.

IR measurements of R-(+)-3-methylcyclohexanone in xenon are shown in Figure 8.8. Temperatures were varied from 203K to 178K. In these spectra the peaks are much better resolved and additional information about the location of the bands was obtained. Fundamental 23b can be separated from the normal mode 23a. Bands 31, 35 and 38, originating from the axial conformer are also visible. The temperature effects are rather small. All bands increase in intensity except for band 23b, that now is clearly separated from band 23a. The other bands originating from the less stable conformer are too small to yield any observable effect.

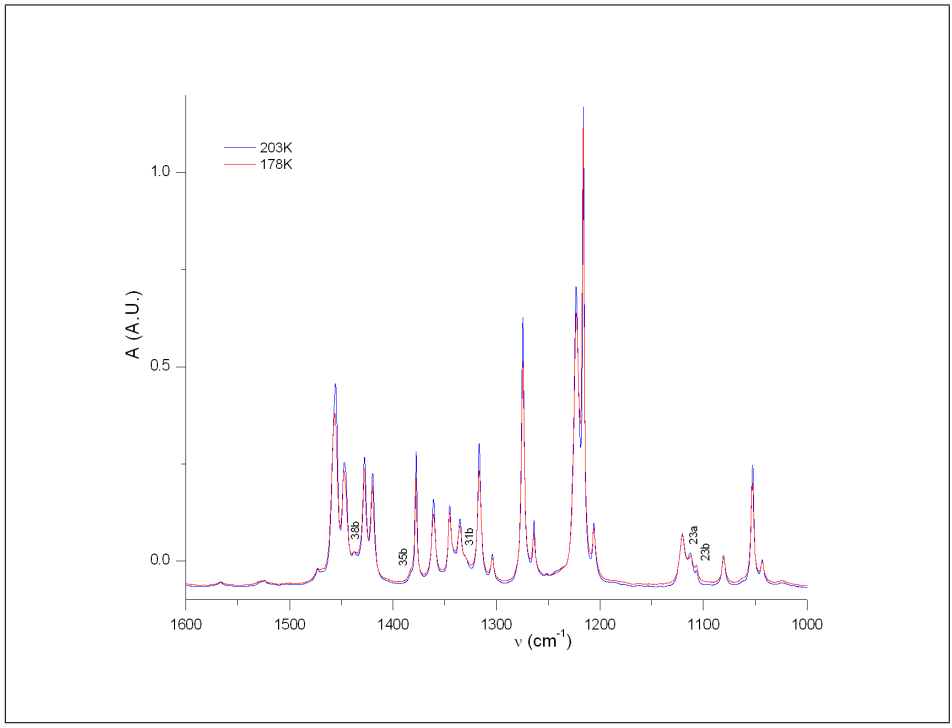


**Figure 8.8:** IR measurements of R-(+)-3-methylcyclohexanone in liquid xenon at various temperatures. (A.U. = Absorbance Units)

The influence of temperature on the VCD spectra was studied in different solvents at different temperatures. The first measurements were performed in $CDCl_3$ at a minimum temperature of 223K. The differences between the spectra, recorded at ambient temperature (298K) and 223K are rather small and it is difficult to assign the changes to temperature

effects or noise. However, it can be concluded that for all bands the intensity increases except for the bands assigned as 25b and 28b. Normal modes 32 and 33 become separable at 223K. The spectra are shown in Figure 8.9.

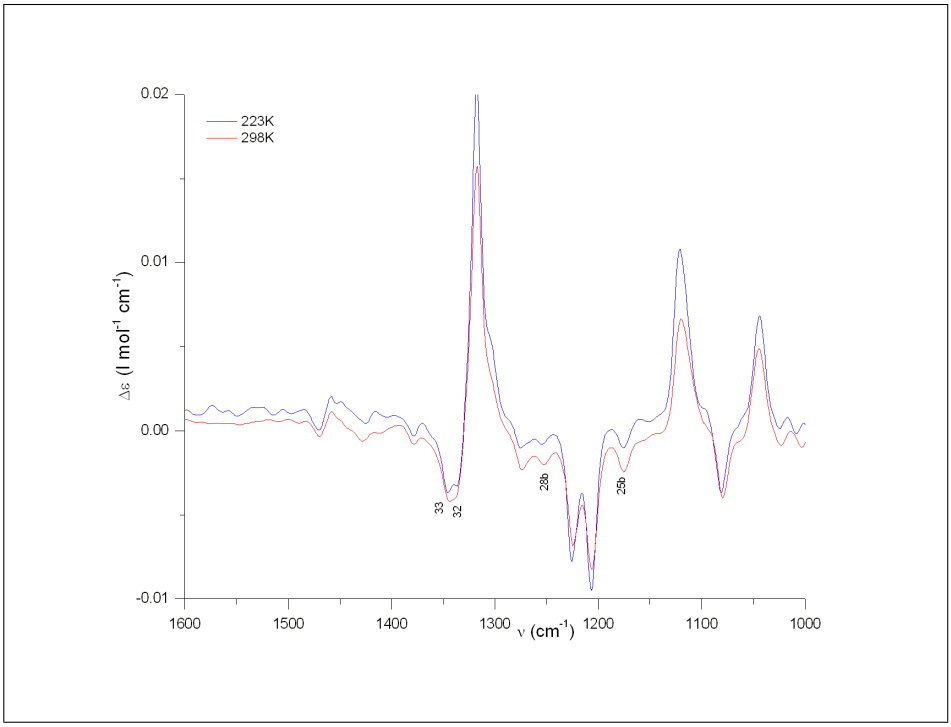


**Figure 8.9:** Comparison of the experimental VCD spectra of R-(+)-3-methylcyclohexanone in $CDCl_3$ at various temperatures.

The temperature effects are more notable for the VCD measurements of R-(+)-3-methylcyclohexanone in $CD_2Cl_2$. The minimum temperature is 183K. The same trends as in $CDCl_3$ are visible, but also additional effects are observed. The intensity of normal mode 28b decreases, while band 28a increases remarkably. The intensity of band 26/27 increases faster than that of band 25a. This can be explained by the fact that the large positive rotational strength of fundamental 26b becomes less important and the overall band will become more negative.

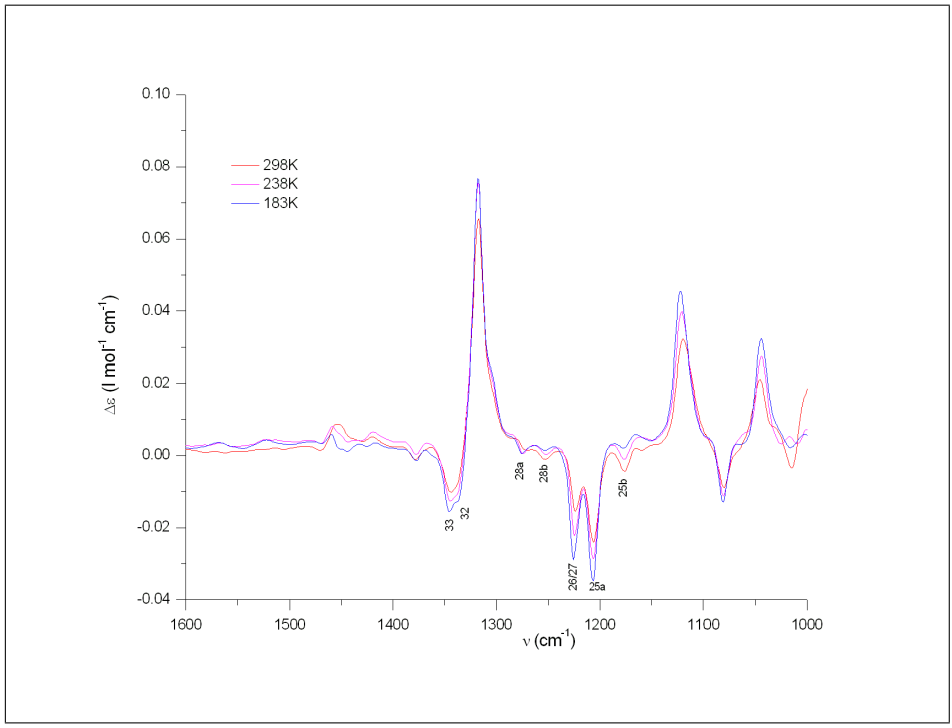


**Figure 8.10:** Comparison of the experimental VCD spectra of R-(+)-3-methylcyclohexanone in $CD_2Cl_2$ at various temperatures.

In $CS_2$ a minimum temperature of 173K was reached. The same trends are visible as for measurements in $CD_2Cl_2$. The spectra in $CD_2Cl_2$ and $CS_2$ are shown in Figure 8.10 and Figure 8.11 respectively.

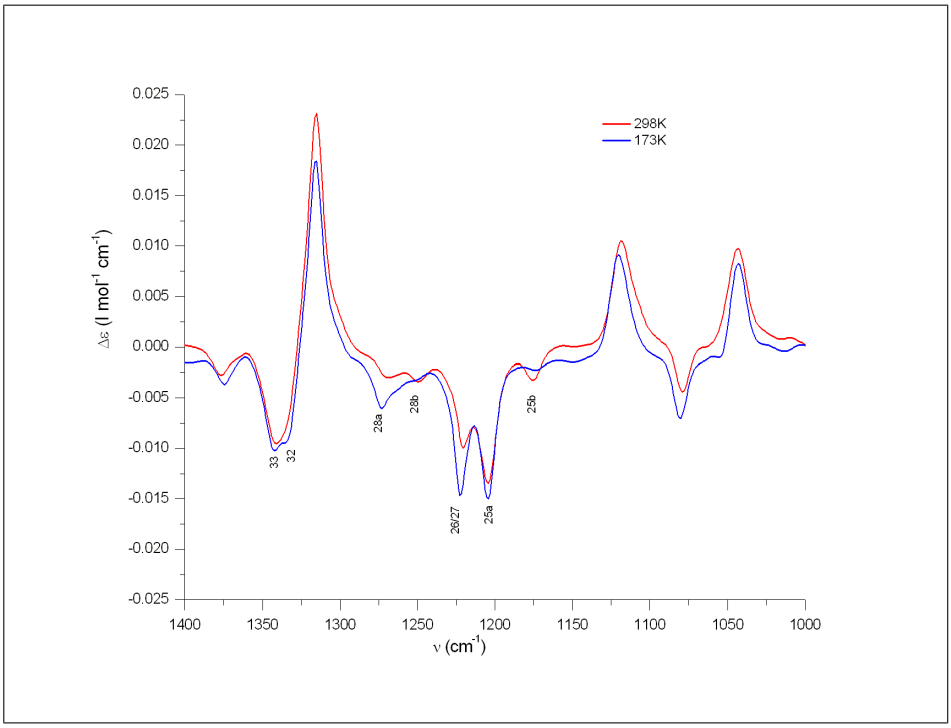


**Figure 8.11:** Comparison of the experimental VCD spectra of R-(+)-3-methylcyclohexanone in $CS_2$ at various temperatures.

### Extraction of the Boltzmann population from the experimental spectra

Up to here Boltzmann populations were determined by the enthalpy or Gibbs free energy differences obtained from the ab initio calculations. Hindered rotation [166], however, can cause some errors in the calculations of the entropy [81]. An alternative method is to compare the dipole or rotational strengths, obtained for bands identifiable with a single mode of one conformer to the corresponding calculated values. This was already done for R-(+)-3-methylcyclohexanone by Devlin and Stephens [165]. Assuming equal accuracy of the calculated dipole strengths of the two conformers, the ratio of the slopes of the linear fits of both conformers equals the ratio of their populations, i.e., the conformational equilibrium constant (K). The slopes of the two trend lines are 0.85 and 0.21 for the equatorial and axial conformation respectively. A $\Delta G^0$ of 0.83 kcal/mol was obtained, through the equation:

$$\Delta G^0 = -RTln(K) \tag{8.1}$$

This corresponds with the following Boltzmann populations: w(eq)= 0.80 and w(ax)=0.20. The same method can be used for VCD spectra. The obtained value for $\Delta G^0$ is 1.08 kcal/mol (w(eq) = 0.86 and w(ax) = 0.14). The major problem with this method is that only a very small number of bands are sufficiently resolved to extract the dipole or rotational strengths for both conformations. The linear fits are shown in Figure 8.12 and Figure 8.13.

Another way to obtain the Boltzmann populations is the construction of a Van 't Hoff plot [167], in which change of temperature is related to the change in equilibrium constant for the conversion between the two conformers. Assuming that the enthalpy change is constant with temperature:

$$ln\left(\frac{K_2}{K_1}\right) = -\frac{\Delta H^0}{R}\left(\frac{1}{T_2} - \frac{1}{T_1}\right) \tag{8.2}$$

In this case, the equilibrium constant at a given temperature is described by the intensities of the bands that solely originate from one conformer. Considering the xenon measurements at different temperatures (203K, 193K, 183K and 173K) various combinations could be studied: 20a-23b, 22a-23b, 30a-23b and 38a-23b. The mean value for

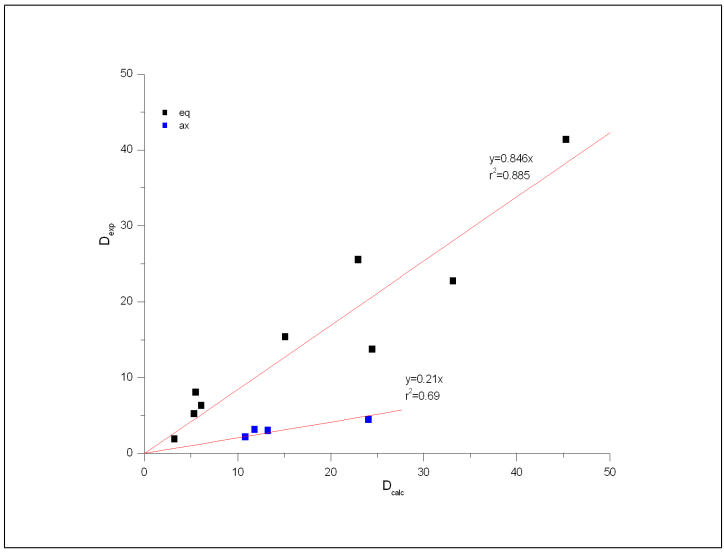


**Figure 8.12:** Comparison of the calculated and experimental dipole strengths (D in $10^{-40}$ $esu^2$ $cm^2$). The black scatters denote fundamentals of the equatorial conformation. Fundamentals 20a, 22a, 25a, 28a, 29a, 30a, 31a, 35a and 38a were used. The blue scatters denote fundamentals originating from vibrations of the axial conformer. Hereto fundamentals 25b, 28b,31b and 38b were used.

$\Delta H^0$ (at 203K) is 1.5 kcal/mol. The corresponding Boltzmann populations are 0.9284 and 0.0716 for the equatorial and axial conformation respectively. The Van 't Hoff plots are shown in Figure 8.14.

A last possibility is a method proposed by Durig [168]. The enthalpy difference $\Delta H^0$ between the conformers is calculated, utilizing a single temperature and the predicted IR intensities from the DFT calculations. The enthalpy difference is then determined by the equation:

$$\Delta H^0 = -kTln\left[\frac{g_{eq} * I_{ax} * \epsilon_{eq}}{g_{ax} * I_{eq} * \epsilon_{ax}}\right] \tag{8.3}$$

in which $g$ represents the degeneracy of each conformation and $I$ is the experimental IR intensity. To obtain the experimental intensities, the area under the band needs to be calculated. $\epsilon$ equals the calculated IR intensity. The same combinations of bands were used as in the Van 't Hoff plot. The mean value of $\Delta H^0$ (at 203K) is 1.5 kcal/mol. This value corresponds to Boltzmann populations of 0.92 and 0.08 for the equatorial and axial conformations respectively. Additional data are given in Table 8.2.

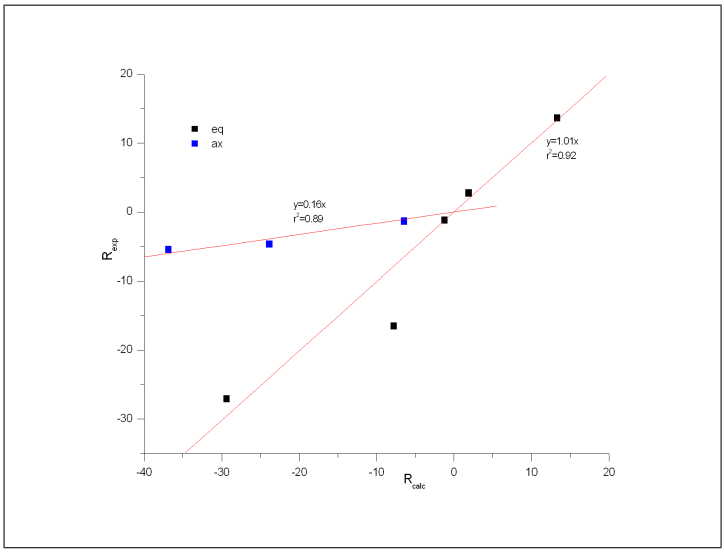


**Figure 8.13:** Comparison of the calculated and experimental rotational strengths (R in $10^{-44}$ $esu^2$ $cm^2$). The black scatters denote fundamentals of the equatorial conformation. Fundamentals 20a, 22a, 25a, 30a, and 35a were used. The blue scatters denote fundamentals originating from vibrations of the axial conformer. Hereto fundamentals 25b, 28b and 35b were used.

Although the results between the three methods are somewhat different, the same conclusions can be drawn. The equatorial conformer is the most stable one, having a Boltzmann population of around 90%. This also is in line with the Boltzmann populations obtained from the DFT calculations.

### 8.2.5 Conclusions

3-Methylcyclohexanone has two stable conformations. The equatorial conformer is the dominant one. This was also proved by comparing the experimental IR and VCD spectra with those calculated for both conformations. The experimental spectra shows the best agreement with the calculated spectra of the equatorial conformer. However not every band could be assigned to this conformer. A mixed spectrum of the equatorial as well as the axial conformer was needed to explain every band of the experimental spectrum. Hereto the Boltzmann populations, extracted from the ab initio calculations, were used. In the IR spectrum

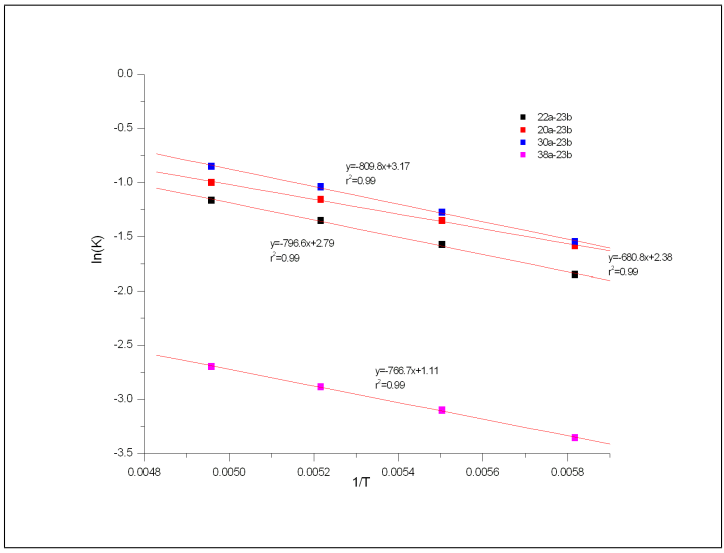


**Figure 8.14:** Van 't Hoff plots for various combinations of bands.(T in K)

**Table 8.2:** The data, necessary to work out the equation proposed by Durig. I equals the experimental Intensity and D refers to the calculated dipole strengths (in $10^{40}$ $esu^2$ $cm^2$). ($\Delta H^0$ in kcal/mol)

| *bands* | $I_{eq}$ | $I_{ax}$ | $D_{eq}$ | $D_{ax}$ | $\Delta H^0$ |
|---|---|---|---|---|---|
| $20a-23b$ | 0.35 | 0.13 | 6.10 | 72.69 | 1.43 |
| $22a-23b$ | 0.41 | 0.13 | 5.51 | 72.69 | 1.52 |
| $30a-23b$ | 0.30 | 0.13 | 3.23 | 72.69 | 1.53 |
| $38a-23b$ | 1.58 | 0.13 | 22.96 | 72.69 | 1.44 |

the assignment of the bands was done in an unambiguous way. The measurements in xenon gave additional information about the frequencies of the fundamentals of both conformers. This knowledge was useful to assign the bands in the VCD spectrum, which was done quite easily for frequencies smaller than 1400 $cm^{-1}$. For the axial conformer, only two fundamentals could be distinguished from the bands originating from the equatorial conformer. A temperature study in $CDCl_3$, $CD_2Cl_2$ and $CS_2$ revealed that these bands decrease in intensity at lower temperatures. This confirms that the contribution of the less stable conformers declines with decrease of temperature. The few trends were well reproduced for each solvent and could all be explained by the ab initio calculations.

Unfortunately, the effects are rather small, due to the fact that even at room temperature the contribution of the axial conformer is already minimal. In order to obtain more noticeable temperature effects, it is necessary to find a molecule for which the energy difference between the different conformers is somewhat smaller. Moreover it is required that the spectrum contains totally resolved bands for each conformer.

There are several ways to determine the Boltzmann populations of each conformer to verify the reliability of the ab initio calculations. The major problem of each of these methods is that no fundamental of the axial conformation is completely separated from the corresponding fundamental of the equatorial conformation. This leads to an uncertain fitting procedure. The Van 't Hoff plots, however, and the method proposed by Durig gave values that agree well with the ab initio calculations. The values of the Boltzmann populations obtained by the methods, described above, differ from the ab initio calculations by about 10%.

## 8.3 The influence of temperature on the IR and VCD spectrum of borneol

### 8.3.1 Introduction

Due to their strong VCD signal, low price and large stability, terpenes are widely used for calibrating vibrational optical activity measurements. Simulated and experimental band shapes are routinely compared to test calculational procedures. Borneol is one of those terpenes for which the VCD spectrum was already studied elaborately [38] and is now widely used as a test molecule [73, 27], especially for the simulation of real-time reaction monitoring [169, 170].

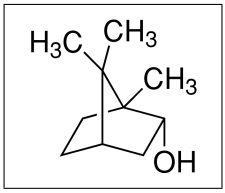


**Figure 8.15:** structure of (-)-borneol

Due to the flexibility of the OH group and, at the same time, conformational simplicity, borneol was chosen to study the influence of temperature on its VCD spectrum. As stated before, recording the spectra at lower temperature is assumed to facilitate the assignment. In the ideal case, at lower temperatures, only the most stable conformer has to be taken into account during the calculations. Unfortunately, in case of borneol, another phenomenon will have to be considered at lower temperatures. As is well known, intermolecular hydrogen bonding between alcohols is strong and solutions of alcohols exhibit aggregation with decreasing temperature or increasing concentration. This, in turn, will complicate the simulation of the vibrational spectra. The problem was skirted in a previous study by Stephens et al. [121],by transforming the alcohol function of borneol to its methyl, acetate, *tert*-butyl and trimethylsilyl derivates. In this study, however, the challenge will be accepted to simulate every feature observed at lower temperatures. As self-association considerably influences the conformational and vibrational properties of the molecules, a suitable model has to be used when computing IR and VCD spectra. The effect of dimerization, re-

cently has been investigated in detail, especially for carboxylic acids [171, 127, 126]. Izumi et al. [129] studied the VCD spectrum of (R)-thalidomide and suggested a dimer form. For the carboxylic acids as well as thalidomide, cyclic dimers were formed. The modeling of the dimers of alcohols, however, is less straightforward. In analogy with a paper of Cappelli et al. [153] the intermolecular hydrogen bond was simulated by considering all possible combinations between the stable conformers, found during conformational analysis of free borneol.

Both monomers and dimers were necessary to explain the observed temperature effects. Even at room temperature the dimers have to be taken into account in order to assign each band of the IR and VCD spectrum.

### 8.3.2 Experimental

(-)-Borneol was purchased from Fluka with more than 99.0% ee and was used without further purification. The solvents $CDCl_3$ (99.8%) and $CD_2Cl_2$ (99.6%) were obtained from Aldrich and Acros respectively. The VCD spectra were recorded on a Bruker IFS 66/S FTIR spectrometer, coupled to a Bruker PMA37 VCD module. A demountable cell with $CaF_2$-windows and 100 $\mu$m path length was used. Samples of (-)-borneol were prepared in $CDCl_3$ and $CD_2Cl_2$ at concentrations varying from 0.1 M to 2.0 M. The unpolarized IR absorbance spectra were measured at a resolution of 4 $cm^{-1}$, while the VCD spectra were recorded with a resolution of 6 $cm^{-1}$. During VCD experiments, a 1800 $cm^{-1}$ long wave pass filter was introduced to improve the S/N ratio between 1000 $cm^{-1}$ and 1800 $cm^{-1}$. The collection time was set to 1.5 h, using six blocks of 15 min. To obtain an estimate of the baseline artefacts, the VCD spectra of the solvents were recorded, in the same conditions as the sample. For the measurements at lower temperature, the adapted experimental setup, described above, was used. The samples were at a concentration of 0.8.

### 8.3.3 Computational Methods

The potential energy surface of the monomer of borneol was thoroughly analyzed to find the lower energy minima. A conformational analysis was done using the MM3 [108, 107] stochastic search method and a sys-

tematic search using the MMFF[109, 110] force field. All unique minima were subsequently optimized at the B3LYP/6-311+G(d,p) level, using Gaussian03 [55]. Modeling the dimers, however, is not straightforward. Two borneol molecules can approach in an infinite number of ways. Therefore, all possible combinations between the minima, found for the monomer, were considered and optimized at the B3LYP/6-311+G(d,p) level. Subsequently, for each optimized structure, the frequencies, dipole and rotational strengths were calculated. For comparison with the experimental spectra, these data were combined in a Boltzmann weighted manner and broadened with a Lorentzian FWHM of 10 $cm^{-1}$. A scaling factor of 0.967 is used to correct for the harmonic approximation [172].

### 8.3.4 Results and Discussion

#### Assignment of the IR and VCD spectra

During conformational analysis of (1*S*,2*R*,4*S*)-borneol, three unique minima were found. As for all alcohols, the OH-group can rotate relatively freely around the adjacent C-O bond, causing the multiple conformations. The three minima can therefore be described by the dihedral angle around the C-O bond, as $gauche^-$ and $gauche^+$ and $trans$. Their relative enthalpies and corresponding Boltzmann weights can be found in Table 8.3. The comparison of the weighted IR spectrum with the experimental spectrum of (-)-borneol in $CDCl_3$ is depicted in Figure 8.16. Allowing for the expected small shift to higher frequency, the calculated spectrum is in good qualitative agreement with the experimental spectrum.

**Table 8.3:** The Boltzmann weights (in %) of the conformers of borneol, together with their relative enthalpies (in kcal/mol).

| $Conformer$ | $torsion$ | $\Delta H^0$ | $w$ |
|---|---|---|---|
| $A$ | $gauche^-$ | 0.00 | 47.5 |
| $B$ | $gauche^+$ | 0.14 | 37.4 |
| $C$ | $trans$ | 0.68 | 15.0 |

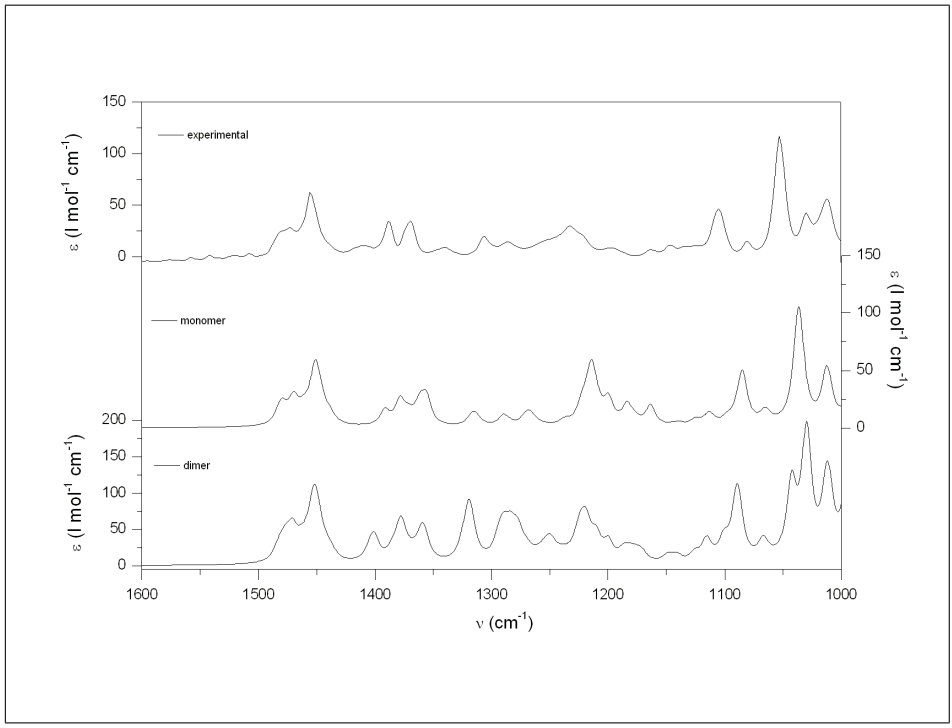


**Figure 8.16:** Comparison of the experimental IR spectrum of (-)-borneol in $CDCl_3$ with the calculated spectrum of (1*S*,2*R*,4*S*)-borneol and the spectrum simulated for the dimers.

Considering the OH-stretching region (3000 $cm^{-1}$-4000 $cm^{-1}$), however, two bands are observed. The narrow band around 3614 $cm^{-1}$ is known to originate from the OH-stretching vibration of a free borneol molecule. This also was verified through the calculations. The broader band at lower frequencies (3454 $cm^{-1}$), however, could not be assigned using the calculations of the monomer and is a proof of the existence of intermolecular hydrogen bonds. As is depicted in Figure 8.17, alcohols exhibit aggregation with increasing concentration. Therefore, it is necessary to take into account the dimers as well. All possible dimers between **A**, **B** and **C** were considered. The nine combinations were optimized and subsequently their vibrational data were calculated. Due to the presence of an imaginary frequency only eight dimers remained for the construction of the Boltzmann weighted spectra. Their relative enthalpies, as well as their Boltzmann weights can be found in Table 8.4. The weighted absorption spectrum of the dimers also is shown in

Figure 8.16. Comparing both calculated spectra, it can be observed that most of the predicted bands from the dimers coincide with those of the monomers, except for the band around 1040 $cm^{-1}$. Unfortunately, this was not the case in the experimental spectrum. Another difference is the pattern of the bands between 1250 $cm^{-1}$ and 1300 $cm^{-1}$. For this frequency range, the spectrum of the monomers is in better agreement with experiment than that of the dimers; whereas for the band around 1196 $cm^{-1}$ the dimers show a better agreement.

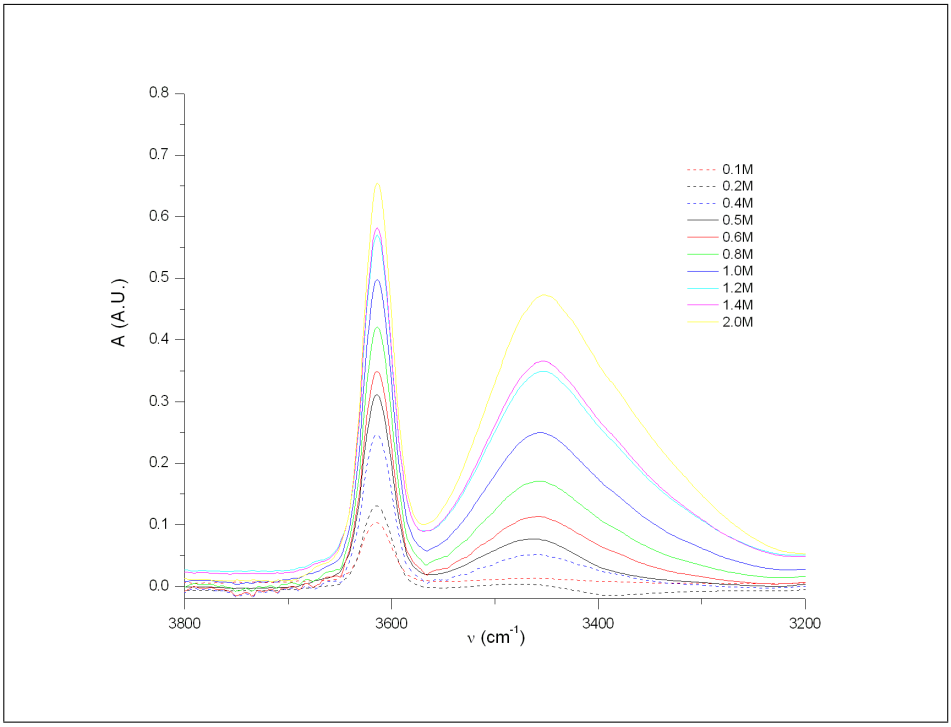


**Figure 8.17:** IR measurements of (-)-borneol in $CDCl_3$ at various concentrations.

**Table 8.4:** Boltzmann weights (in %) of the dimers, together with their corresponding $\Delta H^0$-values (in kcal/mol). The first letter in the designation of the conformers refers to the proton acceptor, while the second letter originates from the proton donor

| $Conformer$ | $\Delta H^0$ | $w$ |
|---|---|---|
| $BB$ | 0.00 | 29.5 |
| $AA$ | 0.39 | 15.4 |
| $CA$ | 0.40 | 15.1 |
| $CB$ | 0.41 | 14.9 |
| $AB$ | 0.42 | 14.6 |
| $BA$ | 0.77 | 8.0 |
| $CC$ | 1.60 | 2.0 |
| $BC$ | 2.41 | 0.5 |

To interpret the experimental IR and VCD spectra in terms of the DFT results the conformational populations need to be assessed for both monomers and dimers. The theoretical populations based on the enthalpy differences between monomer and dimer structures are often largely overestimated and can only partially be corrected by introducing the counterpoise method for the evaluation of the basis set superposition error (BSSE) [173]. Nonetheless, information on the fractions can also be revealed by studying the concentration dependence of the IR band intensities. The procedure, described by Chen et al. [174] and adopted earlier by Kuppens et al. [126] determines the equilibrium constant between the monomers and dimers by analyzing the integrated absorbance as a function of the analytical concentration of the dissolved species. The equilibrium for dimerization $M + M \rightleftharpoons D$ is characterized by the dimerization constant $\mathrm{K} = [\mathrm{D}]/[M]^2$. In this approach $c^0/A_m^2$ was plotted versus $A_m^{-1}$ in order to fit the experimental data to the following equation:

$$\frac{c^0}{A_m^2} = \frac{1}{\epsilon_m l}\frac{1}{A_m} + \frac{2K}{(\epsilon_m l)^2} \tag{8.4}$$

$c^0$ refers to the analytical concentration of the dissolved species, $A_m$ and $\epsilon_m$ respectively are the integrated absorbance ($A = \epsilon cl$) and molar absorptivity of a distinct monomer band and $l$ is the path length (0.01 cm). Since in the region between 1000 $cm^{-1}$ and 2000 $cm^{-1}$ no distinct monomer band was found (see below), the band at 3615 $cm^{-1}$,

originating from the free OH-stretching vibration, was fitted in order to determine the value for $A_m$ at a certain $c^0$. The integrated intensities of the monomer band, obtained by Lorentzian fitting are given in Table 8.5. Subsequently $c^0/A_m^2$ was plotted versus $A_m^{-1}$. The dimerization constants can then be determined with Equation 8.4 on the basis of the intercept and the slope of the linear fit. The equilibrium constant, K ($M^{-1}$), was determined to be 3.8, which corresponds to a $\Delta G^0$ of -0.8 kcal/mol.

**Table 8.5:** The integrated intensities (A.U.) of the free OH stretching band at various analytical concentrations ($c^0$ in M) in $CDCl_3$.

| $c^0$ | $A$ |
|---|---|
| 0.1 | 3.87 |
| 0.2 | 6.25 |
| 0.4 | 10.70 |
| 0.6 | 12.38 |
| 0.8 | 14.24 |
| 0.9 | 18.90 |
| 1.0 | 19.83 |
| 1.2 | 21.46 |
| 1.4 | 22.09 |

The fraction of monomer ($f_m$) and fraction of dimer ($f_d$) can be calculated using the following expressions:

$$f_d + f_m = 1 \tag{8.5}$$

$$f_m^2 = f_d \frac{1}{2Kc^0} \tag{8.6}$$

In Figure 8.18 the fractions of monomers and dimers are plotted as a function of $c^0$. At an analytical concentration of 0.8 M, giving an optimal VCD S/N ratio, dimer and monomer coexist in solution; their fractions are: $f_m$=0.43 and $f_d$=0.57. Based on these values, the populations for the different conformations were determined, taking into account the Boltzmann populations based on the relative enthalpies of each subgroup (monomers and dimers) of structures. During this analysis some approximations were made. Possible solute-solvent interactions

were not taken into account. Neither was the formation of trimers and tetramers. Considering these approximations and the limitations of the fitting procedure, the error on the populations is expected to be on the order of 10% - 15%. However, exact populations were not pursued in this study. Their values were merely estimated as well as possible in order to allow the assessment of experimental IR and VCD in terms of DFT results.

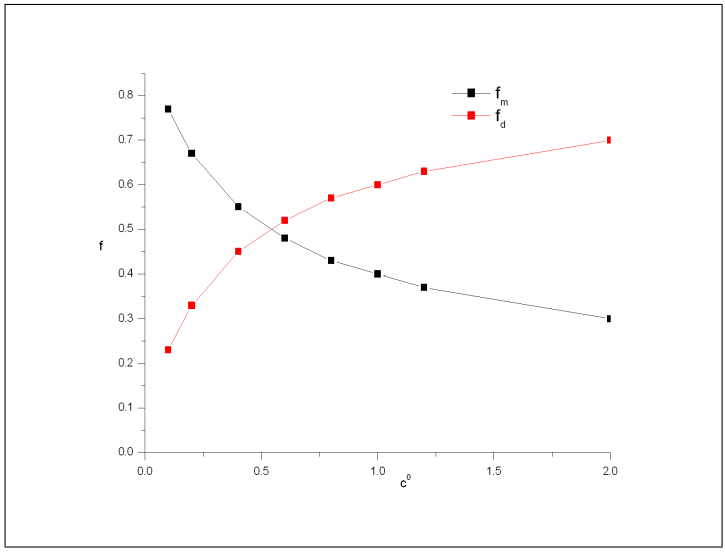


**Figure 8.18:** Fractions of monomers ($f_m$) and dimers ($f_d$) based on experimentally determined values of dimerization equilibrium constants.

In Figure 8.19 the simulated IR spectrum, averaged over all significant monomers and dimers, is compared with the experimental spectrum. The numbers in red refer to the normal modes of the dimers, whereas the black numbers correspond with the normal modes of the monomers. There is a large overall agreement.

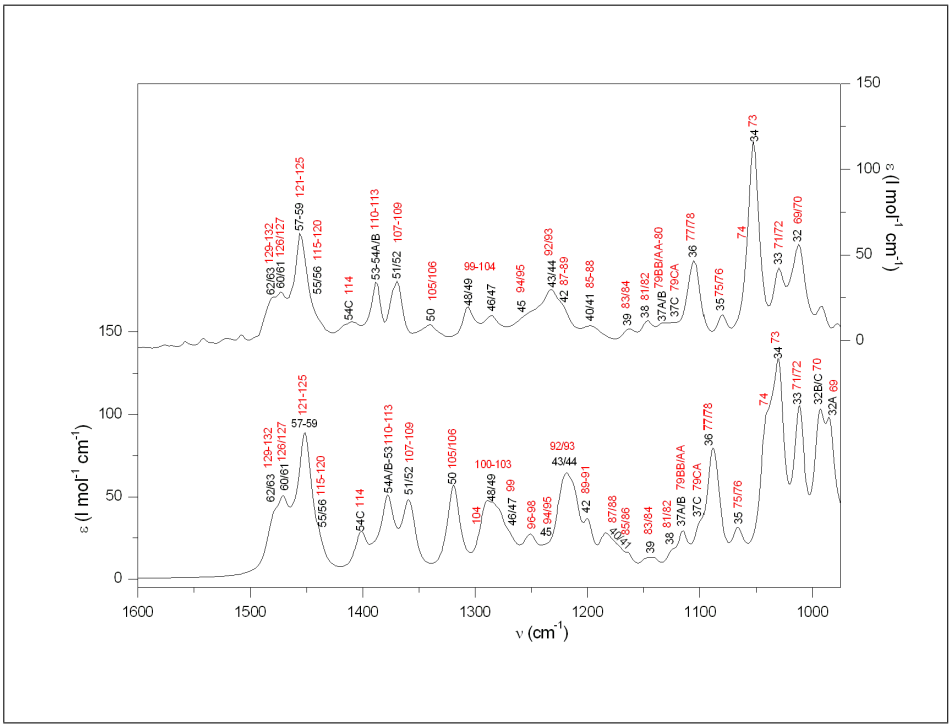


**Figure 8.19:** Comparison of the experimental IR spectrum of (-)-borneol in $CDCl_3$ (top) with the simulated spectrum averaged over the monomers and dimers (bottom). The red normal modes originate from the dimers.

Subsequently, the VCD measurement of (-)-borneol in $CDCl_3$ was considered. In Figure 8.20, the experimental VCD spectrum is compared with the predicted spectrum of the monomers of (1*S*,2*R*,4*S*)-borneol and that of its dimers. For the assignment of the bands, the experimental spectrum was compared to the simulated VCD spectrum, averaged over all significant monomers and dimers. This is shown in Figure 8.21. Again there is a large overall agreement between both spectra. As is the case for the IR spectrum, in the experimental VCD spectrum band 74 cannot be distinguished from band 34/73. In the calculated spectrum band 50/105/106 seems to be overestimated compared with the experimental spectrum. In the frequency range from 1300 $cm^{-1}$ to 1450 $cm^{-1}$ the pattern of the experimental bands is mainly determined by the dimers. The calculated spectrum of the monomers shows very small signals in that region.

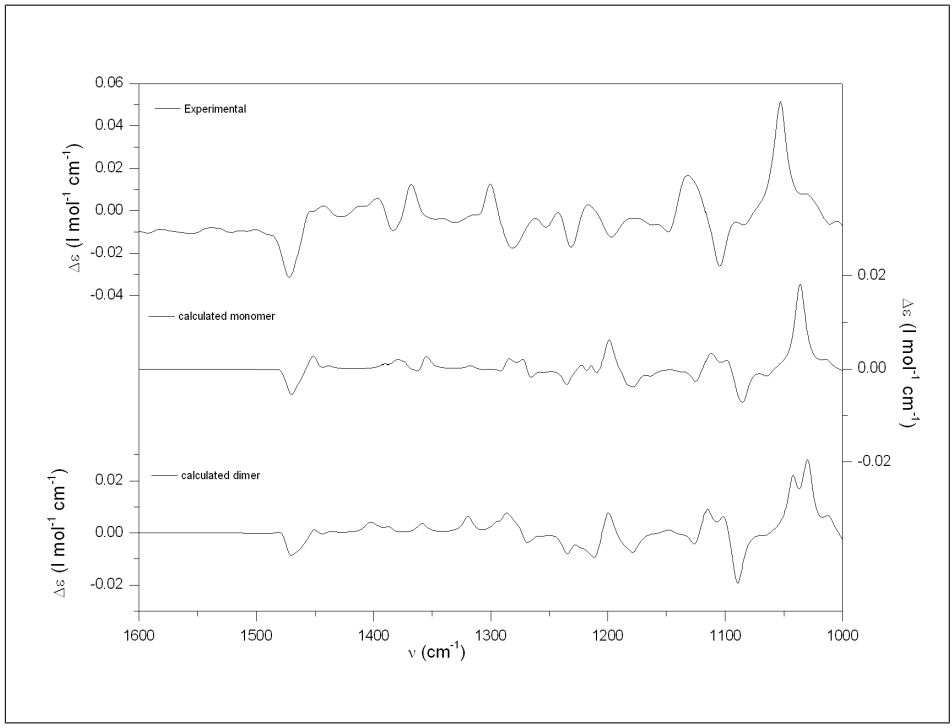


**Figure 8.20:** Comparison of the experimental VCD spectrum of (-)-borneol in $CDCl_3$ with the calculated spectra of the monomers and dimers.

Taking into account these approximations that are used to determine the monomer and dimer populations to simulate their IR and VCD spectra, a quantitative comparison of simulated and experimental spectra would be unreliable. In this study, the situation is even more complex because of the fact that not only bands of different conformations, belonging to one species coincide, but also bands from dimer conformations can overlap with bands of the monomer conformations. Therefore no quantitative comparison will be made. However the qualitative assignment of the bands will be used to explain the effects, observed during the temperature study of the IR and VCD spectra.

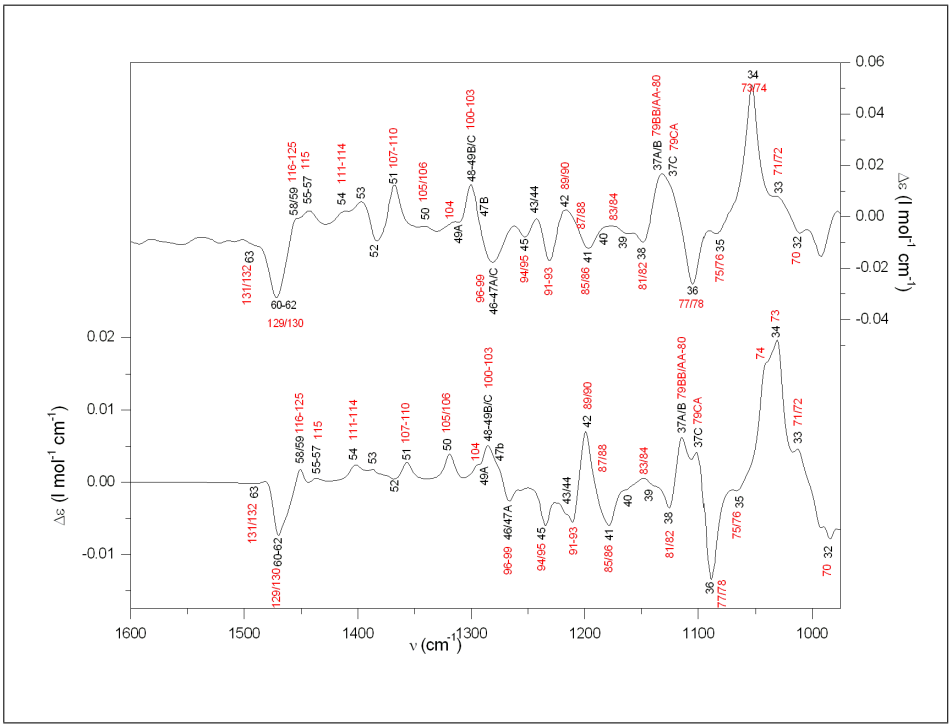


**Figure 8.21:** Comparison of the experimental VCD spectrum of (-)-borneol in $CDCl_3$ with the simulated spectrum, averaged over monomers and dimers. The red normal modes originate from the dimers.

### Temperature study of the IR and VCD spectra

As described above various solvents ($CDCl_3$ and $CD_2Cl_2$) were used in order to reach different minimal temperatures.

**IR spectra**: First, the measurements in $CDCl_3$ were considered. The spectra were recorded at various temperatures: 298 K, 273 K, 248 K and 223 K. In the OH-stretching region, it is observed (in Figure 8.22), that as temperature decreases, the intensity of the band originating from the hydrogen-bonded OH-stretch increases while that from the free OH band is reduced. Moreover, at lower temperatures, both bands are red shifted. This remarkable increase in intensity of the H-bonded OH-stretching band, indicates that as temperature is decreased, intermolecular interaction between the OH-functions gains importance. This is in line with the principle of "Le Chatelier", because the reaction $M + M \rightleftharpoons D$ is known to be exothermic. In Figure 8.23, the region between 1000 $cm^{-1}$ and 1600 $cm^{-1}$ was brought into focus and the observed effects will be discussed. At lower temperatures an additional band appears around 1020 $cm^{-1}$ and its intensity becomes larger than that of the band around 1013 $cm^{-1}$ leading to a greater resemblance with the predicted pattern of the dimers. At room temperature the band is more similar to the predicted pattern of the monomer. For the band at 1056 $cm^{-1}$, however, band 74 still is not separable from band 34/73 at 223 K. With decreasing temperature, the band at 1105 $cm^{-1}$ is blue shifted to 1109 $cm^{-1}$, which is in line with the fact that the predicted frequency of band 36 (1087 $cm^{-1}$) is somewhat lower than that of band 77/78 (1090 $cm^{-1}$). Band 37A/B - 79BB/AA - 80 increases a lot in intensity, while the intensity of band 37C - 79CA is slightly reduced with decrease of temperature. This is explained by the fact that, at lower temperatures, the contributions of the less stable conformers, such as C and CA, decrease, while the stable conformers gain importance. Another effect is that the band around 1232 $cm^{-1}$ is blue shifted to 1236 $cm^{-1}$. This again is due to the fact that the frequency of band 43/44 (1212 $cm^{-1}$) is somewhat lower than the frequency of band 92/93 (1223 $cm^{-1}$). For the measurement at 223 K, the pattern of the bands between 1250 $cm^{-1}$ and 1320 $cm^{-1}$, is different than for the spectra, recorded at higher temperatures. At 223 K bands 96-98 become visible, as well as bands 100-104. This drastic change can be explained by the large differences

observed between the calculated monomer spectrum and the simulated dimer spectrum in that particular frequency range. The intensity of the band at 1345 $cm^{-1}$ increases remarkably with decrease of temperature. This can also be attributed to the increasing contribution of the dimers. Band 105/106 which has a considerably larger intensity than band 50, gains importance at lower temperatures. The same can be said about the intensity of the band at 1412 $cm^{-1}$ which was expected to decrease, if the contribution of the dimers was neglected.

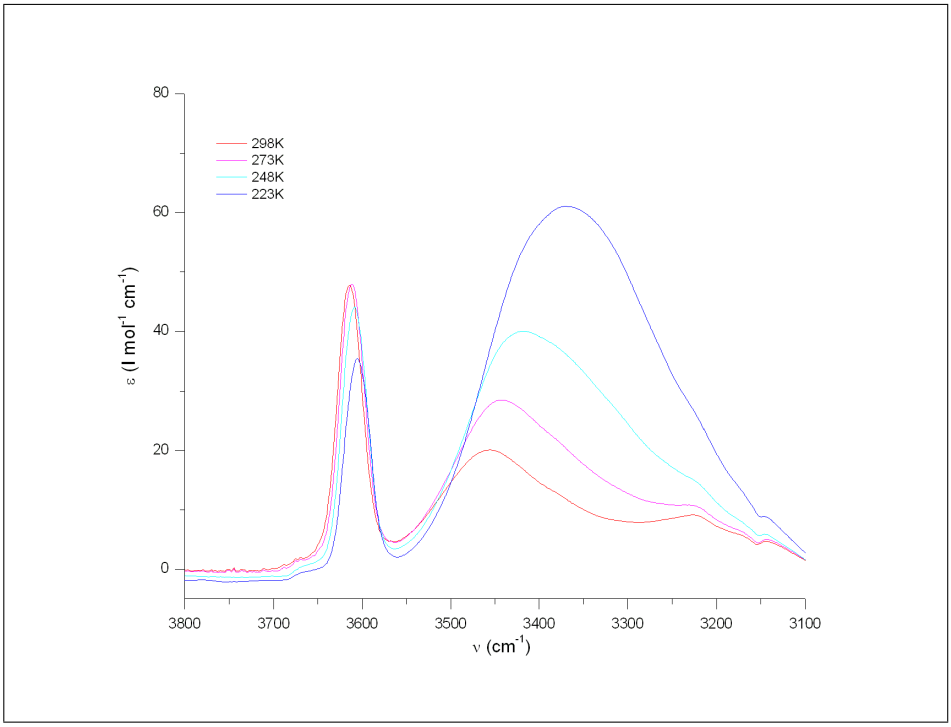


**Figure 8.22:** Comparison of the experimental IR spectra (between 3000 $cm^{-1}$ and 4000 $cm^{-1}$) of (-)-borneol in $CDCl_3$ at various temperatures.

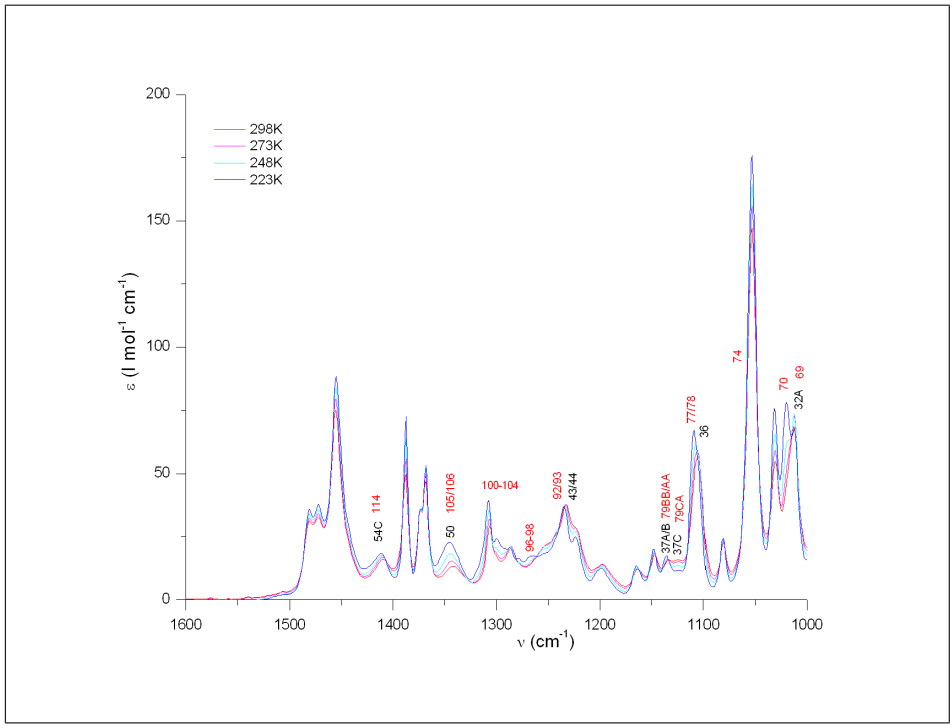


**Figure 8.23:** Comparison of the experimental IR spectra (between 1000 $cm^{-1}$ and 2000 $cm^{-1}$) of (-)-borneol in $CDCl_3$ at various temperatures.

In order to test the reproducibility of these trends, additional experiments were initiated in which $CD_2Cl_2$ was used as a solvent. For these solutions, spectra were recorded at 298 K, 273 K, 253 K, 228 K, 208 K and 183 K; these are depicted in Figure 8.24. The same trends were observed as for the measurements in $CDCl_3$. Since temperatures of 183 K could be reached, the effects are even more pronounced than for $CDCl_3$. It is striking that below 208 K the IR spectrum changes drastically. The introduction of dimers will not be sufficient to explain all features. Larger aggregates will have to be taken into account. As was stated before, these aggregates were not considered during this study.

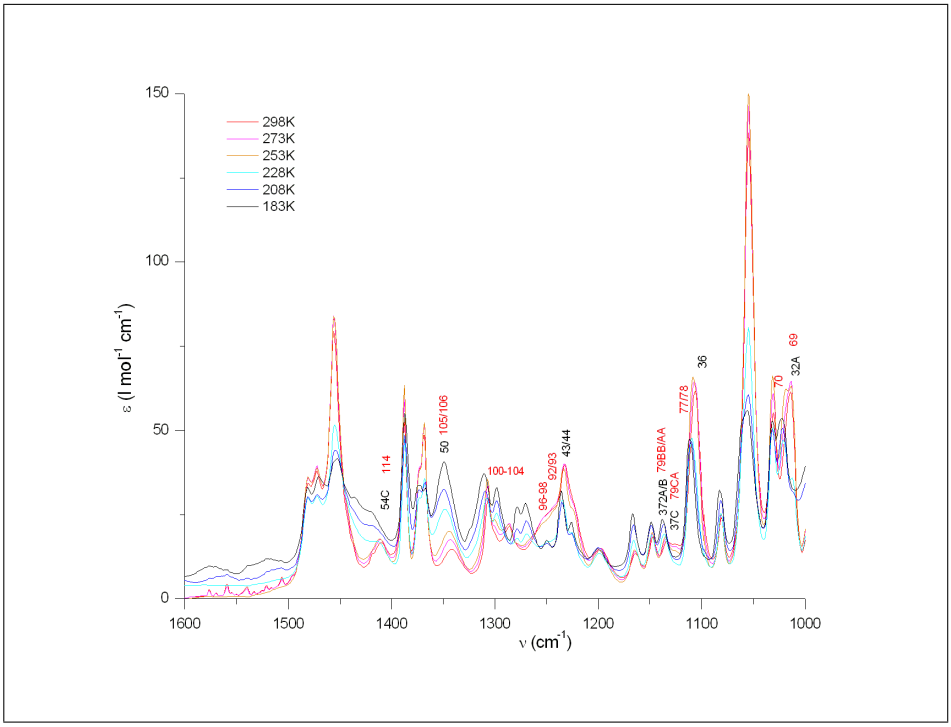


**Figure 8.24:** Comparison of the experimental IR spectra (between 1000 $cm^{-1}$ and 2000 $cm^{-1}$) of (-)-borneol in $CD_2Cl_2$ in various temperatures.

**VCD spectra**: In this section the influence of temperature on the VCD measurements in $CDCl_3$ and $CD_2Cl_2$ will be considered. For samples in $CDCl_3$ the spectra were recorded at 298 K, 258 K and 223 K. These are shown in Figure 8.25. Due to the smaller S/N ratio, the effects are less striking than for the IR spectra. But still some trends were observed.

The positive band around 1130 $cm^{-1}$ is blue shifted to 1134 $cm^{-1}$. The contribution of normal modes 37C and 79CA decreases at lower temperatures. This causes the blue shift of the band around 1130 $cm^{-1}$, originating from normal modes 37C and 79CA at lower frequency and from normal modes 37A/B and 79BB/AA-80 at higher frequency. Band 83/84 gains importance with decrease of temperature. The intensity of the positive band 43/44 decreases, proving that at lower temperatures, the contribution of the dimers increases. This also was confirmed by the noticeable increase of bands 104 and 105/106. Band 53 decreases as temperature is lowered. These observables lead again to the conclusion that dimerization is an exothermic process and that therefore the vibrational data of the dimers need to be taken into account.

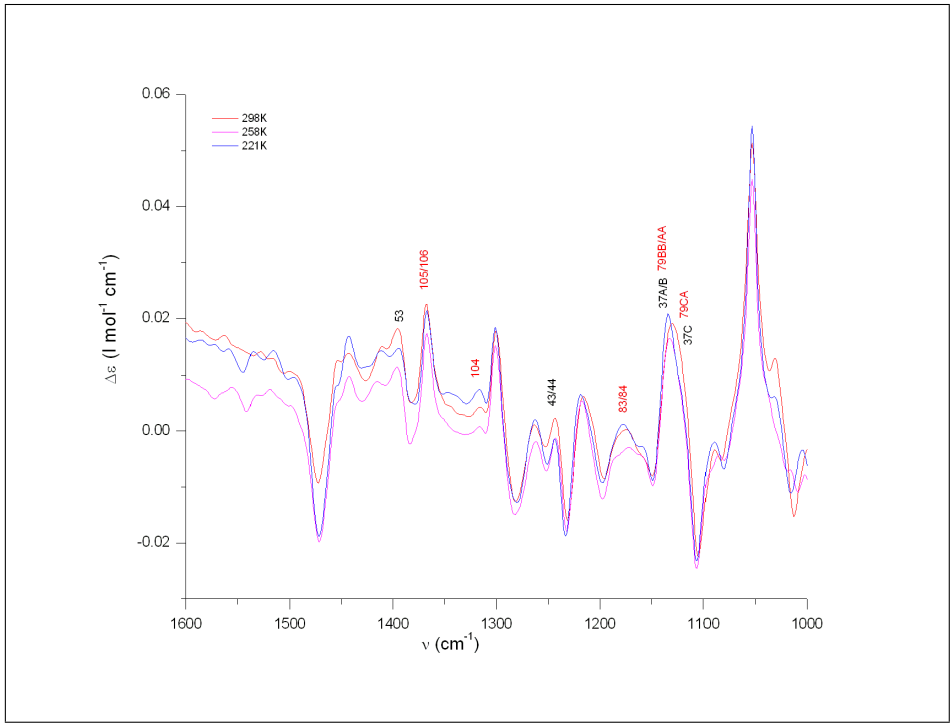


**Figure 8.25:** Comparison of the experimental VCD spectra of (-)-borneol in $CDCl_3$ at various temperatures.

The same study was done for the VCD measurements in $CD_2Cl_2$ at 298 K, 238 K and 183 K. This is shown in Figure 8.26. Measurements at 183 K gave completely different patterns, indicating that at that tem-

perature the sample will form larger aggregates. Trimers, tetramers, etc, however, have not been taken into account during the VCD calculations. Comparing the shape of the VCD spectra at 298 K and 238 K, the same trends were observed as for the measurements in $CDCl_3$, confirming the reproducibility of the temperature study.

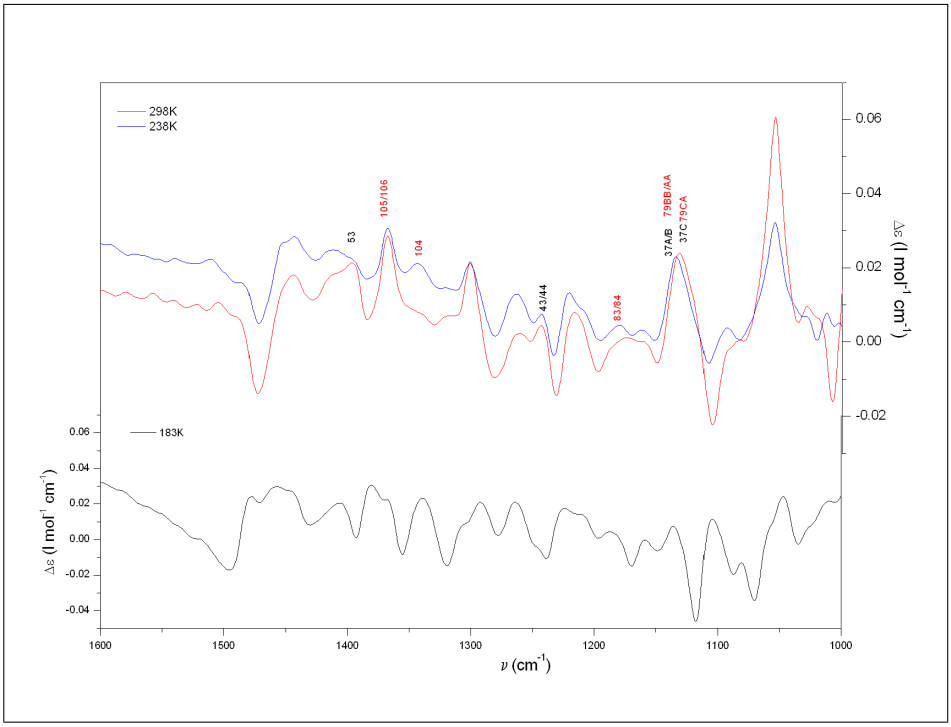


**Figure 8.26:** Comparison of the experimental VCD spectra of (-)-borneol in $CD_2Cl_2$ at various temperatures.

If dimers were not taken into account, it would have been impossible to explain every observed effect. Therefore these temperature measurements illustrate that intermolecular interactions can heavily influence the vibrational spectra and they need to be considered while analyzing the IR or VCD spectra.

Comparing the temperature study with a concentration study in $CDCl_3$ between 1000 $cm^{-1}$ and 1600 $cm^{-1}$ it is observed that, for concentrations between 0.2 M and 2.0 M, the same effects were observed. This means that the contribution of the dimers increases with increase in analytical concentration of borneol. The trends, however, are not as

explicit as for the temperature measurements, which implies that even at concentrations of 2.0 M the dimer portion is smaller than for cooled samples at a concentration of 0.8 M. The IR and VCD spectra, recorded at different concentrations, are shown in Figure 8.27 and Figure 8.28, respectively.

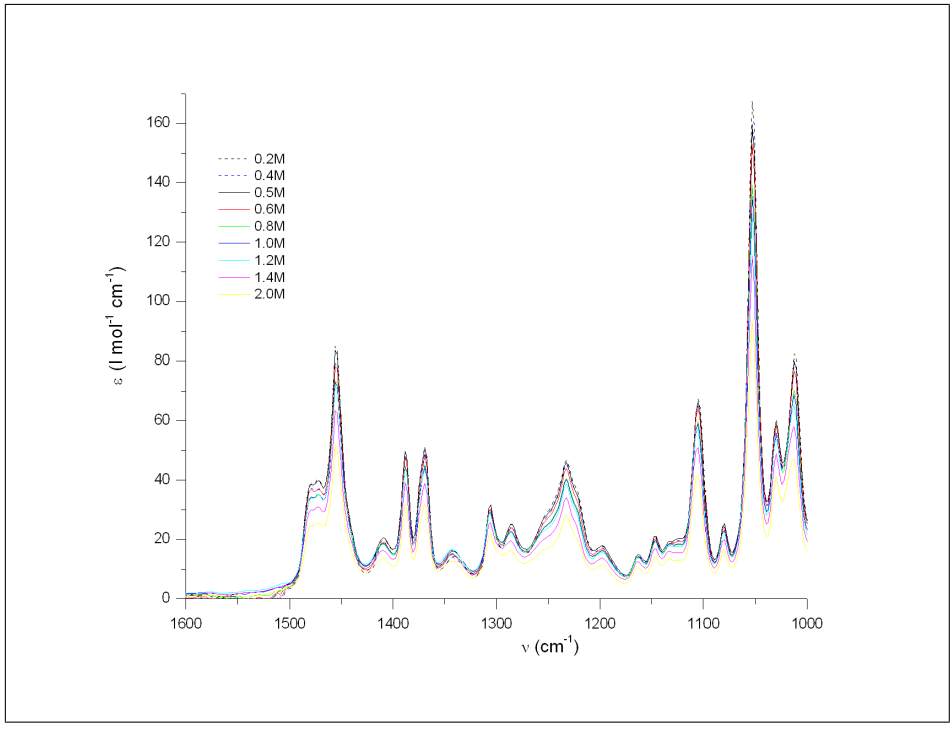


**Figure 8.27:** Comparison of the experimental IR spectra of (-)-borneol in $CDCl_3$ at various concentrations.

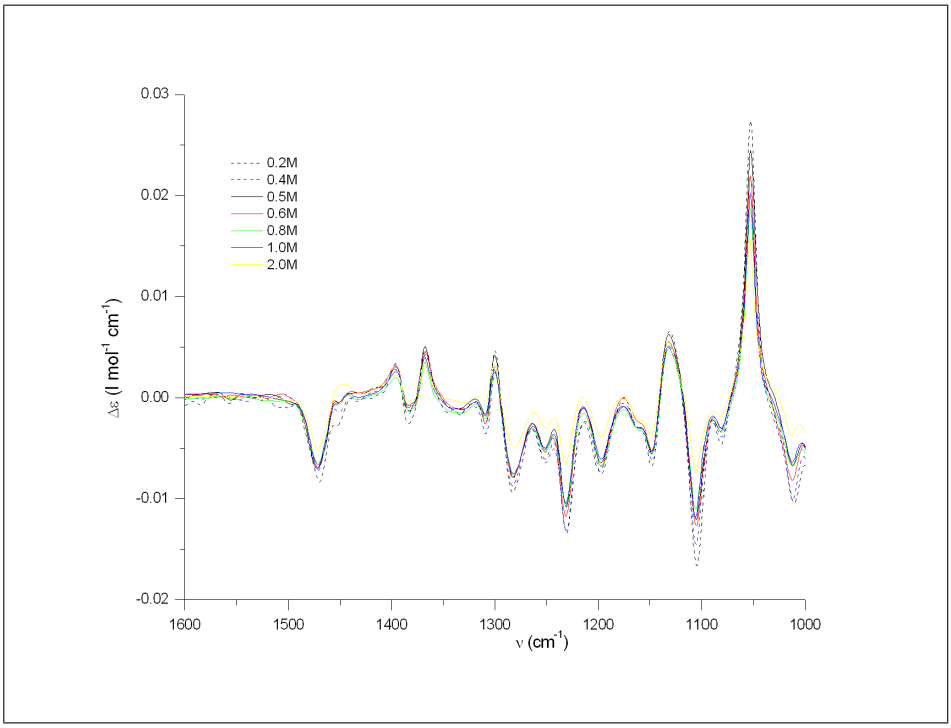


**Figure 8.28:** Comparison of the experimental VCD spectra of (-)-borneol in $CDCl_3$ at various concentrations.

As already described above, interactions with the solvent were not taken into account. To justify this, VCD measurements were performed in the CD stretching region. If associations were to be formed between a solvent molecule and borneol, the C-D stretching vibration of the solvent molecule would become VCD active, as is described in the previous chapter. Around 2250 $cm^{-1}$ no VCD signal could be distinguished from the noise, which justifies the neglect of these type of interactions.

### 8.3.5 Conclusions

In this study the influence of temperature on the VCD spectrum of borneol was discussed. It is shown that, in order to explain every observed feature, it was necessary to take into account the possible dimerization between the borneol molecules, due to the stabilizing effect of an intermolecular hydrogen bonding for two monomer conformations. Therefore the dimers were modeled by considering each possible combination of two

monomer conformations and their corresponding vibrational data were calculated. The equilibrium between the monomer and dimer was evaluated using a concentration variation study in $CDCl_3$. There is a large overall agreement between the experimental IR and VCD spectrum and the simulated ones, averaged over all significant monomers and dimers. This confirms that the proposed model of dimer/monomer equilibrium is valid.

Almost every feature, observed during temperature study, is described by the increasing contribution of the dimers. Hereby it is once more illustrated that, in some cases VCD analysis, is not straightforward. It is shown that the IR and VCD spectra of alcohols may be influenced by intermolecular interactions between monomers. Measurements at lower temperatures did not facilitate the assignment, as was supposed. On the contrary it was necessary to consider all possible interactions that gain importance at lower temperatures.

## 8.4 Influence of experimental and theoretical parameters on the VCD spectrum of limonene

### 8.4.1 Introduction

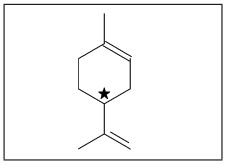

**Figure 8.29:** Structure of limonene

Limonene is one of the few terpenes for which its VCD spectrum between 1000 $cm^{-1}$ and 2000 $cm^{-1}$ has not definitely been assigned yet. Several studies published the recorded VCD spectra from 800 $cm^{-1}$ to 10,000 $cm^{-1}$ without comparing them with calculations [73, 69, 46, 175]. These papers allowed us to check the reproducibility of our recorded VCD spectra of limonene. Others study the CH stretch region in more detail [149, 176]. They state that the dominant VCD signal is a result of the coupling of $CH_2$ groups. Singh and Keiderling verified these conclusions with calculations using the consistent force field-fixed partial charge (CFF-FPC) model [149]. The overtone region was described by Abbate et al [177, 178]. During this study, the VCD spectrum of limonene in the mid-IR region (1000 $cm^{-1}$-2000 $cm^{-1}$) was targetted. The experimental spectra were compared with the VCD calculations and attempts will be made to explain each observed band. The assignment of all bands however did not prove very straightforward. In an attempt to verify the discrepancies between theory and experiment, experimental parameters, such as temperature and solvent, were varied. Working at lower temperatures is assumed to facilitate the assignment since the conformers with low energy gain importance and the contribution of the minima with higher energy decreases. Using the appropriate solvent a minimal temperature of 173K could be obtained. Recording the spectra of the limonene, dissolved in different solvents, enabled us to reveal possible solvent effects. Better resolution of the bands can be obtained by studying the molecule at cryogenic temperatures, using liquefied xenon as a solvent. In other words, whereas bands overlap in other IR spec-

tra, measurements in xenon should reveal some additional information about the frequency of the different modes. This spectroscopic technique is very often used to study hydrogen bonded complexes [179]. During the simulation of the recorded spectra, some theoretical parameters were varied as well such as the basis set and functional. In order to simulate the possible solvent effects, the polarizable continuum model (PCM) [153] was introduced. To explain every feature of the IR and VCD spectra of camphor [6] and pulegone [7] in $CDCl_3$, the vibrational data of the 1:1 associations between the solute and a $CDCl_3$ molecule had to be taken into account. Such a complex was stabilized by an intermolecular $C-D\cdots O$ hydrogen bond. A similar interaction between limonene and a $CDCl_3$ molecule is less likely to be observed as the stabilizing effect of a CH - $\pi$ interaction is known to be smaller than that of a classical hydrogen bond [180]. Both interactions have different origins. CH - $\pi$ interactions on the one hand originate primarily from dispersion effects while hydrogen bonds are due to electrostatic effects. Unfortunately DFT is unable to describe the dispersion interactions very accurately. Generally these calculations were done at the Coupled Cluster level (CCSD(T)). Recently a van der Waals density functional (vdW-DF) was developed, which explicitly includes nonlocal electron correlation without the use of any empirical parameter [181]. For none of these levels of theory VCD calculations were implemented yet. Moreover CCSD(T) calculations are very demanding. Most electronic structure calculations derive harmonic vibrational frequencies by diagonalizing the matrix of second derivatives of energy with respect to nuclear coordinates. These harmonic vibrational frequencies have become an important tool for interpretation of experimental IR (and VCD) spectra. However, in some cases the harmonic approximation is too crude for spectroscopic purposes. As stated before, harmonic frequencies are overestimated toward the experimental ones. This deficiency is usually corrected by scaling factors, which are based on experience of the performance of various theoretical methods. Anharmonicity, however, can be introduced by calculations of the cubic and quartic force constants [182]. The frequencies of the overtones and combination bands can be calculated as well.

### 8.4.2 Experimental

(+)-Limonene (> 99.0 % ee) and (-)-limonene (> 99.0 % ee) were purchased from Aldrich. The solvents, $CDCl_3$ (99.8 %), $CD_2Cl_2$ (99.6 %) and $CS_2$ (99.9 %), were obtained from Aldrich, Acros and Riedel-de Haën respectively. All products were used without further purification. For all samples a cell with $CaF_2$ windows and a 100 $\mu$m spacer was used. The concentration of the solutions was set at 1.0 M. The unpolarized IR absorbance spectra were recorded at a resolution of 4 $cm^{-1}$ and the VCD spectra at a resolution of 6 $cm^{-1}$. A 1830 $cm^{-1}$ long wave pass filter was used to improve the S/N ratio. The collection time for the VCD spectrum was 90 min, using six blocks of 15 min. To obtain an estimate for the baseline artifacts, the VCD spectra of both enantiomers were recorded, both in the same conditions [28]. Limonene was dissolved in $CDCl_3$,$CS_2$, $CCl_4$ and $CD_2Cl_2$. Spectra of the neat liquid were recorded as well. For the measurements at lower temperatures, the adapted setup was used. The experimental setup for the IR measurements in xenon consists of a pressure manifold needed for filling and evacuating the cell. The cell had a path length of 7 cm and was equipped with $CaF_2$ windows. A resolution of 0.5 $cm^{-1}$ was obtained. In order to acquire sufficient absorbance, an amount of limonene was injected into the cell.

### 8.4.3 Computational Methods

To find all stable conformers of limonene, the potential energy surface (PES) was scanned, using different force fields and structure generation methods. A stochastic search in the MM3 [107, 108] force field was executed as well as a systematic search in the MMFF [109, 110] force field. The minima found during these conformational analyses were further optimized at the B3LYP/6-31G(d) level and compared. Subsequently, for all unique conformers, the vibrational data were calculated: i.e. the frequencies, the rotational strengths and the dipole strengths. The obtained line spectrum of each minimum was then broadened by using the Lorentzian band shape with a FWHM of 10 $cm^{-1}$. In order to allow a comparison with the experimental spectra, the spectrum of each minimum was combined in a Boltzmann weighted manner, based on their relative standard enthalpies. The frequency calculations were repeated using different functionals (B3LYP, B1LYP, B3PW91, B3P86,

B98, MPW1PW91, PBE) and/or basis sets (6-31G(d), 6-311G(d,p), 6-31G, 6-311+G(d,p), 6-31G(d,p), cc-pVDZ, cc-pVTZ, cc-pVQZ). For MP2 the vibrational data were obtained as well. At each level, appropriate scaling factors were used to correct for the harmonic approximation [112, 4, 113]. In order to take into account the solvent, the Polarizable Continuum Model (PCM) [153] was introduced. PCM calculations were done, for each solvent, at the B3LYP/6-31G(d) level. To check for the presence of anharmonic effects, the quartic and cubic force constants were calculated, together with the frequencies of the overtones and combination bands. All DFT calculations were performed using Gaussian 03 Revision B05 [55].

### 8.4.4 Results and Discussion

A conformational analysis and optimization of the minima at the B3LYP/6-31G(d) level yielded 6 unique conformers for limonene. Three have their isopropyl group in equatorial position and are the most stable ones. The higher energy structures have an axial isopropyl substituent. The rotamers of the equatorial and axial conformers can be further characterized by the dihedral angle $H - C^* - C = C$. These specifications and the relative enthalpies of each minimum are listed in Table 8.6. The contributions of the axial conformers are much smaller than those of the equatorial conformers. In literature [149], using the CFF-FPC model, however, only three minima were found labeled as: AX (T), EQ (T) and EQ (C). T and C refer to the position of the isopropylene double bond, toward the $C * -H$ bond, as *trans* and *cis*. Their relative enthalpies are 0.00 kcal/mol, 1.294 kcal/mol and 3.282 kcal/mol for EQ (C) ($\equiv$ a), EQ (T) ($\equiv$ b/c) and AX (T) ($\equiv$ d) respectively.

**Table 8.6:** the relative enthalpies (in kcal/mol) and Boltzmann weights (in %) of all stable conformers of limonene, together with their geometric specifications.

| | | $H-C^*-C=C$ | $\Delta H^0$ | w |
|---|---|---|---|---|
| a | EQ | -8 | 0.00 | 44.6 |
| b | EQ | 132 | 0.21 | 31.1 |
| c | EQ | -142 | 0.49 | 19.5 |
| d | AX | -140 | 1.37 | 4.4 |
| e | AX | 20 | 3.14 | 0.2 |
| f | AX | 105 | 3.36 | 0.2 |

In Figure 8.30 and Figure 8.31 the calculated IR and VCD spectrum of each conformer is shown, together with the corresponding Boltzmann weighted spectra. In order to scale the calculated frequencies a factor of 0.967 was used for the B3LYP/6-31G(d) calculation level. Considering the IR spectra, the intensity of the band around 1700 $cm^{-1}$, originating from the CO stretching vibration, is smaller for the axial conformers than for the equatorial ones. The largest differences between the conformers are observed for the region below 1400 $cm^{-1}$.

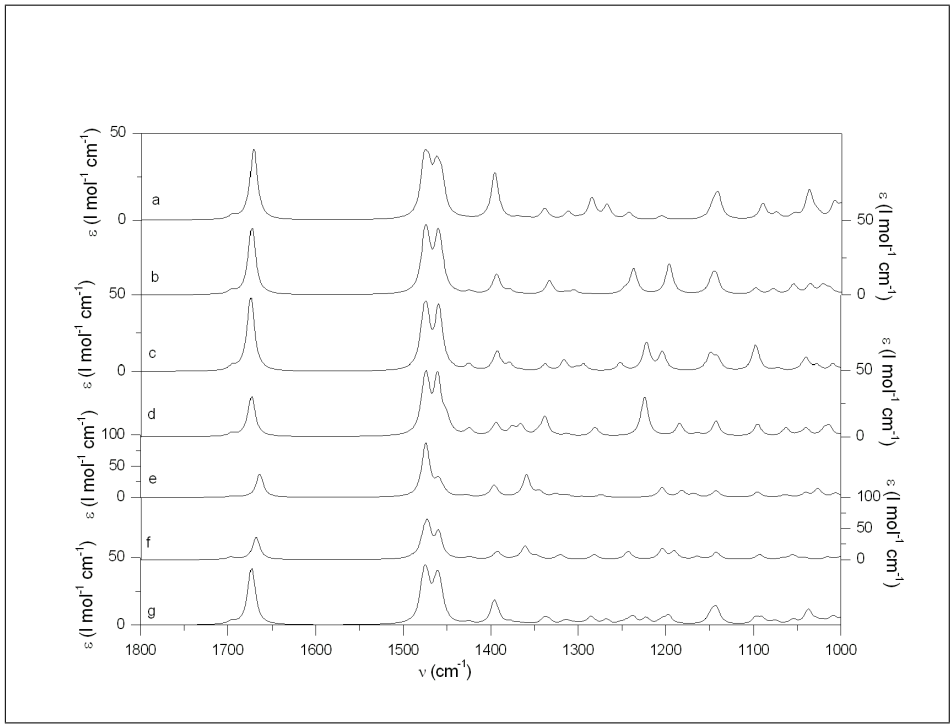


**Figure 8.30:** calculated IR spectrum of each conformer of limonene (a, b, c, d, e and f), together with its Boltzmann weighted IR spectrum (g).

For the VCD spectra, the differences between axial and the equatorial conformers are even more remarkable. Because of the small contribution of the axial conformers, the Boltzmann weighted spectrum shows the best correspondence with the calculated VCD spectra of the equatorial conformers.

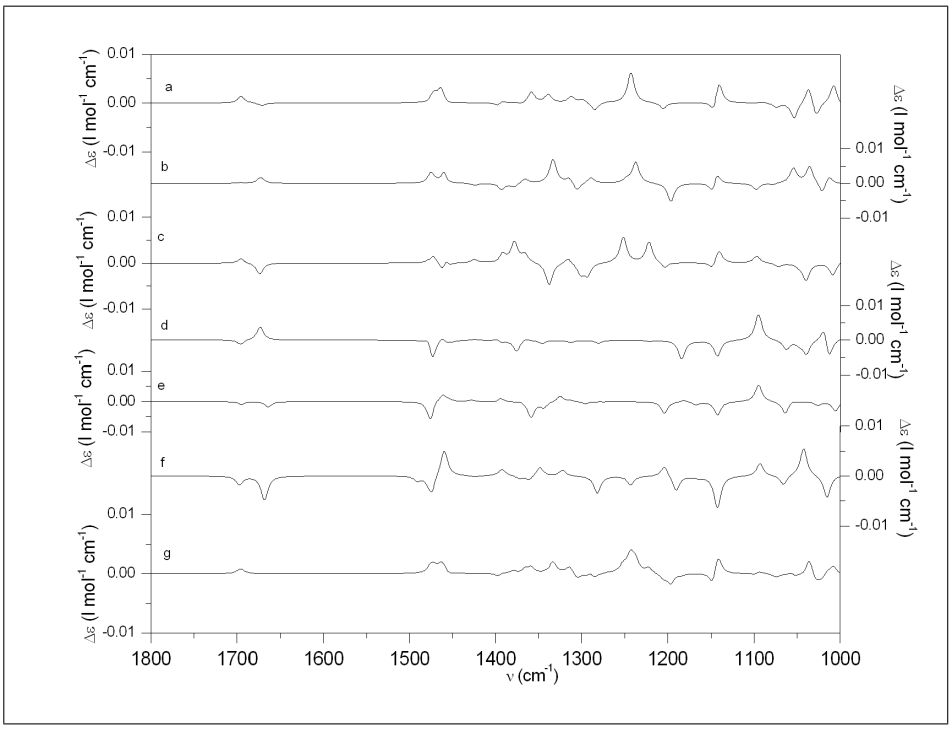


**Figure 8.31:** calculated VCD spectrum of each conformer of R-limonene (a, b, c, d, e and f), together with its Boltzmann weighted IR spectrum (g).

In Figure 8.32 the experimental IR spectrum is compared with the calculated spectrum. Each experimental band is linked with a band from the calculated spectrum. There is a satisfactory correspondence between both spectra. In the experimental spectrum band 48 - 51, however, has a larger intensity than band 52 - 54, while for the calculations the relative intensities are inverted. In the experimental spectrum bands 34 and 35 are resolved; this is not the case for the calculations. There also is some difference between both spectra in the pattern below 1100 $cm^{-1}$.

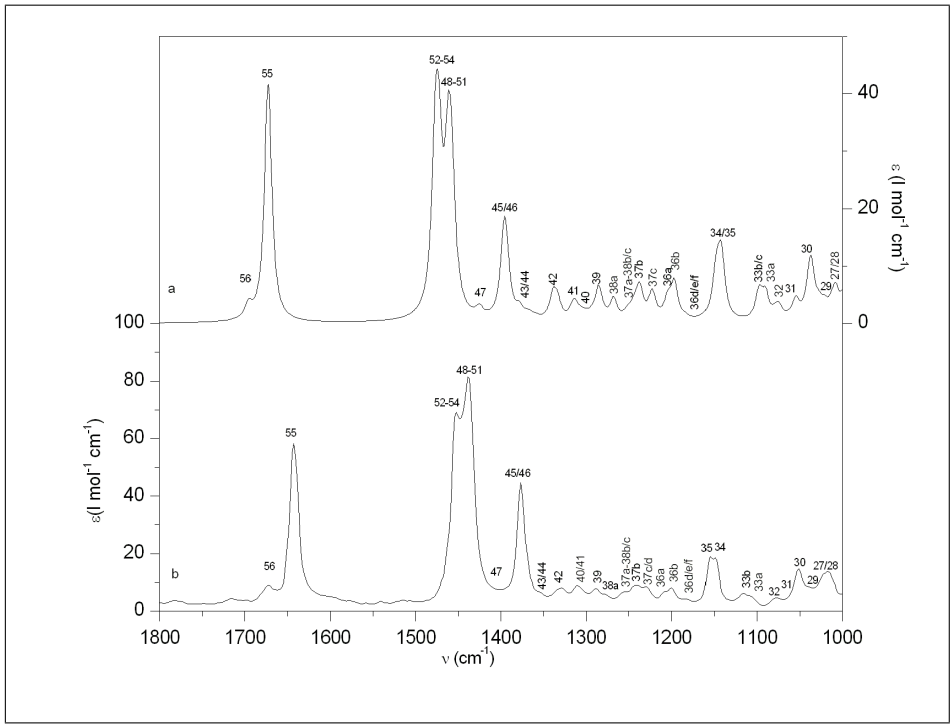


**Figure 8.32:** comparison of the experimental IR spectrum of limonene in $CDCl_3$ (b) with the calculated one of free limonene in vacuum (a).

In Figure 8.33 the experimental VCD spectrum of (+)-limonene is compared with the VCD calculations of R-limonene. There is a large overall agreement between both spectra and one can state that (+)-limonene corresponds to the R configuration. Band 52-54, however, is predicted to have a positive sign, while in the experimental spectrum a negative sign is seen. The pattern of the bands between 1300 $cm^{-1}$ and 1400 $cm^{-1}$ is slightly different in both spectra, but assignment is still possible. The assignment of the bands around 1150 $cm^{-1}$ on the other hand, is much less straightforward. In the calculated spectrum a couplet was observed, bands 34 and 35 are predicted to have positive and negative signs respectively. In the experimental spectrum, however, only one broad negative band is observed. The signs of the bands 34 and 52 - 54 would suggest that the rotamers with its isopropyl substituent in axial position, have a larger abundance than was assumed by the relative enthalpies obtained from the ab initio calculations at the B3LYP/6-

31G(d) level. This is why the Boltzmann weights were recalculated for several levels of theory, as is shown in Table 8.7. For each level, however, similar relative enthalpies were obtained. All calculated VCD spectra show the same pattern for the bands, originating from the normal modes 34 and 35. Neglecting the ab initio relative enthalpies and simulating VCD spectra with higher contributions for the axial rotamers did not lead to a better agreement between theory and experiment. Moreover this would lead to larger differences with experiment in other frequency regions. Hereto other explanations have to be sought for these different patterns of the bands 34, 35 and 52-54.

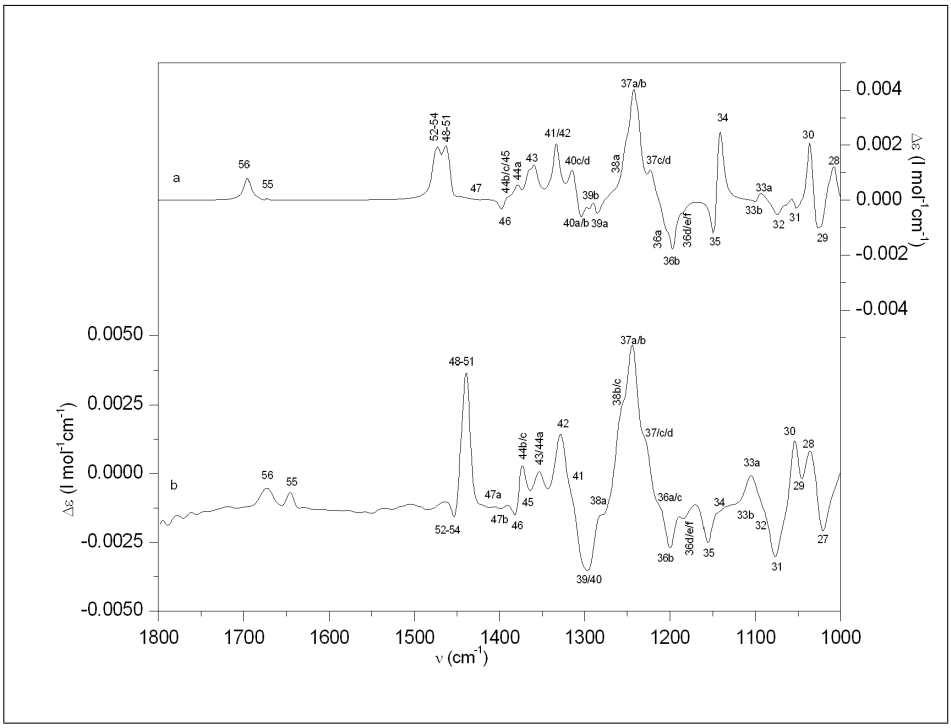


**Figure 8.33:** comparison of the experimental VCD spectrum of (+)-limonene in $CDCl_3$ (b) with the calculated one of free R-limonene in vacuum (a).

**Table 8.7:** The Boltzmann weights of each conformer of limonene calculated, using various functionals and basis sets.

| level | a | b | c | d | e | f |
|---|---|---|---|---|---|---|
| B3LYP/6-31G(d) | 44.7 | 31.1 | 19.4 | 4.4 | 0.2 | 0.2 |
| B3PW/6-31G(d) | 43.0 | 32.2 | 19.1 | 5.3 | 0.2 | 0.2 |
| B3LYP/cc-pVTZ | 45.0 | 30.8 | 21.3 | 2.5 | 0.2 | 0.1 |
| PBE1PBE/6-31G(d,p) | 39.4 | 33.5 | 18.4 | 8.1 | 0.3 | 0.3 |
| B3LYP/6-311G(d,p) | 45.3 | 30.1 | 20.2 | 4.0 | 0.2 | 0.2 |
| B3LYP/6-31G(d) | 43.1 | 31.7 | 20.1 | 4.7 | 0.2 | 0.2 |
| B1LYP/6-31G(d) | 45.2 | 30.9 | 19.3 | 4.2 | 0.2 | 0.1 |
| B3P86/6-31G(d) | 40.2 | 33.2 | 19.3 | 6.8 | 0.3 | 0.3 |
| B98/6-31G(d) | 42.3 | 32.3 | 18.3 | 6.5 | 0.3 | 0.2 |
| B3LYP/6-31G | 42.3 | 31.8 | 20.9 | 4.6 | 0.2 | 0.2 |
| B3LYP/cc-pVDZ | 43.3 | 32.2 | 20.5 | 3.7 | 0.2 | 0.2 |
| MP1PW91/6-31G(d) | 41.3 | 32.9 | 18.5 | 6.8 | 0.3 | 0.2 |

Due to band overlap, some information might be lost. A resolution enhancement technique of Fourier self-deconvolution can be applied when the spectral features are narrower than the instrumental resolution. This technique was used for the deconvolution of the VCD spectrum of limonene in a paper from Lipp [70] and was reproduced in this study using OPUS 6.0. The parameters, bandwidth and noise reduction, were varied until the spectra from the mentioned paper were sufficiently reproduced. During the procedure, Lorentzian bandshapes were used. The deconvolved spectra, together with the original ones are shown in Figure 8.34. For the IR spectrum no large improvements were observed, whereas for the VCD spectrum the resolution is enhanced remarkably. However, in order to reduce the number of variable parameters that may influence our observations and conclusions, during the rest of this discussion, the experimental VCD spectra will not be manipulated either.

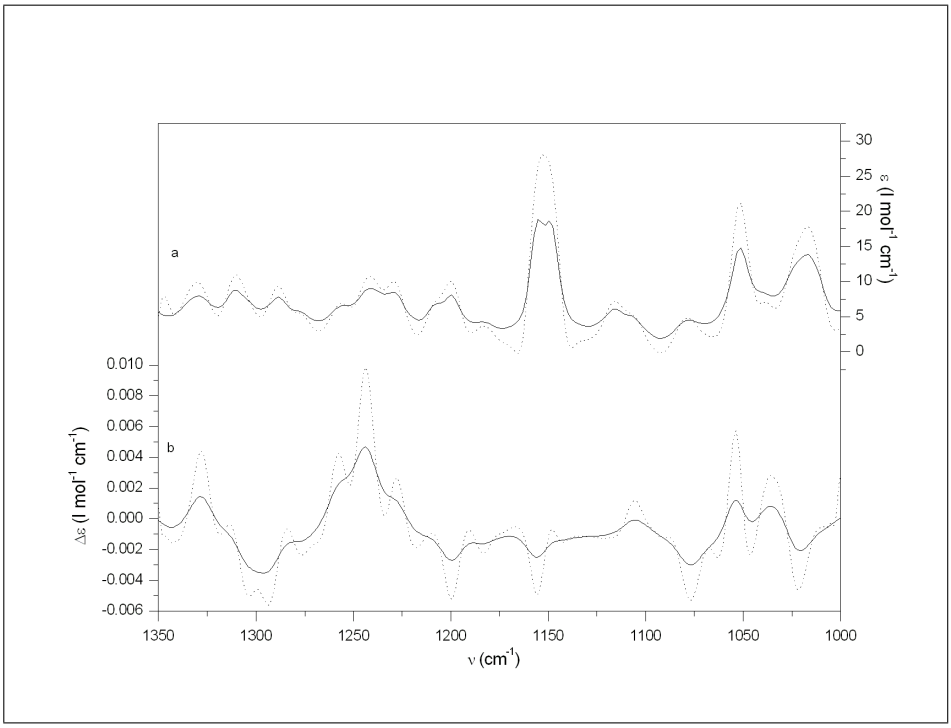


**Figure 8.34:** (a) experimental IR spectrum (solid line) and the deconvolved one (dotted line). During deconvolution the following parameters were used: noise reduction = 0.50 and bandwidth = 7.90. (b) experimental VCD spectrum of (+)limonene in $CDCl_3$ (solid line) and its deconvolved one (dotted line). During deconvolution the parameters were set to: noise reduction = 0.50 and bandwidth = 16.94.

In additional experiments, the IR spectra of limonene were measured in xenon. Due to the better resolution, some bands will now be separated and therefore additional information was obtained. This is especially true for the frequency region from 1000 $cm^{-1}$ to 1050 $cm^{-1}$. As is depicted in Figure 8.35, attempts were made to assign every band. The width of the Lorentzian broadening function, used to simulate these experimental spectra, was set to 2 $cm^{-1}$ instead of 5 $cm^{-1}$. The small shoulder at 1018 $cm^{-1}$ could not be linked to any of the calculated normal modes unless the frequency order of the bands 28a/c and 28b/d were inverted and the shoulder corresponds with normal mode 28 originating from the rotamers b and d. Due to the small frequency difference between the normal modes 28a/c and 28b/d ($< 10$ $cm^{-1}$), it is possible

that the order was switched. Some other bands between 1600 $cm^{-1}$ and 1800 $cm^{-1}$, clearly visible in the experimental spectrum, could not be explained by the harmonic calculations of free limonene in vacuo. It would also have been very interesting to perform VCD measurements in liquid xenon. Unfortunately, this was not achievable, because the sample baseline was irreproducible from sample to sample due to the high pressure on the windows.

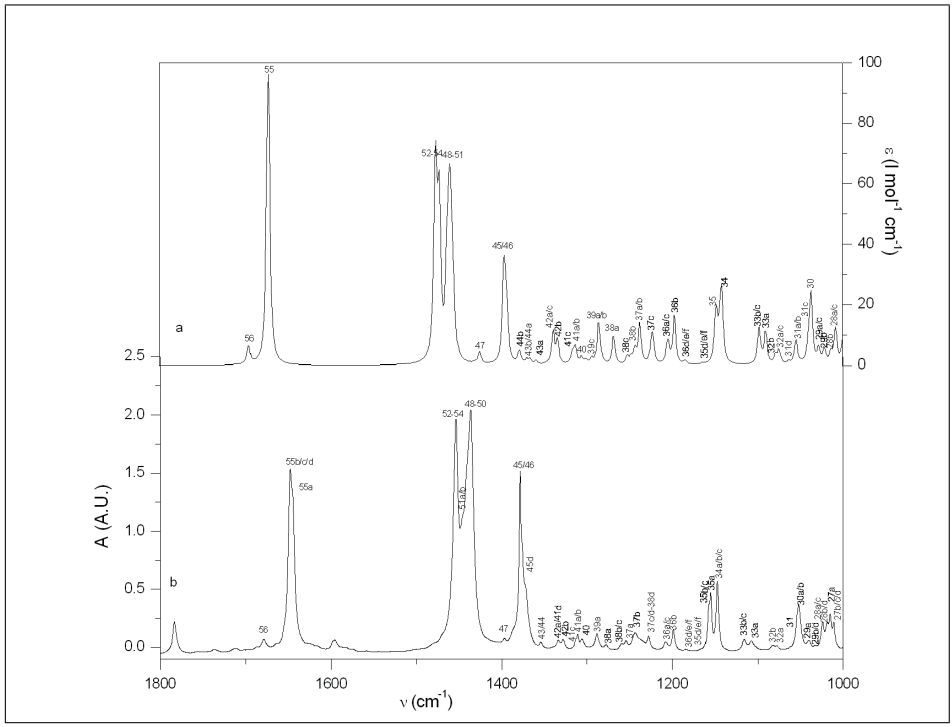


**Figure 8.35:** assignment of the bands of the IR spectrum of limonene recorded in xenon at 208K: a) calculated IR spectrum (lorentzian broadening factor, $\gamma$= 2 $cm^{-1}$), b) experimental IR spectrum.

In an attempt to isolate only one conformer of limonene, solid state IR measurements were also performed. This was done, on one hand, by condensing the vapors of limonene on a cooled KBr-plate. In the second type of experiment, limonene as a neat liquid was cooled far below its melting point. Unfortunately, all experiments to crystallize the supercooled liquid failed. These observations are in line with literature reports [183, 184].

In an attempt to shed light on the conformational behavior of limonene in solution, additional experiments and calculations were performed.

### IR and VCD spectra of limonene using different solvents

IR and VCD measurements were performed for limonene in $CDCl_3$, $CS_2$, $CD_2Cl_2$ and $CCl_4$, all at concentrations near 1.0M. Additional spectra were recorded of the neat liquid and of limonene dissolved in liquid xenon (208K). Below we will compare these spectra with the calculations on limonene in vacuum and the PCM calculations in $CDCl_3$, $CD_2Cl_2$, $CS_2$ and $CCl_4$. The Polarizable Continuum Model is a method to introduce solvent effects into the calculations. In these calculations, the solvent is mainly characterized by its dielectric constants and Van der Waals radii. In Figure 8.36 and Figure 8.37 the IR spectra are compared for the different solvents. The differences are rather small. For band 34, a small frequency shift was observed. For measurements in $CS_2$ the band is red shifted compared to the experiments in neat liquid and in xenon, which in turn is red shifted with respect to measurements in $CDCl_3$ and $CD_2Cl_2$. The frequency of the band originating from the exocyclic C=C stretch (band 55) is the same for the measurements in $CD_2Cl_2$, $CS_2$, $CDCl_3$ and $CCl_4$. For the measurement in xenon the frequency is blue shifted. The same can be said about the band originating from the endocyclic C=C stretch (band 56). A closer look at the relative intensities reveals remarkable differences for those of the bands 34 and 35. For the measurements in $CDCl_3$, $CD_2Cl_2$, $CCl_4$ and $CS_2$ and the IR spectrum of the neat liquid, bands 34 and 35 have almost equal intensity, while for the measurement in xenon, band 34 is larger than band 35. A similar trend was observed for the bands 48 - 51 and 52 - 54. For the xenon measurements both bands have almost equal intensities, while using other solvents, band 48 - 51 is remarkably larger than band 52 - 54.

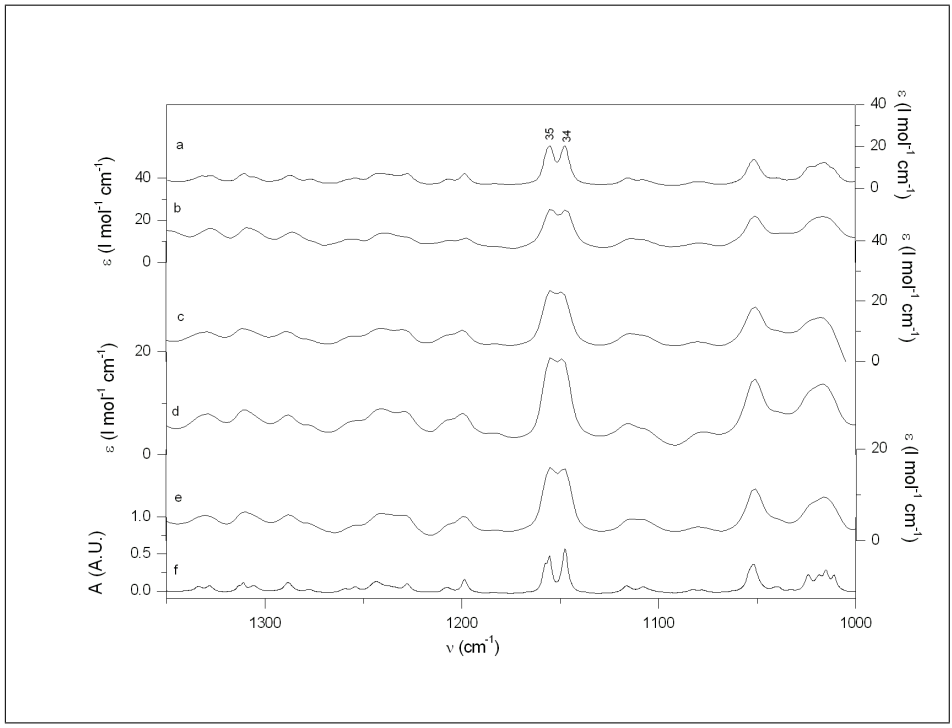


**Figure 8.36:** Experimental IR spectra of limonene as a neat liquid (a), in $CS_2$ (b), $CD_2Cl_2$ (c), $CDCl_3$ (d), $CCl_4$ (e) and Xe (f) between 1000 $cm^{-1}$ and 1350 $cm^{-1}$.

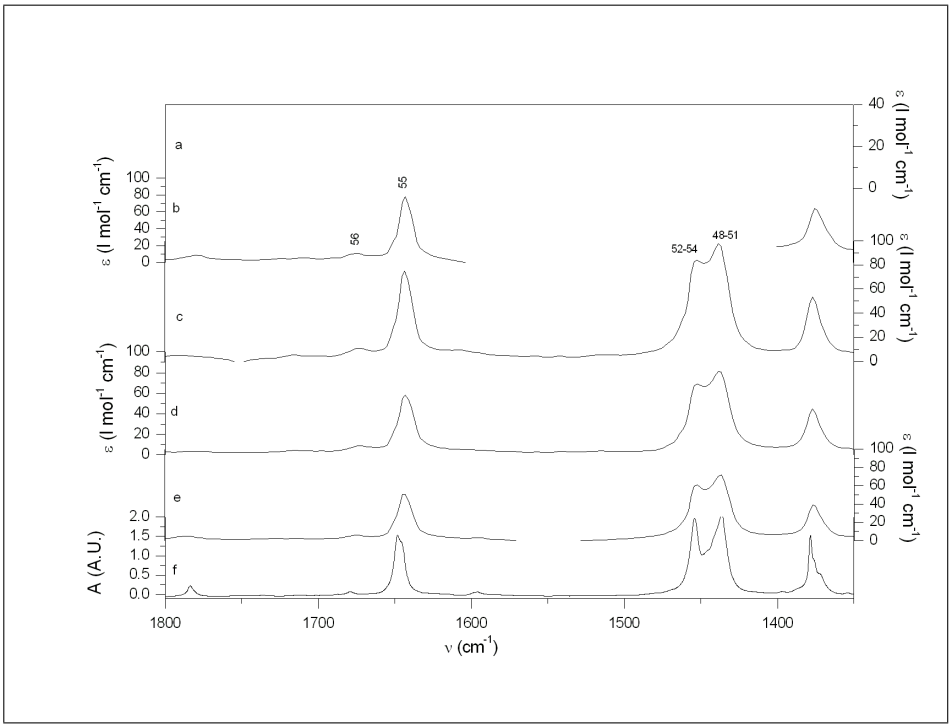


**Figure 8.37:** Experimental IR spectra of limonene as a neat liquid (a), in $CS_2$ (b), $CD_2Cl_2$ (c), $CDCl_3$ (d), $CCl_4$ (e) and Xe (f) between 1350 $cm^{-1}$ and 1800 $cm^{-1}$.

These observations were then compared with the PCM calculations, depicted in Figure 8.38. Except for some small frequency shifts, no other large dissimilarities were observed. For each band, the frequencies of the calculations in vacuum are higher than those of the PCM calculations. Comparing the PCM calculations for the different solvents, the frequencies of the calculations in $CS_2$ and $CCl_4$ are higher than those in $CDCl_3$ and $CD_2Cl_2$. These frequency shifts are the most striking for the C=C stretching vibrations (bands 55 and 56) and the other bands above 1400 $cm^{-1}$. For these C=C stretching vibrations one can state that the frequency order for the solvents is in agreement with the experimental observations. For band 34 the frequency order of the different solvents is inverted compared to the experiments. For each PCM calculation the relative intensity between bands 34 and 35 remains the same; band 35 is smaller than band 34. This, again does not correspond with the experiments, where the relative intensities of both bands somewhat change

with the solvent, as was described above. The same can be said about bands 48 - 51 and 52 - 54, for which the calculated relative intensities remain the same for the different solvents. This again is in disagreement with the experiments.

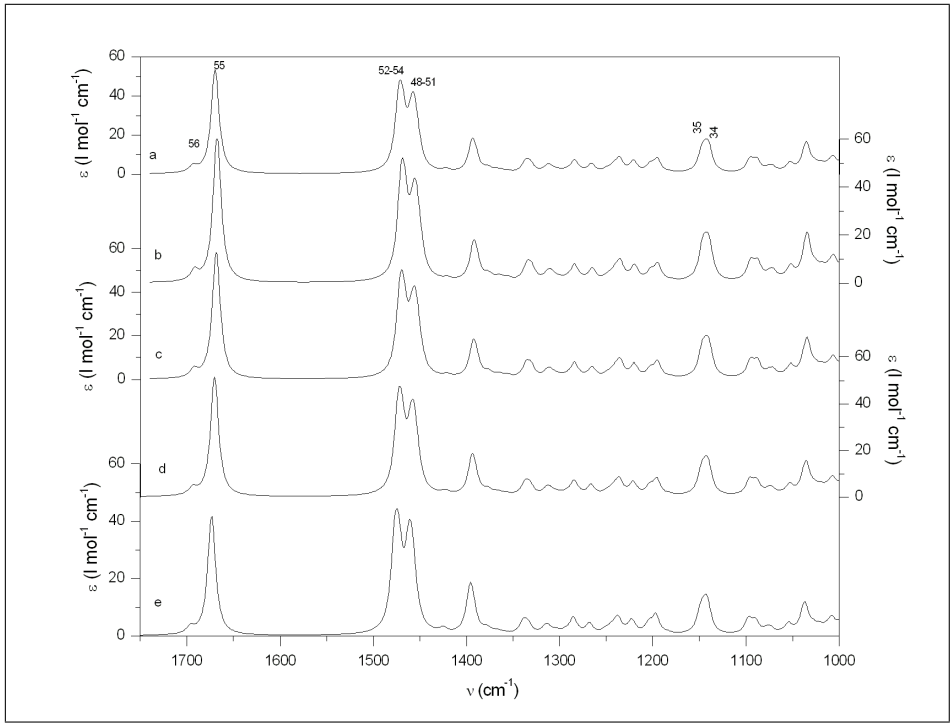


**Figure 8.38:** Comparison of the calculated IR spectra of limonene using PCM, varying the solvent: (a) $CS_2$, (b) $CD_2Cl_2$, (c) $CDCl_3$, (d) $CCl_4$ and (e) vacuo.

The VCD spectra of limonene in various solvents are depicted in Figure 8.39. The most remarkable trend again is the frequency shift of band 34-35. For the measurements in $CDCl_3$ and in $CD_2Cl_2$ the frequency of the band is higher than for the measurements of the neat liquid and those in $CS_2$. Considering the region of the C=C stretching vibrations, the spectra are very similar.

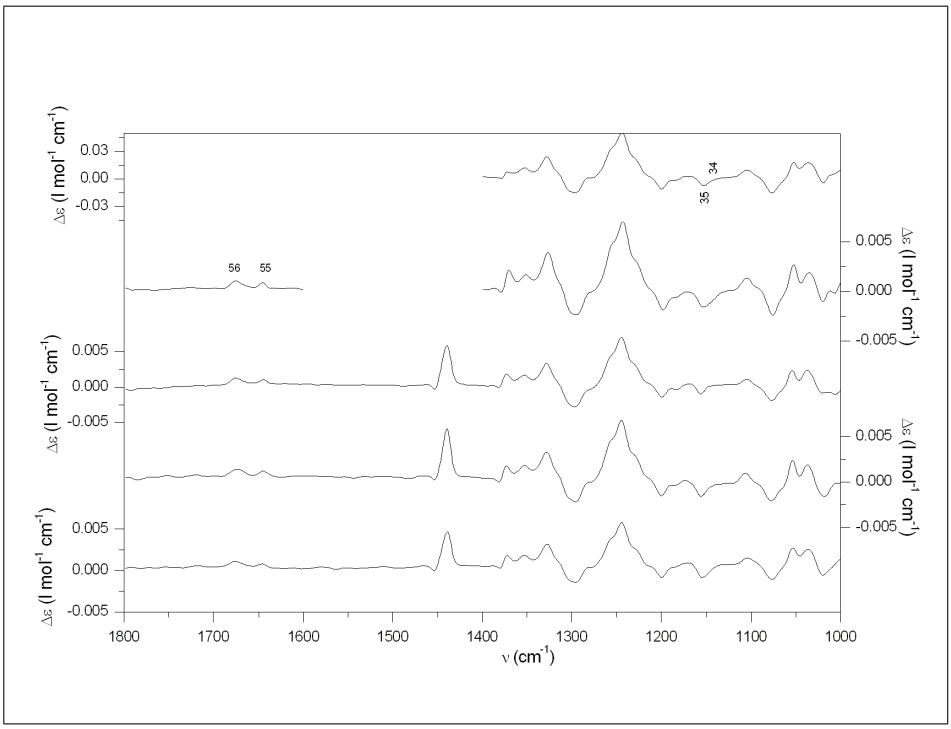


**Figure 8.39:** Comparison of the experimental VCD spectra as a neat liquid (a), in $CS_2$ (b), $CD_2Cl_2$ (c), $CDCl_3$ (d) and $CCl_4$ (e).

These observations again are verified with the aid of the PCM calculations of the various solvents, depicted in Figure 8.40. Unfortunately, the observed frequency shift of band 34-35 was not reproduced by the calculations. On the other hand,the calculated frequency shift linked to the C=C stretching vibrations, is less visible in the experimental VCD spectra.

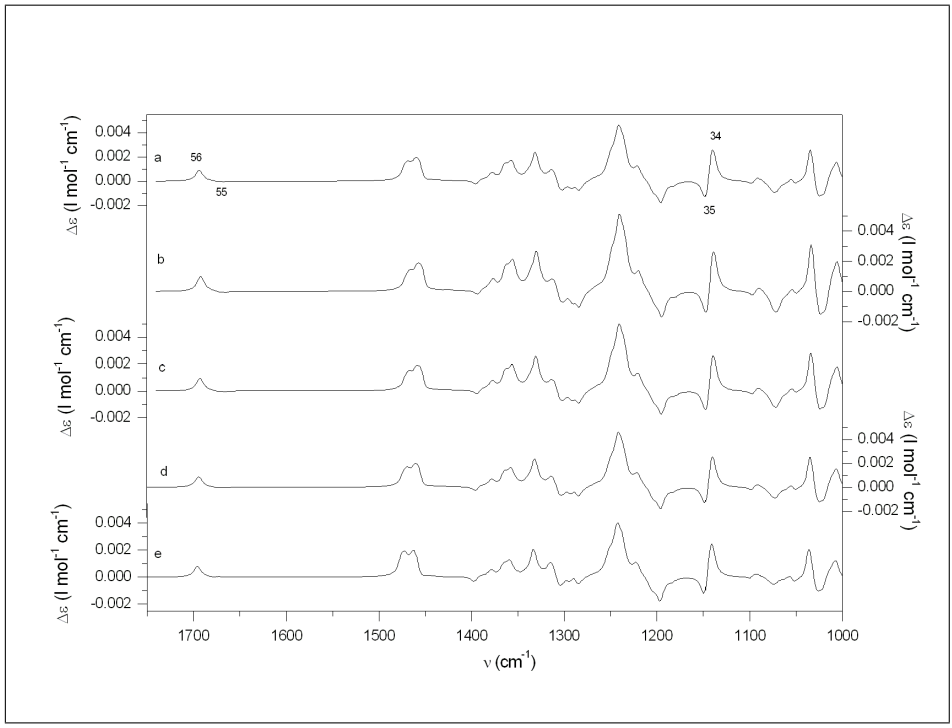


**Figure 8.40:** Comparison of the calculated VCD spectra of limonene using PCM, varying the solvent: (a) $CS_2$, (b)$CD_2Cl_2$, (c) $CDCl_3$, (d) $CCl_4$ and (e) vacuo.

In general, the differences between the spectra in various solvents are rather small. The largest changes arise for bands 34 and 35. Unfortunately the PCM calculations were unable to explain these observations. The observed frequency shifts for the C=C stretching vibrations, on the other hand, are correctly simulated by PCM.

### IR and VCD measurements of limonene at different temperatures

**IR measurements**: For the spectra of limonene in $CDCl_3$, the minimal temperature is limited to 213K. In Figure 8.41 and Figure 8.42 the IR measurements at 298K, 273K, 248K and 223K are shown. Although the interval between the maximum and minimum temperature is rather small, already some trends are observed. As the temperature is decreased, the intensity of most of the bands increases. This

increase,however, is not equal for all bands. The intensity of band 34 for instance increases more than that of band 35. The intensity of band 36d/e/f, on the other hand, remains unchanged. The increase of intensity of the band 37c is inferior to that of the band 37b. These two latter observations confirm that the contributions of the higher energy rotamers are reduced at lower temperatures. At lower temperatures a band appears at 1040 $cm^{-1}$, that can be assigned to normal mode 29. Another remarkable observation, is that although the intensity of the band 55 rises at lower temperatures, as is the case for most of the bands, the intensity of band 56, however, almost remains the same for each temperature.

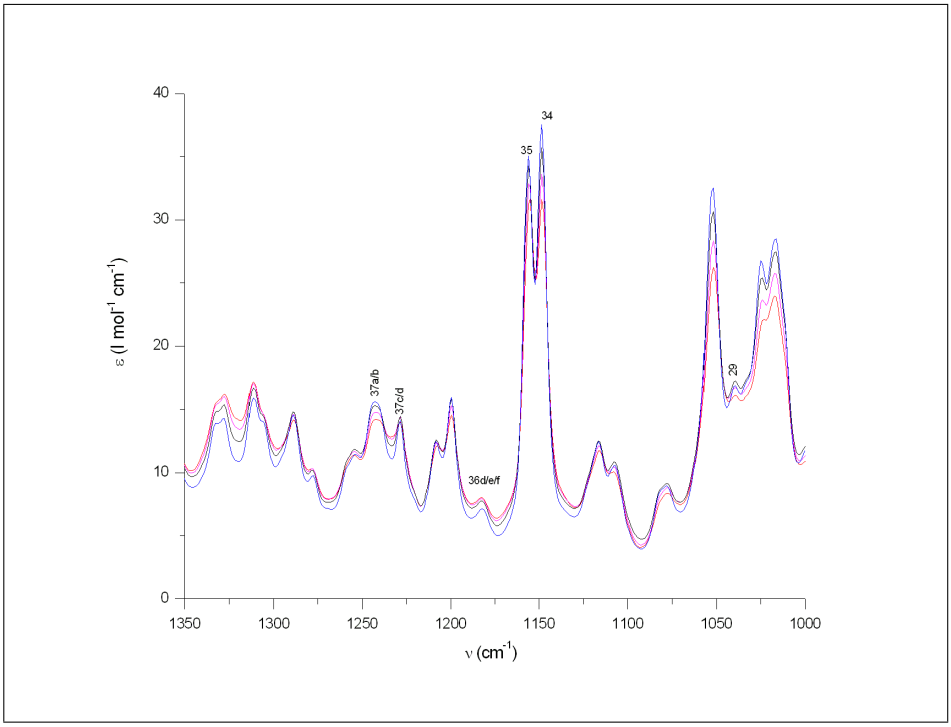


**Figure 8.41:** Experimental IR spectra of limonene in $CDCl_3$ at 298K (red), 273K (pink), 248K (black) and 223K (blue) between 1000 $cm^{-1}$ and 1350 $cm^{-1}$.

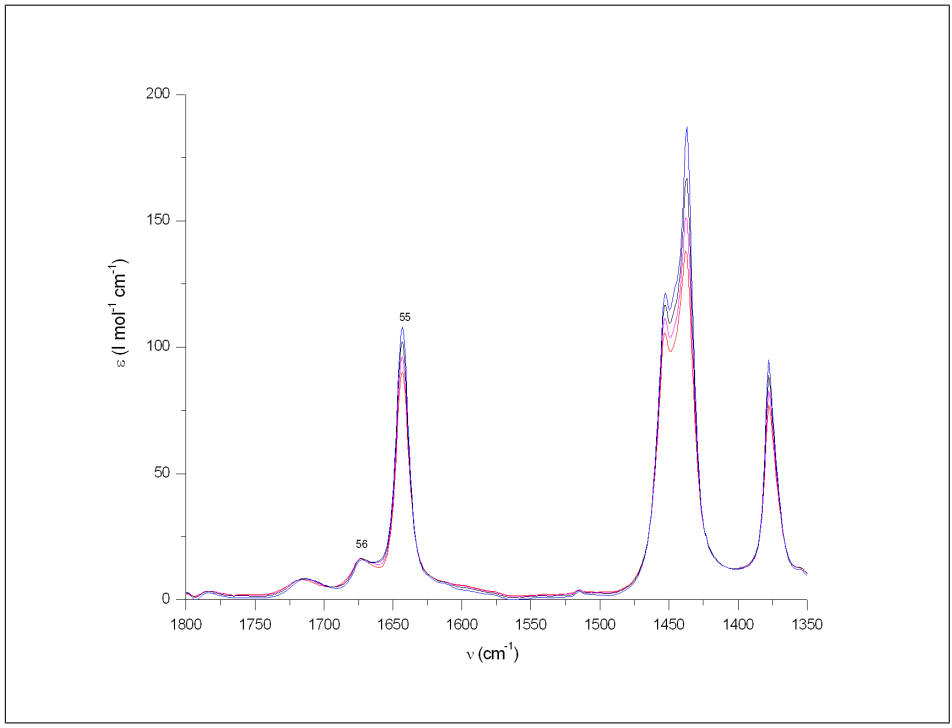


**Figure 8.42:** Experimental IR spectra of limonene in $CDCl_3$ at 298K (red), 273K (pink), 248K (black) and 223K (blue) between 1400 $cm^{-1}$ and 1800 $cm^{-1}$.

In order to check whether the previous observations are reproducible in other solvents, the experiments were repeated for limonene in $CD_2Cl_2$ at 298K, 263K and 233K. The IR spectra are depicted in Figure 8.43 and Figure 8.44. The measurements in $CS_2$ are shown in Figure 8.45. For both solvents the same trends were observed as for the measurements in $CDCl_3$. Additional effects become clearly visible in $CD_2Cl_2$ and $CS_2$. Next to the band at 1040 $cm^{-1}$ that increases in intensity with decrease of temperature, another band around 1032 $cm^{-1}$ becomes visible in $CD_2Cl_2$ and $CS_2$. The band at the lower frequency can be linked with rotamer b, while that at 1040 $cm^{-1}$ originates from the most stable conformer. Secondly, at room temperature band 40/41 has a small shoulder at 1306 $cm^{-1}$. This shoulder gains importance at lower temperatures and can now be distinguished from the other band at 1310 $cm^{-1}$. The band at lower frequency originates from the two most stable equatorial rotamers and the normal modes of the conformers with

higher energy are linked to the band at 1310 $cm^{-1}$. As the contribution of the higher energy conformers is reduced at lower temperatures, it is likely that the shoulder will increase faster than the band at the higher frequency.

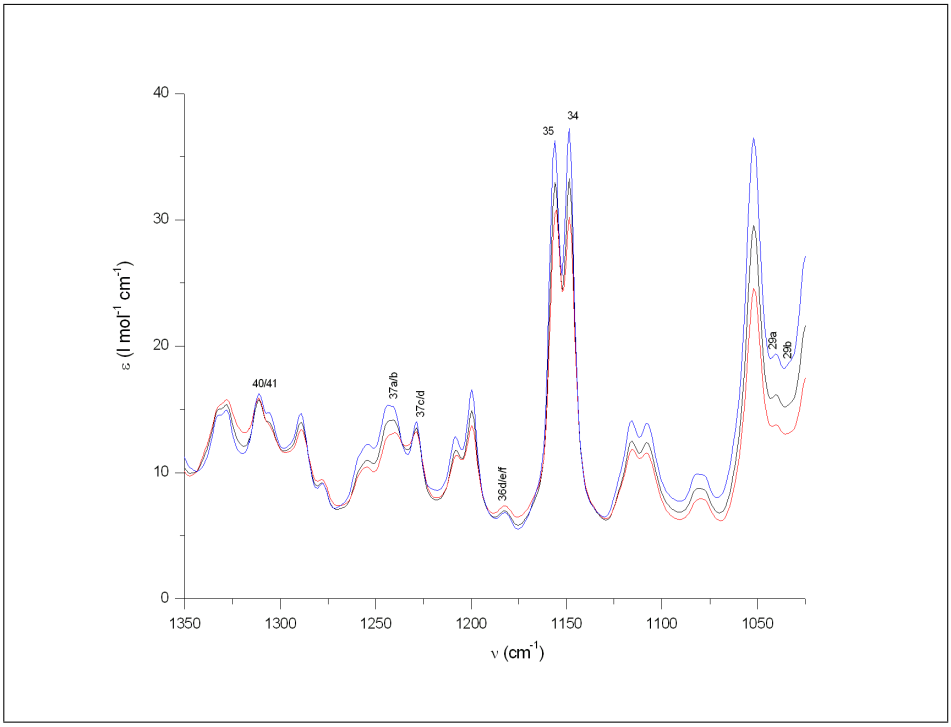


**Figure 8.43:** Experimental IR spectra of limonene in $CD_2Cl_2$ at 298K (red), 263K (black) and 233K (blue) between 1000 $cm^{-1}$ and 1350 $cm^{-1}$.

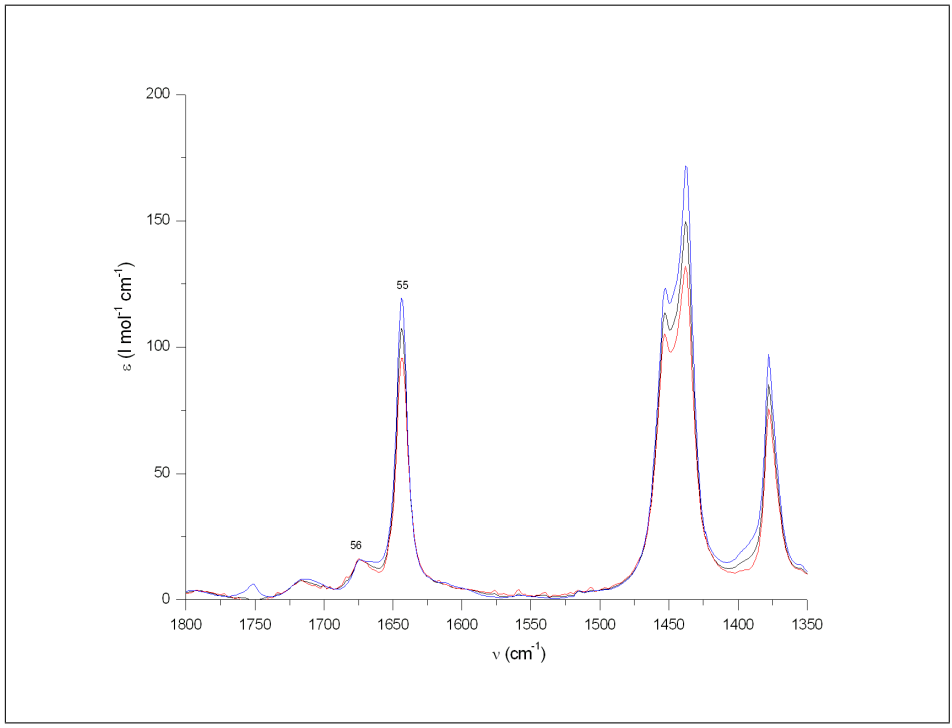


**Figure 8.44:** Experimental IR spectra of limonene in $CD_2Cl_2$ at 298K (red), 263K (black) and 233K (blue) between 1350 $cm^{-1}$ and 1800 $cm^{-1}$.

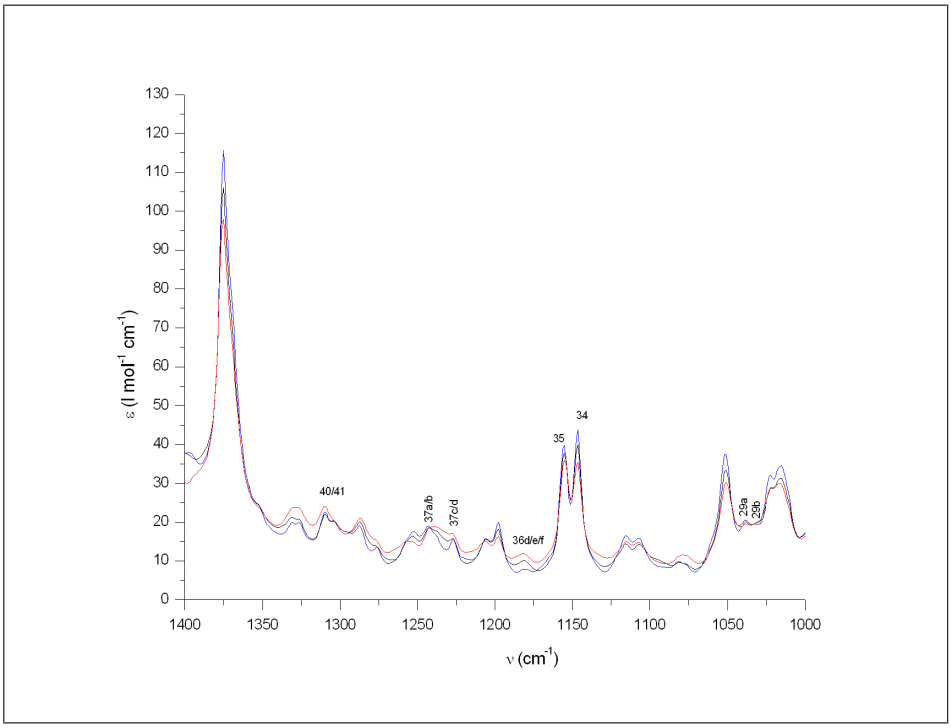


**Figure 8.45:** Experimental IR spectra of limonene in $CS_2$ at 298K (red), 253K (black) and 233K (blue) between 1000 $cm^{-1}$ and 1400 $cm^{-1}$.

Measurements of limonene as a neat liquid at various temperatures (298K, 273K, 253K, 233K, 213K, 193K and 183K) are depicted in Figure 8.46. Due to the large absorption, the studied region is limited to frequencies below 1350 $cm^{-1}$. Again the same trends were observed as for the IR spectra of limonene in solution.

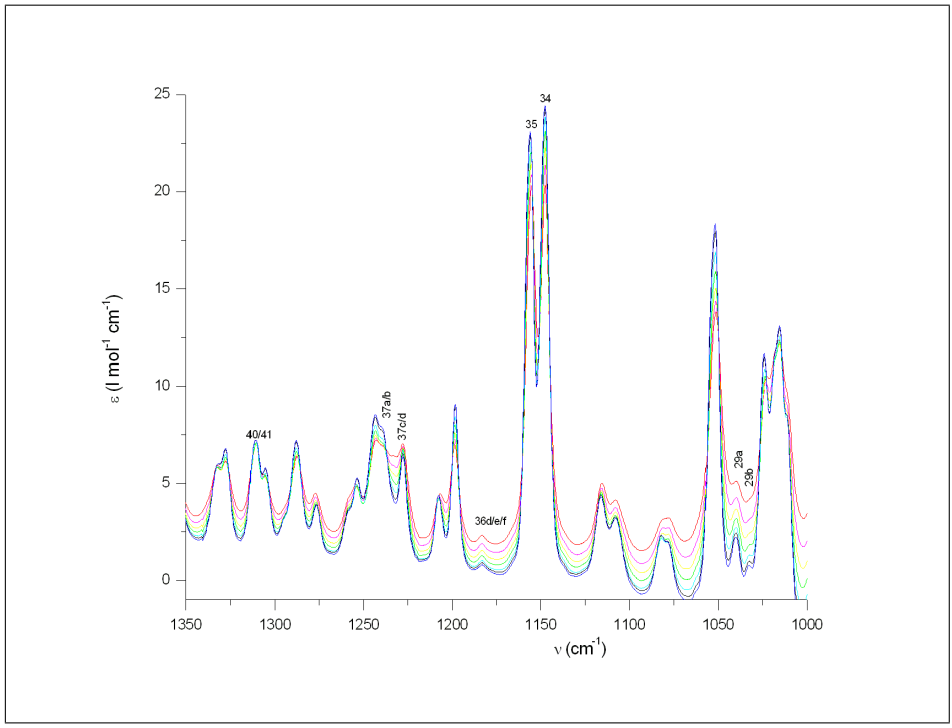


**Figure 8.46:** Comparison of the IR-spectra of limonene as a neat liquid at 298K (red), 273K (pink), 253K (yellow), 233K (green), 213K (cyan), 193K (black) and 183K (blue).

The xenon measurements, recorded at different temperatures, ranging from 208K to 169K, are shown in Figure 8.47 and Figure 8.48. Although the differences between the spectra are rather small, the same trends as for the previous experiments could be observed. Band 34 is increasing faster than band 35 at lower temperature. The intensity of the band 36 d/e/f, on the other hand, is not increasing. The intensity of band 37c is increasing much slower than band 37b and the same can be said about the band 38b/c toward band 37a and the band 41c toward band 41a/b. Due to the good resolution of the bands two additional trends could be observed. The intensity of the small shoulder at 1018 $cm^{-1}$, already discussed above, rises much slower than that of the band 27a (1015 $cm^{-1}$). Previously there were some doubts about the assignment of the shoulder but linking the band with normal modes 28b/d would allow us to explain the observation. These effects confirm that the contribution of the less stable rotamers diminishes with decrease of

temperature.

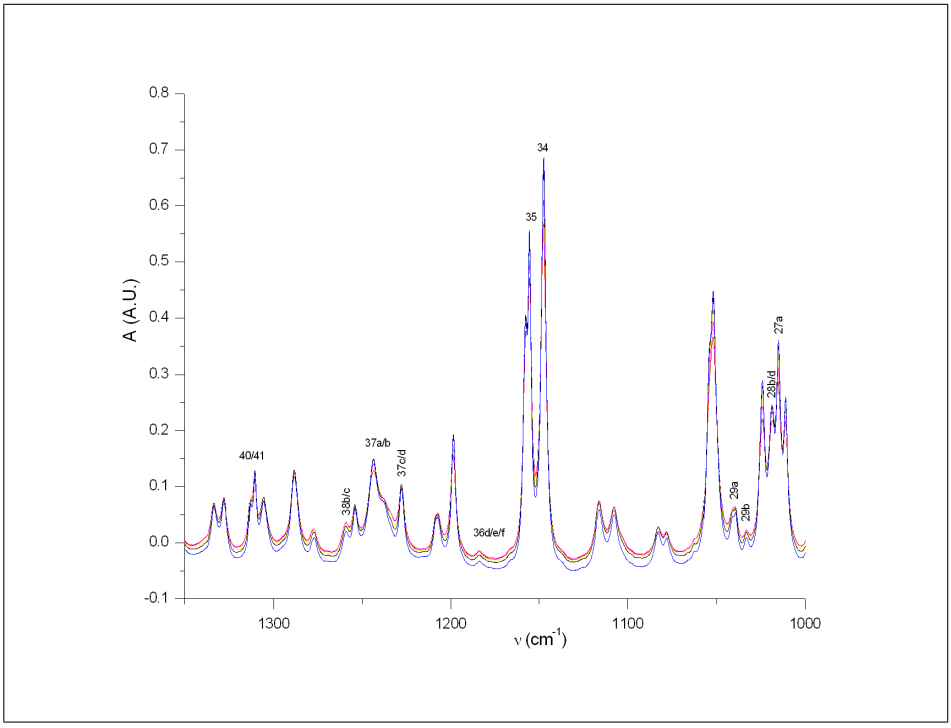


**Figure 8.47:** Comparison of the IR-spectra of limonene in Xe recorded at 208K (red), 198K (pink), 188K (yellow), 178K (black) and 169K (blue) between 1000 $cm^{-1}$ and 1350 $cm^{-1}$.

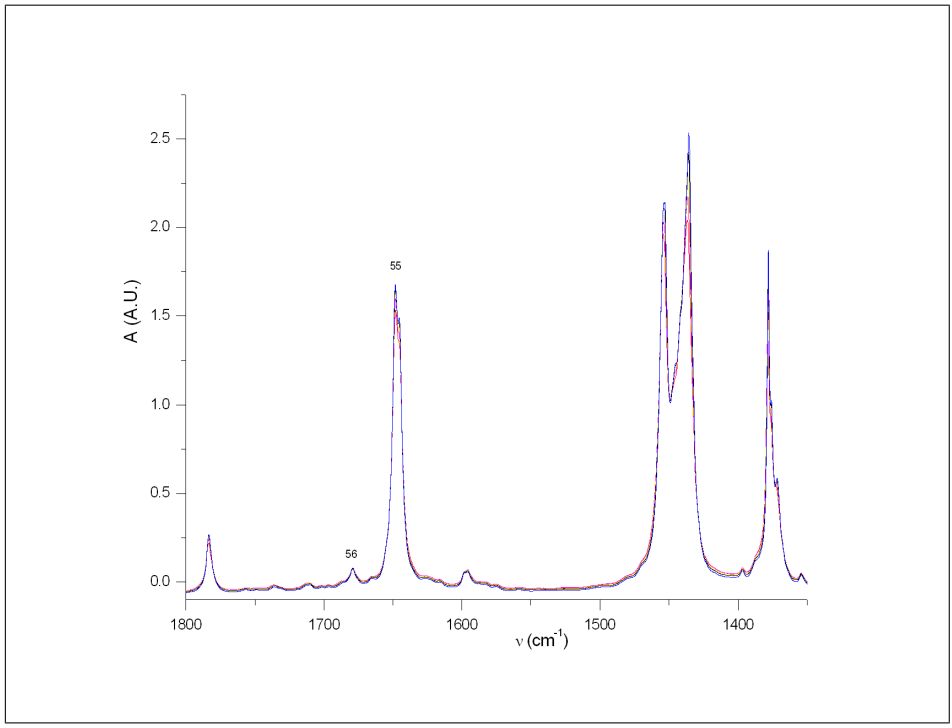


**Figure 8.48:** Comparison of the IR-spectra of limonene in Xe recorded at 208K (red), 198K (pink), 188K (yellow), 178K (black) and 169K (blue) between 1350 $cm^{-1}$ and 1800 $cm^{-1}$.

As a conclusion for the IR experiments, performed in different solvents, at various (lower) temperatures, one can state that all observations were reproducible. Most trends were explained by the decreasing contribution of the less stable conformers. Unfortunately even at 173K we still were not able to explain all bands in the IR spectrum by only taking into account the most stable rotamer.

**VCD measurements**: VCD measurements at lower temperatures are not straightforward. Due to the small S/N ratio, many scans are necessary to average out the noise. Therefore it is essential to keep the temperature steady during the experiment. First the VCD spectra of limonene in $CDCl_3$ were recorded at room temperature and 223K. These are depicted in Figure 8.49. Again most of the bands increase in intensity, except for the negative band 36d/e/f. The intensity of the negative band 35 (1151 $cm^{-1}$) becomes smaller. Furthermore a negative band turns up at 1145 $cm^{-1}$, the frequency where the band originating from

normal mode 34 is located. This is in contradiction with the calculations. With decrease in temperature, the positive intensity of normal mode 34 was predicted to rise even more.

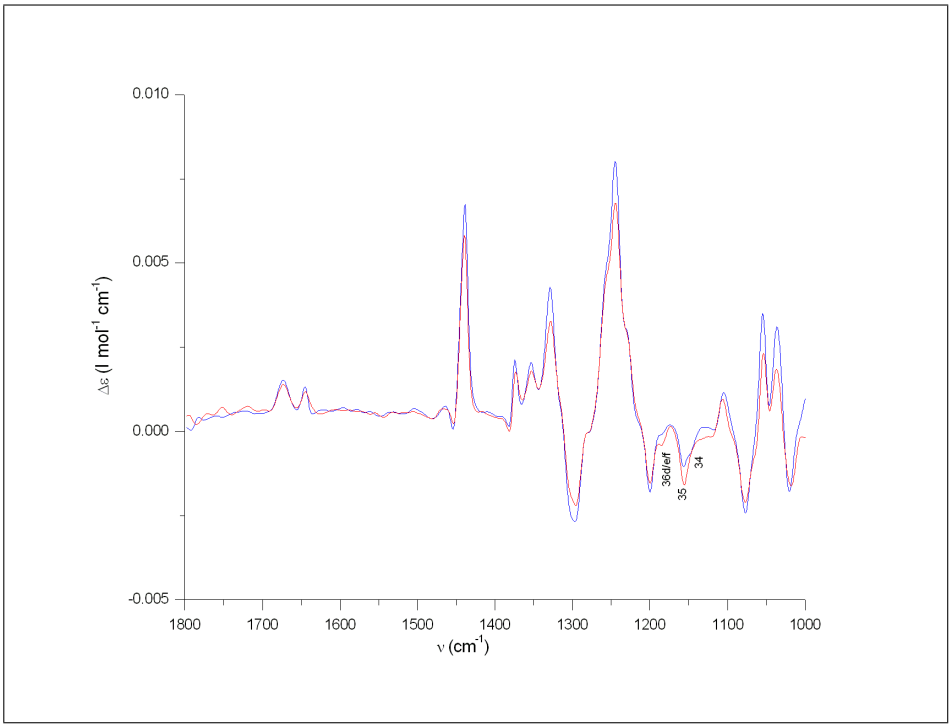


**Figure 8.49:** experimental VCD spectra of (+)-limonene in $CDCl_3$, recorded at 298K (red) and 223K (blue).

Figure 8.50 compares the VCD spectra of limonene in $CD_2Cl_2$, recorded at room temperature and at 183K. Again with decrease of temperature, the intensity of the bands rises except for those, linked with the less stable conformers. This is the case for the band 36d/e/f but also for the band 44b/c. This latter trend was not observed in $CDCl_3$, probably due to the fact that the gap between the extreme temperatures was too small. The most remarkable effect, again is the one observed around 1150 $cm^{-1}$. At 183K the negative bands 35 and 34 are almost equally intense, while at room temperature for normal mode 35 a negative band is seen but for normal mode 34, the VCD signal is almost equal to zero. As already stated above, this is in contradiction with the calculations. Considering the C=C stretching vibrations, another effect

can be observed. At lower temperatures, the band of the endocyclic C=C stretch (band 56) increases faster than the band originating from the exocyclic C=C (band 55) stretch. This is in line with theory, since the most stable conformer gives rise to a negative band for the exocyclic stretch.

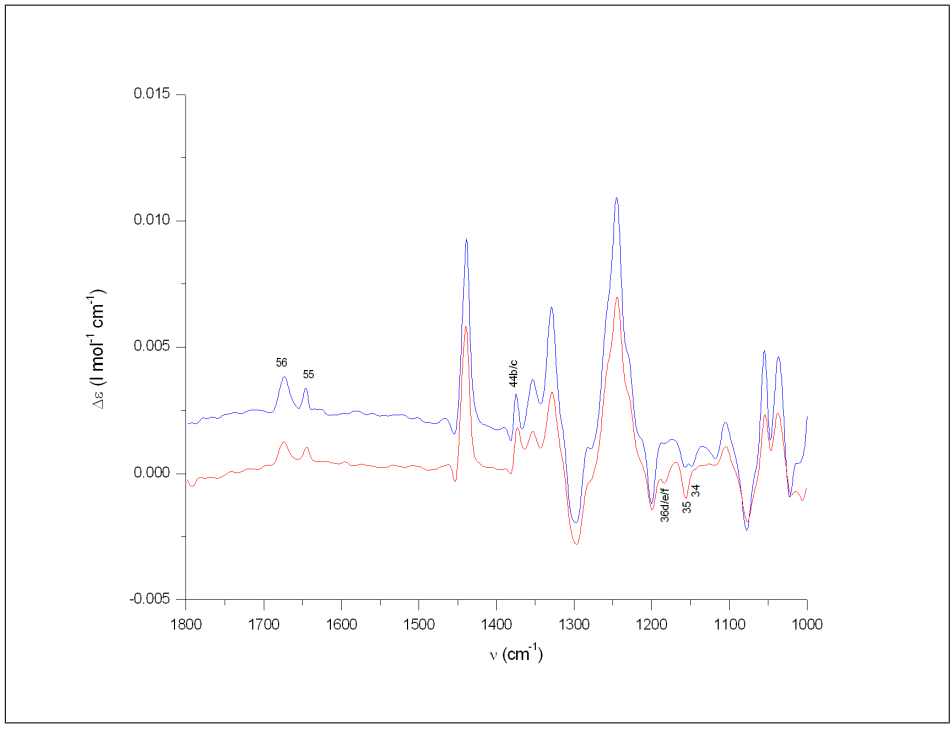


**Figure 8.50:** experimental VCD spectra of (+)-limonene in $CD_2Cl_2$, recorded at 298K (red) and 183K (blue).

VCD measurements were also performed for limonene in $CS_2$, as is depicted in Figure 8.51. Unfortunately, because of solvent absorptions, the region between 1400 $cm^{-1}$ and 1600 $cm^{-1}$ cannot be analyzed, but an advantage is that the minimal temperature is lowered to 173K using $CS_2$ as a solvent. The same temperature effects were observed as for the measurements in the other solvents. The trend concerning the C=C stretches are even more remarkable than for the measurements in $CD_2Cl_2$. Again attention needs to be drawn to the changes observed around 1150 $cm^{-1}$. The effect is somewhat different from the observations in $CDCl_3$ and $CD_2Cl_2$. For $CS_2$, the negative band at 1153 $cm^{-1}$

is shifted to 1145 $cm^{-1}$; while in $CDCl_3$ and especially in $CD_2Cl_2$ two negative bands are observed.

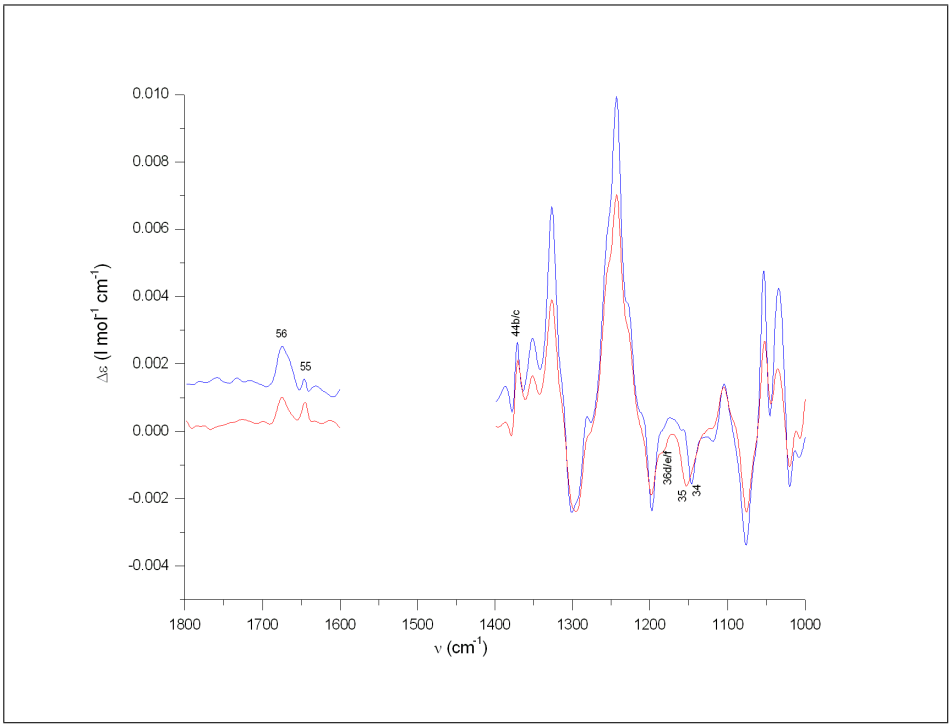


**Figure 8.51:** experimental VCD spectra of (+)-limonene in $CS_2$, recorded at 298K (red) and 173K (blue).

The last VCD experiments at various temperatures were done for the neat liquid. The spectra, recorded at room temperature and at 188K, are shown in Figure 8.52. These measurements were also able to reproduce the previous observations. The pattern around 1150 $cm^{-1}$ is similar to the effect observed in $CS_2$. It seems that this trend largely depends on the solvent used. This most probably due to the fact that the dielectric constants of $CS_2$ (2.7) and limonene (2.3) are very similar as well as those of $CDCl_3$ (4.9) and $CD_2Cl_2$ (8.93). Unfortunately, PCM calculations using the different solvents did not give an explanation for the trend.

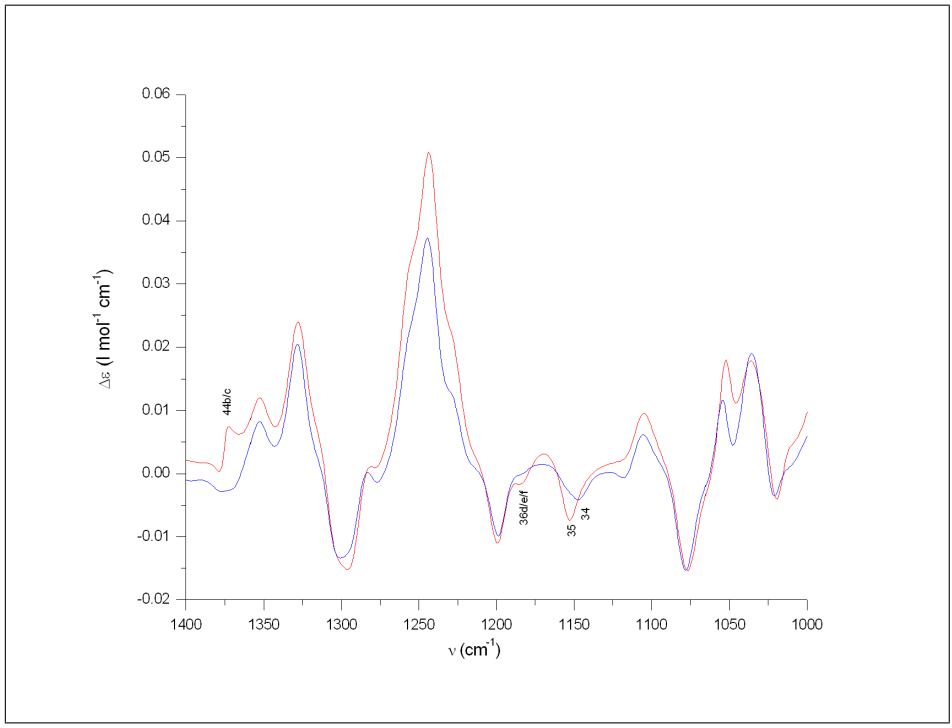


**Figure 8.52:** experimental VCD spectra of (+)-limonene as a neat liquid, recorded at 298K (red) and 188K (blue).

### Anharmonic Calculations

After varying temperature and solvent during the experiments, we still were not able to explain every observable in the VCD spectra. Moreover, by recording the VCD at various temperatures, an inexplicable but reproducible trend was seen. The origin of the effect, however, could not be retrieved by harmonic calculations. The measurements in xenon reveal, due to the better resolution, some additional bands, especially around 1000 $cm^{-1}$ and between 1600 $cm^{-1}$ and 1800 $cm^{-1}$. Again the origin of these bands could not be interpreted. Therefore in an additional attempt to explain each feature of the IR and VCD spectrum of limonene between 1000 $cm^{-1}$ and 2000 $cm^{-1}$, the anharmonic frequencies of the normal modes, overtones and combination bands were calculated. Comparing the anharmonic frequencies toward the harmonic ones in the mid-IR region, a red shift was observed for all fundamentals. In contrast with the C-H stretching region, the sequence of the normal modes remained the same. This is analogous to the anharmonic studies of several other molecules [185, 186, 164]. Therefore, we were still unable to explain the observables around 1150 $cm^{-1}$ and 1450 $cm^{-1}$. During these anharmonic calculations, combination bands were considered as well. Several combination bands were found in the region between 1000 $cm^{-1}$ and 2000 $cm^{-1}$. The possible appearance of such bands might explain the discrepancies between the harmonic calculations and the experiment at 1150 $cm^{-1}$ and 1450 $cm^{-1}$. All calculated combinations bands around 1150 $cm^{-1}$ and 1450 $cm^{-1}$ for each conformer are listed in Table 8.8 and Table 8.9 respectively. Unfortunately, no information was obtained about the intensity of these bands. Correlation corrected vibrational self - consistent field (CC - VSCF) is a method that enables us to calculate the anharmonic intensities by employing a grid representation of the potential over a region of the space of normal coordinates [182]. The algorithm, however, only is suitable for smaller molecules (up to 8 atoms). Codes in which only the interacting normal coordinates were taken into account allow us to calculate larger grid systems, but are limited to 4 normal coordinates. Unfortunately, for limonene this amount is exceeded. Since the intensities of the combination bands could not be retrieved, it is very hard to verify whether they might be responsible for the observed VCD features around 1150 $cm^{-1}$ and 1450

$cm^{-1}$. The bands between 1600 $cm^{-1}$ and 1800 $cm^{-1}$, which could not be linked with any fundamentals, probably also correspond to overtones or combination bands.

**Table 8.8:** Calculated combinations bands around 1150 $cm^{-1}$. The frequencies in $cm^{-1}$ are scaled with a factor of 0.967.

| Conf | Mode | Mode | freq | Conf | Mode | Mode | freq |
|---|---|---|---|---|---|---|---|
| b | 3 | 26 | 1140 | a | 1 | 33 | 1149 |
| b | 1 | 33 | 1142 | a | 4 | 26 | 1149 |
| d | 1 | 33 | 1144 | b | 5 | 26 | 1150 |
| b | 4 | 26 | 1144 | c | 2 | 32 | 1151 |
| a | 6 | 25 | 1144 | c | 7 | 22 | 1152 |
| a | 2 | 32 | 1145 | c | 4 | 26 | 1153 |
| b | 6 | 25 | 1145 | b | 2 | 32 | 1153 |
| a | 8 | 21 | 1146 | a | 5 | 26 | 1154 |
| d | 2 | 32 | 1146 | a | 7 | 24 | 1155 |
| c | 3 | 27 | 1146 | c | 5 | 26 | 1158 |
| b | 7 | 22 | 1147 | b | 15 | 16 | 1160 |
| a | 7 | 23 | 1147 | b | 7 | 23 | 1160 |

**Table 8.9:** A description of the calculated combinations bands around 1450 $cm^{-1}$. The frequencies in $cm^{-1}$ are scaled with a factor of 0.967

| Conf | Mode | Mode | freq | Conf | Mode | Mode | freq |
|---|---|---|---|---|---|---|---|
| a | 11 | 29 | 1450 | d | 4 | 39 | 1457 |
| c | 12 | 28 | 1450 | c | 2 | 44 | 1457 |
| d | 14 | 24 | 1450 | a | 9 | 34 | 1457 |
| d | 12 | 29 | 1450 | d | 15 | 23 | 1457 |
| c | 11 | 29 | 1451 | b | 3 | 39 | 1457 |
| c | 9 | 34 | 1451 | b | 11 | 30 | 1458 |
| a | 7 | 36 | 1451 | d | 6 | 38 | 1458 |
| b | 7 | 36 | 1452 | c | 13 | 26 | 1458 |
| a | 1 | 45 | 1454 | a | 4 | 39 | 1458 |
| b | 2 | 44 | 1454 | d | 11 | 30 | 1458 |
| c | 1 | 47 | 1454 | b | 9 | 34 | 1459 |
| b | 12 | 29 | 1455 | d | 2 | 44 | 1459 |
| d | 14 | 25 | 1455 | c | 9 | 35 | 1459 |
| a | 1 | 46 | 1456 | a | 11 | 30 | 1459 |
| d | 6 | 37 | 1456 | a | 12 | 27 | 1459 |
| d | 8 | 34 | 1456 | a | 14 | 25 | 1460 |
| a | 17 | 18 | 1456 | d | 3 | 40 | 1461 |
| a | 13 | 26 | 1457 | b | 4 | 39 | 1461 |
| c | 3 | 40 | 1457 | | | | |

### 8.4.5 Conclusions

The analysis of the IR and VCD spectra of limonene, a rather simple terpene, is far from straightforward. There are some discrepancies between the harmonic calculations of a free limonene molecule in vacuum and the recorded IR and VCD spectra. In the VCD spectra, two bands show opposite signs compared with the calculations, i.e. band 34 and band 48-52. Measurements in different solvents, at various temperatures did not enable us to elucidate every feature observed in the experimental spectra. Although the frequency shifts of the C=C stretchings were very well reproduced by the PCM calculations; those of modes 34 and 35 were not. Most of the temperature effects were explained by the decrease of contribution of less stable conformers at lower temperatures. The reproducible and very remarkable effect around 1150 $cm^{-1}$ (modes

34 and 35), however, could not be verified this way. Therefore anharmonic frequency calculations were introduced. In the mid-IR region, except from the red shift of the frequencies, no changes were observed. During these calculations, the frequencies of the overtones and combination bands were calculated as well. Some of the combination bands are located around 1150 $cm^{-1}$ and can thus be the reason for the discrepancy with the experiment. This statement could only be verified if the intensities of those bands were known. Unfortunately, this is not the case. The differences between experiment and theory at 1450 $cm^{-1}$ and those between 1600 $cm^{-1}$ and 1800 $cm^{-1}$ can possibly also be explained by the presence of combination bands and overtones. In order to explain every feature of the VCD spectrum of limonene in the mid-IR frequency region, harmonic calculations of the normal modes are not sufficient. Combination bands and overtones need to be taken into account. This is probably why the assignment of the VCD spectrum of limonene between 1000 $cm^{-1}$ and 2000 $cm^{-1}$ has not been published yet.

# 9

# Summary and Conclusions

VCD has become a powerful method to study absolute configurations and conformational properties of chiral molecules. Figure 9.1 reports the number of VCD studies published per year. The interest toward VCD is clearly growing anually. Until 1996, most papers dealt with the fundamentals of FTIR VCD measurements and the theory of VCD intensities. The last years, VCD papers began to appear in experimental and high impact journals such as Journal of the American Chemical Society, Journal of Organic Chemistry, Tetrahedron, Journal of Physical Chemistry, etc. Nowadays, about 30-40 research groups worldwide are using this technique to assign absolute configurations of chiral molecules.

In this thesis the overall applicability of VCD has been studied, with emphasis on the possible pitfalls. In Chapter 5, VCD assignments were performed for four bicylco[3.3.0]octane derivates, each containing four chiral centers. During the VCD analysis, all diastereomers were taken

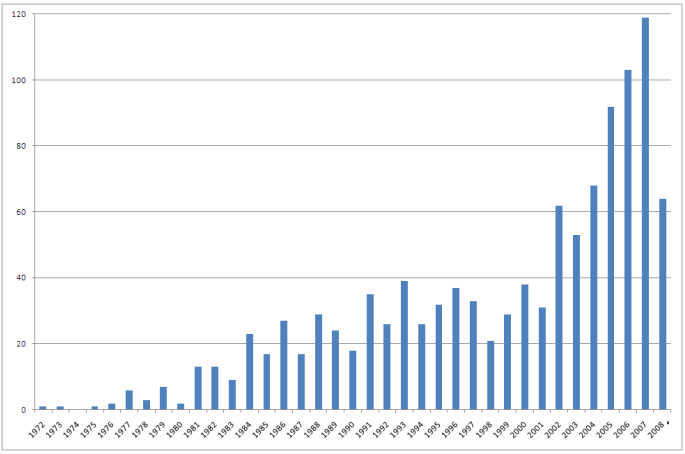


**Figure 9.1:** The number of annual VCD related papers. * The cited number for 2008 is incomplete (August 2008). Source: SciFinder Scholar Database

into account. Additional information about relative stereo chemistries has not been considered. For each molecule, the 6-31G(d) basis set allowed a satisfactory simulation of the experimental spectra. Moreover, no large differences were observed with respect to the cc-pVTZ calculations. The assignment of every product could afterwards be rationalised by the synthetic pathway. This way it has been shown that the VCD technique can also be useful to distinguish diastereomers.

Chapter 6 involves the assignment of absolute configuration of flexible molecules by VCD. In particular the absolute configuration of DPP II inhibitors was confirmed by studying their benzyloxycarbonyl (Z)-protected analogues. These molecules contain 3 chiral centers and have 14 variable dihedral angles. Therefore, conformational analysis is the most critical step during the assignment process. Due to the large flexibility of the molecules we were not able to simulate the experimental IR and VCD spectra. This problem was by-passed by modifying the products to more rigid structures. Moreover, calculations were facilitated by reducing the number of chiral centers from three to two. Since the absolute configuration of one chiral center (5S) was known, and since during truncation the stereochemistry was not altered, it is justified to determine the chirality of the DPP II inhibitors by assigning the truncated molecules through VCD spectroscopy. The calculated IR and VCD spectra of the smaller molecules were in large agreement with

the experiments and a VCD assignment of the inhibitors was possible. This technique can, in theory, readily be transposed to other large and flexible molecules.

In Chapter 7 the influence of the solvent on the VCD spectra is discussed. VCD experiments involve the measurements of solutions, on the one hand, while, on the other hand, VCD calculations are done for one chiral molecule in vacuo. This might lead to several discrepancies between theory and experiment and may therefore influence our assignment. Experimental VCD results of camphor solutions in $CDCl_3$ and $CD_2Cl_2$ have been compared with DFT simulations. For the frequency region between 1000 $cm^{-1}$ to 2000 $cm^{-1}$ no remarkable differences between experiment and theory have been observed. Considering the wavenumbers from 2000 $cm^{-1}$ to 3000 $cm^{-1}$, a VCD band was seen at about 2250 $cm^{-1}$ for solutions in $CDCl_3$. This band, however, could not be reproduced during the calculations. Taking into account the D-interaction between the carbonyl function of camphor and the C-D of the solvent and calculating the VCD spectrum of the 1:1 camphor.$CDCl_3$ association, enabled us to explain the origin of the band. A solvent molecule can become VCD active through interaction with camphor and the CD stretching vibration in $CDCl_3$ gives rise to a VCD signal around 2250 $cm^{-1}$. Both enantiomers of the chiral solute induced opposite signs. This is in agreement with the simulations. In order to prove this trend, the VCD spectra of the solutes in binary mixtures of $CDCl_3$ and $CD_2Cl_2$ have also been recorded. It is shown that as the mole fraction of $CDCl_3$ decreases, the CD stretching band gets smaller. This qualitative agreement between experiment and calculations proves that chirality of the solvent can be induced by intermolecular interactions between the solute and solvent molecules. Subsequently, the VCD spectra of pulegone, dissolved in $CDCl_3$, $CD_2Cl_2$ or $CS_2$, were studied. First, the frequency region from 1000 $cm^{-1}$ to 2000 $cm^{-1}$ was considered. The sign of the band, originating from the C=O stretching vibration, is wrongly predicted by the calculations of free pulegone in vacuo. Taking into account the solvent through the PCM model, enabled us to obtain overall agreement with the experiments. Even for the measurement in $CS_2$, a solvent with a smaller dipole moment, PCM calculations were necessary in order to predict the correct sign. In the experimental IR spectrum of solutions in $CDCl_3$, the band, originating from the C=C stretching

vibration is spread out. This can only be explained by taking into account the stable conformations of the 1:1 pulegone.$CDCl_3$ associations. Studying the VCD spectra of pulegone in $CDCl_3$ in the frequency region between 2000 $cm^{-1}$ and 2500 $cm^{-1}$, a signal was observed at about 2250 $cm^{-1}$. Simulating the VCD spectra of the 1:1 pulegone.$CDCl_3$ associations enabled us explain the origin of the band. Chirality is induced into the solvent and the CD stretch vibrations becomes VCD active. This is completely in line with our previous VCD study of camphor in that region and therefore proves that chirality induction into the solvent is a relatively common effect. Hereby, we demonstrated that even for molecules as simple as pulegone and camphor, some bands only can be explained by taking into account the solvent during the calculations.

In Chapter 8 the influence of temperature on the VCD spectra was studied. It was assumed that lowering temperatures would simplify the assignment. Using the Boltzmann distribution as a model for the conformational weights, measurements at lower temperatures should reduce populations of higher energy conformations in favor of the global minimum. This has been studied for 3-methylcyclohexanone, borneol and limonene. Depending on the solvent, different minimal temperatures could be reached. In order to carry out the experiments, the sample space of the Bruker PMA 37 was modified and a low-temperature cell was introduced. Cooling was performed using liquid nitrogen, while heating was performed with a small electrical heating element. The VCD experiments of 3-methylcyclohexanone confirmed our assumption. During conformational analysis, two conformers were found. The conformer with its methyl substituent in equatorial position was found to be more stable than the minimum with an axial methyl substituent. A temperature study revealed that the bands, originating from the axial conformer, decrease in intensity at lower temperatures. Unfortunately, the effects are rather small, due to the fact that even at room temperature the contribution of the axial conformer already is minimal. Nonetheless, the few trends were well reproduced for each solvent and could all be explained by the ab initio calculations. The measurements of borneol at lower temperatures show that, in order to explain every observed feature, it is necessary to take into account the presence of dimers. An intermolecular hydrogen bonding between two monomer conformations has a stabilizing effect. Therefore the dimers were modeled by considering

every possible combination of two monomer conformations and their corresponding vibrational data were calculated. The equilibrium between the monomer and dimer was evaluated using a concentration variation study in $CDCl_3$. Almost every feature, observed during the temperature study, needed to be explained by the increasing contribution of the dimers. In case of borneol, measurements at lower temperatures did not facilitate the assignment, as was supposed. On the contrary it was necessary to consider the intermolecular interactions that gain importance at lower temperatures. Finally, limonene was subjected to a temperature study. The analysis of the IR and VCD spectra of limonene, a rather simple terpene, however, does not seem to be straightforward. Even at room temperature some discrepancies were observed between the harmonic calculations of a free limonene molecule in vacuum and the recorded IR and VCD spectra. Measurements in different solvents, at various temperatures did not allow us to elucidate every feature observed in the experimental spectra. Therefore anharmonic frequency calculations were introduced. In the mid-IR region, except from the red shift of the frequencies, no changes were observed. The appearance of combination bands can thus be the reason for the discrepancy with the experiment. Unfortunately, this statement could only be verified in case the intensities of those bands were known. The fact that harmonic calculations are insufficient to explain every feature is probably the reason why the assignment of the VCD spectrum of limonene between 1000 $cm^{-1}$ and 2000 $cm^{-1}$ has not been published yet.

Based on this dissertion, it can be stated that VCD assignments are not always straightforward. This is certainly true for large molecules, but even for rather simple molecules, such as e.g. limonene, it can be hard to explain every feature, observed in the experimental spectrum. Although sufficient criticism during the assignment is required, VCD is a very powerful method to study absolute configurations.

Since most pharmaceutical molecules are large and flexible, further research is needed, to simplify the simulation of the observed spectra, thereby reducing the amount of CPU required for these calculations.

# 10

# Samenvatting

## 10.1 Inleiding

Chiraliteit is afgeleid van het Griekse woord voor hand, $\chi\epsilon\iota\rho$. Chirale molecules kunnen niet gesuperponeerd worden op hun spiegelbeeld. Dergelijke molecules en hun spiegelbeelden worden enantiomeren van elkaar genoemd. Chemici omschrijven de enantiomeren via het R/S systeem. Daarbij wordt ieder chiraal centrum gekarakteriseerd door R of S, volgens een methode waarbij aan de substituenten een prioriteit worden toegewezen volgens de Cahn Ingold Prelog prioriteitsregels, gebaseerd op het atoomnummer. Een enantiomeer kan ook benoemd worden volgens de richting waarin het vlak van het gepolariseerde licht draait ((+) voor rotatie in wijzerszin, (-) voor rotatie tegen wijzerszin). Enantiomeren hebben hebben veel met elkaar gemeen (gelijke massa, gelijke NMR en IR spectra,...), maar verschillen zijn zichtbaar in de omgeving van

andere chirale molecules (of objecten). Beide isomeren van limoneen bijvoorbeeld hebben verschillende geuren: (-)-limoneen ruikt naar pijnboom of terpentijn, terwijl zijn enantiomeer, (+)-limoneen, de geur van sinaasappels veroorzaakt. Molecules, met meer den één chiraal centrum kunnen isomeren vormen met omgekeerde absolute configuratie in één (of meerdere) chirale centra en zijn niet per se spiegelbeelden van elkaar. In dit geval spreekt men van diastereomeren.

Omwille van hun verschillende biologische activiteit, worden chirale molecules ook steeds belangrijker in de farmaceutische industrie. Vaak vertoont het ene enantiomeer een farmacologisch effect, terwijl het andere minder actief of zelfs toxisch kan zijn. Het best gekende voorbeeld hiervan is $Thalidomide^{®}$, ook gekend als $Softenon^{®}$. Thalidomide werd voor het eerst op de Europese markt gebracht rond 1950. Het werd gebruikt als slaappil en om ochtend misselijkheid tijdens de zwangerschap te behandelen. Toen wist niemand dat het teratogene S enantiomeer afwijkingen bij de geboorte veroorzaakte. Het is bijgevolg uiterst belangrijk de biologische activiteit van specifieke enantiomeren in chirale geneesmiddelen te kennen. Door de stijgende voorkeur voor het afzonderlijke enantiomeer in de farmaceutische industrie heeft de *Food and Drug Administration* (FDA) richtlijnen opgesteld inzake de ontwikkeling van nieuwe chirale geneesmiddelen. Vanaf 1987 moet de absolute configuratie vermeld worden in het rapport dat het nieuwe geneesmiddel omschrijft. De stijgende vraag naar enantiopure chirale componenten geldt niet enkel in de farmaceutische industrie, maar ook in andere sectoren, waarin smaak en geur chemicaliën, landbouw chemicaliën en hoogwaardige materialen worden geproduceerd. Daarom is er een hoge nood aan toegankelijke technieken voor de bepaling van absolute configuraties. Een zeer belangrijke techniek daarvoor, is éénkristal X-straal diffractie. Deze techniek is niet altijd toepasbaar aangezien de éénkristallen onderhevig zijn aan anomale verstrooiing. Voor standaard X-straal diffractie experimenten komt dat neer op de aanwezigheid van zware atomen. Een alternatieve methode, electronisch circulair dichroisme (ECD), maakt gebruik van UV/VIS-links en rechts draaiend licht dat op verschillende wijze wordt geabsorbeerd door de chirale moleculen. Bij deze techniek is het vereist dat chromofore groepen aanwezig zijn op de moleculen. Nog andere methoden zijn nucleaire magnetische resonantie (NMR), optische rotatie (OR) en stereospecifieke synthese. Een

relatief nieuwe techniek is het vibrationeel circulair dichrosme (VCD).

## 10.2 Vibrational Circular Dichroism

VCD meet, net zoals ECD, het verschil in absorbantie van links- en rechtsdraaiend circulair gepolariseerd licht. Bij VCD wordt IR licht gebruikt. Daardoor combineert de techniek de stereochemische gevoeligheid met de structurele specificiteit van infraroodspectroscopie. Deze methode heeft als bijkomend voordeel dat de metingen op nagenoeg exact dezelfde manier gebeuren als infrarood experimenten, en dat dus relatief weinig eisen worden gesteld aan de moleculen. Zo kunnen VCD metingen ook gebeuren in oplossing. Omdat VCD een differentiële spectroscopische techniek is, kunnen deze intensiteiten ook negatief zijn; bovendien zijn de VCD spectra van twee enantiomeren gespiegeld ten opzichte van de frequentie-as. De interpretatie van experimentele VCD spectra is echter niet voor de hand liggend. Voor een bepaald enantiomeer zijn sommige banden positief en andere negatief zonder dat dit gemakkelijk kan worden gerationaliseerd. Voor een betrouwbare evaluatie van de absolute configuratie, moet het experimentele VCD spectrum vergeleken worden met een gesimuleerd/berekend VCD spectrum. Met behulp van DFT kunnen theoretische spectra van goede kwaliteit bekomen worden, in overeenstemming met experimentele waarnemingen en met aanvaardbare computationele kost.

## 10.3 Doelstellingen van de thesis

Tegenwoordig zijn VCD spectrometers commercieel verkrijgbaar, evenals software pakketten waarin de VCD algorithmes reeds werden ge¨implementeerd. Dit impliceert de routinematige toepasbaarheid van VCD als een methode waarmee de absolute configuratie van chirale moleculen kan worden bepaald. VCD wordt niet enkel meer gebruikt in universiteiten, maar ook industriële bedrijven (vooral farmaceutische bedrijven) hebben een stijgende interesse voor de techniek. De methode werd door de FDA aanvaard als bewijs voor de absolute configuratie. Het doel van deze thesis is om de limieten van de toepasbaarheid van VCD te onderzoeken. Het is van vitaal belang dat alle toewijzingen op een correcte manier worden uitgevoerd. Eén verkeerde toewijzing kan se-

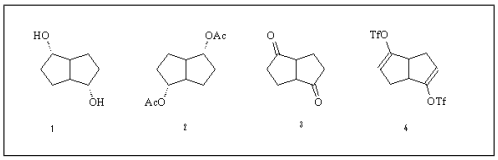


**Figure 10.1:** 1)Bicyclo[3.3.0]octane-2,6-diol, 2) 2,6-diacetoxybicyclo[3.3.0]octane, 3) Bicyclo[3.3.0]octane-2,6-dione and 4) Bicyclo[3.3.0]octa-2,6-dien-2,6-bistriflate.

rieuze gevolgen hebben. Doorheen de verschillende hoofdstukken werd nagegaan:

- of VCD bruikbaar is om diastereomeren van elkaar te onderscheiden.
- of VCD toepasbaar is op zeer flexibele moleculen.
- in hoeverre het solvent een invloed heeft op de experimentele VCD spectra.
- in hoeverre de temperatuur de experimentele VCD spectra zal beïnvloeden.

## 10.4 Samenvatting van de resultaten en conclusie

In hoofdstuk 5 werden vier bicyclo[3.3.0]octaanderivaten bestudeerd met behulp van VCD (zie Figuur 10.1). Elk van deze molecules bezit 4 chirale centra. Tijdens de VCD analyse werden alle diastereomeren in rekening gebracht. Extra informatie in verband met de relatieve stereochemie werd niet beschouwd. Voor iedere molecule bleek de 6-31G(d) basis set voldoende voor de bepaling van de absolute configuratie. De toewijzing werd achteraf gerationaliseerd met behulp van de syntheseweg. Op die manier werd aangetoond dat VCD ook gebruikt kan worden voor het onderscheiden van diastereomeren.

Hoofdstuk 6 behandelt de toewijzing van flexibele moleculen via VCD. Hiervoor werd, in het bijzonder, de absolute configuratie van DPP II inhibitoren bepaald door hun benzyloxycarbonyl (Z)-beschermde analogen te bestuderen (zie Figuur 10.2). Deze moleculen bezitten 3 chirale centra. 14 dihedrale hoeken werden gevarierd tijdens de conforma-

tionele analyse. Door de grote flexibiliteit van de molecule was het onmogelijk de experimentele IR en VCD spectra te simuleren. Dit probleem werd omzeild door de producten te modifiëren naar rigidere structuren (zie Figuur 10.2). Daarenboven werden de berekeningen vereenvoudigd doordat het aantal stereocentra werd gereduceerd naar 2. Aangezien de stereochemie tijdens de modificatie niet werd veranderd, is het verantwoord de absolute configuratie van de DPP II inhibitoren te bepalen via de toewijzing van de verkorte structuren. Hun berekende IR en VCD spectra waren in overeenstemming met het experiment en daardoor was een toewijzing van de inhibitoren mogelijk.

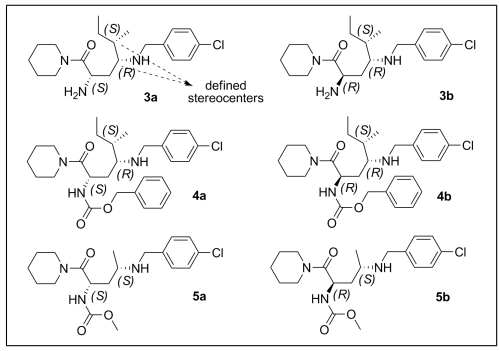


**Figure 10.2:** 4)benzyl(2S/R,4R,5S)-4-(4-chlorobenzylamino)-5-methyl-1-oxo-1-(piperidin-1-yl)heptan-2-ylcarbamate; 5)(2R/S,4S)-4-(4-chlorobenzylamino)-1-oxo-1-(piperidin-1-yl)pentan-2-ylcarbamate

Hoofdstuk 7 beschrijft de invloed van het solvent op de VCD spectra. VCD experimenten worden uitgevoerd in oplossing terwijl de berekeningen worden gedaan voor één enkele vrije molecule in vacuum. Dit kan aanleiding geven tot een aantal verschillen tussen theorie en experiment en kan dus daardoor de toewijzing beïnvloeden. Experimentele VCD resultaten van kamfer (zie Figuur 10.3) in $CDCl_3$ en $CD_2Cl_2$ werden vergeleken met DFT simulaties. Tussen 1000 $cm^{-1}$ en 2000 $cm^{-1}$ werden geen verschillen opgemerkt. Voor het gebied van 2000 $cm^{-1}$ tot 3000 $cm^{-1}$ werd, voor oplossingen in $CDCl_3$, een VCD band geobserveerd bij 2250 $cm^{-1}$, terwijl deze niet zichtbaar was in het berekende spectrum. Door de waterstofbrug tussen de carbonyl functie van kamfer en de C-D binding van het solvent in rekening te brengen en dus het VCD spectrum van de 1:1 kamfer.$CDCl_3$ associatie te berekenen, kon de oorsprong van de band achterhaald worden. Een solvent molecule

kan VCD actief worden door interactie met kamfer en de CD rekvibratie in $CDCl_3$ geeft aanleiding tot een VCD signaal rond 2250 $cm^{-1}$. De kwalitatieve overeenkomst tussen experiment en berekeningen bewijst dat chiraliteit kan geïnduceerd worden in het achirale solvent. Dit gebeurt door intermoleculaire interacties tussen de solvent moleculen en de opgeloste stof. In hetzelfde hoofdstuk werden de VCD spectra van pulegon (zie Figuur 10.3) in $CDCl_3$, $CD_2Cl_2$ en $CS_2$ bestudeerd. De metingen in $CDCl_3$ bevestigden voorgaande observatie. Opnieuw kon het VCD signaal, afkomstig van de CD rekvibratie van $CDCl_3$ worden gereproduceerd via de simulatie van het VCD spectrum van de 1:1 pulegon.$CDCl_3$ associatie. Voor het gebied tussen 1000 $cm^{-1}$ en 2000 $cm^{-1}$ werd een goede overeenkomst gevonden tussen experiment en theorie. Het teken van de band afkomstig van de C=O rekvibratie, daarentegen, werd verkeerd voorspeld via de berekeningen van pulegon in vacuum. Het solvent werd in rekening gebracht via het PCM model en zo werd ook voor de rekvibratie afkomstig van de carbonylfunctie het correcte teken verkregen. Beide voorgaande studies tonen dat, zelfs voor eenvoudige molecules als kamfer en pulegon, sommige banden enkel verklaard konden worden door het solvent in rekening te brengen tijdens de berekeningen.

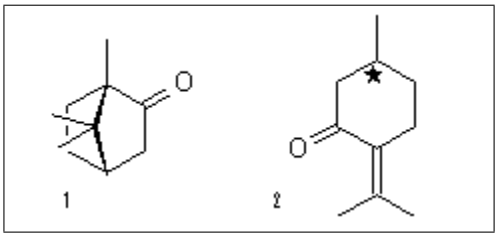


**Figure 10.3:** 1) kamfer, 2) pulegon

Tenslotte werd de invloed van de temperatuur op het VCD experiment bestudeerd (Hoofdstuk 8). Er werd verondersteld dat meten bij lagere temperaturen de toewijzing zou vereenvoudigen. Via de Boltzmannverdeling kan aangetoond worden dat bij lagere temperaturen de populaties van de minst stabiele conformeren worden gereduceerd ten voordele van de meest stabiele conformatie. Deze veronderstelling werd getest met behulp van 3-methylcyclohexanon, borneol en limonene (zie Figuur 10.4). Afhankelijk van het solvent konden verschillende minimale

temperaturen worden bereikt. Om de experimenten te kunnen uitvoeren, moest de monsterhouder worden aangepast en een lage-temperatuurcel werd gebruikt. Koelen gebeurde met behulp van vloeibare stikstof terwijl het monster opnieuw werd verwarmd met een elektrisch verwarmingselement. De VCD experimenten van 3-methylcyclohexanon bevestigden onze veronderstelling. Tijdens de conformationele analyse werden 2 conformeren gevonden. Een temperatuurstudie openbaarde dat intensiteit van de banden afkomstig van het minst stabiele conformeer verminderde bij lagere temperaturen. De effecten waren echter zeer klein. Desalniettemin konden de trends worden gereproduceerd voor de verschillende solventen en konden ze verklaard worden met behulp van de DFT berekeningen. De metingen van borneol bij lagere temperaturen tonen aan dat, om ieder effect te verklaren, dimeren moeten in rekening worden gebracht. Een intermoleculaire H-brug tussen twee monomeren heeft een stabiliserend effect. Bijna iedere trend moest worden verklaard door het stijgende aandeel van de dimeren. In het geval van borneol werd de toewijzing van de banden dus niet vereenvoudigd bij lagere temperaturen. Tenslotte werd limoneen onderworpen aan een temperatuurstudie. De IR en VCD analyse van limoneen, een eenvoudig terpeen, was echter niet vanzelfsprekend. Zelfs bij kamertemperatuur werden verschillen opgemerkt tussen theorie en experiment. Metingen in verschillende solventen en bij verschillende temperaturen hielpen ons niet bij het volledig verklaren van de spectra. Daarom werden anharmonische berekeningen uitgevoerd. In het midden-IR gebied werden, behalve een roodverschuiving van de banden, geen veranderingen ten opzichte van de harmonische berekeningen opgemerkt. De aanwezigheid van combinatiebanden in het gebied zou wel een reden kunnen zijn voor de verschillen met het experiment. Dit kon echter enkel bevestigd worden indien een mogelijkheid bestond de intensiteiten van de combinatiebanden te berekenen. Harmonische berekeningen lijken dus onvoldoende om alle banden in het spectrum te verklaren. Dat is waarschijnlijk de reden waarom een toewijzing van het VCD spectrum van limoneen tussen 1000 $cm^{-1}$ en 2000 $cm^{-1}$ nog niet werd gepubliceerd.

Gebaseerd op deze thesis kan gesteld worden dat VCD toewijzingen niet altijd vanzelfsprekend zijn. Dit is zeker waar voor grote moleculen, maar zelfs voor eenvoudige moleculen (zoals bijvoorbeeld limoneen) kan het moeilijk zijn ieder kenmerk van het experimentele spectrum te verk-

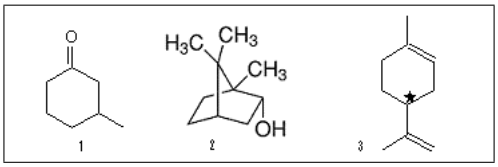


**Figure 10.4:** 1) 3-methylcyclohexanon, 2) borneol, 3) limoneen

laren. Hoewel toewijzingen kritisch moeten worden uitgevoerd, kan men stellen dat VCD een krachtige techniek is om de absolute configuratie van chirale moleculen te bepalen.

# Bibliography


[1] M.J. Frisch, A.E. Frisch, and Foresman J.B. *Gaussian 94 User's Reference*, volume 5. Gaussian Inc., Pittsburgh, January 1995.

[2] N.S. Ostlund and A. Szabo. *Modern Quanturm Chemistry: Introduction to Advanced Electronic Structure Theory.* Dover Publications Inc., 1996.

[3] I.N. Levine. *Quantum Chemistry.* Prentice Hall Inc., 1991.

[4] W. Koch and M.C. Holthausen. *A Chemist's Guide to Density Functional Theory*, volume 2. Strauss Offsetdruck, Germany, 2002.

[5] D. Yang. The a priori calculation of vibrational circular dichroism intensities. In K.B. Lipkowitz and D.B. Boyd, editors, *Reviews in Computational Chemistry*, volume 7, pages 261–301. Wiley-VCH, Inc., 1996.

[6] E. Debie, L Jaspers, P. Bultinck, W. Herrebout, and B. van der Veken. Induced solvent chirality: A vcd study of camphor in $CDCl_3$. *Chemical Physics Letters*, 450:426–430, 2008.

[7] E. Debie, P. Bultinck, W. Herrebout, and B. van der Veken. Solvent effects on IR and VCD spectra of natural products: an experimental and theoretical VCD study of pulegone. *Physical Chemistry Chemical Physics*, 10:3498–3508, 2008.

[8] R.S. Cahn, C.K. Ingold, and V. Prelog. Specification of molecular chirality. *Angewandte Chemie-International Edition*, 5:385–415, 1966.

[9] H. Caner, E. Groner, L. Levy, and I. Agranat. Trends in the development of chiral drugs. *Drug Discovery Today.*, 9:105 – 110, 2004.

[10] M.A. Rouhi. Chiral business. *C&EN Washington*, 81(81):45–55, 2003.

[11] M.A. Rouhi. Chiral chemistry. *C&EN Washington*, 82(24):47–62, 2004.

[12] J. Gal. Chiral drugs from a historical point of view. In E. Francotte and W. Lidner, editors, *Chirality in Drug Research.* Wiley - VCH, 2006.

[13] M.A. Rouhi. Top pharmaceuticals: A look at drugs that changed our world. *C&EN: special issue*, 83(25), 2005.

[14] S.S. Adams, P. Bresloff, and C.G. Manson. Pharmcacological differences between optical isomers of ibuprofen - evidence for metabolic inversion of (-) - isomer. *Journal of Pharmacy and Pharmacology*, 28:256–257, 1976.

[15] FDA policy statement for the development of new stereoisomericdrugs. *Chirality*, 4:338–340, 1992.

[16] H.D. Flack and G. Bernardinelli. Absolute structure and absolute configuration. *Acta Crystallographica Section A*, 55:908–915, 1999.

[17] H.D. Flack and G. Bernardinelli. Reporting and evaluating absolute-structure and absolute-configuration determinations. *Journal of Applied Crystallography*, 33:1143–1148, 2000.

[18] T.R. Hoye and D.O. Koltun. An NMR strategy for determination of configuration of remote stereogenic centers: 3-methylcarboxylic acids. *Journal of the American Chemical Society*, 120(19):4638–4643, 1998.

[19] T.R. Hoye, A.S.S. Hamad, O. Koltund, and M.A. Tennakoon. An NMR method for determination of configuration of beta-substituted carboxylic acids. *Tetrahedron Letters*, 41(14):2289–2293, 2000.

[20] K.M. Specht, J. Nam, D.M. Ho, N. Berova, R.K. Kondru, D.N. Beratan, P. Wipf, R.A. Pascal, and D. Kahne. Determining absolute configuration in flexible molecules: A case study. *Journal of the American Chemical Society*, 123(37):8961–8966, 2001.

[21] A.E. Hansen and K.L. Bak. Ab-initio calculations of electronic circular dichroism. *Enantiomer*, 4(5):455–476, 1999.

[22] F. Pulm, J. Schramm, J. Hormes, S. Grimme, and S.D. Peyerimhoff. Theoretical and experimental investigations of the electronic circular dichroism and absorption spectra of bicyclic ketones. *Chemical Physics*, 224(2-3):143–155, 1997.

[23] J. Novy, M. Urbanova, and K. Volka. Vibrational and electronic circular dichroism and absorption spectral study of the DNA-5,10,15,20-tetrakis(1-methylpyridinium-4-yl)porphyrin interaction. *Journal of Molecular Structure*, 748(1-3):17–25, 2005.

[24] K. Vandyck, B. Matthys, and J. Van der Eycken. Synthesis and absolute configuration of (1*S*,8*S*)-as-hydrindacene-1,8-diolas determined by the circular dichroism exciton chirality method. *Tetrahedron Letters*, 46:75–78, 2005.

[25] J.A. Schellman. Circular-dichroism and optical-rotation. *Chemical Reviews*, 75(3):323–331, 1975.

[26] K.B. Wiberg, P.H. Vaccaro, and J.R. Cheeseman. Conformational effects on optical rotation. 3-substituted 1-butenes. *Journal of the American Chemical Society*, 125(7):1888–1896, 2003.

[27] C.X. Zhao and P.L. Polavarapu. Comparative evaluation of vibrational circular dichroism and optical rotation for determination of enantiomeric purity. *Applied Spectroscopy*, 55(7):913–918, 2001.

[28] P.J. Stephens. Vibrational circular dichroism spectroscopy: A new tool for the stereochemical characterization of chiral molecules. In P. Bultinck, H. De Winter, W. Langenaeker, and J.P. Tollenaere, editors, *Computational medicinal chemistry for drugs discovery*, number 26, pages 699–725. Marcel Dekker Inc., New York, 2004.

[29] L.A. Nafie. Vibrational optical activity. *Applied Spectroscopy*, 50(5):14A–26A, 1996.

[30] P.L. Polavarapu. New spectroscopic tool - absolute-configuration determination of pharmaceutical compounds by vibrational circular-dichroism. *Spectroscopy*, 9(9):48–55, 1994.

[31] L.A. Nafie and R.K. Dukor. Applications of vibrational optical activity in pharmaceutical industry. In D.E. Pivonka, J.M. Chalmers, and P. R. Griffiths, editors, *Applications of Vibrational Spectroscopy*. Wiley, 2007.

[32] T. Kuppens, W. Herrebout, B. van der Veken, D. Corens, A. De Groot, J. Doyon, G. Van Lommen, and P. Bultinck. Elucidation of the absolute configuration of JNJ-27553292, a CCR2 receptor antagonist, by vibrational circular dichroism analysis of two precursors. *Chirality*, 18(8):609–620, 2006.

[33] T. Kuppens, W. Langenaeker, J.P. Tollenaere, and P. Bultinck. Determination of the stereochemistry of 3-hydroxymethyl-2,3-dihydro-[1,4]dioxino[2,3-b]pyridine by vibrational circular dichroism and the effect of DFT integration grids. *Journal of Physical Chemistry A*, 107(4):542–553, 2003.

[34] T. Kuppens, K. Vandyck, J. Van der Eycken, W. Herrebout, B.J. van der Veken, and P. Bultinck. Determination of the absolute configuration of three as-hydrindacene compounds by vibrational circular dichroism. *Journal of Organic Chemistry*, 70(23):9103–9114, 2005.

[35] P.L. Polavarapu, C.X. Zhao, A.L. Cholli, and G.G. Vernice. Vibrational circular dichroism, absolute configuration, and predominant conformations of volatile anesthetics: Desflurane. *Journal of Physical Chemistry B*, 103(29):6127–6132, 1999.

[36] M. Miyazawa, K. Inouye, T. Hayakawa, Y. Kyogoku, and H. Sugeta. Vibrational circular dichroism of proline-containing oligopeptides. *Applied Spectroscopy*, 50(5):644–648, 1996.

[37] K. Frimand, H. Bohr, K.J. Jalkanen, and S. Suhai. Structures, vibrational absorption and vibrational circular dichroism spectra

of l-alanine in aqueous solution: a density functional theory and RHF study. *Chemical Physics*, 255(2-3):165–194, 2000.

[38] P. Bour, J. McCann, and H. Wieser. Measurement and calculation of absolute rotational strengths for camphor, alpha-pinene, and borneol. *Journal of Physical Chemistry A*, 102(1):102–110, 1998.

[39] F.J. Devlin, P.J. Stephens, J.R. Cheeseman, and M.J. Frisch. Ab initio prediction of vibrational absorption and circular dichroism spectra of chiral natural products using density functional theory: alpha-pinene. *Journal of Physical Chemistry A*, 101(51):9912–9924, 1997.

[40] C.W. Deutsche and A. Moscowitz. Optical activity of vibrational origin. I. A model helical polymer. *Journal of Chemical Physics*, 49(7):3257–3272, 1968.

[41] C.W. Deutsche and A. Moscowitz. Optical activity of vibrational origin. II. Consequences of polymer conformation. *Journal of Chemical Physics*, 53(7):2630–2644, 1970.

[42] J.A. Schellman. Vibrational optical-activity. *Journal of Chemical Physics*, 58(7):2882–2886, 1973.

[43] G. Holzwart, E.C. Hsu, H.S. Mosher, T.R. Faulkner, and A. Moscowit. Infrared circular-dichroism of carbon-hydrogen and carbon-deuterium stretching modes - observations. *Journal of the American Chemical Society*, 96(1):251–252, 1974.

[44] L.A. Nafie and M. Diem. Theory of high frequency differential interferometry: Application to the measurement of infrared circular and linear dichroism via fourier transform spectroscopy. *Applied Spectroscopy*, 33:130–135, 1979.

[45] L.A. Nafie, M. Diem, and D.W. Vidrine. Fourier transform infrared vibrational circular dichroism. *Journal of the American Chemical Society*, 101:496–498, 1979.

[46] C.N. Guo, R.D. Shah, R.K. Dukor, T.B. Freedman, X.L. Cao, and L.A. Nafie. Fourier transform vibrational circular dichroism from 800 to 10,000 $cm^{-1}$: Near-IR-VCD spectral standards for terpenes

and related molecules. *Vibrational Spectroscopy*, 42(2):254–272, 2006.

[47] P.J. Stephens. Theory of vibrational circular dichroism. *Journal of Physical Chemistry*, 89(5):748–752, 1985.

[48] P.J. Stephens. Gauge dependence of vibrational magnetic dipole transition moments and rotational strengths. *Journal of Physical Chemistry*, 91(7):1712–1715, 1987.

[49] D.Y. Yang and A. Rauk. Vibrational circular-dichroism intensities by ab-initio 2nd-order Møller-Plesset vibronic coupling theory. *Journal of Chemical Physics*, 100(11):7995–8002, 1994.

[50] P.J. Stephens and F.J. Devlin. Determination of the structure of chiral molecules using ab initio vibrational circular dichroism spectroscopy. *Chirality*, 12(4):172–179, 2000.

[51] P.J. Stephens and M.A. Lowe. Vibrational circular dichroism. *Annual Review of Physical Chemistry*, 36:213–241, 1985.

[52] T.B. Nafie, L.A. Freedman. Vibronic coupling theory of infrared vibrational transitions. *Journal of Chemical Physics*, 78:7108 7116, 1983.

[53] A. Rauk. Vibrational circular dichroism intensities: Ab initio calculations. In P.G. Mezey, editor, *New developments in molecular chirality*, pages 57–92. Kluwer academic publishers, 1991.

[54] I. Lindgren. The Rayleigh - Schrödinger perturbation and the linnked-diagram theorem for a multi-configurational model space. *Journal of Physics B.: Atomic and Molecular Physics*, 7:2441–2470, 1974.

[55] M.J. Frisch, G.W. Trucks, H.B. Schlegel, G.E. Scuseria, M.A. Robb, J.R. Cheeseman, J.A. Montgomery Jr, T. Vreven, K.N. Kudin, J.C. Burant, J.M. Millam, S.S. Iyengar, J. Tomasi, V. Barone, B. Mennucci, M. Cossi, G. Scalmani, N. Rega, G.A. Petersson, H. Nakatsuji, M. Hada, M. Ehara, K. Toyota, R. Fukuda, J. Hasegawa, M. Ishida, T. Nakajima, Y. Honda, O. Kitao, H. Nakai, M. Klene, X. Li, J.E. Knox, H.P. Hratchian, J.B.

Cross, V. Bakken, C. Adamo, J. Jaramillo, R. Gomperts, R.E. Stratmann, O. Yazyev, A.J. Austin, R. Cammi, C. Pomelli, J.W. Ochterski, P.Y. Ayala, K. Morokuma, G.A. Voth, P. Salvador, J.J. Dannenberg, V.G. Zakrewski, S. Dapprich, A.D. Daniels, M.C. Strain, O. Farkas, D.K. Malick, A.D. Rabuck, K. Raghavachari, J.B. Foresman, J.V. Ortiz, Q. Cui, A.G. Baboul, S. Clifford, J. Ciolowski, B.B. Stefanov, G. Liu, A. Liashenko, P. Piskorz, I. Komaromi, R.L. Martin, D.J. Fox, T. Keith, M.A. Al-laham, C.Y. Peng, A. Nanayakkara, M. Challacombe, P.M.W. Gill, B. Johnson, W. Chen, M.W. Wong, C. Gonzalez, and J.A. Pople. Gaussian 03, 2004.

[56] E.W. Weisstein. "permutation tensor.". *From MathWorld–A Wolfram Web Resource.*, http://mathworld.wolfram.com/PermutationTensor.html.

[57] J.P. Perdew, J.A. Chevary, S.H. Vosko, K.A. Jackson, M.R. Pederson, D.J. Singh, and C. Fiolhais. Accurate and simple analytic representation of electron-gas correlation-energy. *Physical Reviews B.*, 46:6671–6687, 1992.

[58] A.D. Becke. Density-functional thermochemistry. 3. The role of exact exchange. *Journal of Chemical Physics*, 98(7):5648–5652, 1993.

[59] S.H. Vosko, L. Wilk, and M. Nusair. Accurate spin - dependent electron liquid correlation energies for local spin-density calculations - a critical analysis. *Canadian Journal of Physics*, 58:1200–1211, 1980.

[60] C.T. Lee, W.T. Yang, and R.G. Parr. Development of the Colle-Salvetti correlation-energy formula into a functional of the electron-density. *Physical Review B-Condensed Matter*, 37(2):785–789, 1988.

[61] P.J. Stephens, F.J. Devlin, C.F. Chabalowski, and M.J. Frisch. Ab-initio calculation of vibrational absorption and circular-dichroism spectra using density-functional force-fields. *Journal of Physical Chemistry*, 98(45):11623–11627, 1994.

[62] J. Gerratt and I.M. Mills. Force constants and dipole-moment derivatives of molecules from perturbed Hartree-Fock calculations. *Journal of Chemical Physics*, 49:1719–1729, 1968.

[63] J.A. Pople, R. Krishnan, H.B. Schlegel, and J.S. Binkley. Derivative studies in Hartree-Fock and Møller-Plesset theories. *International Journal of Quantum Chemical Symposia*, 13:225–241, 1979.

[64] B.G. Johnson, P.M.W. Gill, and J.A. Pople. A rotationally invariant procedure for density-functional calculations. *Chemical Physics Letters*, 220(6):377–384, 1994.

[65] L.A. Nafie. Velocity-gauge formalism in the theory of vibrational circular-dichroism and infrared-absorption. *Journal of Chemical Physics*, 96(8):5687–5702, 1992.

[66] K.L. Bak, P. Jorgensen, T. Helgaker, K. Ruud, and H.J.A. Jensen. Gauge - independent multiconfigurational self-consistent-field theory for vibrational circular dichroism. *Journal of Chemical Physics*, 98:8873, 1993.

[67] J.R. Cheeseman, M.J. Frisch, F.J. Devlin, and P.J. Stephens. Ab initio calculation of atomic axial tensors and vibrational rotational strengths using density functional theory. *Chemical Physics Letters*, 252(3-4):211–220, 1996.

[68] T.A. Keiderling. Vibrational circular dichroism. comparison of techniques and practical considerations. In J.R. Ferraro and K. Krishnan, editors, *Practical Fourier Transform Infrared Spectroscopy. Industrial and Laboratory Chemical Analysis.*, number 5, pages 203–284. Academic Press, San Diego, 1990.

[69] L.A. Nafie, T.A. Keiderling, and P.J. Stephens. Vibrational circular-dichroism. *Journal of the American Chemical Society*, 98(10):2715–2723, 1976.

[70] E.D. Lipp and L.A. Nafie. Application of fourier self-deconvolution to vibrational circular-dichroism spectra. *Applied Spectroscopy*, 38(6):774–778, 1984.

[71] J. Hilario, D. Drapcho, R. Curbelo, and T.A. Keiderling. Polarization modulation Fourier transform infrared spectroscopy with digital signal processing: Comparison of vibrational circular dichroism methods. *Applied Spectroscopy*, 55(11):1435–1447, 2001.

[72] B.L. Wang and T.A. Keiderling. Observations on the measurement of vibrational circular-dichroism with rapid-scan and step-scan FT-IR techniques. *Applied Spectroscopy*, 49(9):1347–1355, 1995.

[73] M. Urbanova, V. Setnicka, and K. Volka. Measurements of concentration dependence and enantiomeric purity of terpene solutions as a test of a new commercial vcd spectrometer. *Chirality*, 12(4):199–203, 2000.

[74] Bruker. *PMA 37 User's manual*, 2001.

[75] P.L. Polavarapu. Fourier transform infrared vibrational circular dichroism. In J.R. Ferraro and L.J. Basile, editors, *Fourier Transform Infrared Spectroscopy, Vol 4*, number 2, pages 61–95. Academic Press, Inc., Orlando, 1995.

[76] T. Kuppens. *Development of methodology to assign absolute configurations using vibrational circular dichroism.* PhD thesis, UGent, 2006.

[77] A. Aamouche, F.J. Devlin, P.J. Stephens, J. Drabowicz, B. Bujnicki, and M. Mikolajczyk. Vibrational circular dichroism and absolute configuration of chiral sulfoxides: tert-butyl methyl sulfoxide. *Chemistry-A European Journal*, 6(24):4479–4486, 2000.

[78] L.A. Nafie. Dual polarization modulation: A real-time, spectral-multiplex separation of circular dichroism from linear birefringence spectral intensities. *Applied Spectroscopy*, 54(11):1634–1645, 2000.

[79] L.A. Nafie. US 6480277. 2002.

[80] X.L. Cao, R.K. Dukor, and L.A. Nafie. Reduction of linear birefringence in vibrational circular dichroism measurement: use of a rotating half-wave plate. *Theoretical Chemistry Accounts*, 119(1-3):69–79, 2008.

[81] D.A. McQuarrie. *Statistical Thermodynamics*. Harper and Row, New York, 1973.

[82] F.J. Devlin, P.J. Stephens, J.R. Cheeseman, and M.J. Frisch. Ab initio prediction of vibrational absorption and circular dichroism spectra of chiral natural products using density functional theory: Camphor and fenchone. *Journal of Physical Chemistry A*, 101(35):6322–6333, 1997.

[83] A. Aamouche, F.J. Devlin, and P.J. Stephens. Structure, vibrational absorption and circular dichroism spectra, and absolute configuration of Troger's base. *Journal of the American Chemical Society*, 122(10):2346–2354, 2000.

[84] J.T. He, A. Petrovich, and P.L. Polavarapu. Quantitative determination of conformer populations: Assessment of specific rotation, vibrational absorption, and vibrational circular dichroism in substituted butynes. *Journal of Physical Chemistry A*, 108(10):1671–1680, 2004.

[85] PeakFit v4.12. Seasolve Software Inc. 1999-2003.

[86] R. De Gelder, R. Wehrens, and J.A. Hageman. A generalized expression for the similarity of spectra: Application to powder diffraction pattern classification. *Journal of Computational Chemistry*, 22(3):273–289, 2001.

[87] T. Kuppens, K. Vandyck, J. van der Eycken, W. Herrebout, B. van der Veken, and P. Bultinck. A DFT conformational analysis and VCD study on methyl tetrahydrofuran-2-carboxylate. *Spectrochimica acta part A - molecular and biomolecular spectroscopy*, 67:402–411, 2007.

[88] K. Lemke, S. Ballschuh, A. Kunath, and F. Theil. An improved procedure for the lipase-catalysed kinetic resolution of endo-endo-cis-bicyclo[3.3.0]octane-2,6-diol - synthesis of potential C-2-symmetric enantiomerically pure bidentate auxiliaries. *Tetrahedron Asymmetry*, 8:2051–2055, 1997.

[89] G. Mehta and K. Srinivas. Enantioselective total syntheses of the novel tricyclic sesquiterpene hydrocarbons (+)- and (-)-kelsoene.

absolute configuration of the natural product. *Tetrahedron Letters.*, 42:2855–2857, 2001.

[90] G. Mehta and K. Srinivas. A stereoselective total synthesis of the novel sesquiterpene kelsoene. *Tetrahedron Letters*, 40:4877 – 4880, 1999.

[91] M.A. Dyadchenko, V.I. Melnikova, and Pivnitskii. Fermentative hydrolysis of racemic 2-endo,6-endo-diacetoxy-cis-bicyclo[3.3.0]octane by plexaura-homomalla coral fiber - method of production of chiral prostaglandin syntons. *Zhurnal Obshei Khimi*, 56:2143–2156, 1986.

[92] N. Cramer, S. Laschat, A. Baro, H. Schwalbe, and C. Richter. Enantioselective total synthesis of cylindramide. *Angewandte Chemie-International Edition*, 44:820–822, 2005.

[93] Y.W. Zhong, C.S. Jiang, M.H. Xu, and G.Q. Lin. Bifunctional pyridyl alcohols with the bicyclo[3.3.0]octane scaffold in the asymmetric addition of diethylzinc to aldehydes. *Tetrahedron*, 60:8861–8868, 2004.

[94] Y.W. Zhong, X.S. Lei, and G.Q. Lin. Amino alcohols with the bicyclo[3.3.0]octane scaffold as ligands for the catalytic enantioselective addition of diethylzinc to aldehydes. *Tetrahedron Asymmetry*, 13:2251–2255, 2002.

[95] Y.W. Zhong, P. Tian, and G.Q. Lin. New $\beta$-amino alcohols with a bicyclo[3.3.0]octane scaffold in an asymmetric Henry reaction. *Tetrahedron Asymmetry*, 15:771–776, 2004.

[96] P.M. Henry, M. Davies, G. Ferguson, S. Phillips, and R. Restivo. Conversion of cyclo-octa-1,5-diene into 2,6-diacetoxybicyclo[3,3,0]octane by palladium(ii) chloridelead tetraacetate in acetic acid; x-ray determination of the structure of the product. *Journal of the Chemical Society Chemical Communications*, pages 112–113, 1974.

[97] M.A. Dyadchenko and K.K. Pivnitsky. Enzymes in organic synthesis. part 3. Synthesis of enantiomerically pure

prostaglandin intermediates by enzyme-catalyzed transesterification of (1SR,2RS,5SR,6RS)-bicyclo[3.3.0]octane-2,6-diol with trichloroethyl acetate in an organic solvent. *Journal of the Chemical Society Perkin Transactions I*, pages 2001–2002, 1989.

[98] B. Hungerhoff, H. Sonnenschein, and F. Theil. Combining lipase-catalyzed enantiomer-selective acylation with fluorous phase labeling: A new method for the resolution of racemic alcohols. *Journal of Organic Chemistry*, 67:1781–1785, 2002.

[99] J. Perard-Viret and A. Rassat. Synthesis of (R,R) and (S,S) bicyclo[3.3.0]octane-2,6-dione-interactions between nonconjugated chromophores. *Tetrahedron Asymmetry*, 5:1–4, 1994.

[100] H. Quast and R. Janiak. An improved synthesis of bicyclo[3.3.0]octane-2,6-dione. *Liebigs Annalen der Chemie*, 12:1305–1308, 1991.

[101] R.M. Moriarty, M.P. Duncan, R.K. Vaid, and O. Prakash. *Organic Synthesis*, 68:175–181, 1990.

[102] A.A. Hagedorn and D.G. Farnum. Bicyclo[3.3.0]octane-2,6-dione and bicyclo[3.3.0]octa-3,7-diene-2,6-dione. *Journal of Organic Chemistry*, 42:3765–3767, 1977.

[103] D.M. Hodgson, I.D. Cameron, M. Christlieb, R. Green, G.P. Lee, and L.A. Robinson. Functionalised bicyclic alcohols by enantioselective $\alpha$-deprotonationrearrangement of meso-epoxides. *Journal of the Chemical Society: Perkin Transactions*, 18:2161–2174, 2001.

[104] T. Horikawa, Y. Norimine, M. Tanaka, K. Sakai, and H. Suemune. Synthesis of optically active bicyclo[3.3.0]octane skeleton using transannular reaction. *Chemical and Pharmaceutical Bulletin*, 46:17–21, 1998.

[105] M.A. Munoz, O. Munoz, and P. Joseph-Nathan. Absolute configuration of natural diastereoisomers of 6 beta-hydroxyhyoscyamine by vibrational circular dichroism. *Journal of Natural Products*, 69:1335–1340, 2006.

[106] A. Solladie-Cavallo, C. Marsol, M. Yaakoub, K. Azyat, A. Klein, M. Roje, C. Suteu, T. Freedman, X Cao, and L. Nafie. erythro-1-naphthyl-1-(2-piperidyl)methanol: Synthesis, resolution, NMR relative configuration, and VCD absolute configuration. *Journal of Organic Chemistry*, 68:7308–7315, 2003.

[107] N.L. Allinger, Y.H. Yuh, and J.H. Lii. Molecular Mechanics - the MM3 force-field for hydrocarbons .1. *Journal of the American Chemical Society*, 111(23):8551–8566, 1989.

[108] N.L. Allinger, K.S. Chen, and J.H. Lii. An improved force field (MM4) for saturated hydrocarbons. *Journal of Computational Chemistry*, 17(5-6):642–668, 1996.

[109] T.A. Halgren. Merck molecular force field .1. Basis, form, scope, parameterization, and performance of MMFF94. *Journal of Computational Chemistry*, 17(5-6):490–519, 1996.

[110] T.A. Halgren. Merck molecular force field .2. MMFF94 van der Waals and electrostatic parameters for intermolecular interactions. *Journal of Computational Chemistry*, 17(5-6):520–552, 1996.

[111] J. Sadowski, C.H. Schwab, and J. Gasteiger. 3D structure generation and conformational searching. In P. Bultinck, H. De Winter, W. Langenaeker, and J.P. Tollenaere, editors, *Computational medicinal chemistry for drugs discovery*, number 7, pages 151–212. Marcel Dekker Inc., New York, 2004.

[112] M.D. Halls, J. Velkovski, and H.B. Schlegel. Harmonic frequency scaling factors for Hartree-Fock, S-VWN, B-LYP, B3-LYP, B3-PW91 and MP2 with the Sadlej pVTZ electric property basis set. *Theoretical Chemistry Accounts*, 105(6):413–421, 2001.

[113] A.P. Scott and L. Radom. Harmonic vibrational frequencies: An evaluation of Hartree-Fock, Møller-Plesset, quadratic configuration interaction, density functional theory, and semiempirical scale factors. *Journal of Physical Chemistry*, 100(41):16502–16513, 1996.

[114] K. Vandyck, B. Matthys, M. Willen, K. Robeyns, L. Van Meervelt, and J. Van der Eycken. Rhodium-catalyzed asymmetric conjugate

additions of boronic acids to enones using diphonane: A novel chiral bisphosphine ligand. *Organic Letters*, 8:363–366, 2006.

[115] K. Ritter. Synthetic transformations of vinyl and aryl triflates. *Synthesis*, 8:735–762, 1993.

[116] P. Van der Veken, A. Haemers, and K. Augustyns. Prolyl peptidases related to dipeptidyl peptidase IV: Potential of specific inhibitors in drug discovery. *Current Topics in Medicinal Chemistry*, 7(6):621–635, 2007.

[117] K. Augustyns, P. Van der Veken, and A. Haemers. Inhibitors of proline-specific a dipeptidyl peptidases: DPP IV inhibitors as a novel approach for the treatment of Type 2 diabetes. *Expert Opinion on Therapeutic Patents*, 15(10):1387–1407, 2005.

[118] A. Soroka, P. Van der Veken, I. De Meester, A.M. Lambeir, M.B. Maes, S. Scharpe, A. Haemers, and K. Augustyns. Synthesis and dipeptidyl peptidase inhibition of N-(4-substituted-2,4-diaminobutanoyl)piperidines. *Bioorganic & Medicinal Chemistry Letters*, 16(18):4777–4779, 2006.

[119] P. Van der Veken, I. De Meester, V. Dubois, A. Soroka, S. Van Goethem, M.B. Maes, I. Brandt, A.M. Lambeir, X. Chen, A. Haemers, S. Scharpe, and K. Augustyns. Inhibitors of dipeptidyl peptidase 8 and dipeptidyl peptidase 9. part 1: Identification of dipeptide derived leads. *Bioorganic & Medicinal Chemistry Letters*, 18:4154–4158, 2008.

[120] S. Van Goethem, P. Van der Veken, V. Dubois, A. Soroka, A.M. Lambeir, X. Chen, A. Haemers, S. Scharpe, and K. Augustyns. Inhibitors of dipeptidyl peptidase 8 and dipeptidyl peptidase 9. part 2: Isoindoline containing inhibitors. *Bioorganic & Medicinal Chemistry Letters*, 18:4159–4162, 2008.

[121] F.J. Devlin, P.J. Stephens, and P. Besse. Conformational rigidification via derivatization facilitates the determination of absolute configuration using chiroptical spectroscopy: A case study of the chiral alcohol endo-borneol. *Journal of Organic Chemistry*, 70(8):2980–2993, 2005.

[122] R.O. Duthaler. Recent developments in the stereoselective synthesis of alpha-amino-acids. *Tetrahedron*, 50(6):1539–1650, 1994.

[123] A. Peter, E. Vekes, G. Toth, D. Tourwe, and F. Borremans. Application of a new chiral derivatizing agent to the enantioseparation of secondary amino acids. *Journal of Chromatography A*, 948(1-2):283–294, 2002.

[124] C. Cappelli, S. Corni, R. Cammi, B. Mennucci, and J. Tomasi. Nonequilibrium formulation of infrared frequencies and intensities in solution: Analytical evaluation within the polarizable continuum model. *Journal of Chemical Physics*, 113(24):11270–11279, 2000.

[125] C. Cappelli, S. Monti, and A. Rizzo. Effect of the environment on vibrational infrared and circular dichroism spectra of (S)-proline. *International Journal of Quantum Chemistry*, 104(5):744–757, 2005.

[126] T. Kuppens, W. Herrebout, B. van der Veken, and P. Bultinck. Intermolecular association of tetrahydrofuran-2-carboxylic acid in solution: A vibrational circular dichroism study. *Journal of Physical Chemistry A*, 110(34):10191–10200, 2006.

[127] T. Buffeteau, D. Cavagnat, A. Bouchet, and T. Brotin. Vibrational absorption and circular dichroism studies of (-)-camphanic acid. *Journal of Physical Chemistry A*, 111(6):1045–1051, 2007.

[128] J. Sadlej, J.C. Dobrowolski, J.E. Rode, and M.H. Jamroz. DFT study of vibrational circular dichroism spectra of D-lactic acid-watercomplexes. *Physical Chemistry Chemical Physics*, 8(1):101–113, 2006.

[129] H. Izumi, S. Futamura, N. Tokita, and Y. Hamada. Fliplike motion in the thalidomide dimer: Conformational analysis of (R)-thalidomide using vibrational circular dichroism spectroscopy. *Journal of Organic Chemistry*, 72(1):277–279, 2007.

[130] M. Losada, H. Tran, and Y.J. Xua. Lactic acid in solution: Investigations of lactic acid self-aggregation and hydrogen bonding

interactions with water and methanol using vibrational absorption and vibrational circular dichroism spectroscopies. *Journal of Chemical Physics*, 128(1):14508–14700, 2008.

[131] D.R. Turner and J. Kubelka. Infrared and vibrational cd spectra of partially solvated alpha-helices: DFT-based simulations with explicit solvent. *Journal of Physical Chemistry B*, 111(7):1834–1845, 2007.

[132] A. Vargas, N. Bonalumi, D. Ferri, and A. Baiker. Solvent-induced conformational changes of O-phenyl-cinchonidine: A theoretical and VCD spectroscopy study. *Journal of Physical Chemistry A*, 110(3):1118–1127, 2006.

[133] A.A. Stolov, W.A. Herrebout, and B.J. van der Veken. Solvent effect on vibrational frequencies: cryosolution experiments and density functional calculations. *Journal of Molecular Structure*, 481:499–503, 1999.

[134] K.I. Oh, J. Han, K.K. Lee, S. Hahn, H. Han, and M. Cho. Site-specific hydrogen-bonding interaction between N-acetylproline amide and protic solvent molecules: Comparisons of IR and VCD measurements with MD simulations. *Journal of Physical Chemistry A*, 110(50):13355–13365, 2006.

[135] M. Urbanova, V. Setnicka, V. Kral, and K. Volka. Noncovalent interactions of peptides with porphyrins in aqueous solution: Conformational study using vibrational CD spectroscopy. *Biopolymers*, 60(4):307–316, 2001.

[136] P.G. Mezey. The holographic electron density theorem and quantum similarity measures. *Molecular Physics*, 96(2):169–178, 1999.

[137] G. Boon, C. Van Alsenoy, F. De Proft, P. Bultinck, and P. Geerlings. Similarity and chirality: Quantum chemical study of dissimilarity of enantiomers. *Journal of Physical Chemistry A*, 107(50):11120–11127, 2003.

[138] G. Boon, C. Van Alsenoy, F. De Proft, P. Bultinck, and P. Geerlings. Molecular quantum similarity of enantiomers of amino acids:

a case study. *Journal of Molecular Structure-Theochem*, 727(1-3):49–56, 2005.

[139] G. Boon, C. Van Alsenoy, F. De Proft, P. Bultinck, and P. Geerlings. Study of molecular quantum similarity of enantiomers of amino acids. *Journal of Physical Chemistry A*, 110(15):5114–5120, 2006.

[140] C. Reichardt. *solute - solvent interactions in solvents and solvent effects in organic chemistry.* VCH, 1990.

[141] X.L. Cao, R.D. Shah, R.K. Dukor, C.N. Guo, T.B. Freedman, and L.A. Nafie. Extension of Fourier transform vibrational circular dichroism into the near-infrared region: Continuous spectral coverage from 800 to 10 000 $cm^{-1}$. *Applied Spectroscopy*, 58(9):1057–1064, 2004.

[142] M.C. Sicilia, A. Nino, and C. Munoz-Caro. Mechanism of pyridine protonation in water clusters of increasing size. *Journal of Physical Chemistry A*, 109(37):8341–8347, 2005.

[143] M.C. Sicilia, C. Munoz-Caro, and A. Nino. Theoretical analysis of pyridine protonation in water clusters of increasing size. *European Journal of Chemical Physics and Physical Chemistry*, 6(1):139–147, 2005.

[144] F. Jensen. *Computational Chemistry.* John Wiley & Sons Ltd., Chichester, 1999.

[145] M. Losada and Y. Xu. Chirality transfer through hydrogen-bonding: Experimental and ab initio analyses of vibrational circular dichroism spectra of methyl lactate in water. *Physical Chemistry Chemical Physics*, 9(24):3127–3135, 2007.

[146] T. Burgi, A. Vargas, and A. Baiker. VCD spectroscopy of chiral cinchona modifiers used in heterogeneous enantioselective hydrogenation: conformation and binding of non-chiral acids. *Journal of the Chemical Society-Perkin Transactions 2*, (9):1596–1601, 2002.

[147] G. Longhi, S. Abbate, R. Gangemi, E. Giorgio, and C. Rosini. Fenchone, camphor, 2-methylenefenchone and 2-methylenecamphor:

A vibrational circular dichroism study. *Journal of Physical Chemistry A*, 110(15):4958–4968, 2006.

[148] F.J. Devlin, P.J. Stephens, J.R. Cheeseman, and M.J. Frisch. Prediction of vibrational circular dichroism spectra using density functional theory: camphor and fenchone. *Journal of the American Chemical Society*, 118(26):6327–6328, 1996.

[149] R.D. Singh and T.A. Keiderling. Vibrational circular-dichroism of 6-membered-ring monoterpenes - consistent force-field, fixed partial charge calculations. *Journal of the American Chemical Society*, 103(9):2387–2394, 1981.

[150] L. Laux, V. Pultz, S. Abbate, H.A. Havel, J. Overend, A. Moscowitz, and D.A. Lightner. Inherently dissymmetric chromophores and vibrational circular-dichroism - the $CH_2$-$CH_2$-C*- H fragment. *Journal of the American Chemical Society*, 104(15):4276–4278, 1982.

[151] S. Abbate, G. Longhi, S. Boiadjiev, D.A. Lightner, C. Bertucci, and P. Salvadori. Analysis of vibrational circular dichroism data in the near infrared and visible range. *Enantiomer*, 3(4-5):337–347, 1998.

[152] Nist. precomputed vibrational scaling factors, 2007.

[153] C. Cappelli, S. Corni, B. Mennucci, R. Cammi, and J. Tomasi. Vibrational circular dichroism within the polarizable continuum model: A theoretical evidence of conformation effects and hydrogen bonding for (S)-(-)-3-butyn-2-ol in $CCl_4$ solution. *Journal of Physical Chemistry A*, 106(51):12331–12339, 2002.

[154] E. Debie, T. Kuppens, K. Vandyck, J. Van der Eycken, B. van der Veken, W. Herrebout, and P. Bultinck. Vibrational circular dichroism dft study on bicyclo[3.3.0]octane derivatives. *Tetrahedron-Asymmetry*, 17(23):3203–3218, 2006.

[155] V.P. Nicu, J. Neugebauer, S.K. Wolff, and E.J. Baerends. A vibrational circular dichroism implementation within a Slater-type-orbital based density functional framework and its application to

hexa- and hepta-helicenes. *Theoretical Chemistry Accounts*, 119(1-3):245–263, 2008.

[156] A.G. Petrovic and P.L. Polavarapu. Structural transitions in polyribocytidylic acid induced by changes in pH and temperature: Vibrational circular dichroism study in solution and film states. *Journal of Physical Chemistry B*, 110(45):22826–22833, 2006.

[157] R.A.G.D. Silva, J. Kubelka, P. Bour, S.M. Decatur, and T.A. Keiderling. Site-specific conformational determination in thermal unfolding studies of helical peptides using vibrational circular dichroism with isotopic substitution. *Proceedings of the National Academy of Sciences of the United States of America*, 97(15):8318–8323, 2000.

[158] T.A. Keiderling, R.A.G.D. Silva, G. Yoder, and R.K. Dukor. Vibrational circular dichroism spectroscopy of selected oligopeptide conformations. *Bioorganic & Medicinal Chemistry*, 7(1):133–141, 1999.

[159] V. Setnicka, M. Urbanova, and S. Pataridis. Sol-gel phase transition of brucine-appended porphyrin gelator: a study by vibrational circular dichroism spectroscopy. *Tetrahedron Assymetry*, 13:2661 – 2666, 2002.

[160] V. Setnicka, M. Urbanova, and K. Volka. Investigation of guanosine-quartet assemblies by vibrational and electronic circular dichroism spectroscopy, a novel approach for studying supramolecular entities. *Chemistry - A European Journal*, 12:8735–8743, 2006.

[161] D.W. Schlosser, F. Devlin, K. Jalkanen, and P.J. Stephens. Vibrational circular-dichroism of matrix-isolated molecules. *Chemical Physics Letters*, 88(3):286–291, 1982.

[162] G. Pohl, A. Perczel, and E. Vass. A matrix isolation study on Ac-Gly-NHMe and Ac-L-Ala-NHMe, the simplest chiral and achiral building blocks of peptides and proteins. *Physical Chemistry Chemical Physics*, 9:4698–4708, 2007.

[163] K. Shin-Ya, H. Sugeta, S Shin, Y. Hamada, Y. Katsumoto, and K. Ohno. Absolute configuration and conformation analysis of 1-phenylethanol by matrix-isolation infrared and vibrational circular dichroism spectroscopy combined with density functional theory calculation. *Journal of Physical Chemistry A.*, 111:8598 – 8605, 2007.

[164] F.J. Devlin and P.J. Stephens. Ab initio density functional theory study of the structure and vibrational spectra of cyclohexanone and its isotopomers. *Journal of Physical Chemistry A*, 103(4):527–538, 1999.

[165] F.J. Devlin and P.J. Stephens. Conformational analysis using ab initio vibrational spectroscopy: 3-methylcyclohexanone. *Journal of the American Chemical Society*, 121(32):7413–7414, 1999.

[166] P.Y. Ayala and H.B. Schlegel. Identification and treatment of internal rotation in normal mode vibrational analysis. *Journal of Chemical Physics*, 108(6):2314–2325, 1998.

[167] P. Atkins and J. De Paula. *Physical Chemistry.* W.H. Freeman and Company, 2006.

[168] J.R. Durig, C. Zheng, G.A. Guirgis, and C.J. Wurrey. Conformational stabilities of 1,1-dicyclopropylethene determined from variable-temperature infrared spectra of xenon solutions and ab initio calculations. *Journal of Physical Chemistry A*, 109(8):1650–1661, 2005.

[169] C.N. Guo, R.D. Shah, R.K. Dukor, X.L. Cao, T.B. Freedman, and L.A. Nafie. Determination of enantiomeric excess in samples of chiral molecules using Fourier transform vibrational circular dichroism spectroscopy: Simulation of real-time reaction monitoring. *Analytical Chemistry*, 76(23):6956–6966, 2004.

[170] C.N. Guo, R.D. Shah, R.K. Dukor, X.L. Cao, T.B. Freedman, and L.A. Nafie. Enantiomeric excess determination by fourier transform near-infrared vibrational circular dichroism spectroscopy: Simulation of real-time process monitoring. *Applied Spectroscopy*, 59(9):1114–1124, 2005.

[171] J.T. He and P.L. Polavarapu. Determination of intermolecular hydrogen bonded conformers of alpha-aryloxypropanoic acids using density functional theory predictions of vibrational absorption and vibrational circular dichroism spectra. *Journal of Chemical Theory and Computation*, 1(3):506–514, 2005.

[172] W.J. Hehre, L. Radom, P.R. Schleyer, and J.A. Pople. *Ab initio molecular orbital theory*. Wiley, 1986.

[173] S. Reiling, J. Brickmann, M. Schlenkrich, and P.A. Bopp. Theoretical investigations on 1,2-ethanediol: The problem of intramolecular hydrogen bonds. *Journal of Computational Chemistry*, 17(2):133–147, 1996.

[174] J.S. Chen, C.C. Wu, and D.Y. Kao. New approach to IR study of monomer-dimer self-association: 2,2-dimethyl-3-ethyl-3-pentanol in tetrachloroethylene as an example. *Spectrochimica Acta Part A-Molecular and Biomolecular Spectroscopy*, 60(10):2287–2293, 2004.

[175] P.L. Polavarapu, D.F. Michalska, and D.M. BACK. On the measurement of vibrational circular-dichroism of a single enantiomer on Fourier-transform infrared spectrometers. *Applied Spectroscopy*, 38(3):438–442, 1984.

[176] P.L. Polavarapu, M. Diem, and L.A. Nafie. Vibrational optical-activity in para-substituted 1-methylcyclohex-1-enes. *Journal of the American Chemical Society*, 102(17):5449–5453, 1980.

[177] S. Abbate, G. Longhi, J.W. Givens, S.E. Boiadjiev, D.A. Lightner, and A. Moscowitz. Observation of vibrational circular dichroism for overtone transitions with commercially available CD spectrometers. *Applied Spectroscopy*, 50(5):642–643, 1996.

[178] S. Abbate, G. Longhi, L. Richard, C. Bertucci, C. Rosini, P. Salvadori, and A. Moscowitz. Vibrational circular-dichroism as a criterion for local-mode versus normal-mode behavior - near-infrared circular-dichroism spectra of some monoterpenes. *Journal of the American Chemical Society*, 111(3):836–840, 1989.

[179] K.S. Rutkowski, W.A. Herrebout, S.M. Melikova, P. Rodziewicz, B.J. van der Veken, and A. Koll. Infrared spectra and relative stability of the $F_3CH/NH_3$ H-bonded complex in liquefied Xe. *Spectrochimica Acta Part A-Molecular and Biomolecular Spectroscopy*, 61(7):1595–1602, 2005.

[180] S. Tsuzuki and A. Fujii. Nature and physical origin of CH/PI interaction: significant difference from conventional hydrogen bonds. *Physical Chemistry Chemical Physics*, 10:2584–2594, 2008.

[181] J. Hooper, V.R. Cooper, T. Thonhauser, N.A. Romero, F. Zerilli, and D.C. Langreth. Predicting C-H/PI interactions with nonlocal density functional theory. *European Journal of Chemical Physics and Physical Chemistry*, 9:891–895, 2008.

[182] J. Lundell. Anharmonic vibrational calculations for trans and cis-conformers of FC(O)OF. *Journal of Molecular Structure*, 614(1-3):87–95, 2002.

[183] H.E. Gallis, J.C. van Miltenburg, and H.A.J. Oonk. Polymorphism of mixtures of enantiomers: A thermodynamic study of mixtures of D- and L-limonene. *Physical Chemistry Chemical Physics*, 2(24):5619–5623, 2000.

[184] T. Calvet, M.A. CuevasDiarte, H.E. Gallis, and H.A.J. Oonk. Spontaneous crystallization in undercooled liquid mixtures of l-limonene plus l-carvone. *Recueil des Travaux Chimiques des Pays-Bas-Journal of the Royal Netherlands Chemical Society*, 115(6):333–336, 1996.

[185] S.F. Tayyari, M. Zahedi-Tabrizi, R. Afzali, S. Laleh, H.A. Mirshahi, and Y.A. Wang. Structure and vibrational assignment of the enol form of 3-chloro-pentane-2,4-dione. *Journal of Molecular Structure*, 873(1-3):79–88, 2008.

[186] S. Abbate, E. Castiglioni, F. Gangemi, R. Gangemi, G. Longhi, R. Ruzziconi, and S. Spizzichino. Harmonic and anharmonic features of IR and NIR absorption and VCD spectra of chiral 4-X-[2.2]paracyclophanes. *Journal of Physical Chemistry A*, 111(30):7031–7040, 2007.

# Publications and presentations

## Publications

The following papers have been published as a direct consequence of the the work undertaken for this thesis:

- **Vibrational circular dichroism DFT study on bicyclo[3.3.0]octane derivatives**
  **Elke Debie**, Tom Kuppens, Koen Vandyck, Johan Van der Eycken, Benjamin Van Der Veken, Wouter Herrebout and Patrick Bultinck
  Tetrahedron Asymmetry **2006**, 17, 3203-3218

- **Induced solvent chirality: A VCD study of camphor in $CDCl_3$**
  **Elke Debie**, Lize Jaspers, Patrick Bultinck, Wouter Herrebout, Benjamin Van Der Veken
  Chemical Physics Letter **2007**, 450, 426-430

- **Solvent effects on IR and VCD spectra of natural products: an experimental and theoretical VCD study of pulegone**
  **Elke Debie**, Patrick Bultinck,Wouter Herrebout and Benjamin van der Veken
  Physical Chemistry Chemical Physics **2008**, 10, 3498-3508

- **A Vibrational Circular Dichroism DFT study of Dipeptidyl Peptidase inhibitors**
  **Elke Debie**, Pieter van der Veken, Koen Augustyns , Wouter Herrebout, Patrick Bultinck, Benjamin van der Veken

*will be submitted for publication in Spectrochimica Acta A.*

The following papers have been published outside the scope of this thesis:

- **A selected ion flow tube study of the reactions of $H_3O^+$, $NO^+$ and $O_2^+$ with a series of C5, C6 and C8 unsaturated biogenic alcohols**
  N. Schoon, C. Amelynck, **E. Debie**, P. Bultinck, E. Arijs
  International Journal of Mass Spectrometry **2007**, 263, 127136
  *I was responsible for the conformational analysis and property calculations for all compounds*

- **A selected ion flow tube study of the reactions of $H_3O^+$, $NO^+$ and $O_2^+$ with a series of sesquiterpenes**
  F. Dhooghe, C. Amelynck, N. Schoon, **E. Debie**, P. Bultinck, F. Vanhaecke International Journal of Mass Spectrometry **2008**, 272, 137148
  *I was responsible for the conformational analysis and property calculations for all compounds*

# Presentations

- **Solute induced solvent chirality: a quantum chemical and vibrational circular dichroism investigation**
  QCB8, Universiteit Hasselt, 8th February 2008

- **A Vibrational Circular Dichroism (VCD) study of pulegone: how the solvent can influence the VCD spectra**
  VJC-9, KVCV, UA, 4th April 2008

- **Solute induced solvent chirality: a quantum chemical and vibrational circular dichroism investigation of camphor and pulegone**
  Chirality 2008, Geneva, 7th July 2008

- **A critical investigation of possible pitfalls in absolute configuration assignment using Vibrational Circular Dichroism**
  First international conference on VOA, Manchester, 27th August 2008

# Dankwoord

Aan het einde van mijn thesis zou ik graag nog een aantal mensen willen bedanken voor hun steun de voorbije 4 jaren.

Vooreerst ben ik mijn promoter, Prof. P. Bultinck en co-promoter, Prof. W. Herrebout heel veel dank verschuldigd, evenals Prof. B. Van der Veken. Zij stonden altijd klaar om mijn vragen te beantwoorden en me een duwtje te geven in de juiste richting. Daarenboven hebben zij heel veel tijd besteed aan het nalezen en verbeteren van mijn thesis.

Daarnaast wil ik mijn dank betuigen aan de fijne S3 collega's/vrienden (dikke knipoog naar Veerle). Ik heb me altijd bijzonder geamuseerd in deze groep! Sofie en Stijn bedankt voor de fijne momenten in ons bureau en bedankt dat ik altijd bij jullie terechtkon/kan. En Dieter, je bent dan wel een S4er, maar toch, ik wil bedanken voor de leuke resto momenten, ze waren de ideale werkonderbrekingen. ;)

Verder zou ik ook de groep in Antwerpen willen bedanken. Ik voelde me vanaf de eerste dag zeer welgekomen.

Uiteraard moet ik ook mijn Gentse en Waregemse vrienden bedanken. Ik heb bijzonder genoten van de momenten van ontspanning: de gezellige etentjes, de talrijke sportevenementen, de citytrips, de zotte feestjes,

de iets filosofischere gesprekken, de cinema uitstapjes,....Het is een hele geruststelling te weten dat ik bij ieder van jullie te raadde kan!

En last but not least wil ik mijn familie bedanken. Bedankt mama en papa voor de jarenlange steun. Bedankt voor de financiële steun tijdens mijn studies (en opvoeding) maar vooral bedankt voor jullie oneindige geduld, want ik ben nu eenmaal niet de gemakkelijkste persoon op aarde. Wouter, ook jou moet ik bedanken, niet alleen voor je hulp bij allerhande PC-gerelateerde problemen, maar vooral bedankt for being my brother!

Muchas gracias!